Selected Topics on the Dark Side

by

Cosmin Ilie

A dissertation submitted in partial fulfillment
of the requirements for the degree of
Doctor of Philosophy
(Physics)
in The University of Michigan
2011

Doctoral Committee:

Professor Katherine Freese, Chair
Professor Gregory Tarle
Assistant Professor David John Baker
Assistant Professor Dragan Huterer
Assistant Research Scientist Monica Valluri

To Raluca

ACKNOWLEDGEMENTS

At this point of finishing my thesis, I can certainly picture numerous people I am indebted to, and here I should thank them all with my sincere heart.

I owe my deepest gratitude to my adviser, Prof. Katherine Freese for her mentoring, teaching, encouragement and support over the years. She set an example of a great scholar and adviser, whose patience and professionalism always motivated me. The depth and breadth of her knowledge are a precious resource and I am fortunate for having first hand access to it. Needles to say, without her guidance and help this dissertation would not have been possible. At times, when I felt discouraged by what seemed like daunting tasks ahead of me, she always knew how to motivate me. And for this I will forever be grateful to her.

I would hereby like to thank Prof. David John Baker, Prof. Dragan Huterer, Prof. Gregory Tarle and Dr. Monica Valluri for agreeing to be a part of my dissertation committee.

I am grateful to Prof. Ratindranath Akhouri and Prof. James Wells for their mentorship and guidance during the early stage of my PhD.

A great deal of thanks also goes to the all the people I have closely collaborated with on the various projects included in this thesis. I am indebted to Prof. Thirtabir Biswas, Dr. Doug Spolyar and Dr. Monica Valluri for their invaluable input and insightful comments. I am grateful to Dr. Pat Scott for TLUSTY spectra for Dark Stars and to Prof. Paul Shapiro and Dr. Ilian Iliev for sharing data from simulations of DM haloes.

Many thanks go to all faculty in the physics department I had the chance to learn from. I would also like to show my gratitude to all the administrative staff in the Physics Student Services or at the MCTP that have helped me countless times. I have to express my gratefulness to the Weinberg Theory Group at the University of Texas Austin for their hospitality during the Spring of 2011 when part of this dissertation was written.

I want to thank Genes Claudiu and Luiza for their support and friendship. In my first few years at Michigan together we were "bridging" an ocean separating us from home. To Bin Wang for his true friendship over the years.

Finally, I would like to thank my family. To my parents for being supportive of all the major decisions I took. To my wife, Raluca, for so many reasons I cannot express in words. For always being there for me. She continued to believe in me and was always was able dissipate my deepest fears. Without her presence by my side, without her tremendous love and continuous support, I could never have gone this far.

TABLE OF CONTENTS

LIST OF FIGURES

Figure

LIST OF TABLES

Table

LIST OF APPENDICES

LIST OF ABBREVIATIONS

ACT Atacama Cosmology Telescope

BAO Baryon Acoustic Oscillations

BBN Big Bang Nucleosynthesis

BH Black Hole

CMB Cosmic Microwave Background

COBE Cosmic Background Explorer

dS de Sitter

DE Dark Energy

DM Dark Matter

DS Dark Stars

EW Electroweak

GMT Giant Magellan Telescope

GUT Grand Unified Theory

HST Hubble Space Telescope

IMF Initial Mass Function

JWST James Webb Space Telescope

MACHOs Massive Compact Halo Objects

NIRCam Near Infrared Camera

QCD Quantum Chromodynamics

SDSS Sloan Digital Sky Survey

SED Spectral Energy Distribution

SMDS Supermassive Dark Star

SSP Single Stellar Population

WIMPs Weakly Interacting Massive Particles

WMAP Wilkinson Microwave Anisotropy Probe

ABSTRACT

Selected topics on the Dark Side

by

Cosmin Ilie

Chair: Katherine Freese

Although significant progress has been made in the past thirty years in understanding the nature and history of our universe there are still many open questions in cosmology. Two of most conspicuous of those questions are esoterically labeled: "dark". The nature of the dark energy and what constitutes dark matter are still elusive.

The first topic discussed in this dissertation relates to Phantom Cosmology, which provides an unique opportunity to "connect" the phantom driven (low energy meV scale) dark energy phase to the inflationary (high energy grand unification scale) era. This connection becomes possible because the energy density increases with the scale factor in phantom cosmology. We present a concrete model where the energy density, but not the scale factor, cycles through several phases. The model predicts transitions from a standard radiation/matter dominated regime to a dark energy/inflationary phases, in a repetitive pattern. An interesting feature of this formalism is that once we include interactions between the "phantom fluid" and ordinary matter, the phantom phase naturally gives way to a near exponential inflationary expansion thus avoiding the Big Rip singularity.

Dark Stars (DS) are the second topic addressed in this dissertation. The first phase of stellar evolution in the history of the Universe may be Dark Stars, powered by dark

matter (DM) heating rather than by nuclear fusion. Weakly Interacting Massive Particles (WIMPs), which may be their own antipartners, collect inside the first stars and annihilate to produce a heat source that can power the stars for millions to billions of years. We investigated the properties of DS assuming that the DM particle has the required properties to explain the excess positron and electron signals in the cosmic rays detected by the PAMELA and FERMI satellites. Any possible DM interpretation of these signals requires exotic DM candidates, with annihilation cross sections a few orders of magnitude higher than the canonical value required for correct thermal relic abundance for Weakly Interacting Dark Matter candidates. Additionally, in most models, the annihilation must be preferentially to leptons. The influence of the concentration parameter of the initial DM density profile of the halos where the first stars are formed on the DS properties was also examined. This study is restricted to the DM in the star being due to simple (vs. extended) adiabatic contraction and minimal (vs. extended) capture. This is sufficient to illustrate dependence of DS properties on the cross section and concentration parameter. Our results show that the final stellar properties, once the star enters the main sequence, are always roughly the same. This is valid regardless of the value of boosted annihilation or concentration parameter in the range between c=2 and c=5: stellar mass $\sim 1000 M_{\odot}$, luminosity $\sim 10^7 L_{\odot}$, lifetime $\sim 10^6$ yrs (for the minimal DM models considered here; additional DM would lead to more massive dark stars). However the lifetime, final mass, and final luminosity of the DS show moderate dependence on boost factor and concentration parameter.

We propose two mechanisms that could explain the growth of Dark Stars to become supermassive (SMDS) with masses $\gtrsim (10^5 - 10^7) M_{\odot}$. The growth continues as long as dark matter heating persists, since dark stars are large and cool (surface temperature $\lesssim 5 \times 10^4$K) and do not emit enough ionizing photons to prevent further accretion of baryons onto the star. The dark matter may be provided by two mechanisms: (1) gravitational attraction of dark matter particles on a variety of orbits not previously considered, and (2) capture of WIMPs due to elastic scattering. Once the dark matter fuel is exhausted, the SMDS becomes a heavy main sequence star. These stars eventually collapse to form massive black holes that may provide seeds for supermassive black holes in the Universe. SMDS are very bright, with luminosities exceeding $(10^9 - 10^{11})L_\odot$. The launch of the James Webb Space Telescope (JWST) opens up the possibility of detecting Dark Stars. Using various dropout redshift selection functions we show that JWST could detect SMDS in a typical deep field survey. Specifically, at $z \sim 10$ there could be several $10^6 M_\odot$ SMDS detected in a 5.8 arcmin^2 field of view (FOV) survey with an exposure time of 10^4s. However the detection of $10^7 M_\odot$ SMDS is relatively slim at the same $z \sim 10$. This apparent paradox, that the brighter DS is less detectable can be explained by the following: at a given redshift, the formation rate of DM halos hosting the lower mass DS is higher by about one order of magnitude, therefore those objects are much more abundant. However if one uses filters with center wavelength between $1.5\ \mu\mathrm{m}$ (i.e. F150W) and $2.0\ \mu\mathrm{m}$ (i.e. F200W) of Near Infrared Camera (NIRCam) even the 10^7 have a significant chance of being observed as a dropout at $z \sim 12$, whereas the $10^6 M_\odot$ SMDS could show up in extremely large numbers (~ 200) in a typical deep field survey as an F150W dropout. At $z \sim 15$ the $10^6 M_\odot$ SMDS could still be easily detected as F200 band dropout in a JWST survey but for the more massive $10^7 M_\odot$ DS this occurrence is relatively unlikely. Therefore, we conclude that the most promising technique to use in searching for SMDS would be the F150W dropouts. Their colours in the various filters JWST could detect them are different from the colours of high redshift PopIII galaxies and this test could be used as a confirmation of the detection of a SMDS, as we shall see in Chapter V. Such an observational discovery would confirm the existence of a new phase of stellar evolution powered by dark matter.

CHAPTER I

Introduction

1.1 The Big Bang scenario

During the early universe there are several distinct epochs, each with their unique observational signatures and imprint on the future stages of the cosmological evolution. The Big Bang is generally thought to be the event that is responsible for the creation of our universe. This is indicated by all large scale structures being subject to what is generally called the Hubble flow. Derived based on experimental data in 1929 by Edwin Hubble [1] and confirmed in the entire cosmological data available to date, this phenomenon describes the trend of galaxies and other large scale structures to recede from one another, as fragments of an explosion would. Assuming the universe is homogeneous (looks smooth at large scales) and isotropic (no preferred direction) its evolution is described by the Friedmann equation: $\Omega + \Omega_k = 1$. Where $\Omega = \frac{\rho}{\rho_c}$ and ρ represents the energy density of matter, radiation and any other exotic sources (such as Dark Matter (DM) and Dark Energy (DE)) combined. Ω_k could be defined in terms of the spatial curvature of the Universe. A value of $\Omega_k = 0$ would imply a spatially flat universe with a density equal to the critical density, ρ_c. The situation where $\Omega_k < 0$ would describe a closed universe (with positive spatial curvature), whereas $\Omega_k > 0$ corresponds to the case of an open universe, with negative curvature. The

[1] It is interesting to note that the possibility of an expanding universe and the derivation of its expansion rate was actually derived based on general relativity by Georges Lemaitre in 1927

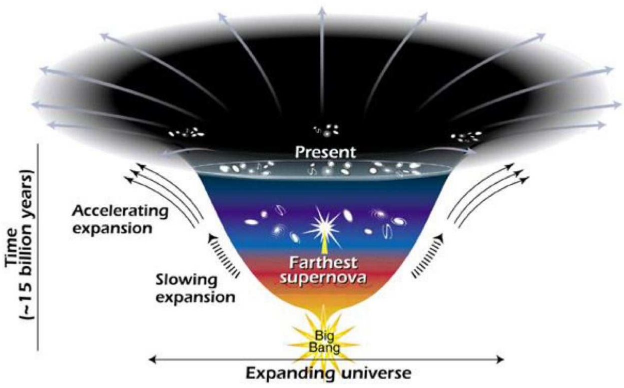

Figure 1.1: Illustration describing the different expansion phases of the universe. Image Credit: NASA

Wilkinson Microwave Anisotropy Probe (WMAP) team has produced amazingly accurate results describing the various contributions to Ω for the past 8 years, improving with each set of data released our knowledge of the cosmological parameters. We believe now that the universe today is dominated (72%) by some strange component called Dark Energy. It is a non-clumpy component, uniformly distributed over all scales. This is responsible for the current acceleration of the expansion of the universe, effectively providing a repulsive type of gravity. Roughly 23% of the energy density of the universe today is due to Dark Matter and the rest 4.6% is comprised of baryonic matter. This is summarised in Fig. 1.2. As all of the numbers add to almost 100% we can confidently conclude that the universe is very close to being flat. There is no room for Ω_k to deviate from zero significantly.

One of the most important successes of the Big Bang paradigm is the prediction of the primordial abundance of light elements. The most prevalent chemical element in the universe is, as expected, the lightest one: hydrogen. This constitutes about 75% of all the baryonic matter. Helium-4 ($^4\mathrm{He}$) constitutes roughly the other 25%. The other elements combined account for much less than 1% of the matter in the universe. Heavier elements can and are actually produced inside the stars, as results of fusion reactions. However, only a minute fraction of the $^4\mathrm{He}$ (the second most abundant element in the universe by far) was

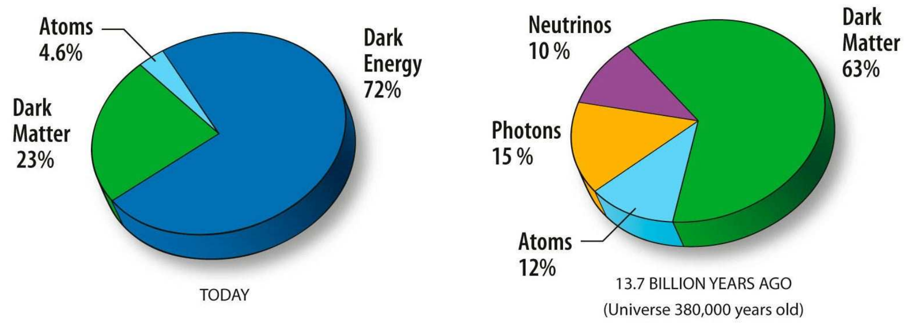

Figure 1.2: WMAP data revealing the contents of the Universe. Note that the energy density of various components is diluted by cosmic expansion at different rates, therefore earlier times would have a completely different energy density budget, as illustrated by the left panel. Image Credit: NASA / WMAP Science Team

produced by stars. Assuming that the stars were able to produce most of it over predicts the observed mass-to-light ratio of the observable universe by a couple of orders of magnitude. In other words, if stars were indeed the source of all the $^4\mathrm{He}$ we observe in the universe today, then, on large scales the universe would have appeared much brighter. We are lead to conclude that actually most of $^4\mathrm{He}$ is primordial in nature, having being produced in the early universe, when the temperature dropped below its the binding energy (~ 28MeV).

This remarkable theory that has been formulated to predict the abundance of primordial elements is called Big Bang Nucleosynthesis (BBN). The original idea is due to *Gamow* (1946). Since then numerous improvements have been made, and elaborated numerical codes have been developed to calculate the abundances of primordial elements. Its results depend on three parameters: i) the half life of the neutron ($\sim$10 minutes), ii) the number of light neutrino species and iii) the density parameter, η, which is a measure of the present ratio between the number density of baryons and number of photons in the universe. Of the three parameters listed above, η was the least constrained at the time the first predictions of BBN were made. Surprisingly, one finds that roughly the same value of η (4-7 10^{-10}) can be used to fit the values for the abundance of light nuclei predicted by BBN with observations. Admittedly the dependence of the BBN results on this parameter is small, being only logarithmic. But the fact that there is such a great concordance between the various four possible ranges that could be used to fit the observed values of abundances of primordial deuterium (D), Helium-3 ($^3\mathrm{He}$), Helium-4 ($^4\mathrm{He}$) and Lithium-7 ($^7\mathrm{Li}$) is considered as a clear indication that the Big Bang scenario and its implications could be used to describe our universe to times as far back as 10^{-2} seconds after the Big Bang, when nucleosynthesis is believed to take place. That age (10^{-2}s) corresponds to an energy scale of 10 MeV when the average temperature of radiation in the universe was 10^{10}K. This might seem high, but from a particle physics point of view those are very moderate energies. If during its early days BBN was regarded as an indication that the Big Bang model is correct, nowadays it is used to place indirect bounds on the values of both cosmological and particle physics parameters. Using only the measured value of primordial abundances for light elements and assuming that the BBN scenario holds, one can actually set bounds on present day cosmological quantities. One such example is the density of baryons (Ω_{B}), which is directly related to the density parameter, η. Regarding the particle content of the Universe, BBN sets bounds on the number of light neutrino species. Therefore confronting BBN predictions with observations also serves as a probe for the conditions in the early Universe.

1.1.1 Universe pre-BBN

Before BBN the universe underwent several important phase transitions. First, the quarks hadronized (formed nucleons and mesons) at an energy of around 1GeV, corresponding roughly to an universe 10^{-6} seconds old. Additionally, particle physics theory predicts that the Electroweak (EW) symmetry of the Standard Model must be broken at energies lower than $\lesssim 1$ TeV. This corresponds to an age of the Universe of 10^{-12} seconds. The Higgs mechanism is the most widely accepted scenario for the spontaneous EW symmetry breaking. At higher energies the Electromagnetic and Weak forces are unified in a single force, with massless force carriers. At lower energies some of the force carriers acquire mass along with the fermions (matter particles) of the theory. From this energy scale until the next interesting phase transition that *might* occur in the early universe lies a huge desert spanning about *twelve* orders of magnitude!

The EW theory along with Quantum Chromodynamics (QCD) survived the test of time very well, passing all experimental tests they were subjected to. This theory describing three of the four fundamental forces of nature (the electromagnetic, the weak and the strong forces) became known as the Standard Model of Particle Physics. Its based on a beautiful concept, the one of symmetry. We cannot be sure that nature works this way, but to the present day we do not have any compelling reason to believe otherwise.

In what is reminiscent of Kepler's model of the Universe based on Pythagoras Music of Spheres, physicists use the symmetry patterns found in group theory to match patterns found in nature. Grand Unified Theories are an attempt to tie together the EW and strong forces of the standard model. The energy scale where this phase transition is thought to happen is $\sim 10^{16}$GeV (GUT scale) and corresponds to an universe 10^{-35} seconds old. Quantum Field Theory predicts that the coupling constants (or the strength) of forces mediated by the exchange of fields (such as the gauge bosons of the standard model) change with the energy scale one probes. Approaching the GUT scale the couping constants of the EW and strong forces are almost converging. It is worth noting that in supersymmetric extensions of the SM this match of the strength of the three forces can be made more precise.

As opposed to the EW phase transition discussed before the phase transition responsible for the end of grand unification produces unwanted relics, such as magnetic monopoles. Those are neither observed nor allowed by classical electromagnetism as described by Maxwell's equations. The pragmatic approach would be to argue that actually classical electromagnetism could be easily modified to accommodate the presence of a magnetic charge (monopole). Moreover, this would render Maxwell's theory even more symmetric, as now the electric and the magnetic field could be interchanged (electric-magnetic duality).

Therefore there is no reason to immediately dismiss the possibility of magnetic monopoles based solely on theoretical grounds. If anything, our approach of treating physics based on symmetry principles should favour their existence. However estimating the relic abundance of those magnetic monopoles would imply a total value for the density parameter Ω much greater than unity. At the time those calculations were first made an exact value for Ω was not known, but there was an upper bound ($\Omega \lesssim 6$) based on the lower bound on the age of the universe. Therefore, if GUT were right, they would have been inconsistent with cosmological data, as the monopoles would overclose the universe. We now know that actually Ω is very close to unity, so this problem is only made worse.

We will shortly see in Section 1.2.1 that one possible resolution to this problem comes in the form of a phase of a very rapid exponential expansion of the universe that must occur around the GUT scale. During this phase those relics would be "washed away", as their abundances are greatly diluted by this fast expansion.

1.1.2 Universe post-BBN

As the universe expanded, the radiation was no longer the dominant component, giving way to matter. The moment the two had comparable contributions to the energy density of the universe is called matter radiation equality and happened when the universe was roughly 1.8×10^{12} seconds (only 56000 years) old. This might seem like a lot, but remember that the age of the universe today is estimated to be ~ 13.7 Gyrs, roughly a million times older than it was at the epoch of matter radiation equality.

As the nuclei and electrons started to cool enough, they begun forming neutral atoms. This is a very important event in the cosmological history of the universe because it marks how far back in time we can look with any instrument that is sensitive to photons. Prior to this event the universe was a dense soup of charged particles and radiation. The latter would have had a very short mean free path, scattering off of charged particles extremely often. Therefore the Universe before this epoch was opaque to radiation. However, as neutral atoms were formed, this scattering became inefficient leaving the primordial radiation from the big bang to travel through space unhindered. This radiation, called the Cosmic Microwave Background (CMB), offers the best clues regarding the early universe.

The experimental discovery of the CMB radiation is among the most fortuitous accidents in modern science. Predicted in 1948 by George Gamow (*Gamow*, 1948), Ralph Alpher, and Robert Herman (*Alpher and Herman*, 1948) the CMB become one of the most important clues we have regarding the early universe. They estimated that this radiation should have had a temperature of 5K today, assuming it was left over radiation from the Big Bang. The mainstream physics community had yet to accept the Big Bang theory and with the technology available at the time, CMB radiation was not readily detectable. During the 1960s this idea was revised by Yakov Zel'dovich and Robert Dicke independently when it became clear that CMB temperature should have very small (one part in 10000) inhomogeneities due to quantum fluctuations.

Only in 1964 a feasible proposal for the detection of CMB was put forth by A.G. Doroshkevich and Igor Nivikov. The same year a Dicke radiometer started to be built at Princeton by David Todd Wilkinson and Peter Roll for the purpose of measuring the CMB radiation. In 1965 Arno Penzias and Robert Woodrow Wilson begun using a Dicke radiometer for radio astronomy and communication satellite experiments. After several attempts to calibrate their instrument they realized that this would have been impossible. There was an excess 3.5K antenna temperature, which corresponded almost precisely to the predicted temperature of the CMB! This was one of the earliest experimental indications that the Big Bang model is correct.

Interest in the anisotropies of this radiation became increasingly large, as it was realized that those are the seeds of the gravitationally bound structures that are so apparent in the universe today at scales of $\lesssim 100$ Mpc: galaxies, clusters, etc. In 1989, the first space based instrument designed to study CMB was launched by NASA aboard the Cosmic Background Explorer (COBE) satellite. In 2001 this was replaced by WMAP and in 2009 the Planck satellite was launched by the European Space Agency. Preliminary data from Planck has already been released and made the community very optimistic regarding the first complete set of data that is expected to be released in 2012. Those three experiments are just the most known of very long list of experiments that have as a mission the study of the CMB. In Fig 1.3 one can see the different levels of detail in the measuring of the CMB radiation over the years.

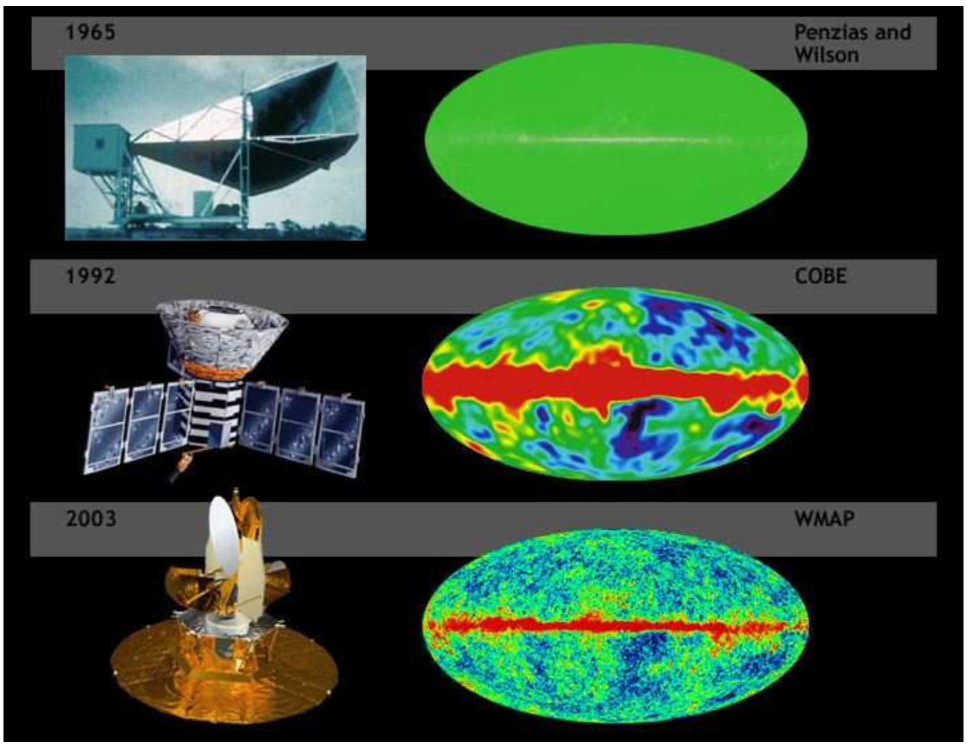

Figure 1.3: CMB temperature as measured over the years. In the lower two pictures the color scale is chosen in such a way to magnify the inhomogeneities found. One should remember that they are less than one part in 10^5. Image Credit: NASA / WMAP Science Team.

The history of the universe after this "surface of last scattering" can be best summarized in Fig. 1.4. Between moment radiation and matter became decoupled, which in the figure corresponds to the slice labeled Afterglow Light Patterns (380,000 yrs after the Big Bang) the universe went through what is called the Dark Ages, as there were no stars yet formed. Around 400 million years after the Big Bang the first stars were born. This event will be a major topic of my dissertation. The influence of DM heating on the formation of the first stars is discussed at length in Chapters III-V and introduced in later in the Introduction in Section 1.4 .

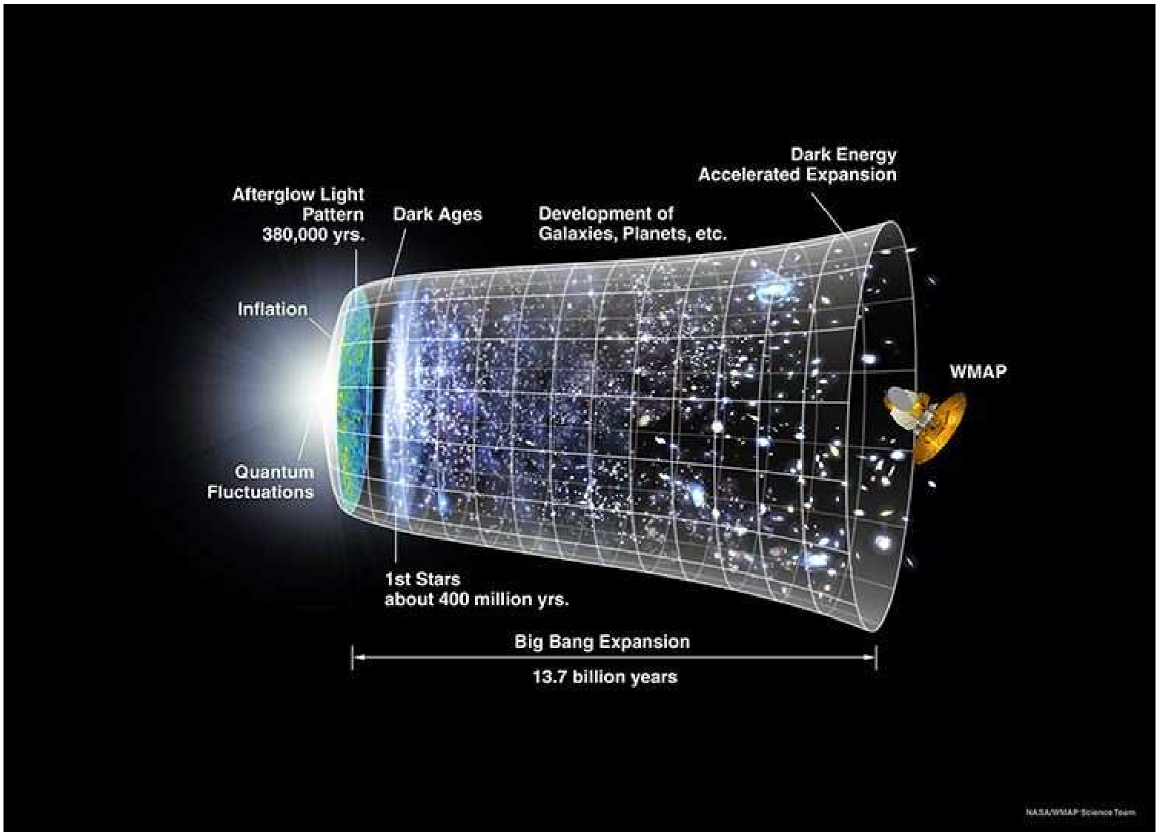

Figure 1.4: Time Line of the Universe: Very shortly after the Big Bang a phase of rapid exponential expansion occurred. The quantum fluctuations were stretched by an enormous factor during that age and they eventually formed the seeds of large scale structures we see today, such as Galaxies, Clusters, etc. Those were formed as the universe cooled enough for gravitational instabilities to start growing. Approximately 9 billion years ago a new phase of accelerated expansion begun due to DE becoming the dominant component. Image Credit: NASA / WMAP Science Team.

1.1.3 Limitations of standard Big Bang scenario

As compelling as the Big Bang idea would be, one has to recognize several of its drawbacks. Asides from the monopole problem which would arise if one tries to include a grand unified theory of the EW and strong forces within a standard cosmological evolution there are several other problems one would need to address. First if we imagine unwinding the cosmic time closer and closer to the Big Bang event itself, the energy density becomes unbound, in other words we encounter an initial singularity. Phenomena at that point can no longer be described coherently with the physical theories we have under control. Even before reaching a cosmological time of zero (corresponding to the Big Bang), as we approach the Planck energy scale (10^{19}GeV), general relativity (GR) becomes just another classical theory in desperate need of quantization. Above the energy scale set by the Planck mass, $M_P \sim 10^{19}$GeV, quantum fluctuations of the gravitational (metric) field can no longer be neglected. As one approaches the Planck scale the non-renormalizbility of General Relativity (GR) becomes transparent, rendering the theory incapable of making any predictions.

While string theory and its extension M-theory are good candidates for techniques to quantize gravity, they too have their limitations. One trades the lack of predictive power of a nonrenormalizable theory for the extremely large number ($\sim 10^{500}$) of possible background solutions (vacua) of string theory.

Even from a phenomenological standpoint the Big Bang model suffers from several shortcomings:

The horizon problem: Our observable universe, the size of which is set by the value of the present horizon scale ($\sim 10^{28}$cm), is homogeneous and isotropic. The best indication of this is the uniform temperature (2.72 K with a fractional variation not exceeding 10^{-4}) of the CMB radiation as measured by WMAP. Explaining this uniformity runs into immediate trouble due to the causality principle. If the expansion of the universe is decelerated, as a standard Big Bang scenario would predict, then points that are in causal contact now would have started as being causally disconnected. Therefore homogeneity cannot be explained without involving an extreme fine tuning of the matter distribution.

The flatness problem: This relates to the unnaturally large value of the radius of curvature of the universe compared with the Hubble scale at early times. As mentioned before, CMB data indicates that we live a universe very close to being flat, with a present value for Ω_k very close to zero. The important thing to realize here is that at earlier times the universe would have been even flatter! This is due to Ω_k increasing with the scale factor (as opposed to all the other contributions to Ω that either decrease or remain constant) and therefore increasing with cosmic time. It is hard to justify such a the small value for the initial curvature of the universe. To put it in numbers, $\Omega_k \lesssim \mathcal{O}(10^{-60})$ at the Planck epoch. Physicist have a hard time accepting unnaturally small numbers, especially if they come in the form of initial conditions.

Initial Perturbations: The structures we observe in the universe today indicate that at scales $\lesssim 100$Mpc our universe inhomogeneous. The seeds of those structures are generated by primordial inhomogeneities in the matter distribution of the early universe. Those tiny fluctuations grow to ever larger structures via gravitational instabilities in a hierarchical fashion, i.e. larger structures forming latter. CMB data constrains the value of the initial inhomogeneities. The overdensity of those primordial perturbations (difference between the value of the density of those structures and the average density of the universe at a given epoch) has to be less than a part in 10^5. Invoking a mechanism that would produce those perturbations during the early universe and maintain them to be so uniform, runs again into conflict with causality. The Hubble radius (H^{-1}) determines the size of a patch where causality operates. Perturbations of modes with physical wavelength larger than the horizon scale cannot be causally connected, as they are “outside of the horizon”. Modes with physical wavelengths corresponding to the large scale structures we see today would cross outside of the horizon somewhere around the epoch of matter radiation equality. Therefore at earlier times they could not have been causally connected, unless somehow they reenter the horizon. This would require modifying the standard Big Bang paradigm.

1.2 Connecting Dark Energy and Inflation

1.2.1 Inflation

As we have just seen, the Big Bang scenario suffers from serious drawbacks. A very elegant solution has been put forth in 1980 by Allan Guth (*Guth*, 1981) to address the magnetic monopole problem of GUT theories. He postulated that the universe underwent a rapid phase of exponential expansions when it was about 10^{-36} second old. This phase is extremely short lived, and in most models of inflation it must end when the age of the universe is roughly 10^{-32} seconds.

With this modification, the Universe we see today could have originated in the same causal patch, therefore most of the problems of the standard Big Bang model we have listed in Section 1.1.3 are addressed. During this phase the Hubble rate (a parameter that determines how fast the scale of the universe changes) is relatively constant, leading to an exponential expansion. For this reason this epoch is also known as the de Sitter (dS) phase, which would be the solution for a universe dominated by a constant positive energy density. Causally connected patches are before the inflation much smaller (10^{84} times!) than the size of the region corresponding to our observable universe extrapolated back at that epoch. This is the main reason behind the flatness horizon problems. However an inflationary era would stretch those causal patches to sizes large enough to encompass the patch corresponding to our observable universe.

In order to be able to successfully address the flatness and horizon problems of the Big Bang scenario, during inflation the universe must have expanded roughly by a 10^{26} factor. This is usually quoted as a requirement of at least 60-efoldings. At the end of this phase the universe must enter a “reheating” stage where the particles of the standard model are generated from quantum fluctuations of the inflaton field.

There are so many realizations of this idea in the literature that an attempt to summarize them all here would be almost impossible. We will refer the reader to the excellent review by *Lyth and Riotto* (1999). In any case most models fall under three different scenarios, depending on the shape of the potential for the inflaton field. For a schematic description of the inflaton potentials see Fig. 1.5. First is the “old inflation” scenario, where the decay of a metastable vacuum state, in which the inflaton field is trapped, is responsible for inflation. This first order phase transition has a very common counterpart in day to day life: boiling of water. Bubbles (or domains) where the inflaton field is in its true vacuum are nucleated via quantum tunneling effects. Even if a feature of this model is an accelerated expansion there is one immediate problem: all the energy that would be available for the generation of the particle fields during a potential “reheating” stage is concentrated in the walls of the bubble. Unfortunately, the expansion rate is so large that the bubbles have no chance of ever colliding, therefore leaving the universe empty.

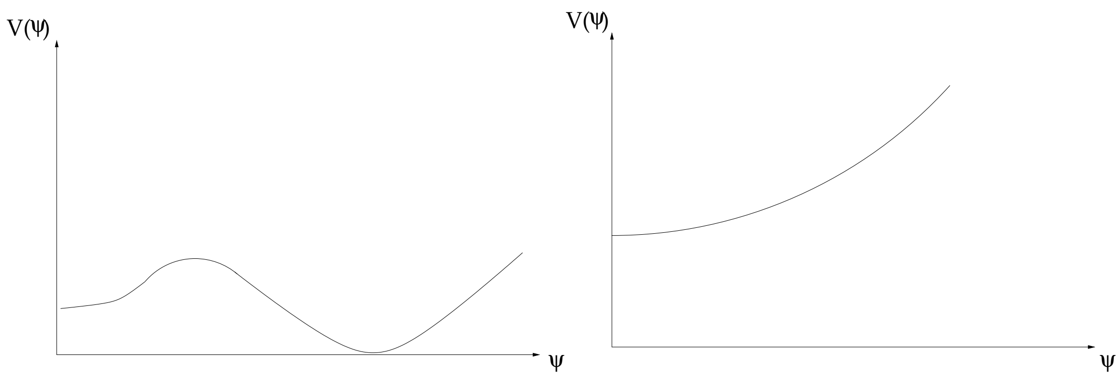

Figure 1.5: Schematic shape of the inflaton potential. Left Panel: This corresponds to the “old inflation” scenario, where at the first the field is trapped in a false vacuum state and tunnels to the true vacuum via bubble nucleation. Right Panel: This would be a generic potential for “chaotic inflation”.

In recent years the “old inflation” scenario has been revisited by *Freese and Spolyar* (2005). In this model, called chain inflation, the inflaton field tunnels through a succession of false vacua states (at least ~ 180) and reheating is achieved at each stage. However, shortly after Guth’s proposal and the realization that it would lead to an empty universe, another solution to the reheating problem of “old inflation” was proposed: “new inflation”. This is based on removing the false vacuum state altogether, and flattening the potential in its initial phase, i.e. a Coleman-Weinberg type potential. In this case there is an initial phase of slow roll, where the potential is relatively flat. This will lead to the exponential expansion phase. Reheating is achieved by quantum fluctuations of the inflaton field once it reaches the minimum of the potential.

The third broad class of inflationary models is called “Chaotic inflation”. Its name is illustrative, as the initial conditions for the inflaton field are almost arbitrary, albeit its value is constrained to be larger than the Planck scale (for this reason sometimes this class of models is referred to as “large field” models). Other than that, the scalar field responsible for inflation in this class of models could have changed from one spatial patch to another, leading to a very interesting global structure of the universe. To state it differently, chaotic inflation cold lead to a very inhomogeneous universe on scales much larger than our observable universe but extremely homogeneous (as required by CMB data) for scales corresponding to our observable domain!

One might ask, and rightfully so, why a treatment of inflation within the formalism of classical general relativity works so well. Depending on the energy scale set by the inflaton field potential, quantum corrections to GR can become relevant. If the scale of inflation is around the GUT scale, quantum corrections to GR are small, as we are still four orders of magnitude below the Planck scale, where quantum fluctuations for gravity can no longer be neglected. It is interesting to note here that one of the first realizations of a scenario where the universe went through a brief phase of exponential (de Sitter) expansion was proposed by *Starobinskiĭ* (1979) in the context of studying the importance of quantum corrections to the Hilbert-Einstein action for gravity in the early universe.

For completeness we should mention the possibility of hybrid inflation models, where more than one scalar field is invoked. Model building in this type of scenarios is motivated by the multitude of scalar fields that are present in String Theory and its extensions.

1.2.1.1 Constraining Models of Inflation

With more and more precise measurements of the CMB radiation and galaxy surveys such as Sloan Digital Sky Survey (SDSS), it became possible to constrain models of inflation (although it is still impossible to break the degeneracies between the many different models that can lead to the same predictions for observables). There are several generic predictions of inflationary models, almost independent of their class. Among those are: i) Flatness of the universe, ii) nearly scale invariant power spectrum of primordial curvature perturbations and iii) long-wavelength gravitational waves.

The following parameters of any inflationary model should be within bounds set by WMAP+SDSS (and later by Planck) or else that particular model is ruled out. A detailed discussion of those parameters and how they are measured would set us off track, so we resume here with listing only the main ideas. The interested reader could find a more comprehensive discussion in *Komatsu et al.* (2009) and references therein for instance.

- *The spectral index of the primordial curvature perturbations*, n_s[2]. A purely scale invariant power spectrum (Harrison-Zel'dovich-Peebles spectrum) would correspond to $n_s = 1$. This would be the case if the potential during inflation would be exactly flat. However, most inflationary model predict slight deviations from this. A value slightly greater than one is referred to as perturbation with a slightly blue-tilted spectrum, whereas values for $n_s \lesssim 1$ correspond to slightly red-tilted spectra. In a general, single field inflation model the spectral index is given by the following combination of the inflaton field potential and its derivatives:

$$1 - n_s = 3M_{Pl}^2(V'/V)^2 - 2M_{Pl}^2(V''/V)$$

- *The running index*, $dn_s/d\ln k$. A pure power low spectrum is equivalent to the running index being identically zero. However if one allows for the possibility of the running of the spectral index, WMAP data places quite strong constraints.

[2] n_s is also commonly referred to as the tilt of the spectrum.

In models that do not include tensor (gravitational) perturbations the value of the $dn_s/d\ln k$ to be in the range 0.034 ± 0.026. If one includes data from Baryon Acoustic Oscillations (BAO) and the measurement of the Hubble constant (H_0) the limits change slightly, but not significantly. There is still no compelling evidence for the running of the spectral index, nor is this possibility unequivocally ruled out.

- *Tensor to scalar ratio, r.* This quantity is defined as the ratio between the amplitude of relic gravitational waves from inflation and the amplitude of primordial curvature perturbations. For this parameter only upper bounds are obtained from WMAP data. Allowing for the running of the spectral index WMAP+BAO+H_0 measurements restricts $r < 0.49$ at 95% confidence limit (CL), whereas in scenarios where the running of the spectral index is set to zero the bounds become $r < 0.24$ at the same 95% CL.

For completeness, we mention that there are other parameters that can be used to constrain models of inflation. One of the most important general prediction of inflationary models is the near gaussianity of primordial fluctuations. If the curvature perturbations would be purely gaussian, as is the case for most inflationary models, then all the information about the primordial perturbations would be contained in the two point correlation function. All the other correlators would be either zero or related to the two point function. Non-gaussianity would imply for instance a nonzero three point function, also known as bi-spectrum. To parametrize this one commonly uses a non-linear parameter, f_{NL}. Single field slow roll inflation models have the feature that f_{NL} coefficients are suppressed by the slow roll parameters, rendering them unobservable. Whether or not the fluctuations in the CMB radiation show signs of non-gaussianity is still a subject of debate. Data from the Planck satellite will hopefully settle this issue.

1.2.2 Dark Energy

The possibility of a constant vacuum energy (i.e. cosmological constant) was first considered by Einstein. When he formulated general relativity he quickly realized that ordinary matter alone would have led to a scenario where the universe would have either collapsed or expanded forever. At that time, about a decade before Hubble made his discovery that galaxies recede from one another, it was believed that the universe is quasi-static. The addition of simple cosmological constant as a source term to Einstein's equations would have solved the problem. The Universe could be in a frozen state (static) at the expense of introducing a vacuum energy of a precisely tuned value to counteract for the effects of the gravity of the matter fields. However after Hubble's discovery this scenario was ruled out. Today this idea of an expanding universe is so soldered into our consciousness that one would find it hard to believe that there were at least several interesting attempts to refute Hubble's claim. One such example is Fritz Zwicky's theory of "tired light" proposed in 1929, the same year as Hubble's discovery. Zwicky postulated that the photons emitted from galaxies farther away seem redder (less energetic) not due to the recessional velocities of those sources with respect to us but rather to the photons colliding with other particles and loosing energy.

However, once Hubble's conclusion became widely accepted there was no need for a cosmological constant any longer, and that term started collecting dust in cosmology textbooks. That is until 1998 when it came back with a vengeance. What Einstein wrote to Lemaître in 1947 seems very ironic now: "The introduction of such a constant implies a considerable renunciation of the logical simplicity of the theory... Since I introduced this term, I had always a bad conscience... I am unable to believe that such an ugly thing should be realized in nature." Ugly or not this term is realized in nature, as first indicated by the data published in 1998 by the High-z Supernova Search Team. This suggested that the expansion of the universe is actually accelerated. In later years this fact was confirmed by the WMAP satellite data on CMB anisotropies, which indicates that the universe is very close to being flat, i.e. the energy density of all of its components must add up to a critical value, ρ_c. Well before the WMAP satellite was launched it was estimated based on dynamical determinations that dark matter and ordinary matter (components that clump to form structures) could not account for more than 30% of the critical energy density. As the photons and all other light degrees of freedom have a negligible contribution to the energy budget today, one is led to conclude that, in order for the universe to be flat, as indicated by the WMAP data there must be some other, yet unaccounted for component, dark energy.

Both supernovae data and the WMAP data converge on the same value for the contribution to the total energy density of DE. This fluid with negative pressure must account for roughly 73% today. One major problem is related to the value of the cosmological constant, which is incredibly small compared to what one would expect by quantum field theory. If the vacuum energy is due to the quantum fluctuations of all fields, then its natural value is of order unity, if expressed in reduced Planck units. But its measured value is 120 of orders of magnitude lower! This is a huge discrepancy and the cosmological constant problem remains one of the most important open problems in physics. One should remember that the value of the energy density of the universe today is extremely small compared to the Planck energy scale. As the universe expanded its energy density was vastly diluted.

Another problem can be restated in terms of what has been coined as the " coincidence problem". Basically, if DE would have started to dominate the universe earlier than it did, then gravitationally bound structures such as galaxies would not have been formed. Realizing this, some physicists have proposed solutions to the cosmological constant problem based on the anthropic principle.

Another problem, perhaps less stringent, would be to explain the nature of the dark energy component. Even if WMAP data strongly suggests that DE is indeed a constant, and therefore does not evolve dynamically, an explanation for its source is required. This concordance model of the universe became known as ΛCDM. However a dynamical scenario for DE is not ruled out yet. Therefore models where DE is due to some dynamical field are still actively researched. Among those are the quintessence class of models where a new light scalar field is responsible for the current accelerated expansion. The equation of state, defined by the ratio between the pressure and energy density of a component, reads for a cosmological constant: $w = p_\Lambda/\rho_\Lambda = -1$. Phantom models (with $w < -1$) are extremely intriguing. First, WMAP-7 data for the equation of state of DE actually favors a phantom type scenario as the quoted value of w is -1.1$\pm$0.14!

Usually the fate of a universe with a phantom driven expansion is extremely different than that of the case of a cosmological constant. In the latter case the universe would become ever colder, and given enough time, most of what we can observe today would get outside of our horizon. We would still have the stars in the Milky Way and the local cluster to gaze at, but telescopes pointing at other galaxies far away would "soon" no longer be able to observe them (as they would no longer be in our causality patch). A very sorrow end for an universe that started with a Big Bang. However, phantom models typically end in the Big Rip singularity. As we move forward in time and the scale factor expands, the energy density of phantom fields increases indefinitely. Therefore all bound structures will be torn apart by those tremendous energies. We should mention however that a consistent quantum description of phantom fields is extremely delicate, as they suffer from vacuum instabilities.

1.2.3 One possible connecting scenario

Phantom Cosmology provides an unique opportunity to "connect" the phantom driven (low energy meV scale) dark energy phase to the (high energy GUT scale) inflationary era. This is possible because the energy density increases in phantom cosmology. In Chapter II we present a concrete model where the energy density, but not the scale factor, cycles through phases of standard radiation/matter domination followed by dark energy/inflationary phases, and the pattern repeating itself. An interesting feature of the model is that once we include interactions between the "phantom fluid" and ordinary matter, the Big rip singularity is avoided with the phantom phase naturally giving way to a near exponential inflationary expansion. This effectively provides a connection between the accelerated expansion we observe today and the inflationary era in the past. The scale factor continues to grow from one cycle to the next (there is no ”turnaround”). In order to achieve this model we postulated the existence of some ‘hidden’ sector matter coupled to a ghost like scalar field. This mechanism is responsible for a super-accelerated phantom expansion. Allowing for hidden sector particles to be converted to light degrees of freedom of the standard model ameliorates the phantom behavior, effectively transitioning to a de Sitter like expansion, therefore avoiding the Big-Rip singularity. Although dominated by radiation, in this phase all the energy densities remain constant. Therefore, if most of the cosmological perturbations are generated during this exponential inflationary era, the spectrum is expected to be scale invariant. Even if not favored by the data, this is still a possibility. Another possibility would be to have some of the fluctuations generated during the phantom phase which will show up as a blue tilt in the spectrum. In that case we will see a running of the tilt which could be a unique possible signature of the model.

In order to achieve the cyclic behavior we have postulated that the coupling between the ghost scalar field and the hidden sector is constant piecewise. This procedure might seem ad-hoc, but it is just the simplest possibility. We found that no fine tuning seems to be involved when requiring to have a long enough radiation/matter dominated phase. It is also worth mentioning that the “smallness” problem associated with dark energy is circumvented. The only parameter we need in order to describe the current acceleration is the coupling between the hidden sector and the ghost field, and it has a value not much greater than one.

1.3 Dark Matter

1.3.1 Evidence of its existence

In 1933 Fritz Zwicky (see *Zwicky*, 1933, 1937) obtained the first evidence of the existence of significant amounts of non-luminous matter by studying Coma cluster of galaxies and estimating its mass. At the time, there were two different methods to determine the mass of clusters of nebulae: i) based on their measured luminosities and ii) based on the study of the rotation of galaxies at the edge of the cluster (internal rotations). He found severe incompatibilities in the two methods, as method ii) would give an estimate much larger than method i) for the total mass. His resolution to this “missing mass” problem was to postulate the presence of an additional, non-luminous, component that would provide the extra gravity needed to hold the clusters together. It is interesting to note that he also suggested that gravitational lensing[3] could provide us with “a simple and most accurate determination of nebular mass”. Today, one important technique used for the determination the distribution of dark matter is based on gravitational lensing. In Fig. 1.6 we can see this effect as observed by Hubble Space Telescope (HST) in the Abell 1689 cluster.

The next indication of the need for some non-luminous matter was presented in 1970 by Vera Rubin (see *Rubin and Ford*, 1970). When studying the rotation curves of spiral galaxies, she found inconsistencies with theoretical predictions based on Newtonian dynamics. If one would include only the luminous matter distribution, the velocities of stars at the edge of galaxies should be much smaller than those closer to the center. Her findings were in stark contrast with those expectations: the velocities were reaching a plateau regime, never entering the regime where they should have tapered off. It took almost a decade for the community to finally accept those results as evidence of dark matter halos surrounding galaxies.

As we have seen in Section 1.1 the study of CMB anisotropies is the best tool we have

[3]One of the consequences of General Relativity is the bending of light by gravity fields. This is what makes gravitational lensing possible.

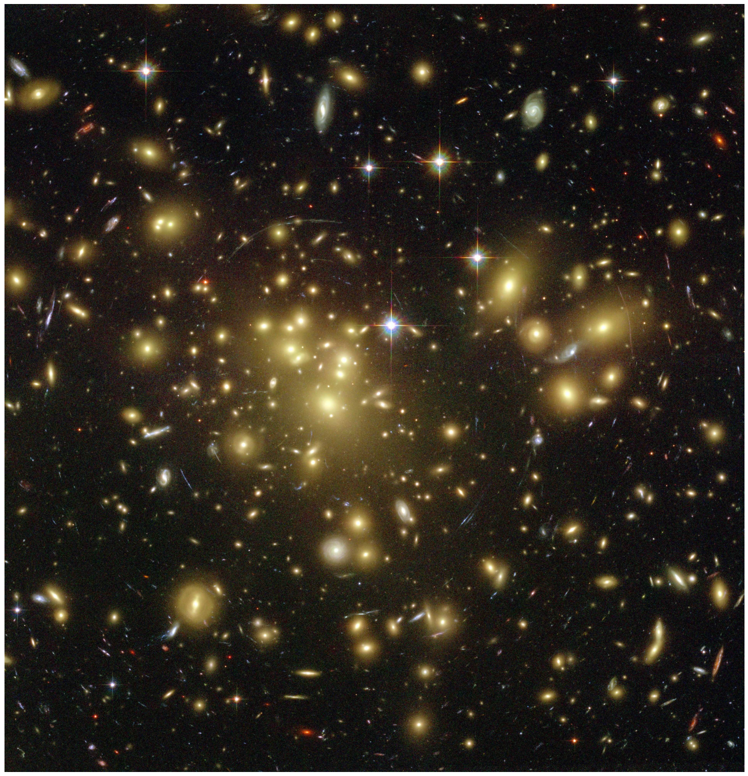

Figure 1.6: Image of the Abell 1689 cluster as seen by HST. Lensing arcs in the image and the clear distortion of the background (red and blue) galaxies are an indication of strong gravitational lensing. Credit:NASA, N. Benitez (JHU), T. Broadhurst (Racah Institute of Physics/The Hebrew University), H. Ford (JHU), M. Clampin (STScI),G. Hartig (STScI), G. Illingworth (UCO/Lick Observatory), the ACS Science Team and ESA.

to determine the cosmological parameters. The parameters fitting the observed spectrum of density perturbations correspond to the "concordance model": $\Omega_{baryons} \simeq 0.04$, $\Omega_{\Lambda} \simeq 0.73$ and $\Omega_{DM} \simeq 0.23$. One could ask if Dark Matter could be formed by clouds of non-luminous baryonic matter. The answer is no, as those have a clear observational signature: absorption of light passing through them. Another explanation of DM, that does not invoke exotic particles, is Massive Compact Halo Objects (MACHOs). Those are celestial objects that do not emit enough light to be detected, such as: brown dwarfs, neutron stars or black holes. There is no evidence as of yet that those objects could be common enough to account for the total amount of DM.

Therefore most of dark matter has to be some, as of yet undetected, form of non-baryonic matter which interacts weakly, or Weakly Interacting Massive Particles (WIMPs). A strong indirect evidence supporting the conclusion that DM is indeed of this type comes from what is commonly known as "the WIMP miracle". Using basic principles of thermodynamics in an expanding universe one can compute the relic abundance of a massive species, knowing its annihilation cross section. Using a value for this cross section typical for weak interactions its extremely easy to get the required value of $\sim$23% for a wide range of DM particle masses.

There are three categories of DM particles, depending on their mass. Hot dark matter would consist of ultra-relativistic nearly massless particles. Warm dark matter corresponds to particles that are relativistic, but with speeds not exceeding 95% of the speed of light. However, if DM would be comprised mostly of hot or warm particles then one would not be able to explain the formation of galaxies and other large scale structures, as those particles are too fast to become unstable to gravitational instabilities. The most promising type of DM candidate is what is referred to as cold dark matter, with average speeds today less than 10% of the speed of light. There is no natural candidate for cold dark matter (CDM) within the standard model of particle physics. However, the axion could fit the bill. Introduced as one possible solution of the charge-parity (CP) problem of strong interactions in the standard model, this particle has many cosmological and even astrophysical implications. Another possibility would be to identify a DM candidate within extensions of the standard model. Supersymmetry already has build in such a particle, the Lightest Supersymmetric Partner (LSP).

1.3.2 Searches for DM

There are two conceptually different type of searches for dark matter: indirect detection and direct detection. In the former case one looks for the product of annihilation of DM particles in regions where this phenomenon happens at relatively high rates, i.e. in regions where a high DM density would be expected. The core of the Sun (*Silk et al.*, 1985), Earth (*Freese*, 1986; *Krauss et al.*, 1986) could be good candidates for such places, as DM is expected to have been captured by multiple scattering processes with the nuclei of the matter forming those objects. The center of galaxies is another region where DM density is expected to be high enough. Neutrinos would escape, independently of where this annihilation took place. IceCube and SuperKamiokande are large neutrino detectors searching for such signals.

If the DM annihilation happens in places where photons and other particles could escape, such as the galactic center then one could search for signals of DM in terms of gamma rays, neutrinos or radio waves from the galactic center (*Gondolo and Silk*, 2000). The EGRET, PAMELA and the LAT on the Fermi satellite are space based experiments that measure the spectrum of cosmic rays. Anomalous signals in the form of excess positrons could be explained as DM annihilations, although it is still compatible with other, more mundane explanations such as astrophysical sources. For a more detailed discussion of this aspect see Section 3.1.1.

In direct detection experiments one looks for the minute energy transferred when a DM particle collides with the atoms in the detector. They use various techniques such as scintillation, lattice vibration or ionization. Some of the experiments ongoing today: CDMS, CREST, ROSEBUD, DAMA/LIBRA, XMASS, KIMS, DEAP/CLEAN, XENON, LUX, ZEPLIN, PICASSO, COUPP. DAMA/LIBRA has claimed DM detection based on annual modulation of the event rate, a phenomenon that was predicted by *Drukier et al.* (1986). It is hard to reconcile this with null results from other experiments. Also, in 2009 CDMS reported two candidate events. However those cannot yet be conclusively separated from possible contaminating backgrounds. The prospects of detecting DM, either directly or indirectly are promising, as recent years have brought at least several hints in this direction.

1.4 Dark Stars

The topic of chapters III-V will be Dark Stars (DS) and their detectability. They may constitute the first phase of stellar evolution, powered by DM annihilation. *Spolyar et al.* (2008) first considered the effect of dark matter annihilation on the first stars during their formation. The first stars formed when the universe was about 200 million years old, at $z = 10 - 50$, in $10^6 M_\odot$ haloes consisting of 85% DM and 15% baryons predominantly in the form of H and He from big bang nucleosynthesis. In many theories WIMPs are their own antiparticles and annihilate with themselves wherever the DM density is high. The first stars are particularly good sites for annihilation because they form at high redshifts (density scales as $(1+z)^3$) and in the high density centers of DM haloes. *Spolyar et al.* (2008) found that dark matter annihilation provides a powerful heat source in the first stars and suggested that the very first stellar objects might be *Dark Stars* (DS), a new phase of stellar evolution in which the DM – while only a negligible fraction of the star's mass – provides the key power source for the star through DM heating. Note that the term 'Dark' refers to the power source, not the appearance of the star. Dark Stars are stars made primarily of hydrogen and helium with a smattering of dark matter ($<$1% of the mass consists of DM); yet they shine due to DM heating.

In subsequent work, *Freese et al.* (2008a) and *Spolyar et al.* (2009) studied the stellar structure of the dark stars, and found that these objects grow to be large, puffy ($\sim$ 10 A.U.), bright ($\sim 10^7 L_\odot$), massive (they grow to at least $\sim 500 M_\odot$), and yet cool ($\sim 6000 - 10,000$K surface temperature) objects. They last as long as they are fed by dark matter. Furthermore, *Freese et al.* (2010b) considered the possibility of an extended period of dark matter heating and the consequent growth to Supermassive Dark Stars $> 10^5 M_\odot$. By contrast, in the standard case, when DM heating is not included, Population III stars (the standard fusion powered first stars) [4] form by accretion onto a smaller protostar $\sim 10^{-3} M_\odot$

[4]Pop. III stars refer to the first stars to form in the universe and are uncontaminated by previous stellar evolution. They consist only of the elements produced during Big Bang Nucleosynthesis.

(*Omukai and Nishi*, 1998) up to $\sim 140 M_\odot$ and surface temperatures exceeding 5×10^5K. This higher surface temperature in the standard picture inhibits the accretion of the gas, as various feedback mechanisms become effective at those high temperatures (*McKee and Tan*, 2008). For reviews of first stars formation in the standard scenario, where DM heating is not included see e.g. *Barkana and Loeb* (2001); *Yoshida et al.* (2003); *Bromm and Larson* (2004); *Ripamonti and Abel* (2005); *Yoshida et al.* (2006); *Gao et al.* (2007).

WIMP annihilation produces energy at a rate per unit volume

$$\hat{Q}_{DM} = n_\chi^2 \langle \sigma v \rangle m_\chi = \langle \sigma v \rangle \rho_\chi^2 / m_\chi, \tag{1.1}$$

where n_χ is the WIMP number density, m$_\chi$ is the WIMP mass, and ρ_χ is the WIMP energy density. The final annihilation products typically are electrons, photons, and neutrinos. The neutrinos escape the star, while the other annihilation products are trapped in the dark star, thermalize with the star, and heat it up. The luminosity from the DM heating is given by:

$$L_{DM} \sim f_Q \int \hat{Q}_{DM} dV \tag{1.2}$$

where f_Q is the fraction of the annihilation energy deposited in the star (not lost to neutrinos) and dV is the volume element.

The DM heating rate in Dark Stars scales as the square of the WIMP density times the annihilation cross section, as can be seen from Eq.(1.1). The WIMP density inside the star adjusts in response to changes in the star's baryonic mass profile, since the gravitational potential well of the star is determined by the baryons. (The DM profile responds to changes in the gravitational potential due to the conservation of adiabatic invariants.)

For a short list of papers by various other authors that have continued the work of *Spolyar et al.* (2008) and explored the repercussions of DM heating in the first stars see *Iocco* (2008); *Iocco et al.* (2008); *Taoso et al.* (2008); *Yoon et al.* (2008); *Ripamonti et al.* (2009); *Gondolo et al.* (2010); *Ripamonti et al.* (2010); *Sivertsson and Gondolo* (2010).

Their potential observability has been discussed in *Freese et al.* (2010b); *Zackrisson et al.* (2010b,a). Today there are in orbit several very powerful near IR telescopes, such as the Spitzer Space Telescope, the AKARI satellite, and the Hubble Space Telescope (HST). Results from those instruments are essential in the understanding the formation of the first stars in the universe and the end of the 'dark ages'. One unique signature of Dark Stars has been discussed in *Zackrisson et al.* (2010b), where the authors have shown that for Dark Stars with masses ranging between $700 - 1000 M_\odot$, "which contribute only 0.7% of the stellar mass in this galaxy, give rise to a conspicuous red bump in the spectrum at rest-frame wavelengths longward of $0.36\mu m$ (this corresponds to wavelengths longer than $3.96\mu m$ at $z = 10$). Because of this, galaxies that contain many cool dark stars are expected to display anomalously red colours. A feature like this is very difficult to produce through other means." The upcoming James Webb Space Telescope (JWST) could even detect this signature, assuming Dark Stars are not exceedingly rare. Another technique for detection, that is extensively used in high redshift object searches is looking for dropouts J, H, or even K band dropouts in deep field surveys of the sky. The Atacama Cosmology Telescope (ACT), a ground based instrument could also be used to detect IR backgrounds at high redshifts. In order to actually determine if a detection with a near IR instrument is indeed due to a Dark Star one would need a confirmation from a spectral analysis. The Giant Magellan Telescope (GMT), scheduled for completion in 2018, could be used for this purpose.

The possibility that DM annihilation might have effects on *today's* stars was actually considered in the $`80s$ by various authors such as *Krauss et al.* (1985); *Bouquet and Salati* (1989); *Salati and Silk* (1989). More recently the effect on today's stars has been re-examined under the assumption that DM is made of WIMPs (*Moskalenko and Wai*, 2007; *Scott et al.*, 2007; *Bertone and Fairbairn*, 2008; *Scott et al.*, 2008) or within the hypothesis of inelastic dark matter (*Hooper et al.*, 2010).

In Chapter III, we investigate the dependence of Dark Star properties on these two quantities: (i) the annihilation cross section and (ii) the density of the halo within which the star forms, as characterized by the concentration parameter.

In Chapter IV we show that these objects can grow to be supermassive dark stars (SMDS) with masses $\gtrsim (10^5 - 10^7)M_\odot$. The growth continues as long as dark matter heating persists, since dark stars are large and cool (surface temperature $\lesssim 5 \times 10^4$K) and do not emit enough ionizing photons to prevent further accretion of baryons onto the star. The dark matter may be provided by two mechanisms: (1) gravitational attraction of dark matter particles on a variety of orbits not previously considered, and (2) capture of WIMPs due to elastic scattering. Once the dark matter fuel is exhausted, the SMDS becomes a heavy main sequence star; these stars eventually collapse to form massive black holes that may provide seeds for supermassive black holes in the Universe. SMDS are very bright, with luminosities exceeding $(10^9 - 10^{11})L_\odot$. We demonstrate that for several reasonable parameters, these objects will be detectable with JWST. Such an observational discovery would confirm the existence of a new phase of stellar evolution powered by dark matter. In Chapter V we extend this study using various JWST redshift dropout selection functions and bounds on the fraction of DM halos that could host dark stars obtained from null results in HST. We have also included the effect of stellar atmosphere on the DS Spectral Energy Distribution (SED) by using results generated by the TLUSTY code. An important finding is that SMDS will have different colors than PopIII galaxies in the filters JWST is sensitive enough to detect them. This could be used as a criterion to differentiate high redshift galaxies from supermassive dark stars.

CHAPTER II

Are we seeing the beginnings of Inflation?

The current accelerated expansion of the universe is usually explained by invoking a DE component[1] which today comprises more than 70% of the total energy in the universe (for Celerier2007 see *Peebles and Ratra* (2003); *Caldwell and Kamionkowski* (2009); *Silvestri and Trodden* (2009)). The case of a pure cosmological constant, with $w_\Lambda \equiv p_\Lambda/\rho_\Lambda = -1$ marks the divide to the 'phantom' realm. Phantom dark energy models are described by systems with

$$w_p = \frac{p_p}{\rho_p} < -1 \tag{2.1}$$

and have the intriguing feature that the energy density in the universe increases with expansion,

$$\rho_p \sim a^{-3(1+w_p)}. \tag{2.2}$$

Hence a universe with low $\sim mev$ scale accelerated expansion can eventually reach energy scales close to the Grand Unified Theory (GUT) scale, for instance. For some examples of cosmological scenarios using phantom energy see *Schulz and White* (2001); *Caldwell* (2002); *Caldwell et al.* (2003); *Dabrowski et al.* (2003); *Gibbons* (2003); *Hao and Li* (2003); *Nojiri and Odintsov* (2003); *Singh et al.* (2003); *Alam et al.* (2004); *Hao and Li* (2004); *Johri* (2004); *Sami and Toporensky* (2004); *Aref'eva et al.* (2005); *Feng et al.*

[1] For alternative approaches which try to avoid dark energy by invoking large scale inhomogeneities see, for instance, *Alexander et al.* (2009); *Biswas et al.* (2007); *Célérier* (2007).

(2005); *Guo et al.* (2005); *Brown et al.* (2008). The question that we want to ask is whether it is possible to exploit this feature of phantom cosmology and turn the dark energy driven acceleration into a GUT scale inflationary phase[2]. The idea then would be to construct a cyclic model where dark-energy/inflationary phases are interspersed with decelerating radiation/matter phases.

Several problems immediately appear. Firstly, unless the equation of state for the phantom phase, w_p, is extremely close to -1, the phantom acceleration will be much faster than the deSitter expansion, and cannot be reconciled with data. Density perturbations produced during a phantom phase will give rise to a blue spectrum, and consistency with the current WMAP 5-yr data at the 2σ level with tensor modes included *Komatsu et al.* (2009) requires $-1 > w_p > -1.01$. Secondly, it is well known that phantom cosmology typically ends in a Big-rip singularity, rather than the standard radiation phase which follows inflation. Remarkably, we find that both these problems can be addressed when we include interactions between the "phantom fluid" and some hidden sector matter. Such interactions ameliorate the phantom acceleration phase to an asymptotic dS type expansion, once the phantom energy density reaches a critical value. It is easy to arrange this transition to occur around the GUT scale, which is appropriate for inflationary cosmology. This also automatically avoids the big rip singularity as the space time now approaches a deSitter universe. The density perturbations can have a variety of possibilities, allowing for agreement with observations *Komatsu et al.* (2009). Moreover, in our scenario the universe transitions to an asymptotic deSitter phase independent of the value of ω_p, and thus avoids having to fine-tune w_p very close to -1. As an additional advantage over the usual slow-roll inflationary scenario, in our phantom-driven inflationary model one does not have to tune the flatness of the potential usually necessary to obtain the large number of efoldings and near scale-invariant spectrum. In addition, the hierarchy between the $\sim meV$ dark energy scale and the GUT

[2] For a brief list of papers that propose various mechanism of connecting the current accelerated expansion to inflation see *Barenboim and Lykken* (2006); *Cognola et al.* (2008); *Nojiri and Odintsov* (2008); *Cognola et al.* (2009)

inflation scale can be ameliorated in our model (expressed in terms of factors of a few) as we will show. We cannot however address the "coincidence" problem in our picture. Finally, there is the question of how to construct a theoretically self-consistent model of phantom energy. We will comment on this problem shortly.

Before delving into the details of our specific realization of the "phantom cyclic model", let us outline the basic picture by considering just a simple two fluid model, phantom matter (ρ_p) + radiation (ρ_r). The cosmology we want to realize is the following: although the scale factor always increases monotonically with time, the energy density "cycles", at least approximately. Each cycle is divided into two different phases: (a) Radiation dominated phase, which starts at an energy density $\rho_r = \lambda_{\mathtt{max}}^4$. As the universe expands radiation gets diluted, the Hubble parameter decreases and reaches a minimum when $\rho_r = \rho_p = \lambda_{\mathtt{min}}^4$. From here on we enter (b) the phantom energy dominated phase. In realistic cosmology the radiation phase should give way to matter domination at energy densities $\sim (10\ eV)^4$, before giving way to phantom domination, but for simplicity we are going to ignore this slight complication. Thus for a typical scenario which would be consistent with dark energy and inflationary paradigm, $\lambda_{\mathtt{max}} \sim 10^{15}\ GeV \sim 10^{-3} M_p$ or the GUT scale, and $\lambda_{\mathtt{min}} \sim meV \sim 10^{-30} M_p$ corresponding to the scale of current energy density. Now, in the phantom phase, as the universe expands the energy density increases, and so does the Hubble rate. Initially, depending upon how negative the phantom equation of state parameter, ω_p, is this increase in energy density can be quite fast. However, in our model we will see that once the energy density reaches close to a critical scale $\lambda_{\mathtt{max}}$, which is determined by the interactions between the hidden and ordinary matter sector, the energy density and the Hubble parameter asymptote to a constant giving rise to a near exponential expansion. This inflationary phase can end via the reheating mechanism described in section 2.2, 2.3 after which we enter the radiation dominated era of the next cycle.

A similar idea to the one in this paper has previously been presented by *Creminelli et al.* (2006) who dubbed this model "the eternally expanding cyclic universe." They too (in their

Section 4.3) suggested an alternating increasing/decreasing energy density. However the theory behind their model is quite different from ours, and consequently their predictions for resultant density perturbations are different as well [3]. One major problem of all phantom type models is the vacuum stability due to the null energy condition violation. *Creminelli et al.* (2006) examine a consistent way to solve this problem, based on a deformation of the ghost condensate model of *Hamed et al.* (2004).

Although the interactions between phantom fluid and ordinary matter can lead to an inflationary spacetime, we are still left with a graceful exit problem, or how to ensure that the universe enters the standard radiation dominated era. Depending upon the specific model different "reheating mechanisms" may be able to trigger such a transition. We focus on a model where the phantom fluid consists of a ghost like scalar field coupled to some hidden matter sector. Such a fluid closely resembles the interacting DE-DM models *Amendola* (2000); *Amendola and Tocchini-Valentini* (2001); *Amendola and Quercellini* (2003); *Amendola et al.* (2004); *Biswas and Mazumdar* (2005); *Biswas and Mazumdar* (2006); *Biswas et al.* (2006); *Bean et al.* (2008a,b) except that the scalar field instead of being an ordinary quintessence field, has negative kinetic energy like a ghost. Although field theory with ghosts is plagued with problems of unitarity/instability *Carroll et al.* (2003); *Cline et al.* (2004), recent developments attempting to address these problems include progress in non-local *Moeller and Zwiebach* (2002); *Aref'eva et al.* (2007); *Aref'eva* (2007); *Barnaby et al.* (2007) and Lee-Wick *Lee and Wick* (1969); *Lee and Wick* (1970); *Grinstein et al.* (2008); *Lee* (2008); *Shalaby* (2009); *van Tonder* (2008) higher derivative models; see also *Creminelli et al.* (2006) and *Dubovsky et al.* (2006); *Rubakov* (2006); *Libanov et al.* (2007); *Barrow and Tsagas* (2009); *Creminelli et al.* (2009); *Sadeghi et al.* (2009). As we will see, in our model the transition from phantom to radiation phase and vice-versa is achieved partly by suitably choosing the interaction strength between the scalar field and the hidden matter sector, and partly due to the presence of interactions between the hidden and

[3] They always predict a negative, even if extremely small, tilt of the spectral index while our model will allow a variety of possibilities (as discussed in later sections of this paper).

ordinary matter sector. (There is no direct coupling between the ghost field and ordinary matter.)

As emphasized before, the main reason why the cosmology described above can replace the standard inflationary paradigm is because in the phantom phase the energy density increases even though the universe continues to expand. Thus after the usual dilution in a radiation dominated phase, the phantom phase followed by reheating ensures that the universe again becomes hot and therefore can reproduce the successes of the Big Bang Model, such as BBN and CMB. There is another essential similarity between our scenario and the inflationary paradigm. The essential reason why inflation solves the standard cosmological puzzles is because our observable universe (of radius $\sim H_0^{-1}$) can originate from a very tiny region at the beginning of inflation. Something very similar happens in our model as well, the universe expands by a huge factor in every cycle. In our model the number of e-foldings in the radiation and the phantom phase is given by

$$\mathcal{N}_{\tt rad} \sim \ln\left(\frac{\lambda_{\tt max}}{\lambda_{\tt min}}\right) \text{ and } \mathcal{N}_{\tt phan} \sim \frac{-4}{3(1+\omega_p)} \ln\left(\frac{\lambda_{\tt max}}{\lambda_{\tt min}}\right). \tag{2.3}$$

In order to have a successful GUT scale inflationary paradigm we need $\mathcal{N}_{\tt inf} \gtrsim 60$. Thus one gets:

$$\begin{aligned} \mathcal{N}_{\tt tot} &= \mathcal{N}_{\tt phan} + \mathcal{N}_{\tt rad} + \mathcal{N}_{\tt inf} \\ &\sim \left(1 - \frac{4}{3(1+\omega_p)}\right) \ln\left(\frac{\lambda_{\tt max}}{\lambda_{\tt min}}\right) + \mathcal{N}_{\tt inf} \end{aligned} \tag{2.4}$$

Just to get an idea, if we take $\lambda_{\tt min} \sim mev$, $\lambda_{\tt max} \sim 10^{15} Gev$, $\omega_p \sim -1.3$, and $\mathcal{N}_{\tt inf} \sim 60$, we get $\mathcal{N}_{\tt tot} \sim 400$. What this means is that only a very very tiny portion (for the chosen example, e^{-400} th) of our observable universe will ultimately grow to become the observable universe in the next cycle at the same energy density scale. Another essential similarity between the standard inflationary scenario and our phantom based model, is the production of a huge amount of entropy in every cycle. Even in a “cyclic” scenario if one wants to address the usual cosmological puzzles, such as flatness, homogeneity, etc, as well as produce cosmological perturbations with the correct amplitude required for galaxy formation, entropy production seems to be an inevitable requirement *Biswas* (2008); *Biswas and Alexander* (2009); *Biswas and Mazumdar* (2009). Like in inflation, in our scenario a huge amount of entropy is produced during reheating when most of the phantom energy is converted into radiation. This is essential to ensuring the cyclicity of energy density even though the scale factor of the universe is monotonically increasing [4].

It is worth mentioning that in most cyclic models proposed the scale factor $a(t)$ has a contracting-expanding behaviour, where both a bounce, near the Big Bang, and a turnaround, when the scale factor becomes large are needed. A brief and incomplete compilation of some of the papers that have proposed cyclic cosmologies can be found in *Khoury et al.* (2001, 2002); *Lidsey et al.* (2004); *Mulryne et al.* (2005a,b); *Brown et al.* (2008). Such cosmologies provide natural solutions to the flatness and horizon problems of standard Big Bang scenario. Some variants also avoid the issue of initial conditions, provided entropy produced during one cycle is not transferred to the next. In this case the cycles will not grow, i.e. become larger (Tolman's argument*Tolman* (1934)) from one to the next, so we can no longer define a beginning of the universe. For instance the authors of *Steinhardt and Turok* (2002); *Steinhardt and Turok* (2002); *Steinhardt and Turok* (2005) developed an ekpyrotic inspired cyclical model as an alternative to inflation, where a phase of slow contraction before the bang is responsible for generating a nearly scale invariant spectrum of perturbations that seed the large scale structure formation. In contrast, the standard inflationary scenario assumes a short phase that occurs after the big bang when the universe is rapidly expanding and nearly scale invariant perturbations are generated.

The paper is organized as follows. In section 2.1 we present our model of phantom fluid and discuss the cosmology relevant for dark energy. In section 2.2, we discuss how including interactions can lead to an inflationary space-time along with partially reheating

[4]It may be possible to embed the scenario in phantom cyclic models *Cai et al.* (2007); *Brown et al.* (2008) with actual phases of contraction, but we are not going to explore this possibility here.

the universe. In section 2.3 we provide a specific example where transitions from the phantom-inflation phase to radiation and vice-versa can be orchestrated giving us a cyclic model of the universe. In section 2.4 we discuss the different observational constraints coming from inflation, Big Bang Nucleosynthesis (BBN), and dark energy experiments. Finally, we conclude with a summary of the scenario presented and issues that needs to be addressed further.

2.1 Phantom Dark Energy

The purpose of this section is to implement a model for the phantom component that would drive the super-accelarated expansion. For now we will not include regular matter nor radiation, but rather focus solely on the components necessary to obtain a phantom phase. One can possibly implement the cosmology sketched before in many different ways. Here we are going to realize the above picture using a ghost-like scalar field (with negative kinetic energy) ϕ coupled to a hidden matter sector which we denote by index "h". There are two equivalent approaches to describe this type of coupling. One starting from an action, where we allow for a direct coupling term between the hidden sector and the scalar field. The second approach is to consider two fluids that can exchange energy while maintaining the conservation of the total stress-energy tensor, as required by diffeomorphism invariance, although the individual stress-energy tensors are not conserved.

Our system will be described by the following action:

$$S = \int \mathrm{d}^4x\sqrt{-g}\left[M_p^2\frac{R}{2} + \frac{(\nabla\phi)^2}{2} + C(\phi)\mathcal{L}_h\right] \,, \tag{2.5}$$

where $\mathcal{L}_h$ does not depend on ϕ, being the action describing a perfect barotropic fluid. Here we work with a spatially flat FRW metric with signature $(-,+++)$. Notice that the kinetic term for the scalar field comes with the 'wrong' sign, as appropriate for a ghost. In the phantom dominated phase, described here, the Hubble equation derived from the action above looks like

$$H^2 = \frac{1}{3M_p^2}(\rho_\phi + \rho_h) = \frac{1}{3M_p^2}\left[-\frac{\dot{\phi}^2}{2} + C(\phi)\tilde{\rho}_h\right] , \tag{2.6}$$

where we have assumed the field ϕ to be homogenous. Here a dot represents the derivative with respect to cosmic time, t and $\tilde{\rho}_h$ denotes the bare energy density of the hidden sector, which is ϕ independent. We will assume that it behaves like a perfect barotropic fluid, satisfying the continuity equation:

$$\dot{\tilde{\rho}}_h + 3H(\tilde{\rho}_h + \tilde{p}_h) = 0 \tag{2.7}$$

with an equation of state

$$\tilde{p}_h = \omega\tilde{\rho}_h \tag{2.8}$$

One can also include a potential for the scalar field, and its effects are discussed briefly in the appendix, but for the purpose of illustration we are going to set it to zero.

The interaction that we are going to consider between the hidden matter sector and ϕ is going to be very similar to the interactions considered in coupled quintessence (or interacting DE-DM) models *Biswas and Mazumdar* (2005); *Biswas and Mazumdar* (2006); *Biswas et al.* (2006); *Bean et al.* (2008a,b). From the action in equation (2.5) we get two additional equations of motion.

$$\ddot{\phi} + 3H\dot{\phi} \;=\; 2\rho_h\mu(\phi)/M_p \tag{2.9}$$

$$\dot{\rho}_h + 3H(1+\omega)\rho_h \;=\; 2\rho_h\dot{\phi}\mu(\phi)/M_p \, , \tag{2.10}$$

where we have defined

$$\mu(\phi) \equiv \frac{1}{C}\frac{dC}{d\phi} , \tag{2.11}$$

and we are going to assume hence forth that $\mu(\phi)$ always remains positive. As one can see, both the Klein-Gordon equation for ϕ and the continuity equation for the hidden matter sector ρ_h are augmented by interaction terms in the right hand side of the equations (2.9,2.10). Although μ in general depends on ϕ, to understand the phantom phase let us consider a constant μ to begin with. It is easy to check that the above interaction is consistent with the conservation of the total energy momentum tensor:

$$\dot{\rho}_{\mathtt{tot}} + 3H(\rho_{\mathtt{tot}} + p_{\mathtt{tot}}) = 0 \tag{2.12}$$

where $\rho_{\mathtt{tot}} \equiv \rho_h + \rho_\phi$. To see this we remind the readers that the Klein-Gordon equation can be recast as

$$\begin{aligned} \frac{d}{dt}\left[-\frac{\dot{\phi}^2}{2}\right] - 3H\dot{\phi}^2 &= -2\rho_h\mu\dot{\phi} \\ \Rightarrow \dot{\rho}_\phi + 3H(\rho_\phi + p_\phi) &= -2\rho_\phi\dot{\phi}\mu(\phi)\ , \end{aligned} \tag{2.13}$$

since the energy density and pressure for a phantom scalar field are given by

$$\rho_\phi = p_\phi = K = -\frac{\dot{\phi}^2}{2} \tag{2.14}$$

Thus the source terms in the individual conservation equations (2.10) and (2.13) cancel each other.

One can solve the hidden matter continuity equation exactly to find

$$\rho_h = \rho_{h0}C(\phi)\left(\frac{a}{a_0}\right)^{-3(1+\omega)} \tag{2.15}$$

where we have chosen the convention that at $a = a_0$, $C(\phi) = 1$ and $\rho_h = \rho_{h0}$. The $a^{-3(1+\omega)}$ dependence reflects the usual dilution of the energy density of an ideal fluid with expansion. Depending upon the scale of energy density relative to the mass of the hidden matter particles, they can either behave as non-relativistic matter $(\omega = 0)$ or like a relativistic species ($\omega = 1/3$)[5]. We will for most part consider a light degree of freedom, so that approximately it behaves like radiation.

For the special case when μ is a constant the Coupling function is given by

$$C(\phi) = e^{2\mu(\phi-\phi_0)/M_p} \tag{2.16}$$

Now, coming back to the evolution equations, we only need to solve the Hubble equation (2.6) and the Klein-Gordon equation, the latter simplifying to

$$\ddot{\phi} + 3H\dot{\phi} = \frac{2\mu\rho_{h0}}{M_p} e^{2\mu(\phi-\phi_0)/M_p} \left(\frac{a}{a_0}\right)^{-3(1+\omega)} \equiv V'_{\texttt{eff}}(\phi) \tag{2.17}$$

It is as if the phantom scalar field is evolving under the influence of an "effective potential" given by

$$V_{\texttt{eff}}(\phi) = \rho_h(\phi) = \rho_{h0} e^{2\mu(\phi-\phi_0)/M_p} \left(\frac{a}{a_0}\right)^{-3(1+\omega)} \tag{2.18}$$

An important thing to note is the +ve sign appearing in front of $V'_{\texttt{eff}}$ in equation (2.17) because ϕ is a ghost field with negative kinetic energy. It is clear now that because of the peculiar properties of the phantom field, ϕ actually rolls up the effective potential $e^{2\mu\phi/M_p}$.

We have the following late time attractor power-law solutions:

$$\begin{aligned} a(t) &= a_0 \left(\frac{t}{t_0}\right)^n \text{ \& } \phi = \phi_0 + pM_p \ln\left(\frac{t}{t_0}\right) \\ \Longleftrightarrow & \quad e^{\frac{\phi}{M_p}} = e^{\frac{\phi_0}{M_p}} \left(\frac{t}{t_0}\right)^p \end{aligned} \tag{2.19}$$

with

$$n = -\frac{1-\omega}{4\mu^2 - 3/2(1-\omega^2)} \text{ and } p = -\frac{4\mu}{4\mu^2 - 3/2(1-\omega^2)} \tag{2.20}$$

[5] In this context we note that we have a choice in how we interpret the augmentation of the energy density with growth of ϕ. One can either think of this growth as simply the increase in mass of the hidden matter particles if the mass depends on ϕ, or creation of the hidden matter particles through its interactions with ϕ, or a combination of the two. To keep things simple we are going to assume that the mass of the hidden matter particles remains a constant, but its number density increases.

We have verified (see appendix A) that these late time attractors are indeed stable[6].

In this phase the scalar field and the hidden matter are tightly coupled and evolve as a single fluid with an effective equation of state parameter

$$\omega_p \equiv \frac{p_\phi + p_h}{\rho_\phi + \rho_h} \to -\frac{8}{3}\frac{\mu^2}{(1-\omega)} + \omega \tag{2.21}$$

The asymptotic value is attained during the late time attractor phase. In the phantom phase, expansion of the scale factor is controlled by ω_p, since $a(t) \sim t^{\frac{2}{3(1+\omega_p)}}$. These are analogues to the coupled quintessence solutions *Biswas and Mazumdar* (2005); *Biswas and Mazumdar* (2006); *Biswas et al.* (2006); *Bean et al.* (2008a,b). A detailed derivation of all results presented in this section can be found in the appendix A. The crucial thing to note is that as long as

$$\mu^2 > \frac{3}{8}(1-\omega^2) \tag{2.22}$$

we have a phantom phase, i.e. $\omega_p < -1$. In particular for $\omega = 1/3$ the last condition gives a constraint on μ,

$$\mu > \frac{1}{\sqrt{3}} \tag{2.23}$$

In passing we also note that in this phase most of the energy density is actually stored in the hidden sector; one can check that the tracking ratio between scalar field and the hidden matter density is given by

$$-\frac{\rho_\phi}{\rho_h} = -\frac{K}{\rho_h} = \frac{8\mu^2}{3(1-\omega)^2 + 8\mu^2} < 1 \tag{2.24}$$

One can also calculate the amount by which ϕ evolves during this phase. A straight

[6]We have not investigated whether these solutions suffer from any hydrodynamic instabilities of the nature found in some interacting quintessence models *Bean et al.* (2008b), and we leave this for a future exercise.

forward calculation gives us

$$\Delta\phi_p = \frac{2}{\mu}\left[1 - \frac{4}{3(1+\omega)}\right]\ln\left(\frac{\lambda_{\mathtt{max}}}{\lambda_{\mathtt{min}}}\right) \tag{2.25}$$

Here $\lambda_{\mathtt{min}}$ and $\lambda_{\mathtt{max}}$ represent the energy scale at which the phantom phase begins and ends respectively.

In summary, in this section we have found under what conditions a phantom phase could be described by a stable late time attractor for ghost-like fields coupled exponentially to a perfect fluid. The purely phantom sector we have studied in this section is problematic as an inflationary model. For example, for a constant (purely) phantom equation of state $\omega_p < -1$, typically one would obtain a blue spectrum (see equation (2.59)) which would be inconsistent with the WMAP data. This conclusion is of course valid with the assumption that primordial perturbations are generated mostly during the phantom phase. Thus unless μ is fine tuned to be very close to the critical value (which gives rise to $\omega_p = -1$), we will not be able to reproduce the inflationary near scale-invariant spectrum. Thus far we have considered the phantom sector alone; in the next section we include interactions with the standard model which ameliorate some of the problems of a phantom sector alone.

2.2 “Partial Reheating” and Late time deSitter Phase

In the previous section we realized the phantom phase through an interacting phantom scalar field and hidden matter sector. In the absence of any new physics this phase is going to last till the Big Rip singularity, as is well known in phantom cosmology. In order for the next cycle to begin we need to first find a “reheating” mechanism which converts most of the phantom energy density to radiation.

What we find, quite remarkably, is that once we include interaction between the hidden matter sector and Standard Model particles (namely we allow the hidden sector particles to be converted to light degrees of freedom of the standard model), which generically exist, it naturally ameliorates the phantom like acceleration to a near exponential inflationary expansion.

As we will see, such interactions begin the process of reheating the universe by producing a radiation bath. Unfortunately the interactions don't provide us with a graceful exit from the inflationary phase, but we will discuss how this issue can also be addressed in the next section.

To understand how interactions effect the cosmological evolution we will use Boltzmann equations in the following form:

$$\dot{\rho}_h + 3H(1+\omega)\rho_h = -\rho_h\Gamma + 2\rho_h\dot{\phi}\frac{\mu}{M_p} \tag{2.26}$$

$$\ddot{\phi} + 3H\dot{\phi} = \frac{2\rho_h\mu}{M_p} \tag{2.27}$$

$$\dot{\rho}_\gamma + 4H\rho_\gamma = \rho_h\Gamma \tag{2.28}$$

along with the Hubble equation

$$H^2 = \frac{1}{3M_p^2}\left(\rho_h - \frac{\dot{\phi}^2}{2} + \rho_\gamma\right) \tag{2.29}$$

Here by ρ_γ we include all the light degrees of freedom which do not couple to the phantom field, and Γ is the annihilation rate of the hidden matter particles into all these other light degrees of freedom. We have ignored the inverse process of creation of the hidden matter particles from the rest of the matter under the assumption that the equilibrium density of the hidden matter sector is small compared to normal radiation. Now, the annihilation rate, per hidden sector particle, is given in general by

$$\Gamma_{h\bar{h}\to\gamma\gamma} = n_h < \sigma|v| >_{h\bar{h}\to\gamma\gamma} \tag{2.30}$$

where $< \sigma|v| >$ is the average over all initial and final states of the differential cross-section times the relative velocities of the annihilating particles. Usually one is used to consider the opposite process while trying to determine when a given species freezes out. In the latter case since the photons are in thermal equilibrium, one can use thermal distribution functions to compute the "thermally averaged" $<\sigma|v|>$. However, in our case in order to compute $<\sigma|v|>$ we would need information regarding the velocity distribution of the produced hidden particles from ϕ. In the absence of any micro-physical theory of such an interaction, for the purpose of illustration, here we are simply going to assume that $<\sigma|v|>$ is a constant set by the details of the interaction, so that the interaction rate per hidden sector particle is given by

$$\Gamma = \frac{\rho_h}{m^3} \tag{2.31}$$

Here m is an energy scale we introduce as a free parameter. More generally one expects Γ to go as some power law, $\Gamma \sim \rho_h^\lambda$, the power being determined by the micro-physics, but most of our results and conclusions should hold qualitatively as long as $\lambda > 1$.

It is easy to check that the above set of equations (2.26-2.28) have an asymptotic de Sitter late time attractor solution where all the energy densities and the Hubble parameter tend to a constant. Defining the following dimensionless variables,

$$\xi \equiv \frac{\rho_h}{M_p^2 H^2} \quad \text{and} \quad \eta \equiv \frac{\Gamma}{H} = \frac{\rho_h}{m^3 H}$$

we have:

$$\begin{aligned}
\xi &\to \frac{27\omega - 9 + 3\sqrt{9(3\omega-1)^2 + 192\mu^2}}{8\mu^2} && (2.32)\\
\eta &\to \frac{3\omega - 9}{2} + \frac{1}{2}\sqrt{9(3\omega-1)^2 + 192\mu^2} && (2.33)\\
\dot{\phi} &= \frac{2\rho_h\mu}{3H} \to \frac{2\mu m^3\eta}{3M_p} && (2.34)\\
\rho_\gamma &= \frac{\rho_h^2}{4Hm^3} \to \frac{m^6\eta^3}{4M_p^2\xi} && (2.35)
\end{aligned}$$

As a consistency check we have evolved these equations numerically, see Fig.1, and have verified that the asymptotic values are exactly the ones predicted by the above set of equations. Let us make a few observations. Since we are specializing to $\omega = 1/3$, let us look at the asymptotic value of the energy densities in this case:

$$
\begin{aligned}
\rho_\gamma &= \frac{16\sqrt{3}\mu\, m^6}{9M_p^2}\left(\sqrt{3}\mu - 1\right)^3 \\
\rho_h &= \frac{16\sqrt{3}\mu\, m^6}{9M_p^2}\left(\sqrt{3}\mu - 1\right)^2 \\
\rho_\phi &= -\frac{32\,\mu^2\, m^6}{9M_p^2}\left(\sqrt{3}\mu - 1\right)^2
\end{aligned}
\tag{2.36}
$$

Note that the solutions above are consistent only if $\mu > \frac{1}{\sqrt{3}}$, but we know this is also a requirement for the existence of a phantom phase[7] which will eventually settle to this deSitter attractor. In particular, we find that for $\mu \gg 1$, which is the case we will eventually be focusing on, radiation dominates over the hidden sector:

$$
\mathcal{R} \equiv \frac{\rho_h}{\rho_\gamma} \approx \frac{1}{4\sqrt{3}\mu} \ll 1 \text{ for } \mu \gg 1
\tag{2.37}
$$

In other words, as μ increases, the conversion from hidden matter to radiation becomes more efficient, and in particular radiation can easily dominate the total energy density. However, this does not mean that we can enter into the usual radiation dominated epoch because the equation of state for all the energy densities essentially approach $\omega_p = -1$, as all the energy densities approach the constant asymptotic values in equation (2.36). Physically, the energy density that the phantom field was pumping into the hidden matter sector is now transferred to radiation through its interaction with the hidden sector, in such a way that we approach a deSitter universe. This phase however is good for inflationary cosmology as fluctuations produced during this de Sitter phase are expected to give rise to a near scale-invariant spectrum (allowed, although not favored, by the WMAP data). In order for

[7] see equation (2.23)

the amplitude of the fluctuations to be consistent with observations we require

$$\rho_\gamma \approx 10^{-12} M_p^4 \Rightarrow m \sim 10^{-2} M_p \,. \tag{2.38}$$

We will return to the constraint coming from the number of efoldings required for a successful inflationary paradigm later.

In this section we have found that the big rip singularity could be avoided in this model if the hidden sector particles are converted to light degrees of freedom of the Standard Model. As the energy densities approach their asymptotic values the universe will enter in a deSitter phase. Of the three components, radiation is dominant, yet the universe is inflating. This is due to the interplay between the coupling of the hidden sector to the phantom field and light degrees of freedom of the Standard Model which leads to a state where all the energy densities approach a constant value.

2.3 Transition to Radiation and Cyclicity

In the above section we saw that interactions between hidden matter and radiation can ameliorate the phantom like acceleration to exponential inflation but cannot provide a graceful exit from the deSitter inflationary phase. So far we have assumed that μ remains a constant leading to an exponential coupling between the hidden sector and the phantom field as in equation (2.16). If $\mu(\phi)$ is not a constant a graceful exit becomes possible. Here we explore the case when $\mu(\phi)$ is periodic. For simplicity we will just assume a step function for $\mu(\phi)$, where

$$\mu = \mu_p \gg 1 \text{ for } 0 < \phi < \phi_R \tag{2.39}$$

$$\mu = \mu_r \ll 1 \text{ for } \phi_R < \phi < \phi_0 \tag{2.40}$$

and then the pattern repeats itself. The first phase, when $\mu \gg 1$, reproduces the phantom phase discussed in the previous section, leading eventually to the late time de Sitter like attractor evolution. However, now this inflationary phase ends once ϕ reaches the transition value ϕ_R. We are also going to assume that $\omega = 1/3$ in this scenario. We remind the readers that ω describes the hidden sector, as in equation (2.8). As we will see shortly, the periodicity in μ will ensure that we enter the standard radiation dominated era which lasts till ϕ rolls to ϕ_0.

The evolution of the universe during one cycle can be described in our model using three phases, as indicated in Fig. 1. Phase I provides the “Reheating” from inflationary expansion. Phase II describes a standard radiation dominated era. Then a short phantom phase IIIA ensues, during which the energy is driven from the meV to the GUT scale. This is followed by a deSitter inflationary phase IIIB. After one such cycle is complete, the next one begins, again cycling through Phases I, II, IIIA, and IIIB successively.

2.3.1 Phase I: Reheating

The reheating process is most easily understood when $\mu_r = 0$ (defined in equation (2.40)), so let us first focus on this simple case. As we discussed in the previous section, as long as μ is large, although radiation is the dominant energy density, the deSitter phase continues. However, if and when μ sharply falls to zero, the phantom phase indeed ends. Two things happen. Firstly, since initially Γ is comparable to H, as it can be seen from equation (2.33), there is rapid conversion of the hidden matter to radiation, but the hidden matter sector now no longer gets replenished by the scalar field. Secondly, the driving term in the right hand side of the Klein-Gordon equation for the phantom scalar field (2.9) is now absent and as a result ϕ slows due to Hubble damping, $\rho_\phi \sim a^{-6}$ and eventually comes to a halt. At the beginning of the reheating phase the energy densities of radiation, hidden matter and ϕ are approximately given by the asymptotic values of the late time de Sitter phase (2.36). As we had pointed out before, for $\mu \gg 1$ radiation is the dominant energy density component in this asymptotic phase. The “reheating” phase further ensures that radiation continues to dominate the energy density. If one tracks the ratio of the energy densities between hidden matter and radiation, $\mathscr{R}$, then it starts with the asymptotic value given by equation (2.37), decreases rapidly during conversion, and then approaches a constant, $\mathscr{R}_{\texttt{min}}$, once the conversion ends. Note, since ϕ slows down, ρ_h redshifts almost as radiation and therefore maintains an approximately constant tracking ratio approaching $\mathscr{R}_{\texttt{min}}$. In appendix B we calculated this asymptotic ratio to be

$$\mathscr{R}_{\texttt{min}} \approx \frac{1}{6}\frac{\sqrt{3}}{\mu_p^2} \text{ for } \mu_r = 0\ , \mu_p \gg 1 \tag{2.41}$$

Qualitatively, it turns out that one can distinguish two different regimes in the reheating phase depicted in Fig.1 as phases I.A and I.B. Numerically we found that even after $\mu \to 0$, it takes a while for the radiation energy density to start decreasing substantially. The reason is somewhat technical and the reader is referred to the appendix B for details. Intuitively, the main reason is that initially the Hubble damping of radiation is compensated by the hidden matter decays into radiation, $4H\rho_\gamma \sim \rho_h\Gamma$. Since radiation is the dominant component of the energy density, this in turn leads to H being approximately constant, as can be seen in phase I.A of Fig.1. Once ρ_h decreases appreciably so that $\rho_h\Gamma \ll 4H\rho_\gamma$, the radiation energy density starts to decrease appreciably and therefore so does the Hubble rate. This is depicted in phase I.B of Fig.1. At some point, the conversion from hidden matter to radiation effectively stops, marking the end of the reheating phase.

Although the above discussion has been for $\mu_r = 0$, we note that for a non-zero but small μ_r, the reheating phases (I.A, B) follow basically the same pattern as in the $\mu_r = 0$ case. The asymptotic tracking ratio [8] between hidden matter and radiation receives a slight

[8] Unlike in the $\mu_r = 0$ case where the tracking ratio keeps decreasing and asymptotically approaches $\mathscr{R}_{\texttt{min}}$, when $\mu_r \neq 0$, $\mathscr{R}_{\texttt{min}}$ is actually a minimum of the tracking ratio that is attained. Since ϕ never comes to a halt, the ratio does increase from its minimum value of $\mathscr{R}_{\texttt{min}}$, but this increase is very slight.

correction:

$$\mathscr{R}_{\texttt{min}} \sim \frac{1}{18}\frac{\sqrt{3}(3+8\mu_r)}{\mu_p^2} \text{ for } \mu_r \ll 1\ ,\ \mu_p \gg 1 \tag{2.42}$$

We have checked this numerically, and some of the more technical details are discussed in Appendix B.

2.3.2 Phase II: "Standard" Radiation Domination

After the reheating phase, since hidden matter is no longer converted into radiation, the latter starts to evolve as $a(t)^{-4}$, and consequently $H \sim 1/2t$ as in the standard radiation dominated era. In the meantime ϕ continues to be Hubble damped. Once the scalar field effectively stops evolving, the hidden matter starts redshifting as radiation and thus settles down to its constant tracking ratio given in equation (2.41). In particular, one can see from (2.42) that for sufficiently large values of μ_p, this ratio can be quite small and easily satisfy constraints coming from BBN and CMB. BBN/CMB only constrains the abundance of dark radiation component to be less than around 10% *Olive et al.* (2000); *Ichiki et al.* (2002). In Fig.1 we refer to the phase when ϕ is being Hubble damped as phase II.A, and the subsequent radiative phase as phase II.B.

If μ_r is precisely zero, then the radiation dominated phase IIA can continue forever because ϕ will effectively come to a halt, and unless the value of ϕ_0 is fine-tuned, ϕ will never make it to the next large μ phase. As a result the next phantom phase will not begin and the cyclic picture cannot be sustained. This is why a small but non-zero value of μ_r is essential to maintaining cyclicity without having to resort to unnatural fine-tuning.

For a non-zero but small μ_r, the reheating phases (I.A,B) and the Hubble damping phase (II.A) follow very much the same pattern as in the $\mu_r = 0$ case, as discussed at the end of the previous section 2.3.1. The main difference when $\mu_r \neq 0$, as compared to the $\mu_r = 0$ case, appears in the radiative phase II.B. This is because the non-zero driving term in the Klein-Gordon equation now ensures that instead of coming to a halt, ϕ now tracks radiation. After the initial phase of Hubble damping, the driving term on the right hand side of the KG equation catches up with the Hubble damping term. At this point the scalar field enters a phase where its energy density approximately tracks that of radiation. This can be seen in Fig.1 where we have divided the radiation phase into two parts. II.A refers to the regime when the scalar energy density is still being Hubble damped, while phase II.B refers to the tracking phase where both the hidden matter and the scalar energy densities are tracking that of radiation.

This tracking behavior can be approximately obtained as follows: From the KG equation we have

$$3H\dot{\phi} = \frac{2\rho_h\mu_r}{M_p} \approx \frac{2\mathscr{R}_{\mathtt{min}}\rho_\gamma\mu_r}{M_p} \approx 6\mathscr{R}_{\mathtt{min}}M_p\mu_r H^2 \tag{2.43}$$

In the above we have ignored the $e^{2\mu_r\phi}$ dependence of ρ_h, as ϕ is rolling very slowly, and $\mu_r \ll 1$. We will perform a consistency check later. Also, we have ignored the contributions to the energy density coming from the hidden matter and the scalar field as compared to normal radiation. Again, this is justified as $\mathcal{R}_{\mathtt{min}} \ll 1$ and ϕ is rolling slowly. Choosing the ansatz

$$\phi = M_p p_r \ln\left(\frac{t}{t_R}\right) \Rightarrow \dot{\phi} = \frac{M_p p_r}{t} \tag{2.44}$$

we find that (2.43) can indeed be satisfied provided

$$p_r = \mathscr{R}_{\mathtt{min}}\mu_r \tag{2.45}$$

In the above analysis we have used the fact that in a radiation dominated universe $H \sim 1/2t$. In particular our analysis tells us that the tracking ratio between the kinetic energy of ϕ and radiation is indeed very small

$$\frac{K_\phi}{\rho_\gamma} = -\frac{2}{3}(\mu_r\mathscr{R}_{\mathtt{min}})^2 \tag{2.46}$$

justifying our earlier assumption. In the next subsection we will also see that during this phase ϕ evolves rather slowly, so that $C(\phi)$ changes only by an $\mathcal{O}(1)$ factor ensuring that

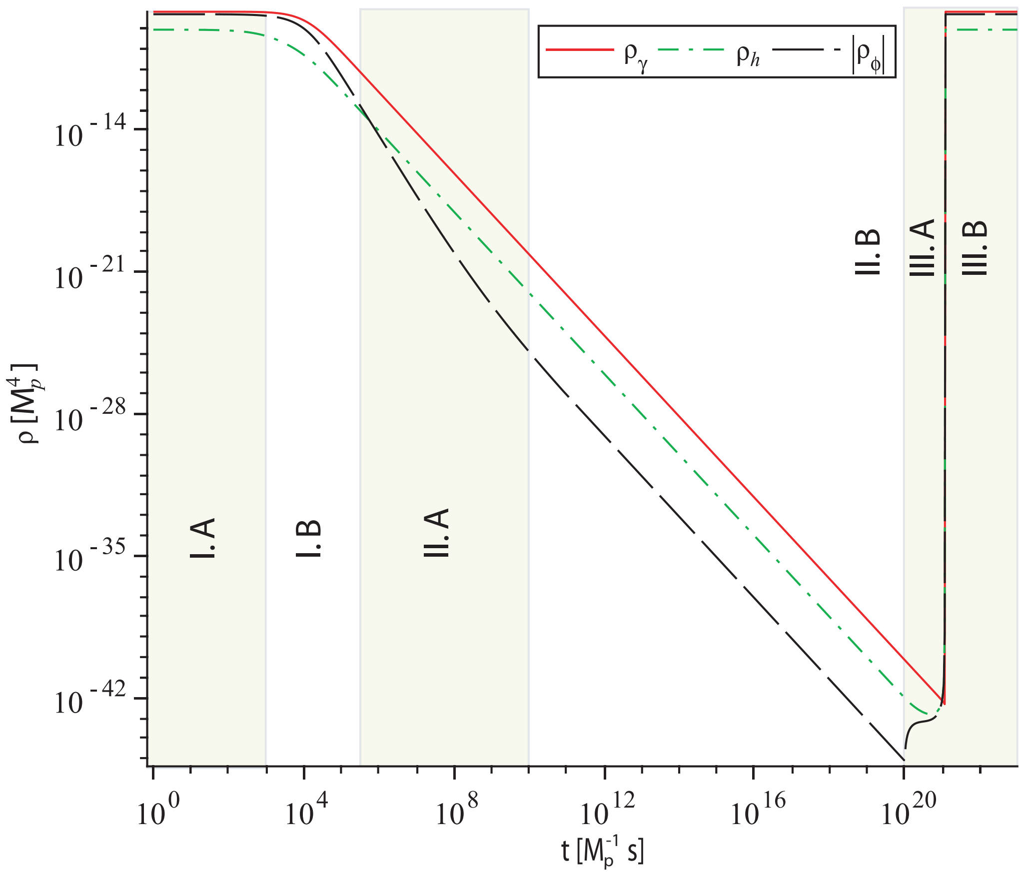

Figure 2.1: Numerical solutions for the energy densities as we complete a cycle from a deStiter phase back to it. Here we have chosen: $\omega = \frac{1}{3}$, $\mu_p = 5$, $\mu_r = .1$, $m = 10^{-2}M_p$ and we have set M_p to one. Note the six distinct phases: I.A and I.B corresponding to reheating; II.A and II.B corresponding to a radiation dominated universe; III.A and III.B corresponding to the phantom and dS phase respectively. In order to make all phases clearly distinct we chose the transition set the minimum energy density at around 10^{-45} instead of the realistic meV^4

the hidden matter indeed behaves as radiation to a very good approximation.

This radiation dominated tracking era lasts till ϕ reaches ϕ_0 and rolls over to the large μ region. The next phase of phantom domination, phase III.A, can now begin.

2.3.3 Cyclicity

To better understand the transition from one cycle to the next let us discuss the various phases we observe in Fig. 1, where we plot a numerical solution for the energy densities of the three components from one deSitter inflationary phase to the next. The plot does not correspond to realistic values for $\lambda_{\tt max}$ or $\lambda_{\tt min}$, but captures all the essential features of the different phases. The plot starts (extreme left) at $t = 0$ and $\phi = \phi_R$, corresponding to the beginning of the reheating phase I.A. We have estimated in Appendix B, equation (B.8) how long (t_{1A}) the I.A sub-phase lasts

$$t_{1A} = \left(\frac{3M_p^4 \xi}{m^6 \eta^3} \right)^{\frac{1}{2}} \tag{2.47}$$

During this phase the field ϕ evolves approximately a distance of:

$$\Delta\phi_{1A} = \dot{\phi}_{dS} \int_0^{t_{1A}} \mathrm{d}t \, e^{-3H_{dS}t} = \frac{\dot{\phi}_{dS}}{3H_{dS}} \left[1 - e^{-3H_{dS}t_{1A}} \right] \tag{2.48}$$

Above we have used:

$$\dot{\phi}(t_{1A}) = \dot{\phi}_{dS} e^{-3H_{dS}t_{1A}} \tag{2.49}$$

where $\dot{\phi}_{dS}$ represents the asymptotic value in the deSitter phase, given by (2.34) and H_{dS} is the Hubble rate during the inflationary phase and can be solved for from the definitions of ξ and η.

Phase I.A is followed by phase I.B, where although the conversion from hidden matter to radiation takes place, the Hubble rate starts to decrease appreciably as well. As soon as the conversion is no longer efficient we enter a regime, phase II.A, where radiation starts to redshift as a^{-4} marking the beginning of a Standard radiation dominated era. In Phase II.A radiation and the hidden sector energies approximately track each other while the field ϕ is still being Hubble damped. This phase ends when the scalar field is no longer Hubble damped and starts to track radiation as well, a phase we refer to as II.B. Next we estimate the time t_{2A}, when this transition from the Hubble damping phase II.A to tracking phase II.B occurs. It can be defined as the time when the Hubble damping term in the l.h.s. of equation (2.27) is equal to the coupling term on the r.h.s. Under the assumption that we are in a radiation dominated phase and that the hidden sector energy density tracks the radiation energy density with the ratio $\mathscr{R}_{\mathtt{min}}$ we get:

$$\begin{aligned}\frac{3\dot{\phi}(t_{2A})}{2t_{2A}} &= \frac{2\mu_r}{M_p}\mathscr{R}_{\mathtt{min}}\rho_\gamma(t_{2A}) \\ \Rightarrow t_{2A} &= \frac{t_{1A}^3\dot{\phi}^2(t_{1A})}{M_p^2\mu_r^2\mathscr{R}_{\mathtt{min}}^2}\end{aligned} \tag{2.50}$$

This last equation can be rewritten in terms of our parameters in the following form:

$$\frac{t_{1A}}{t_{2A}} = \frac{1}{144}\frac{\mu_r^2(3+8\mu_r)^2\eta}{\xi\mu_p^6}e^{6H_{dS}t_{1A}} \tag{2.51}$$

With $\omega = 1/3$ and in the limit $\mu_p \gg 1$ the exponent $6H_{dS}t_{1A}$ becomes $\sqrt{3}$, so we see, as expected, that $t_{2A} \gg t_{1A}$.

We can compute the distance the field ϕ evolves during the phases I.B and II.A since the Hubble friction term is dominant during this time.

$$\begin{aligned}\Delta\phi_{1B+2A} &= \int_{t_{1A}}^{t_{2A}} \mathrm{d}t\dot{\phi} = 2\dot{\phi}(t_{1A})t_{1A}\left(1-\sqrt{\frac{t_{1A}}{t_{2A}}}\right) \\ &\approx \frac{4\mu_p}{\sqrt{3}}\sqrt{\frac{\xi}{\eta}}M_p e^{-\frac{\sqrt{3}}{2}}\end{aligned} \tag{2.52}$$

In the next phase, II.B, as one can see from the plot, all the energy components are tracking each other. Since this phase will lasts until almost 'today' and it began at t_{2A} we have:

$$\frac{\Delta\phi_{2B}}{M_p} \approx 2\mathscr{R}_{\mathtt{min}}\mu_r \ln\left(\frac{(\rho_\gamma(t_{2A}))^{\frac{1}{4}}}{meV}\right) \approx 120\mathscr{R}_{\mathtt{min}}\mu_r \tag{2.53}$$

where $\Delta\phi_{2B}$ is the distance the scalar field evolves during phase II.B. In particular we note that this means

$$e^{\frac{\mu_r\Delta\phi_{2B}}{M_p}} \approx e^{120\mathscr{R}_{\mathtt{min}}\mu_r^2} \tag{2.54}$$

Since $\mathscr{R}_{\mathtt{min}}$ is a small number, for sufficiently small values of μ_r it is easy to see that the exponential will only contribute to an $\mathcal{O}(1)$ factor to the energy density of the hidden matter sector. In other words unlike the $\mu_r = 0$ case, although the ratio $\mathscr{R}$ does not monotonically decrease during the radiation phase, but rather starts to increase as ϕ evolves, this increase is very slow. This justifies our earlier assumption of hidden matter approximately behaving as radiation.

The advantage of having a non-zero μ_r is that it keeps the scalar field rolling, albeit slowly, ensuring passage to the next phantom phase when ϕ reaches ϕ_0. Therefore, no fine-tuning is involved in restarting the phantom era. To see this observe that

$$\Delta\phi_{2B} = (\phi_0 - \phi_R) - (\Delta\phi_{1A} + \Delta\phi_{1B+2A}) \tag{2.55}$$

and crucially for realistic values of the parameters the three different $\Delta\phi$'s are of the same order of magnitude. If for instance, it turned out that $\Delta\phi_{2B} \ll \Delta\phi_{1A} + \Delta\phi_{1B+2A}$, that would have meant fine tuning the range $\phi_0 - \phi_R$ to cancel $\Delta\phi_{1A} + \Delta\phi_{1B+2A}$ to very high precision. In fact, this is what one has to do as $\mu_r \to 0$.

A related nice feature of the model is that the exponential hierarchy between the scales of inflation and dark energy is rather easy to arrange. To see this let us try to obtain $\lambda_{\tt min}$ in terms of $\phi_0 - \phi_R$. By re-arranging equation (2.53) one finds that the energy density at the beginning of the phantom phase is given by [9]

$$\begin{aligned}\lambda_{\tt min} &\sim \lambda_{\tt max} \exp\left(-\frac{\Delta\phi_{2B}}{2\mathscr{R}_{\tt min}\mu_r M_p}\right)\\ &\sim 10^{-3} M_p \exp\left(-\frac{\phi_0 - \phi_R - \Delta\phi_{1A} - \Delta\phi_{1B+2A}}{2\mathscr{R}_{\tt min}\mu_r M_p}\right)\end{aligned} \tag{2.56}$$

Since $\mathscr{R}_{\tt min}, \mu_r$ are small numbers as compared to $\Delta\phi/M_p$'s, it is easy to arrange the exponential suppression of ρ_0 as compared to the GUT scale. Conversely, we can refor-

[9] Above we have used a value for $\rho_\gamma^{1/4}(t_{2A})$ of $10^{-3} M_P$, slightly overestimating it. The actual value is typically lower than this, because of the additional Hubble dilution of the energy density of radiation from t_{1A} to t_{2A}. For instance, with the parameters used in the numerical solution for Fig. 1 we have $\rho_\gamma^{1/4}(t_{2A}) \sim 10^{-5} M_p$.

mulate the "smallness" problem associated with dark energy in terms of four parameters: $\mu_p, \mu_r, \phi_R, \phi_0$, which as we shall see shortly have much milder hierarchies than $\sim 10^{-27}$ corresponding to the meV/GUT scale ratio. In the next section (below equation (2.62)) we will provide specific numerical examples which make this more evident.

Finally, we come to the phantom phases III.A, B. The transition to the phantom phase, which is supposed to be happening during the present cosmological epoch, occurs once ϕ reaches ϕ_0 and μ transitions suddenly to its high value, μ_p. The hidden matter + scalar field energy densities catch up with radiation, start evolving as a phantom fluid with equation of state given by (2.21), and come to dominate the universe. The radiation keeps getting diluted as a^{-4} during this phase which we refer to as phase III.A. Since the increase in energy density in the phantom phase occurs at a very short time scale, all the features of this phase are not very discernable in the log-log plot in Fig.1, but we have checked them numerically. As we have seen before, the annihilation term will ultimately cause this behavior to transition to a de Sitter phase, when $\Gamma \sim H$ or $\rho_h \sim m^6/M_p^2$. At this point we enter, what we call phase III.B, when all the energy densities become comparable and then tend towards constant values, leading to an asymptotic de Sitter space-time. It is during this phase we expect to generate a scale invariant spectrum of perturbations. This phase will last until the field ϕ has evolved a distance of $\phi_0 + \phi_R$, when we re-start the cycle.

2.4 Numbers and Constraints

So far we have provided general constraints coming from different observations on the couplings and the scales. For the purpose of illustration let us provide some typical values which conform to these constraints and in the process we will also be able to understand the different phases of evolution better. Let us start with the inflationary phase. As already discussed, to obtain the correct amplitude of inflationary fluctuations we will take the reheating to occur at approximately GUT scale energy densities which implies

$$m \sim 10^{-2} M_p \tag{2.57}$$

During the course of 60 e-foldings[10], we find, using equations (2.33,2.34), that the field ϕ evolves a distance of:

$$\Delta\phi_{3B} = 40 M_p \mu_p \xi \tag{2.58}$$

As a prototype example, for $\mu_p = 4$ this gives us $\Delta\phi_{3B} \sim 200$. This only gives us a constraint on the range when μ is large. For instance, for $\mu_p = 4$ the number of efoldings during the phantom phase turns out to be (using equation (2.25)) $\Delta\phi_{3A} \sim 30$. To be consistent with inflation we must have $\phi_R \gtrsim 200 + 30 = 230$. Given the fact that these field values are transPlanckian, it is possible that higher order terms in the Lagrangian should not be neglected; we proceed here with the assumption that our starting point is sensible nonetheless.

Depending on the number of e-foldings during the de Sitter phase we find two distinct cases for the spectrum of fluctuations. Case I. If the range of ϕ is such that one gets more than 60 e-foldings of de Sitter, then the CMB fluctuations are scale invariant. As we noted in the introduction, $n_s \approx 1$ is still consistent with observations *Komatsu et al.* (2009) once one allows the possibility of running of the tilt and/or tensor modes. If the range in ϕ is such that we have only around 60 e-foldings then the CMB fluctuations at large scales can show a transition from a blue (when the phantom phase will be operating and the reheating mechanism hasn't kicked in completely) to a scale invariant spectrum. This could be an interesting and rather unique signature of the model. Case II. If the number of efoldings in the dS phase is shorter than 60 e-foldings, the fluctuations that we are observing in the sky must have been generated in the phantom phase. This gives a rather stringent constraint on how far below -1 the phantom equation of state ω_p can be. For a "super-inflationary"

[10]We choose 60 as a generic typical example for GUT scale inflation; the actual number of e-foldings might be lower or larger than this.

space-time sourced by phantom fluid, the spectral tilt is expected to be given by

$$\eta_s - 1 = \frac{6(1+\omega_p)}{1+3\omega_p} > 0 \tag{2.59}$$

implying a blue spectrum. Therefore to be consistent with the observations ω_p has to be very close to -1. For instance, if we include tensor modes, according to *Komatsu et al.* (2009) at the 2σ level we find

$$\eta_s < 1.01 \Rightarrow \omega_p > -1.01 \tag{2.60}$$

implying $\mu_p < .581$. This bound is very restrictive, remembering that in order to have a phantom phase we need $\mu_p > 1/\sqrt{3} \approx 0.577$. In the rest of the section we are not going to discuss this possibility any further and concentrate on Case I with $\mu_p \gg 1$ which seems more attractive.

Let's next look at the constraint coming from BBN and WMAP on the amount of dark radiation *Olive et al.* (2000); *Ichiki et al.* (2002). To be consistent with the data the amount of dark radiation has to be limited to within 10% of ordinary radiation. This essentially imposes a constraint on μ_p, but a rather weak one

$$\mathscr{R}_{\mathtt{min}} < 0.1 \Rightarrow \mu_p \gtrsim 0.17 \tag{2.61}$$

which is easily satisfied.

What about the range of $\Delta\phi$ during radiation domination? This of course depends on the value of μ_p, μ_r. Just to get an idea, we find for $\mu_p = 4, \mu_r = 0.2$, we need

$$\begin{aligned} \Delta\phi &= \Delta\phi_{1A} + \Delta\phi_{1B+2A} + \Delta\phi_{2B} = \phi_0 - \phi_R \sim \\ &\sim 0.70 + 2.16 + 0.66 \end{aligned} \tag{2.62}$$

As one can see, all the values in the above equation are of the same order of magnitude and therefore no fine tuning seems to be involved.

Thus the picture that emerges from the above estimates is that for the scenario to work we need a relatively longer phases in ϕ when μ is large (2.58), followed by shorter phases when μ is small. However, even the discrepancy in $\Delta\phi$ between equations (2.58) and (2.62) is only a few orders of magnitude. Similarly, μ_r and μ_p (in the above example) differ again by only a few orders of magnitude. It is the heirarchy between these values (the two values of $\Delta\phi$ and the two values of μ) that determines the heirarchy between today's meV scale and the GUT scale of inflation via equation (2.56). So we see that, indeed, the required heirarchy to explain these disparate mass scales is relatively small.

Finally, let us come to constraints from dark energy. The main constraint comes from the equation of state parameter. A combined 2σ bound from CMB+BAO+SN is given by $-0.88 > \omega_p > -1.14$ *Komatsu et al.* (2009). This provides a constraint on μ_p

$$\mu_p < 0.61 \tag{2.63}$$

This may seem too small, but we realize that currently we are undergoing the phase transition from small μ to a large μ region, and therefore it is easy to arrange that the "current" value of μ satisfies inequality (2.63) and has not yet reached the constant maximum value μ_p. Equivalently, the equation of state parameter today has not yet reached its late time phantom phase value given by equation (2.21).

2.5 Conclusions

In this paper we have studied a cyclical model of the universe where the energy density cycles between a minimum value, typically of the order of meV^4 and a maximum value roughly set by the GUT scale. This effectively provides a connection between the current accelerated expansion we observe today and the inflationary era in the past. The scale factor continues to grow from one cycle to the next (there is no ”turnaround”). In order to achieve this model we postulated the existence of some ‘hidden’ sector matter coupled to a ghost like scalar field. This mechanism is responsible for a super-accelerated phantom expansion. Allowing for hidden sector particles to be converted to light degrees of freedom of the standard model ameliorates the phantom behavior, effectively transitioning to a deSitter like expansion, therefore avoiding the Big-Rip singularity. Although dominated by radiation, in this phase all the energy densities remain constant. Therefore, if most of the cosmological perturbations are generated during this exponential inflationary era the spectrum is expected to be scale invariant. Even if not favored by the data, this is still a possibility. Another possibility would be to have some of the fluctuations generated during the phantom phase which will show up as a blue tilt in the spectrum. In that case we will see a running of the tilt which could be a unique possible signature of the model.

In order to achieve the cyclic behavior we have postulated that the coupling between the ghost scalar field and the hidden sector is constant piecewise. This procedure might seem ad-hoc, but it is just the simplest possibility. We found that no fine tuning seems to be involved when requiring to have a long enough radiation/matter dominated phase. It is also worth mentioning that the “smallnesss” problem associated with dark energy is circumvented. The only parameter we need in order to describe the current acceleration is the coupling between the hidden sector and the ghost field, and it has a value not much greater than one.

CHAPTER III

Dark Stars and Boosted DM annihilation rates

3.1 Introduction

We have introduced the concept of Dark Stars and reviewed some of the relevant literature in Section 1.4. Spolyar et al. (2008) first considered the effect of dark matter (DM) particles powering the first stars. The first stars formed when the universe was about 200 million years old, at $z = 10-50$, in $10^6 M_\odot$ haloes consisting of 85% DM and 15% baryons in the form of H and He from big bang nucleosynthesis; for reviews of the standard picture of the formation of the first stars, see Barkana & Loeb (2001), Yoshida et al. (2003), Bromm & Larson (2004), and Ripamonti & Abel (2005). The canonical example of particle DM is Weakly Interacting Massive Particles (WIMPs). In many theories WIMPs are their own antiparticles and annihilate among themselves wherever the DM density is high. Recently there has been much excitement in the dark matter community about possible detections of WIMPs via annihilation to positrons seen by the PAMELA satellite (Adriani et al. 2009); annihilation to γ-rays seen by FERMI (Abdo et al. 2009, Dobler et al. 2009), and in the direct detection experiments DAMA and CDMS (Bernabei et al. 2009, Ahmed et al. 2009). The annihilation rate is $n_\chi^2 \langle \sigma v \rangle$ where n_χ is WIMP density and we take the standard annihilation cross section[1]

$$\langle \sigma v \rangle = 3 \times 10^{-26} \mathrm{cm}^3/\mathrm{s}, \tag{3.1}$$

and WIMP masses in the range 1 GeV-10 TeV. The first stars are particularly good sites for annihilation: they form in the right place — in the high density centers of DM haloes — and at the right time — at high redshifts (density scales as $(1+z)^3$). Spolyar et al. (2008) found that above a certain density ($\approx 10^{13}$ cm^{-3}) the WIMP annihilation products remain trapped in the star, thermalize with the star, and thereby provide a heat source. These first Dark Stars (DS) are stars made primarily of hydrogen and helium with only ~ 0.1% of the mass in the form of DM; yet they shine due to DM heating. Note that the term 'Dark' refers to the power source, not the appearance or the primary matter constituent of the star.

Dark stars are born with masses $\sim 1 M_\odot$. They are giant puffy (~ 10 AU), cool (surface temperatures $< 10,000$K), yet bright $> 10^6 L_\odot$ objects (Freese et al. 2008a). They reside in a large reservoir ($\sim 10^5 M_\odot$) of baryons, i.e., ~ 15% of the total halo mass. These baryons can start to accrete onto the dark stars. Previous work (Freese et al. 2008a; Spolyar et al. 2009) followed the evolution of dark stars from their inception at $1 M_\odot$, as they accreted baryons from the surrounding halo, up to $\sim 1000 M_\odot$. Dark stars can continue to grow in mass as long as there is a supply of DM fuel.

3.1.1 Boosted Leptophilic Annihilation Motivated by PAMELA data

Recent measurements of cosmic ray positrons and electrons in the GeV-TeV range could have significant implications on our understanding of dark matter (DM). The PAMELA collaboration (*Adriani et al.*, 2009a, 2010) reported a e^+ flux excess in the cosmic energy spectrum from 10 to 100 GeV, reinforcing what was previously observed up to an energy of 50 GeV by the HEAT experiment (*Barwick et al.*, 1997). The FERMI-LAT collabo-

[1]Annihilation in the early universe with this value of the cross section leaves behind the correct relic WIMP DM abundance today, ~ 24% of the energy density of the universe.

ration (*Abdo et al.*, 2009a,b) has found an excess in the $e^+ + e^-$ flux in the $100 - 1000$ GeV energy range above the background given by a conventional diffusive model, albeit in conflict with a much larger excesses in flux in the 500 GeV range previously reported by ATIC collaboration.[2] It is worth mentioning that a simple power-law fit of the FERMI-LAT electron energy spectrum is possible, being consistent with both astrophysical sources, or DM annihilation (e.g *Di Bernardo et al.*, 2009; *Grasso et al.*, 2009).

If confirmed, there are several possible explanations for the positron excess. The signals could be generated by astrophysical sources, such as pulsars or supernova shocks (e.g. *Boulares*, 1989; *Profumo*, 2008; *Hooper et al.*, 2009a; *Ahlers et al.*, 2009; *Blasi*, 2009; *Fujita et al.*, 2009; *Malyshev et al.*, 2009; *Mertsch and Sarkar*, 2009; *Shaviv et al.*, 2009). Uncertainties in cosmic ray propagation in the galaxy leave open the possibility that standard cosmic ray physics could explain the signal (*Delahaye et al.*, 2009). Another possible interpretation of the data could be in terms of a signal from DM annihilation (*Baltz et al.*, 2002; *Kane et al.*, 2002; *de Boer et al.*, 2002; *Hooper et al.*, 2004; *Hooper and Silk*, 2005; *Cirelli et al.*, 2008; *Cirelli and Strumia*, 2008; *Grajek et al.*, 2009; *Nelson and Spitzer*, 2008; *Nomura and Thaler*, 2009; *Arkani-Hamed et al.*, 2009; *Barger et al.*, 2009b,a; *Bergstrom et al.*, 2009; *Bai et al.*, 2009; *Bi et al.*, 2009; *Cholis et al.*, 2009a,b,c; *Cirelli et al.*, 2009; *Fox and Poppitz*, 2009; *Hooper and Zurek*, 2009; *Meade et al.*, 2009; *Zurek*, 2009; *Meade et al.*, 2010) or decay (*Chen and Takahashi*, 2009; *Chen et al.*, 2009a,b; *Ibarra and Tran*, 2009; *Ibarra et al.*, 2009; *Ibe et al.*, 2009a; *Ishiwata et al.*, 2009; *Shirai et al.*, 2009; *Yin et al.*, 2009; *Bajc et al.*, 2010; *Chen et al.*, 2010). Others point out constraints against such an interpretation (*Abdo et al.*, 2010; *Abazajian et al.*, 2010).

The prospect that DM has been detected, although indirectly, has stirred a lot of excitement and a flurry of interest. There are several model-building challenges, however. If dark matter is to explain the positron flux excess in the cosmic-ray spectrum, in most models the products of decay or annihilation must be primarily leptonic since an excess in

[2]The ATIC balloon experiment (*Chang et al.*, 2008) found an increase in the $e^+ + e^-$ spectrum between 300 and 800 GeV above background which has apparently been ruled out by FERMI.

the anti-proton fluxes is not found (*Adriani et al.*, 2009b) .

Moreover, in order to explain the observed signals the annihilation rate needs to be on the order of $10 - 10^3$ larger than for thermal relic. This could be explained by non-relativistic enhancements to the cross-section, such as the Sommerfeld enhancement (*Sommerfeld*, 1931; *Hisano et al.*, 2004; *Profumo*, 2005; *March-Russell et al.*, 2008; *Cirelli et al.*, 2009; *Lattanzi and Silk*, 2009) or a Breit-Wigner enhancement (*Feldman et al.*, 2009; *Guo and Wu*, 2009; *Ibe et al.*, 2009b; *Kadota et al.*, 2010). Scenarios involving non-standard cosmologies have also been considered as a possible solution (e.g *Gelmini and Gondolo*, 2008; *Catena et al.*, 2009; *Pallis*, 2010). Alternatively, the annihilation rate could be greater than the standard prediction if the dark matter is not smoothly distributed in the local halo of the Milky Way (*Diemand et al.*, 2008; *Hooper et al.*, 2009b; *Kamionkowski et al.*, 2010). For a review of the DM explanation for the the cosmic ray $e^{\pm}$ excess see *He* (2009).

In light of these new dark matter models, we study the possible modifications to the evolution of a Dark Star (DS) for the case of leptophilic boosted dark matter. In *Spolyar et al.* (2009) a comprehensive study of DS for various WIMP masses was done, but the annihilation cross section was kept to its fiducial unboosted value. We return here to this problem, including the possibility of a boost factor for the cross section. Our starting point will be *Bergstrom et al.* (2009), where the authors find regions in the (m_χ, B) parameter space (mass of WIMP vs. boost factor) that fits PAMELA/FERMI data based on three different classes of DM models. For simplicity we consider only two of those models in our study: from the leptophilic class, the μ channel case, where 100% direct annihilation to $\mu^+\mu^-$ is assumed and the $AH4$ model, a subclass of the Arkani-Hamed model (*Arkani-Hamed et al.*, 2009) which postulates that the Somerfeld enhancement is due to the exchange of a new type of light (sub- GeV) particle. In the $AH4$ case the new force carrier is a scalar, ϕ, which subsequently decays 100% to $\mu^+\mu^-$. Somerfeld enhancement is now generated naturally via ladder diagrams for the $\chi\chi \to \phi\phi$ process, producing 4 muons per annihilation versus 2 muons in the direct annihilation case.

3.1.2 Effect of Concentration Parameter

A second focus will be the study the dependence of DS properties on the concentration parameter of the initial density profile of the halo within which the first stars form. To remind the reader, the concentration parameter (c) characterizes how centrally condensed the initial density profile is: a larger concentration parameter means that more of the mass is concentrated at the center rather than at the outside of the dark matter halo (the precise definition is given below in Sec.3.2.3.2). Previous studies of DS considered $c = 10$ and $c = 2$. Here we systematically examine a sensible range of concentration parameters. The most recent results of numerical simulations of structure formation seem to favor a ”floor” of $c = 3.5$ on the concentration parameter of early structures (*Zhao et al.*, 2003, 2009; *Tinker et al.*, 2010) (Some halos can have a smaller concentration parameter if star formation begins before the halo is fully formed). At any rate the value will differ from halo to halo, even at the same redshift. Thus to explore how the properties of the DS are affected by a change in the concentration parameter, we run the same simulation with three different values for it: $c = (2, 3.5, 5)$, which characterizes the overall range for the concentration parameter DM halos hosting the first stars.

3.1.3 Canonical Values

We assume a redshift of formation $z = 20$ for the first stars, a dark matter halo of $10^6 M_\odot$, and concentration parameters $c = (2, 3.5, 5)$. We take the annihilation cross section to be

$$\langle \sigma v \rangle = B \times 3 \times 10^{-26} \mathrm{cm}^3/\mathrm{s} \tag{3.2}$$

where the boost factor B varies between 100 and 5000 (depending on the particle physics model). The corresponding WIMP mass is taken from the models in *Bergstrom et al.* (2009) described above and ranges from 100 GeV-4 TeV.

A key question for DS is the final mass, as the DS accretes more and more material. As long as there is a reservoir of DM to heat the DS, the star continues to grow. In the original work of *Spolyar et al.* (2009), the assumption was made that the initial DM inside the DS annihilates away in $\sim 500,000$ years for a spherical DM halo; here the DS grow to $\sim 1000 M_\odot$. In later work of *Freese et al.* (2010b), this assumption was questioned due to the fact that DM haloes are instead triaxial, so that a variety of DM orbits can keep the central DM density higher for longer periods of time and the DS can grow supermassive $> 10^5 M_\odot$. In reality dark stars will form in a variety of dark matter environments and will grow to a variety of masses. For the purpose of illustrating how DS vary due to differences in the halo concentration parameter and also due to enhanced annihilation rates, we restrict ourselves to the first option for adiabatic contraction, in which the DM originally in the star (due to adiabatic contraction) is the only DM available to the DS; i.e. the DS can grow to $\sim 1000 M_\odot$.

In addition to this simple adiabatic contraction, we also consider the effect of captured DM on the first stars (Iocco 2008; Freese, Spolyar, and Aguirre 2008).

In this case, DM passing through the first stars can scatter off the baryons multiple times, lose energy, and become bound to the star (direct detection experiments are based on the same physics: scattering of DM particles off of nuclei). Subsequently, the star builds up a reservoir made up of captured DM, which can power stars. In the 'minimal capture case,' DM heating from captured DM and fusion powers the star in equal measure once it reaches the main sequence.

In section 3.2 we describe the elements necessary to study the stellar structure of the DS. In Section 3.3 we present results for the influence of varying the concentration parameter and the boost factor on the formation and evolution of Dark Stars and their properties. We summarize in Section 3.4.

3.2 Equilibrium Structure of the Dark Star

3.2.1 Initial Conditions and Accretion Rates

The standard picture of Pop. III star formation starts with a protostellar gas cloud that is collapsing and cooling via hydrogen cooling into a protostar (*Omukai and Nishi*, 1998) at the centre of the halo. However, as was found in *Spolyar et al.* (2008), DM heating could alter the evolution of the first stars significantly. As soon as the protostellar gas reaches a critical core density, DM heating dominates over all possible cooling mechanisms. The cloud condenses a bit more but then stop collapsing, and becomes a dark star in equilibrium. At this point dark matter annihilation can power the dark star.

As the initial conditions for our simulations we take a DS in which the baryons are fully ionized. This luminous object powered by DM annihilations has a mass of $3M_{\odot}$, a radius $1-10$ AU, and a central baryon number density $\sim 10^{17}$cm^{-3}. We look for equilibrium solutions as described below. From this starting point we follow the evolution of the DS as it accretes baryonic mass from its surroundings. We use the accretion rate of *Tan and McKee* (2004), which decreases from $1.5\times10^{-2}M_{\odot}/$yr at $3M_{\odot}$ to $1.5\times10^{-3}M_{\odot}/$yr at $1000M_{\odot}$. At each stage in the accretion process we again find solutions in hydrostatic and thermal equilibrium. Eventually the accretion is cutoff by feedback effects; as the dark matter runs out due to annihilation, the DS heats up to the point where it emits ionizing photons that shut down further accretion. Feedback turns on once the surface temperature T_{eff} reaches 50,000K and is accounted for by introducing a linear reduction factor which shuts off accretion completely once the stars surface temperature reaches 10^5K.

3.2.2 Basic Equations

We use the numerical code previously discussed in detail by *Spolyar et al.* (2009). We make the assumption that a DS can be described as a polytrope

$$P = K\rho^{1+1/n} \tag{3.3}$$

in hydrostatic equilibrium. Here P is the pressure, ρ is the density, and K is a constant. We solve the equations of stellar structure with polytropic index n initially 1.5, as appropriate for convective stars, and made a gradual transition to $n = 3$ as the star becomes radiative in the later phases. We require that at each time-step during the accretion process the star is in hydrostatic equilibrium,

$$\frac{dP}{dr} = -\rho(r)\frac{GM_r}{r^2}. \tag{3.4}$$

Above P denotes the pressure, $\rho(r)$ is the total density and M_r is the mass enclosed in a spherical shell of radius r. We assume that the star can be described as a polytrope with

$$P = K\rho^{1+1/n}, \tag{3.5}$$

where the "constant" K is determined once we know the total mass and radius (*Chandrasekhar*, 1939).

The energy transport is initially convective with polytropic index $n = 3/2$ but as the star approaches the Zero Age Main Sequence (ZAMS) it becomes radiative with $n = 3$. The code interpolates between $n = 3/2$ and $n = 3$ to account for the shift in energy transport as the star grows in mass. We can determine the temperature at each point in the radial grid via the equation of state of a gas-radiation mixture,

$$P(r) = \frac{k_B\rho(r)T(r)}{m_u\mu} + \frac{1}{3}aT(r)^4 \equiv P_g + P_{rad}. \tag{3.6}$$

Here k_B is the Boltzmann constant, m_u is the atomic mass unit and $\mu = (2X + 3/4Y)^{-1}$ is the mean atomic weight. In all resulting models $T \gg 10^4$K except near the surface, so we use the mean atomic weight for fully ionized H and He. We assume a H mass fraction of $X = 0.76$ and a He mass fraction $Y = 0.24$, and that they will remain constant throughout the simulation.

At each point in the radial grid, $T(r)$ and $\rho(r)$ are used to determine the Rosseland mean opacity κ from a zero metallicity table from OPAL (*Iglesias and Rogers*, 1996) supplemented at low temperatures by opacities from *Lenzuni et al.* (1991) for $T < 6000$K. The location of the photosphere is determined by the hydrostatic condition:

$$\kappa P = \frac{2}{3} g \tag{3.7}$$

where g is the acceleration due to gravity at that particular location. This corresponds to a point with inward integrated optical depth $\tau \sim 2/3$; here the local temperature is set to T_{eff} and the stellar radiated luminosity is therefore:

$$L_* = 4\pi R_*^2 \sigma_B T_{eff}^4, \tag{3.8}$$

with R_* being the photospheric radius. The thermal equilibrium condition is

$$L_* = L_{\rm tot} \tag{3.9}$$

where L_{tot} is the total luminosity output from all energy sources as described below in Sec.4.2.3.

Starting with a mass M and an estimate for the outer radius R_*, the code integrates Eqns. (4.4) and (4.5) outward from the center.

The total luminosity output L_{tot} is compared to the stellar radiated luminosity, as in Eq.(3.8) and the radius is adjusted until the condition of thermal equilibrium is met (a convergence of 1 in 10^4 is reached).

3.2.3 Dark Matter Densities

3.2.3.1 Initial Profile and Concentration Parameter

The first stars form inside $\sim 10^6 M_\odot$ haloes. Simulations imply that DM halos have a naturally cuspy profile, but there is still some uncertainty about the exact inner slope of a DM halo: *Diemand et al.* (2007); *Springel et al.* (2008); *Klypin et al.* (2010). Luckily, a previous paper (*Freese et al.*, 2009) showed that a dark star results regardless of the details of the initial density profile, even for the extreme case of a cored Burkert profile (such a Burkert profile is completely unrealistic). We will use a Navarro, Frenk, & White (NFW) profile (*Navarro et al.*, 1996) for concreteness. We assume that initially both the baryons (15% of the mass) and the DM (85% of the mass) can be described with the same NFW profile

$$\rho(r) = \frac{\rho_0}{r/r_s(1+r/r_s)^2}, \tag{3.10}$$

where ρ_0 is the ”central” density and r_s is the scale radius. Clearly at any point of the profile, baryons will only make up 15% of the mass. The density scale, ρ_0 can be re-expressed in terms of the critical density of the universe at a given redshift, $\rho_c(z)$ via

$$\rho_0 = \rho_c(z)\frac{200}{3}\frac{c^3}{ln(1+c) - c/(c+1)}, \tag{3.11}$$

where $c \equiv r_{vir}/r_s$ is the concentration parameter and r_{vir} is the virial radius of the halo. We assume a flat ΛCDM universe with current matter density $\Omega_m = 0.24$ and dark energy density $\Omega_\Lambda = 0.76$.

One of our aims is the study is the dependence of DS properties on the value of the concentration parameter c. Hence we consider a variety of values, ranging from c=2 to c=5.

3.2.3.2 Adiabatic Contraction

As the baryons start to collapse into a protostellar cloud at the center of the DM halo, the DM responds to the changing gravitational potential well and becomes compressed. As described in our previous work, we use adiabatic contraction (AC) to calculate the effect of baryons on the DM profile. With an initial DM and gas profile and a final gas profile, we can use the adiabatic invariants to solve for the final DM profile. We use the Blumenthal method (*Barnes and White*, 1984; *Blumenthal et al.*, 1986; *Ryden and Gunn*, 1987) to calculate the adiabatic compression of the halo. In this case the simplifying assumption of circular orbits is made. Angular momentum is the only non-zero invariant. Its conservation implies that $M_f(r_f)r_f = M_i(r_i)r_i$. In the case of circular orbits M is the mass interior to the radius r of an orbit and the indices f and i refer to final and initial orbits respectively. As mass grows inside of the orbit, its radius must shrink and the DM profile steepens.

The validity of this method in this context has been checked in *Freese et al.* (2009), where a more precise algorithm, developed by Young (*Young*, 1980), has been used and a difference within at most a factor of 2 has been found. Whereas the Blumenthal method assumes circular orbits, Young's method only assumes spherical symmetry of the system. Therefore only one of the three conserved actions is identically zero in this case. Namely the plane of each orbit does not change. The other two actions, angular momentum and the radial action respectively are non-zero and conserved. In view of *Freese et al.* (2009) we are confident that the simple Blumenthal method is sufficiently accurate for our purpose.

We will assume that all of the DM moves on circular orbits. The DM will become exhausted once all of the DM on orbits interior to the DS have been depleted. The timescale for this to happen is on the order a million years. This is probably an unduly cautious assumption. In Chapter IV we studythe case of triaxial haloes with large numbers of centrophilic orbits, which provided a much larger DM reservoir than we are considering, leading to supermassive DS. In reality dark stars will form in a variety of dark matter environments and will grow to a variety of masses. We could have included the possibility of DS growing to supermassive sizes, but do not consider it necessary for showing the dependence of DS properties on the two effects we are studying.

3.2.3.3 Dark Matter Capture

Until now we have only discussed the DM inside the DS due to adiabatic contraction. However, dark star's DM reservoir can be refueled by DM capture. This refueling requires an additional piece of particle physics: scattering of DM off the atomic nuclei inside the star. Some of the WIMPs from far out in the halo have orbits passing through the star. This DM can be captured and sink to the stars center, where they can annihilate efficiently. The capture process is irrelevant during the early evolutionary stage of the DS, since the baryon density is not high enough to efficiently capture DM. However, at the later stages as the DS contracts towards the ZAMS, the baryon densities become high enough for substantial capture to be possible. This mechanism was first noticed simultaneously by (*Iocco*, 2008) and (*Freese et al.*, 2008b).

The capture rate is sensitive to two uncertain quantities: the scattering cross section of WIMP interactions with the nuclei and the background DM density. In terms of the relevant particle physics, we consider only spin-dependent (SD) scattering cross sections with

$$\sigma_c = 10^{-39}\mathrm{cm}^2. \tag{3.12}$$

The details of our capture study have previously been presented in *Freese et al.* (2008b) and will not be repeated here. We do wish to emphasize that we assume the same case of minimal capture that we previously studied in *Spolyar et al.* (2009), in which case the heating from fusion and from DM heating are taken to be comparable. The more extreme and interesting case of dominant capture, which could last as long as the DS continues to exist in a high DM density environment, was studied elsewhere (*Freese et al.*, 2010b) and can lead to supermassive $> 10^5 M_\odot$ DS.

3.2.4 Energy Sources

There are four possible contributions to the DS luminosity:

$$L_{tot} = L_{DM} + L_{grav} + L_{nuc} + L_{cap} \tag{3.13}$$

from DM annihilation, gravitational contraction, nuclear fusion, and captured DM respectively.

3.2.4.1 DM Annihilation

WIMP annihilation produces energy at a rate per unit volume

$$\hat{Q}_{DM} = n_\chi^2 \langle \sigma v \rangle m_\chi = \langle \sigma v \rangle \rho_\chi^2 / m_\chi, \tag{3.14}$$

where n_χ is the WIMP number density, m_χ is the WIMP mass, and ρ_χ is the WIMP energy density. The final annihilation products typically are electrons, photons, and neutrinos. The neutrinos escape the star, while the other annihilation products are trapped in the dark star, thermalize with the star, and heat it up. The luminosity from the DM heating is given by:

$$L_{DM} \sim f_Q \int \hat{Q}_{DM} dV \tag{3.15}$$

where f_Q is the fraction of the annihilation energy deposited in the star (not lost to neutrinos) and dV is the volume element.

The heating due to DM annihilation is given in Eqns. (3.14) and (3.15) and dominates from the time of DS formation until the adiabatically contracted DM runs out. In order to compute the luminosity generated by DM heating, one needs to know what fraction of the total energy generated by WIMP annihilations is deposited in the star. This quantity, which we name f_Q, will be different for various models for DM. In previous work (e.g. in *Spolyar et al.* (2009)) a fiducial value for f_Q of $2/3$ was used as appropriate for many typical

WIMPS, under the following assumptions. First, the final products of DM annihilation, after all unstable particles have decayed to the lightest states, are taken to be three types: i) stable charged particles (i.e. $e^{\pm}$), ii) photons and iii) neutrinos. Second, the energy distribution was assumed to be roughly equal among the three final products listed above. The electrons and photons were taken to thermalize in a very short timescale with the star and deposit their energy, whereas the neutrinos escape; hence $f_Q \simeq 2/3$.

On the other hand, given a specific model for DM, one could compute the precise value for f_Q using the energy distribution of all final annihilation products for the model under consideration. While this procedure could be done for the specific models in study, still we use the standard $f_Q = 2/3$ in order to make simple comparisons with our previous work [3]. Since our aim is to understand the effect of the boost factor on the DS properties, we fix the value of f_Q to $2/3$, the same as in *Spolyar et al.* (2009). The differences between the boosted and unboosted cases will now be due only to the boost factor itself and the different masses of the WIMP in the two cases (rather than to the detailed values of f_Q). Since f_Q appears always multiplied by $\langle\sigma v\rangle$, any ambiguity we have introduced by fixing the energy deposition factor to $2/3$ can be traded for an ambiguity in the annihilation cross section. To further justify our assumption of $f_Q \sim 1$ we use a result of *Gondolo et al.* (2010), where the authors have shown, using PYTHIA, that in the case of leptophilic DM models used to explain PAMELA excess positrons as well as the excess in Fermi-LAT electrons "one gets $f_Q \simeq 0.56$ almost constant in the range 200 GeV$\lesssim m \lesssim$ 2TeV". Both models we are investigating, namely the AH4 and the μ channel, belong to the leptophilic class, as the annihilation products in both cases are muons.

[3]For the leptophilic models we are considering here, DM annihilates either directly or via exchange of a light scalar to $100\%\mu^{\pm}$ so that one might more reasonably expect smaller values since the muons decay to electrons and two neutrinos. The actual value will be closer to $\sim 1/3$ but will depend on the energy distribution among the various final products; still it will be a number of $\mathcal{O}(1)$.

3.2.4.2 Gravitational energy

Once the DS runs out of DM, it begins to contract; gravity turns on and powers the star. Although relatively short, this Kelvin-Helmholtz (KH) contraction phase has important consequences: it drives up the baryon density and increases the temperature, therefore leading to an environment where nuclear fusion can take place. For a polytrope of index $n = 3$ the gravitational contribution to the luminosity was found in *Freese et al.* (2009) using the virial theorem,

$$L_{grav} = \frac{3}{4}\frac{d}{dt}\left(\frac{GM^2}{R}\right) - \frac{1}{2}\frac{d}{dt}E_{rad}, \tag{3.16}$$

where $E_{rad} = \int dV aT^4$ is the radiation energy.

3.2.4.3 Nuclear Reactions

Subsequently nuclear reactions become important. We include the following nuclear reactions, which are typical for a zero metallicity star during the pre main sequence evolution: *i*- burning of primordial deuterium (assumed to have a mass fraction of 4×10^{-5}) which turns on rapidly once the stars central temperature reaches $\sim 10^6$K, *ii*- the equilibrium proton-proton cycle for hydrogen burning, and *iii*- the alpha-alpha reaction for helium burning. Since we track the evolution of the DS only until it reaches ZAMS we do not need to consider the changes in stars atomic abundances. In order to calculate the nuclear luminosity, defined as

$$L_{nuc} = \int dM \epsilon_{nuc}. \tag{3.17}$$

We use the methods described in *Clayton* (1968) to obtain the energy generation rate, ϵ_{nuc}. For the proton-proton reaction we use the astrophysical cross section factors from *Bahcall* (1989) and the He burning parameters from *Kippenhahn and Weigert* (1990).

3.2.4.4 Luminosity due to captured DM

As we have seen in Sec.3.2.3.3, during the later stages of the pre main sequence evolution captured DM can become an important energy source. The luminosity due to DM capture is

$$L_{cap} = 2m_\chi \Gamma_{cap}, \tag{3.18}$$

where

$$\Gamma_{cap} = f_Q \int dV \rho_{cap}^2 \langle \sigma v \rangle / m_\chi \tag{3.19}$$

and the factor of 2 in Eq.(4.8) reflects the fact that the energy per annihilation is twice the WIMP mass. In Eq. (3.19) ρ_{cap} stands for the captured DM density profile. In all simulations we consider the case of "minimal capture", which corresponds to equal contribution to the luminosity from capture and nuclear fusion when the star reaches the main sequence.

3.3 Results

On the whole, for all the values of boost factor and concentration parameter we have considered, the results are roughly the same: the final DS is roughly $\sim 1000 M_\odot$, $\sim 10^7 L_\odot$, and lives $\sim 10^6$yrs. Thus if the e^+ excess seen in PAMELA is due to WIMP annihilation, the required leptophilic boosted cross section is certainly compatible with the DS picture. However there are interesting differences between models which we discuss.

Other than in the subsection immediately following this one, we consider four WIMP models. As motivated below, we focus on one boosted model denoted by AH4 with the following set of parameters: $B = 1500$, $m_\chi = 2.35$ TeV and $c = 3.5$. As our unboosted models, we take 100 GeV WIMPs with the canonical cross section of 3×10^{-26}cm^3/s , and we consider three values of the concentration parameter, c = (2, 3.5, 5). For comparison, the "canonical case" considered in *Spolyar et al.* (2009) was the unboosted 100 GeV case with c=2. The relative boost factor between the AH4 model and the unboosted models is best described as follows: since Eq.(1) tells us that DM heating scales as $\langle\sigma v\rangle/M_\chi$, one can see that the AH4 is exactly equivalent to a 100 GeV WIMP mass with Boost Factor $150/2.35 \simeq 64$. In other words the relative boost factor between the AH4 model and the unboosted cases is actually 64. It is important to stress out that all results we will present depend only on this relative boost factor, and not the actual boost B for the annihilation rate. Therefore it might be somewhat misleading to refer to the models we are considering in terms of a specific particle physics model, as any two models that have the same relative boost factor will produce identical results for the DS. However we keep the terminology established in the literature, i.e. AH4 and μ channel models for conciseness.

Also, we assume throughout that the value of the boost factor is such as to give the $\langle\sigma v\rangle$ required to explain the PAMELA/Fermi data" Namely $\langle\sigma v\rangle_{ds} = \langle\sigma v\rangle_{gal}$, where the two correspond to the value of the DM annihilation cross sections in the Dark Star and our galaxy respectively. If we assume Sommerfeld enhancement as the source of the boost factor we might have $\langle\sigma v\rangle_{ds} \gtrsim \langle\sigma v\rangle_{gal}$, as the velocity inside the star, roughly $\sim 10km/s$, is much lower than $v_{gal} \simeq 300km/s$ and the Sommerfeld enhancement is higher at lower velocities, up to a certain saturation limit. Therefore the values we take for the boost factor should be seen as conservative. For clarity, we fix the boost factor to the values given by *Bergstrom et al.* (2009).

3.3.1 'Final' Luminosity for Dark Stars with boosted DM

We investigate the 'final' luminosities and masses of Dark Stars as they enter the main sequence. We study a variety of WIMP parameter ranges capable of explaining the PAMELA data; in particular we follow the work of *Bergstrom et al.* (2009) and take various boosted DM annihilation rates and WIMP masses from fig. 1 or their paper, which gives 2σ contours in the enhancement factor - mass plane needed to fit PAMELA and Fermi data. In this section we consider two of the particle physics models they consider: the μ channel and AH4 type of models.

In Fig. 3.1 we plot the 'final' luminosity at the end of the DS lifetime, when the DS has accreted to its maximum mass: the dark matter has run out and the star is about to enter the zero age main sequence where it will be powered by fusion. We plot the luminosity as a function of the boost factor. The points represent individual simulation outputs. The solid (dashed) lines connect simulation outputs generated with the DM mass and Boost factors from the 2σ contours in fig.1 from *Bergstrom et al.* (2009) corresponding to the Fermi (PAMELA) confidence regions in *Bergstrom et al.* (2009). We note that even if the boost factors range over more than one order of magnitude, from 100 to 5000 (the corresponding WIMP masses take values in the 1-4 TeV range) the final luminosities in all cases are relatively similar, ranging from $\sim 7 \times 10^6 L_\odot$ to $\sim 9 \times 10^6 L_\odot$ (The variation in luminosity for a fixed boost factor corresponds to the range of allowed m_χ in *Bergstrom et al.* (2009). For instance for a boost factor of 1000, the upper bound of the Fermi contour in left panel of Fig. 3.1 corresponds to a $m_\chi = 1.4$ TeV; the lower bound to $m_\chi = 1.9$ TeV). As the boost factor increases, we note that the final luminosity gets slightly smaller. This is due to the fact that the ratio $\langle \sigma v \rangle / M_{DM}$ typically also increases in most cases. This leads to a faster depletion of the adiabatically contracted DM from the star, shortening the time until it reaches the main sequence, therefore reducing the amount of mass accreted and consequently the luminosity at that point.

3.3.2 Structure and Evolution of DS

In this section, we analyze the two effects of i) boosting the annihilation cross section and ii) a variety of concentration parameters on the structure of a Dark Star. As mentioned above, for the "boosted" case we choose one sample point from the AH4 type models, which corresponds to the large star shaped point at the center of the right panel of Fig. 3.1. Henceforth we denote by AH4 this point which has $B = 1500$, $m_\chi = 2.35$ TeV and $c = 3.5$.

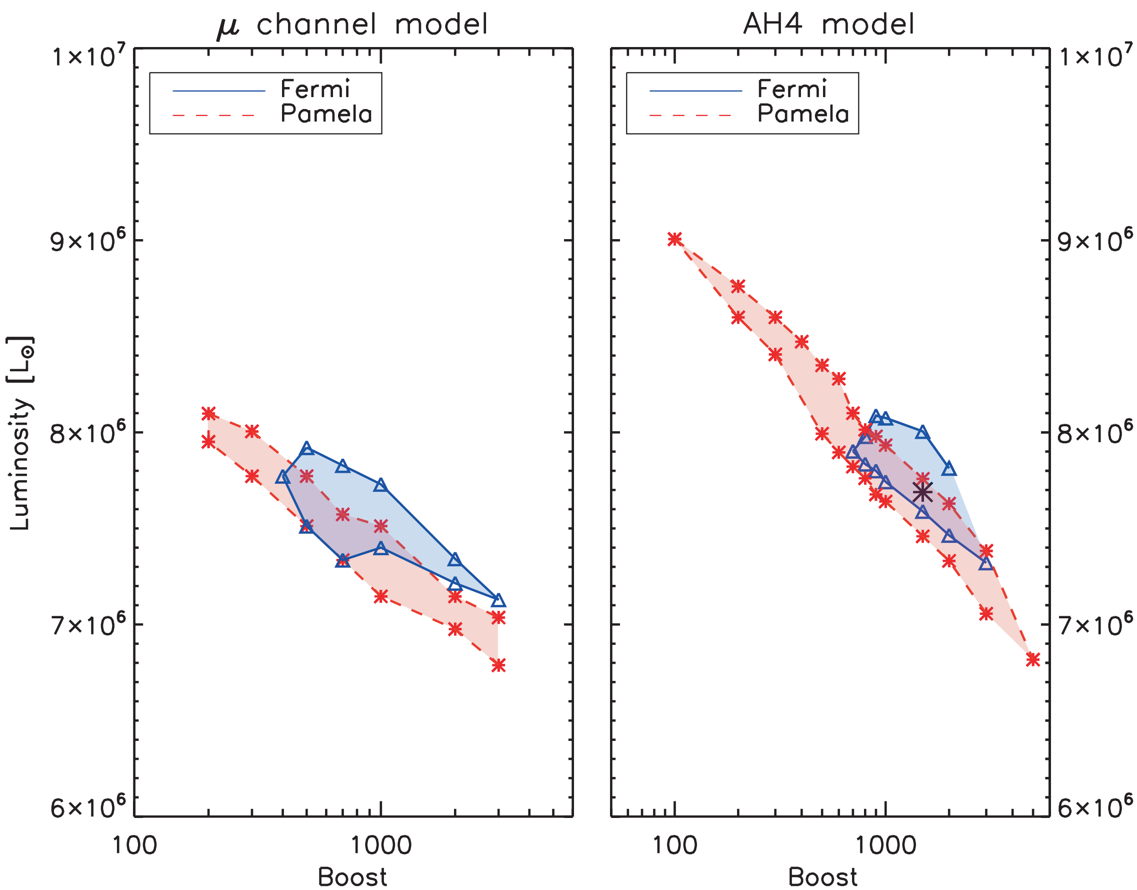

Figure 3.1: "Final" luminosities (as the Dark Star enters the ZAMS) as a function of Boost factor for the μ-channel and AH4 models examined in *Bergstrom et al.* (2009). The contour regions are generated using the range of WIMP masses for a fixed boost factor taken from the corresponding 2σ contours in fig. 1 in *Bergstrom et al.* (2009). The central star-shaped point in the right panel will be taken to be our designated boosted AH4 model and is consistent with both Fermi and PAMELA.

3.3.2.1 Luminosity Evolution

In Fig. 3.2 we compare the luminosity evolution for the four cases we have just described. In all cases, DM annihilation heating provides the dominant contribution to the DS luminosity until the DM runs out. At this point Kelvin-Helmholtz contraction sets in and briefly provides the dominant heat source, until the star becomes hot and dense enough for fusion to begin. In the cases where we include capture, DM annihilation may again become important at the later stages leading to a new DS phase.

In both upper panels of Fig. 3.2 we take $c = 3.5$: the left panel is the boosted AH4 model while the right panel is unboosted (the relative ratio of boost factors is effectively 64 as mentioned before). Due to the ambiguity in the value of the concentration parameter we also study its implications on the evolution of the Dark Star by running the unboosted 100 GeV case for $c = (2, 3.5, 5)$ respectively; the lower two panels are the unboosted case with $c = 2$ and 5. The lower left panel is the same as the canonical case studied in *Spolyar et al.* (2009).

Effects of Boost: The DM heating is the most powerful in the boosted AH4 case, since Eq.(1) indicates that heating scales with cross section. Thus at any given time during the DS phase, this model has the brightest luminosity, as can be seen in Fig. 3.2. Consequently, the DM is burned up the more quickly in the boosted AH4 case, leading to the shortest DS lifetime.

In order to balance the higher DM heating, a larger radius is required, which leads to a lower central temperature and density. See Fig. 3.9. As the adiabatically contracted DM runs out the evolution is similar in all cases, the final luminosity being on the order of $10^7 L_\odot$.

Effects of concentration parameter: When we compare the three different concentration parameter cases, we notice that the nuclear fusion sets in earlier for smaller values of c. The higher the concentration parameter the more adiabatically contracted DM available, therefore it takes longer to start the transition to the main sequence. This will lead to slightly

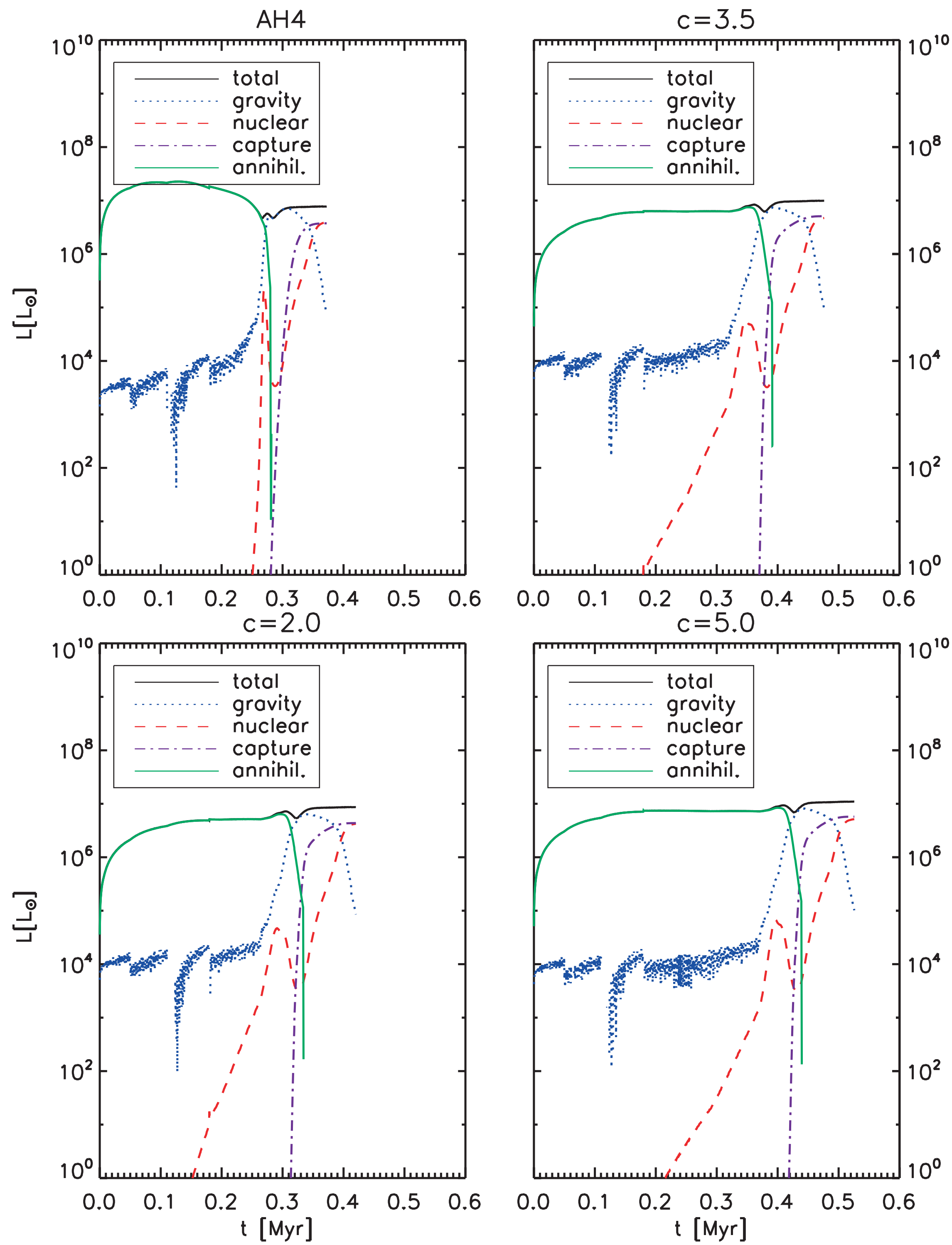

Figure 3.2: Luminosity evolution as a function of time for the four cases under consideration. The upper left panel displays the only boosted case, the AH4 model, with $B = 1500$, $m_\chi = 2.35$ TeV and $c = 3.5$. The other panels correspond to the unboosted case of a 100 GeV WIMP with $\langle \sigma v \rangle = 3 \times 10^{26} \mathrm{cm}^3/\mathrm{s}$ and concentration parameters as labeled.

higher final masses, which in turn translate to higher final luminosities. Nevertheless, as pointed out before they are all very close to $10^7 L_\odot$. In all three cases where $\langle\sigma v\rangle = 3\times10^{-26}\mathrm{cm}^3/\mathrm{s}$ we notice a flash in the luminosity when both the gravitational energy and the energy due to annihilations of the adiabatically contracted DM are relevant. This happens at a time somewhere between 0.31 Myr (for $c = 2$) and 0.42 Myr (for $c = 5$). The same flash can be seen for the AH4 panel, but now the true maximum of the luminosity occurs after only 0.1 Myr. The maximum luminosity is $\sim 4\times10^7 L_\odot$.

The main differences between the different WIMP models as regards the luminosity evolution in Fig.3.2 are in the time the "pure" dark star phase lasts. The higher the boost factor, the shorter this phase. Conversely a larger concentration parameter c prolongs the DS phase, since more DM is available.

3.3.2.2 Pre main sequence evolution, HR diagram

In Fig. 3.3 we plot Hertzsprung-Russell (H-R) diagrams for the four cases. One can see two distinct phases. First, the DS goes up the Hayashi track with a very steep increase of the luminosity yet relatively cool surface temperature, $T_{eff}\leq 10^4$ K. At the end of the Hayashi track the star enters the Henyey track. This path corresponds to an almost constant luminosity while the temperature increases fast, mostly due to the KH contraction phase. As a rule of thumb once a star is on the Heyney track its core should be fully radiative. The graphs end at a temperature of $\sim 10^5$ K when the star reaches the main sequence.

Effects of Boost: From the left panel of Fig. 3.3 one can see that the boosted AH4 case has the highest luminosity, due to the extremely efficient DM heating $Q_{DM}\sim\langle\sigma v\rangle/m_\chi$ forming a luminosity peak. However, as the AH4 case burns up its DM, the its luminosity falls. The boosted and unboosted cases eventually cross over at a temperature of $\sim 10^4$ K, and henceforth the unboosted case has a higher luminosity. Consequently, the boosted AH4 case has the lowest luminosity as the star moves onto the main sequence, as discussed above.

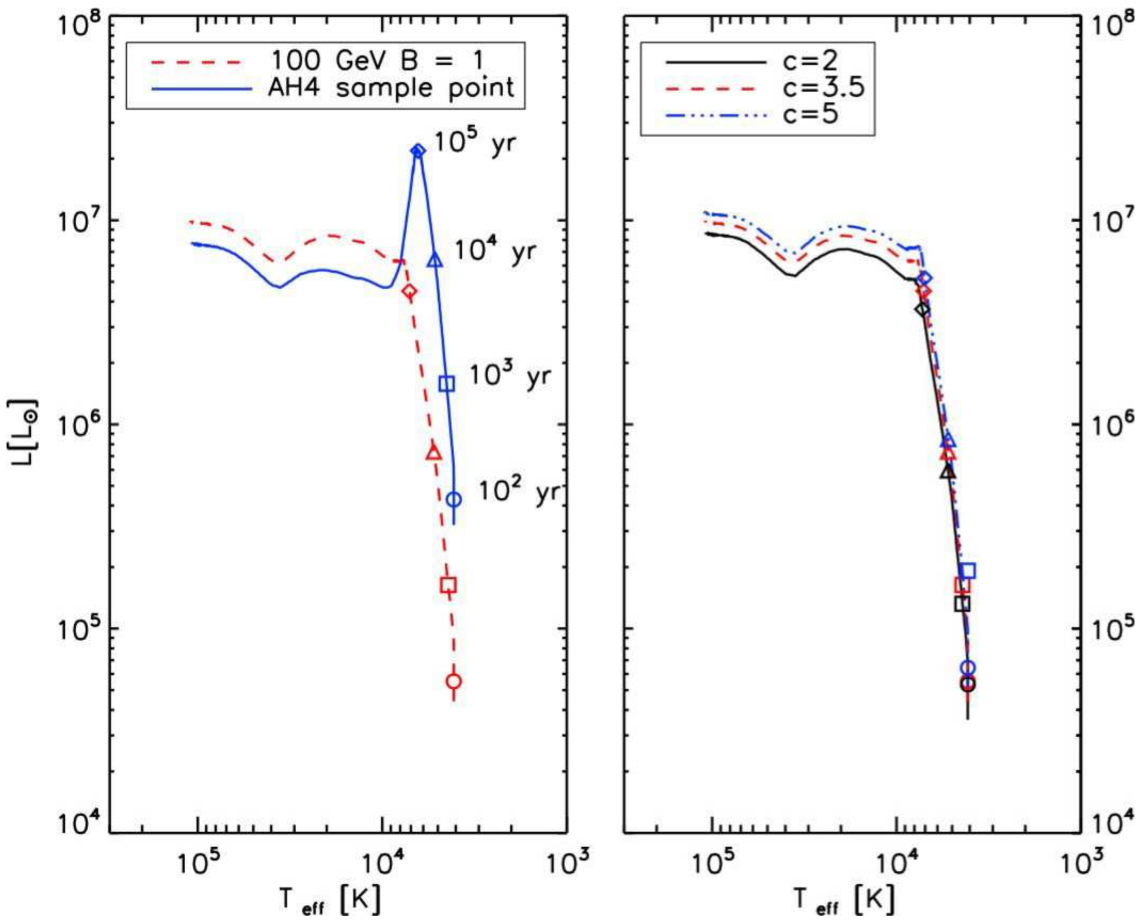

Figure 3.3: Hertzsprung-Russell diagram for DS. The left panel displays the unboosted 100 GeV case (dashed line) and the AH4 case, both for c=3.5. The right panel displays the unboosted 100 GeV case for a variety of concentration parameters as labeled. Also labeled are a series of points corresponding to the evolution of the DS towards the ZAMS at different times.

Effects of concentration parameter: In the right panel of Fig. 3.3 the trend is uniform: an increase in the concentration parameter leads to an increase in the luminosity. The difference is relatively small in the early stages of the evolution, at low temperatures. This is due to the fact that the adiabatically contracted DM density profile is not very sensitive to the concentration parameter, therefore about the same amount of DM heating will be generated in each case. However, for a lower value of the concentration parameter, the adiabatically contracted DM runs out faster, as there is less DM available. This leads to a shorter "pure" DS phase, as can also be seen from Fig. 3.2, and consequently to slightly lower final mass and luminosities.

3.3.2.3 Radius and Effective Temperature of DS

Effects of Boost on Radii: In the "pure" DS phase the star will be puffier for a higher $\langle\sigma v\rangle/m_\chi$ ratio, as can be seen from the left panel of Fig.3.4. This is expected due to the much higher DM heating in that case: a larger radius is required to balance the DM energy production and the radiated luminosity, which scales as R^2. For instance, in the boosted AH4 case the maximum radius is at about 2×10^{14}cm, whereas for the 100 GeV non-boosted WIMP, the DS will have a maximum radius of 10^{14}cm. However, as mentioned before, the KH contraction will set in earlier in the boosted case. This phase corresponds to the sharp decrease in radius in Fig.3.4. The final radii, as the DS enters the ZAMS are similar in both cases, at around 6×10^{11}cm.

Effects of Concentration Parameter on Radii: From the right panel of Fig.3.4 we notice an uniform increase in the radius with the concentration parameter. Again, more efficient DM heating leads to a puffier DS. The maximum radii range from 8×10^{13}cm to 10^{14}cm for $c = (2 - 5)$. After the KH contraction phase the DS settles to a radius very close to 6×10^{11}cm as it enters the ZAMS.

Effective Temperatures: In Fig. 3.5 we plot the effective surface temperature as a function of time. At first, during the DS phase, T_{eff} is relatively constant below 10^4K. Once

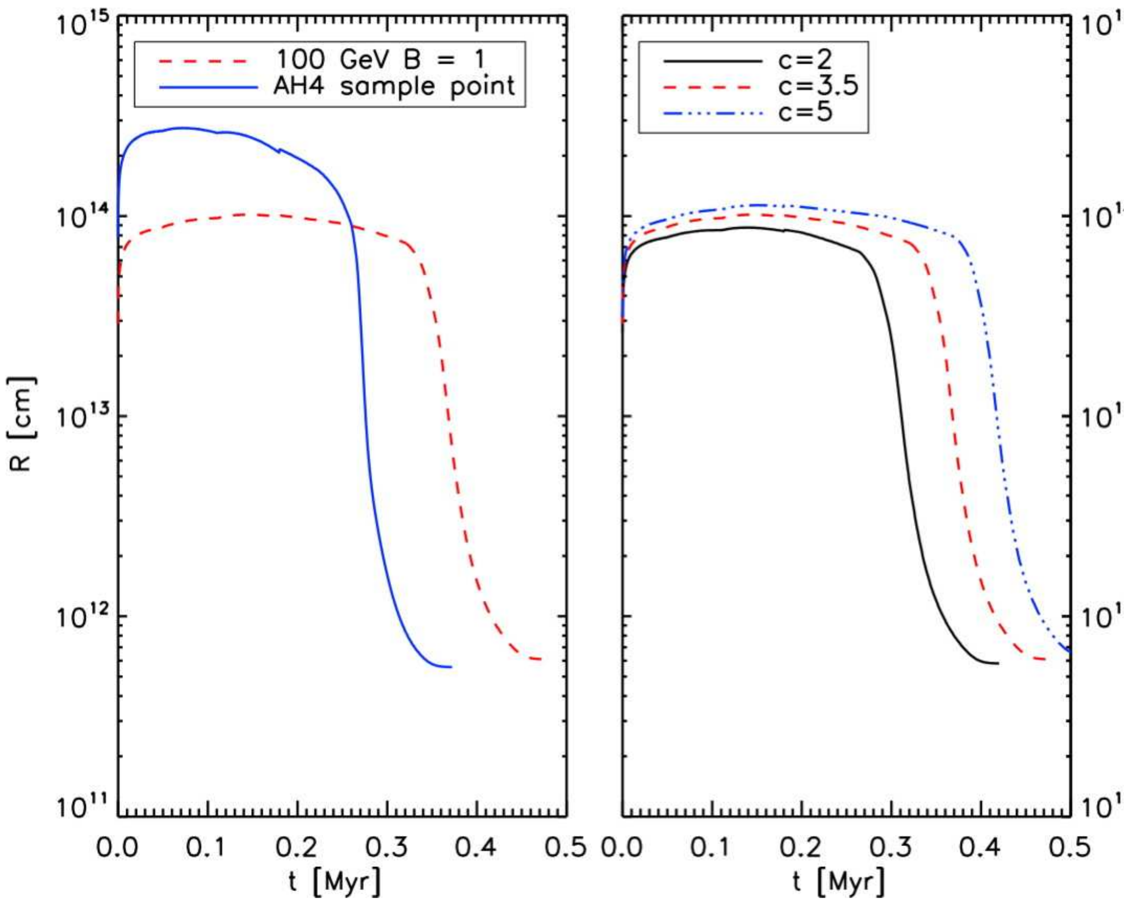

Figure 3.4: DS radius as a function of time. The left panel displays the unboosted 100 GeV case (dashed line) and the AH4 case (solid line), both for $c = 3.5$ The right panel corresponds to various concentration parameters c, for the unboosted 100 GeV WIMP.

the DM starts to run out, the star contracts and heats up, leading to a sharp increase in T_{eff} due to the onset of the KH contraction phase. Once nuclear fusion becomes the dominant energy supply and the star ceases to contract, the surface temperature reaches a plateau. The final value of $T_{eff} \sim 10^5$K is always the same for all cases, regardless of value of boost factor or concentration parameter. The AH4 case (left panel in Fig.3.5) starts as a cooler star, again typical of more efficient DM heating in that case due to the boost factor. In addition, in the AH4 case the DM runs out more quickly, leading to an earlier increase in temperature. Regarding the various concentration parameters: during the DS phase, the surface temperature is roughly the same in all cases, $\sim 7 \times 10^3$K. The DS phase lasts the longest for the highest value of c as this case has the most DM to begin with; thus the temperature starts to rise later for ever larger concentration parameters c.

3.3.2.4 Energy Transport near the Core

The DS starts with a fully convective structure, modeled by a fluid with a polytropic index $n = 1.5$. Then a radiative core starts to develop, that grows outwards, until most of the star is described by a polytrope of index $n = 3$. In Fig. 3.6 we plot the radiative gradient in the innermost zone at the center of the DS. The dashed horizontal line illustrates the critical value for convection. Models above the line have a convective core, while models below the line have radiative cores. Models with more efficient DM heating – i.e. the models with higher values of c or the AH4 model — transition to radiative energy transport later; stars with more efficient DM heating require a larger radius. At a fixed luminosity with more efficient DM heating, the star must have a larger radius and a lower densities to keep DM heating and the stellar luminosity in balance. With a lower density, the star has a lower central temperatures. At lower temperatures, the number of bound states increases, which increases the number of bound-free transitions. Also, the number of free-free transitions increase. These two effects increase the opacity which produces a larger radiative gradient and delays the transition from convective to radiative transport.

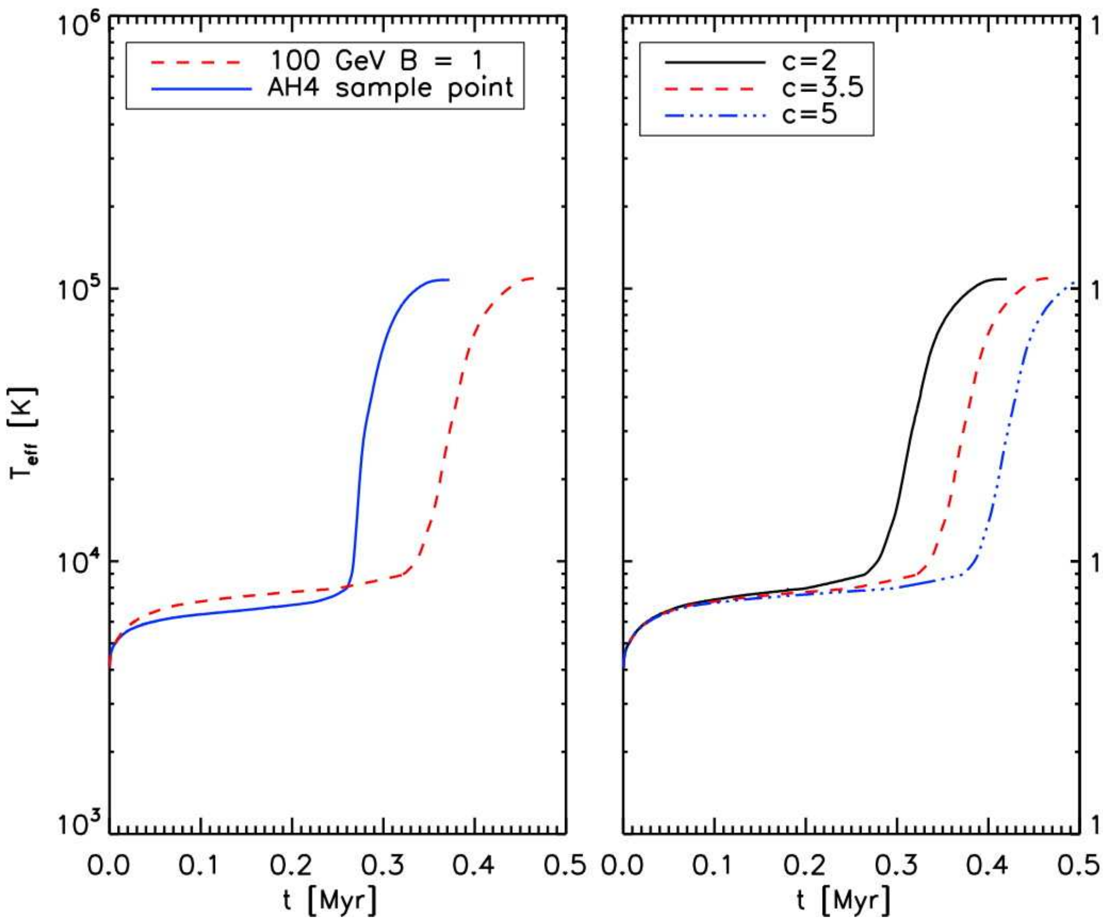

Figure 3.5: Effective temperature as a function of time. The left panel corresponds to the unboosted 100 GeV case (dashed line) and the boosted AH4 WIMP parameters defined previously (the solid line), both for $c = 3.5$. The right panel corresponds to various concentration parameters c, for the unboosted 100 GeV WIMP.

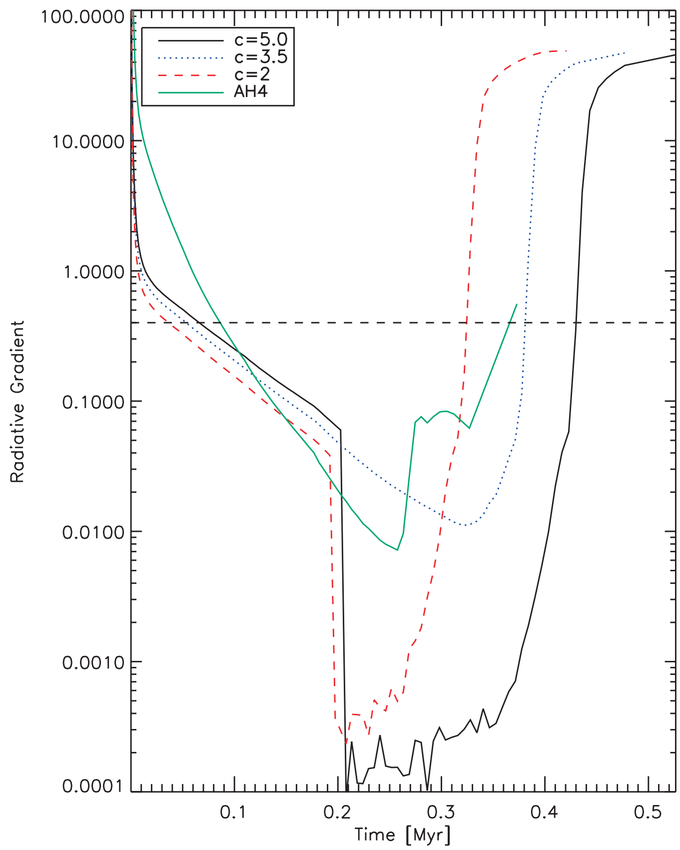

Figure 3.6: Radiative gradient at the center of the DS as a function of time. Models with the gradient above the horizontal line are unstable to convection. The lines labeled by the value of the concentration parameter c correspond to a DS powered by 100 GeV WIMPs with canonical unboosted cross section. The model AH4 is as defined previously in Fig. 1.

Once the original DM in the star runs out and nuclear fusion begins, a convective core develops in all cases. The central gradient is high due to the fact that nuclear fusion takes place primarily in the core of the star. Similarly, once the star repopulates its DM due to capture, this new DM population is thermalized with the star and its density is also sharply peaked at the center of the star. Thus both nuclear fusion and captured DM lead to a large radiative gradient in the core and therefore favor convection.

Again, the transition happens later for higher values of c. The time when the convective core develops corresponds almost precisely to the time when the captured DM heating becomes significant, as can be seen by comparing with Fig. 3.2: 0.31 Myr, 0.37 Myr and 0.42 Myr for $c = 2, 3.5$ and 5 respectively.

3.3.2.5 Baryonic Central Density

The baryon central density is plotted in Fig. 3.7 for the four cases we considered.

The higher cross section of the AH4 case at first leads to a puffier star (larger radius to keep the radiated luminosity at a level to balance the higher DM heating); thus it is not surprising that the AH4 case initially has a relatively lower central density. However, the initial DM in the DS runs out earlier in the AH4 case due to more efficient burning; hence in the left panel the two lines cross due to the earlier onset of the KH contraction (marked in the plot by the sharp increase of the densities) in the AH4 case.

The central density $\rho_b(0)$ scales inversely with the concentration parameter, as can be seen from the right panel of the same plot. Again, more DM heating (higher c) will lead to larger radii, therefore smaller densities. However, as opposed to the situation depicted in the left panel, In the right panel, the curves do not cross since the models with a larger concentration parameter have more DM, which delays the onset Helmholtz contraction. we come back to this in Sec.3.3.2.7. In all cases considered here once the star goes onto the main sequence, the central density is close to 100g/cm^3.

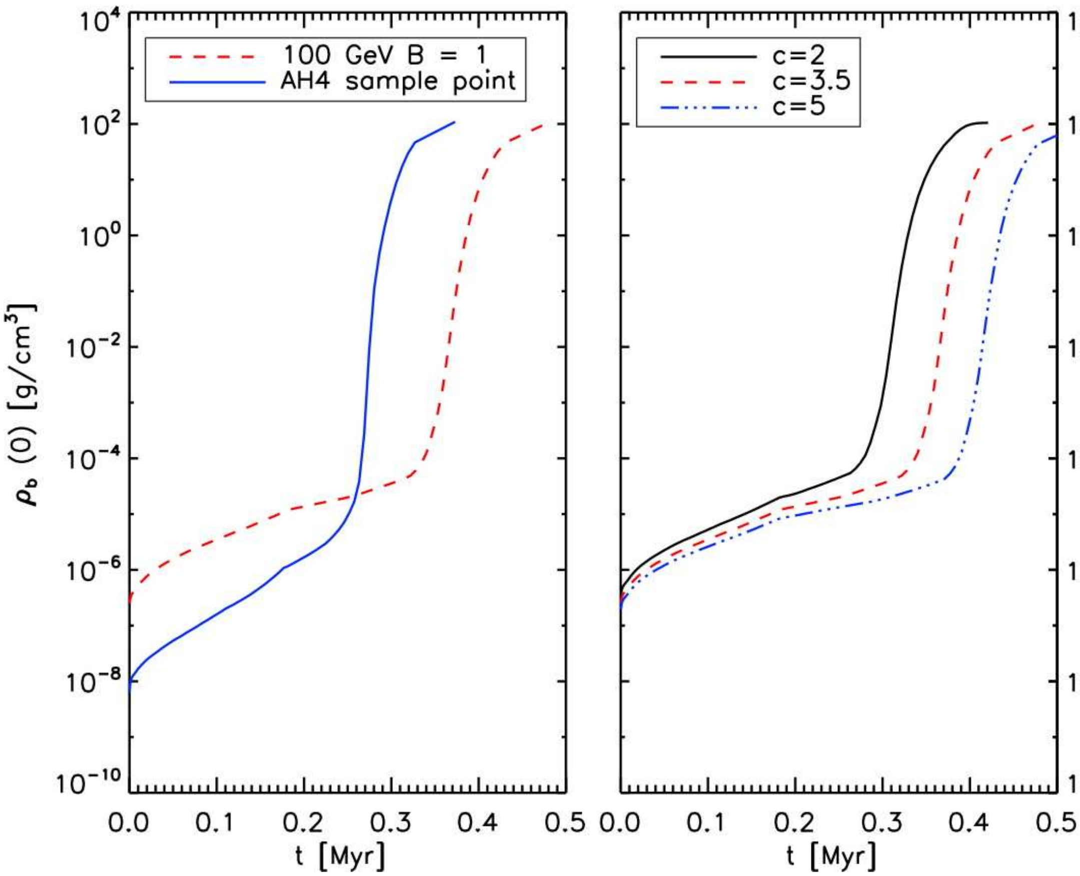

Figure 3.7: Central baryon density as a function of time. The left panel displays the unboosted 100 GeV WIMP case (dashed line) and the boosted AH4 case (the solid line), both for c=3.5. The right panel corresponds to various concentration parameters c for the 100 GeV WIMP case with unboosted canonical cross section.

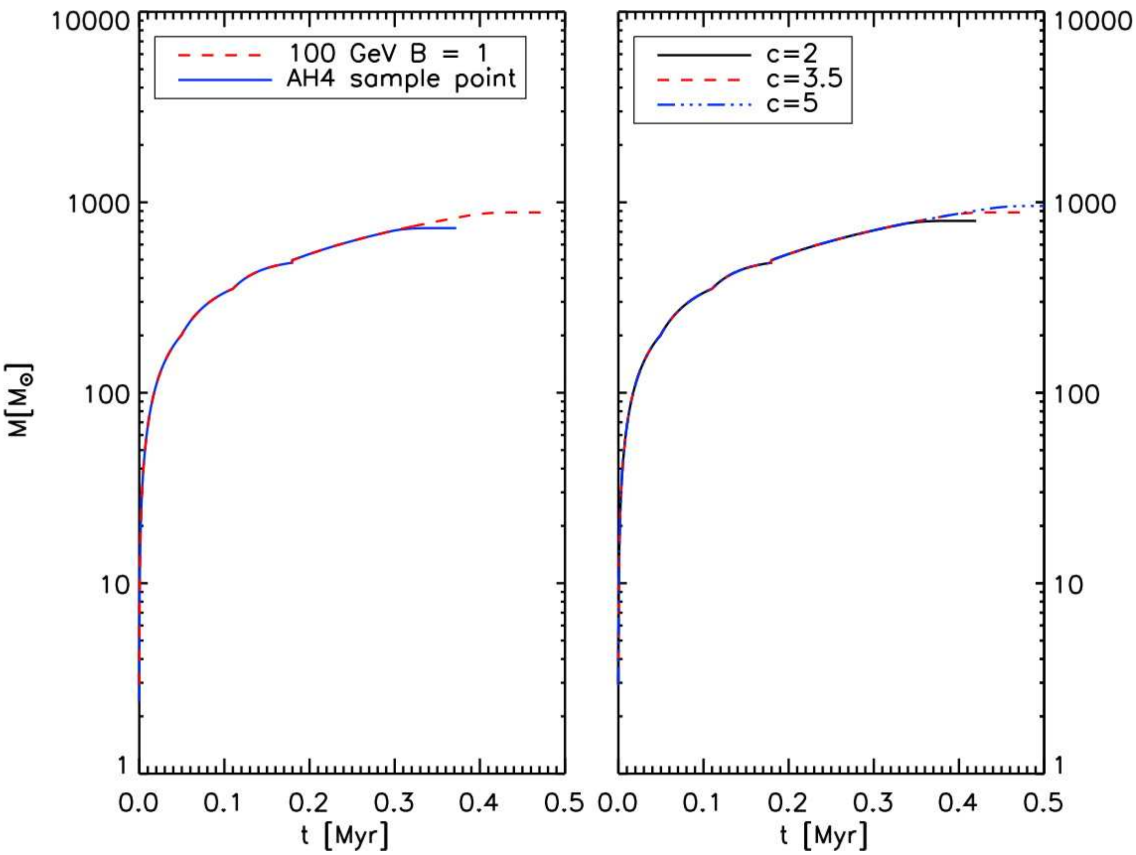

Figure 3.8: DS mass as a function of time. The left panel displays the unboosted 100 GeV case (dashed line) and the AH4 model, both for c=3.5. The right panel displays the unboosted 100 GeV case for a variety of concentration parameters c.

3.3.2.6 Mass as DS enters the ZAMS

In Fig. 3.8, we have plotted the DS mass as a function of time. In all cases, the final mass when the DS enters the main sequence is $\sim 700 - 1000 M_{\odot}$; however, there are slight differences for different models. The models with more effective DM heating – i.e. the AH4 model compared to the 100 GeV unboosted case – burn up their original adiabatically contracted DM the most quickly and enter the KH contraction phase the soonest. This in turn leads to a smaller final mass, as feedback effects will shut off accretion sooner. When comparing the cases with different concentration parameter we notice that the DS final mass is an increasing function of c. As previously explained an increase in the concentration parameter leads to a longer DS phase, and hence to more mass accreted. For the case of the unboosted 100 GeV WIMP with $c = 3.5$ the final mass is around $900M_\odot$, whereas for the $AH4$ case it is close to $700M_\odot$. For c ranging from $2-5$ the DS will have a mass in the $800M_\odot - 1000M_\odot$ as it reaches the main sequence.

3.3.2.7 Density Profiles for DM and Baryons inside the DS; amount of adiabatically contracted DM

In Fig. 3.9 and Fig.4.1, we have plotted the density profiles of the adiabatically contracted DM and baryons respectively. The AH4 model for the same stellar mass has a lower DM density than the canonical unboosted 100 GeV case by roughly an order of magnitude, and also has a more extended profile. For instance, in the case of a DS of $300M_\odot$ the values are 5×10^{-11}g/cm^3 (AH4) and $\sim 1 \times 10^{-9}$g/cm^3 (canonical) respectively. This effect can be attributed to the fact that at a higher annihilation cross sections or a lower particle masses[4], a larger radius and a lower density are needed to balance the DM heating and the stellar luminosity (which scales as R^2).

During the early stages of the DS evolution the dependence of the adiabatically contracted DM density on the concentration parameter is very small at least for the range we have considered here. As it can be seen from Fig.3.7, prior to the onset of the KH contraction phase, the central baryon densities for models with different values of the concentration parameter have similar baryon density and DM density as well. Models with a larger concentration parameter have slightly more dark matter, have slightly lower central DM densities, and are also more extended. Before the contraction phase, the central DM density of the $c = 5$ case's density is 10% lower than the $c = 2$ case. The radius is 20% larger. Models with different concentration parameters only begin to dramatically diverge once the star begins to contract and enters its Kelvin-Helmholz contraction phase. At this point, the star begins to shrink, which cause the DM densities to increase dramatically.

[4]A similar effect was noticed in *Spolyar et al.* (2009), where it was found that "the average DM density in the star is an increasing function of M_χ"; n.b. the higher annihilation cross section of the AH4 case can be traded for a lower WIMP mass since heating scales as $\langle\sigma v\rangle/M_\chi$.

DS in halos with a larger concentration parameter have more DM and thus delay the onset of the KH phase. For $c = 2$, the contraction phase begins at $t \sim 0.28$ Myr; See Fig.3.4. At this time, the stellar mass has reached $\sim 700 M_\odot$. For $c = 3.5$ and 5, the contraction phase begins later. In the case of $c = 5$, the star has a mass of $\sim 850 M_\odot$. Thus the contraction begins once the star is more massive.

At a fixed stellar mass, the DM densities will differ dramatically between models which are in the contraction phase compared to those which are not contacting . For instance, let us consider a $750 M_\odot$ DS. In the case of $c = 2$, the star has entered the contraction phase. While the cases with a larger concentration parameter (3.5,5) have yet to begin their contraction phase. Hence the stars with a larger concentration, have a lower DM density and are more extended, which can be seen in Fig. 3.9.

Finally, in Fig. 4.2 we have plotted the amount of adiabatically contracted DM inside the DS as a function of time. One can also see that DM densities are many orders of magnitude lower than their baryonic counterparts at all times. Although the amount of DM never exceeds $0.4 M_\odot$, yet this is sufficient to power the DS all the way up to $\sim 1000 M_\odot$ (where most of the mass is baryons) and $10^7 L_\odot$. Indeed DM heating is a very powerful energy source.

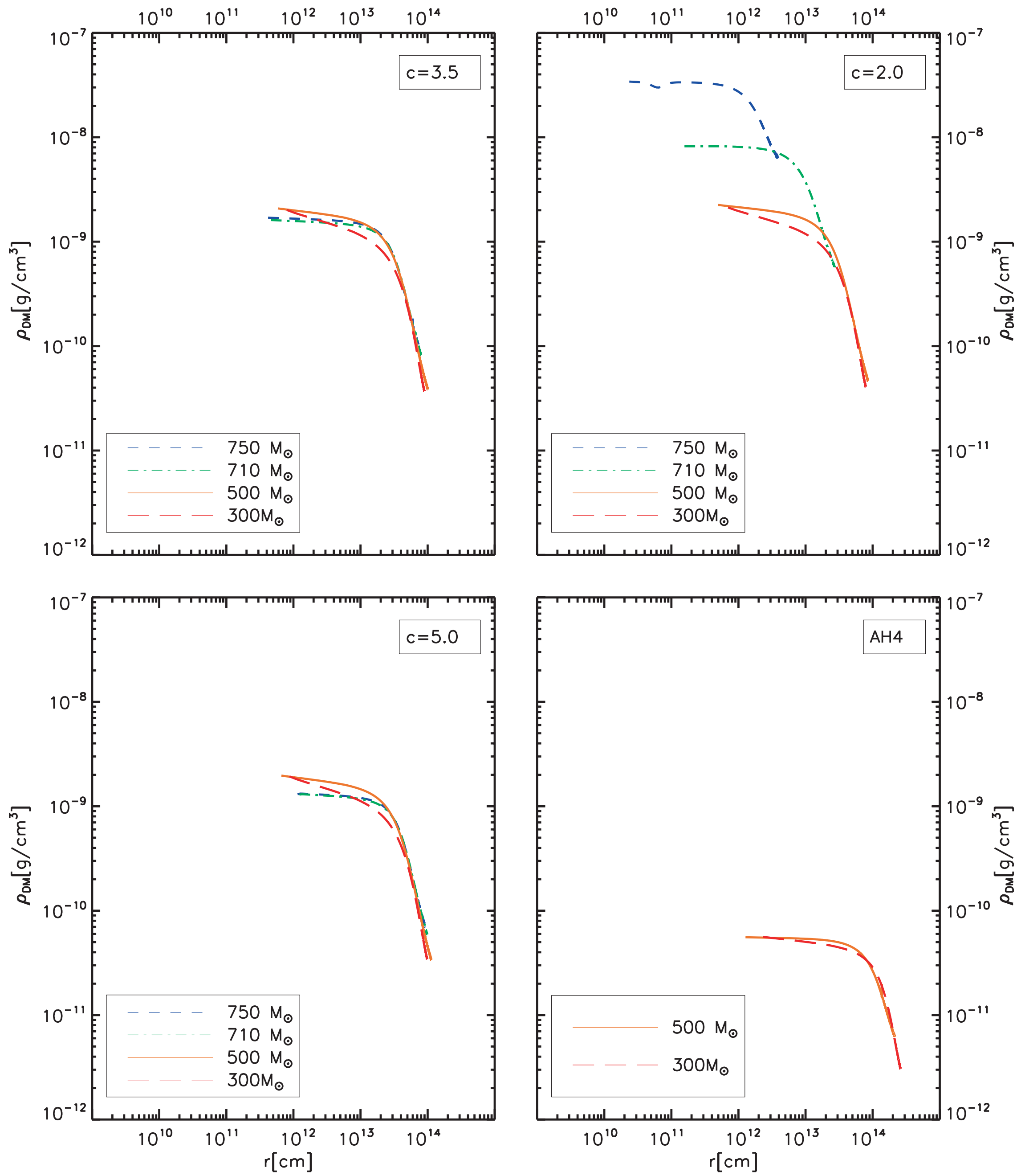

Figure 3.9: Adiabatically contracted DM density profiles. Each line corresponds to a fixed value of the mass of the DS during its evolution. Note that certain lines that are mentioned in the legend do not appear plotted in all four panels. This is due to the fact that at that stage the DS has exhausted all the DM.

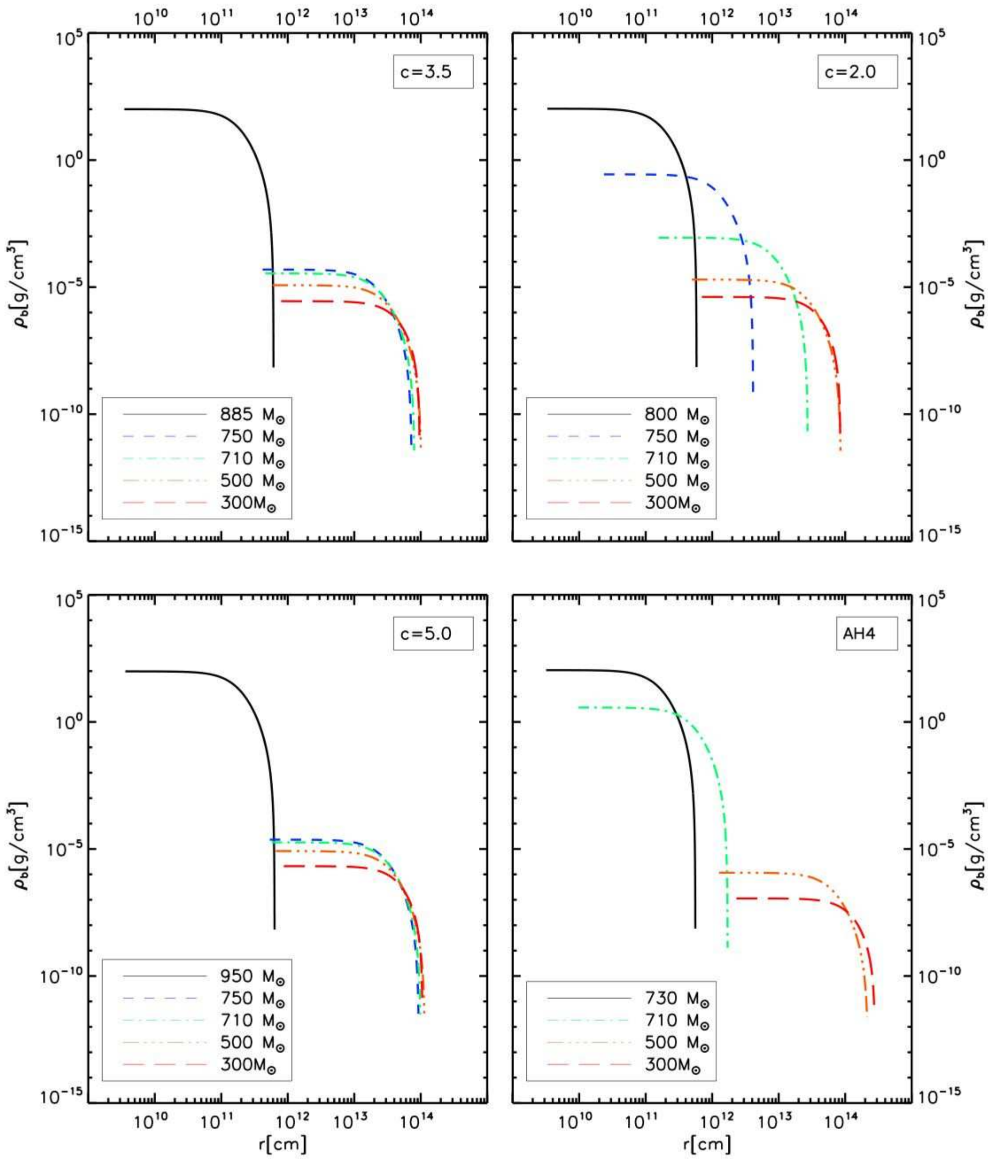

Figure 3.10: Baryonic density profiles at different stellar masses for the four cases under consideration. The solid line corresponds to the mass of the DS as it enters the ZAMS.

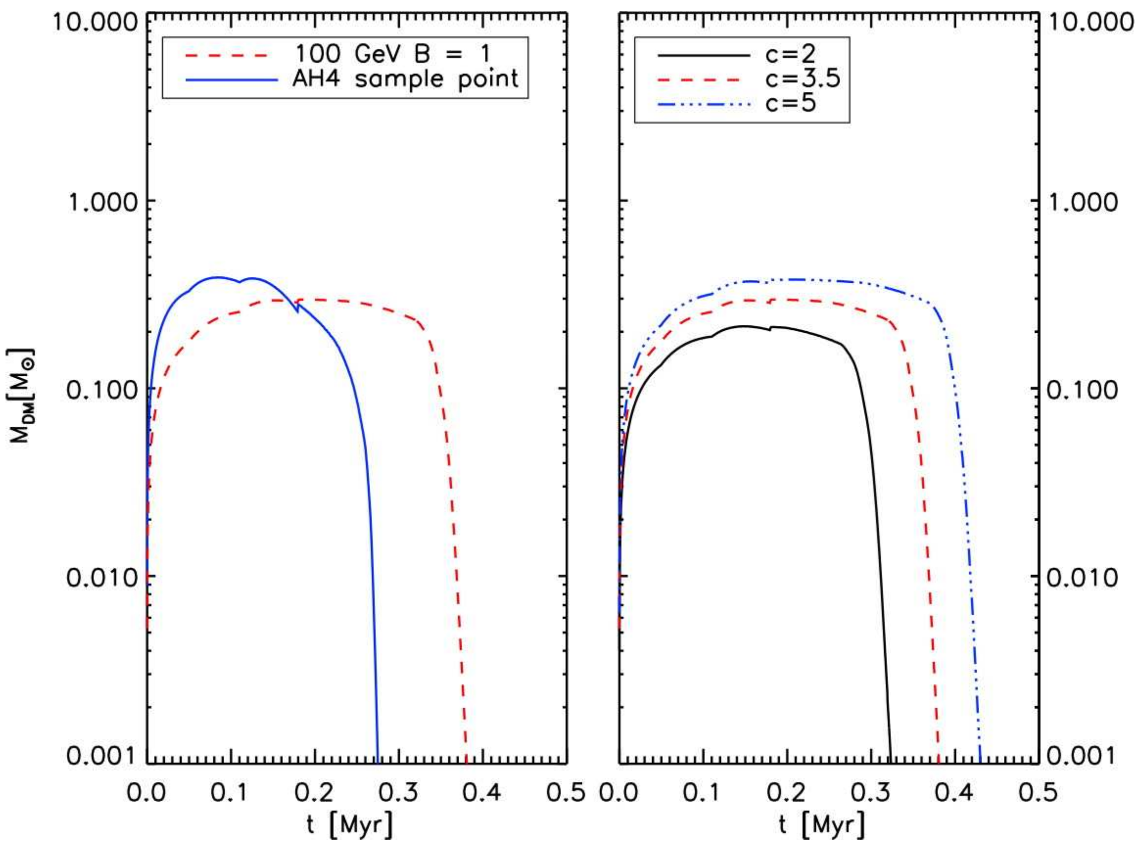

Figure 3.11: Amount of adiabatically contracted DM inside the star as a function of time. The left panel displays the unboosted 100 GeV case (dashed line) and the AH4 model (solid line), both for $c = 3.5$ The right panel displays the unboosted 100 GeV case for a variety of concentration parameters c.

3.4 Summary and Conclusions

We have considered the effect on DS of leptophilic boosted DM annihilation cross sections, as would typically be required to explain PAMELA data. Second, we have varied the concentration parameter in a host of DS models. We have restricted our study to include the following two sources of DM: i) the DM originally contained in the star due to adiabatic contraction and ii) the minimal capture scenario. We have not included the additional DM due to extended adiabatic contraction or to maximal capture models discussed in *Freese et al.* (2010b). Nonetheless, the dependence of DS properties on boost factor and concentration parameter can easily be seen. As our prototypical boosted case, we have focused on the AH4 model with the following parameters: $B = 1500$, $m_\chi = 2.35$ TeV and $c = 3.5$. In the unboosted cases, we have taken $M_\chi = 100$ GeV and three values of the concentration parameter, $c = 2, 3.5,$ and 5.

We have found that, if the positron excess observed by PAMELA is indeed due to leptophilic boosted DM, then there would be an early DS phase of stellar evolution powered by DM heating, lasting long enough to bring the star to substantially higher mass and luminosity than predicted for regular Pop.III zero metallicity stars. Our basic results are that the final stellar properties, after the DS runs out of or its original adiabatically contracted DM fuel, undergoes Kelvin Helmholtz contraction and enters the main sequence, are always roughly the same: $\sim 1000 M_\odot$, $\sim 10^7 L_\odot$, lifetime $\sim 10^6$ yrs. Similarly, these same DS properties are also the basic result independent of the value of the concentration parameter in the range between c=2 and c=5.

We reiterate that these values are only for the case of simple adiabatic contraction and minimal capture; if we were to include the additional DM due to extended AC or maximal capture, then these values would be different by many orders of magnitude. However, the basic dependence on the parameters of interest would generalize. In particular, the result that the final mass, luminosity, and lifetime are relatively *independent* of boosted cross section or value of c would still hold up. In addition, the slight differences from model to model, discussed in the next paragraph, would also hold up.

We have found that the lifetime, final mass, and final luminosity of the DS, though roughly similar in all cases, do show some dependence on boost factor and concentration parameter. We have found that the DS lifetime is shorter in the boosted case, since the DM is exhausted sooner. On the other hand, the lifetime is longer for higher concentration parameter since there is more DM to begin with. Thus nuclear burning becomes effective earlier in the case of boosted cross section or low concentration parameter. The DS accretes matter continuously while it remains powered by DM heating. Hence the largest final stellar mass results for the longest living DS, i.e. the unboosted case with the highest values of c. In all cases, the final mass is $\sim 1000 M_\odot$. We have shown the H-R diagram for all cases, studying both the Hayashi track and the approach to fusion power. We have showed that the 'final' luminosity at the end of the DS lifetime is $\sim 10^7 L_\odot$ in all cases, with the luminosity decreasing slightly as a function of increasing boost factor or decreasing c, again because of the more rapidly depleted pool of DM. We have also examined the luminosity evolution of the DS as a function of time. During the DS phase itself, the luminosity is higher/lower for boosted/unboosted cross sections. The reduced luminosity during the DS evolution in the unboosted case is a consequence of the reduced energy production, since DM heating is proportional to annihilation cross section and the square of the DM density. Then at lower cross section (unboosted), a smaller radius is needed to balance the DM energy production and the radiated luminosity. Consequently the unboosted case has higher central densities (both for baryons and DM). Similarly, lower values of c have lower luminosity during the DS phase, smaller radii, and higher central density. In all cases the DM density is a minute fraction of the total density, with baryons dominating the gravitational potential; we have shown the density profiles of both components. Again in all cases, the amount of DM inside the star never amounts to more than $0.4 M_\odot$, a tiny fraction of a star that grows to $\sim 1000 M_\odot$; yet this DM is sufficient to power the star. This is "the power of darkness."

CHAPTER IV

Supermassive Dark Stars

4.1 Motivation

The main introductory ideas related to Dark Stars were already discussed in Sections 1.4 and 3.1. Here we will present the main differences compared with the scenario of Chapter III, where the mass of the DS was $\sim 10^3 M_\odot$. By identifying sources of DM we have not previously considered we are able to show that dark stars could grow as massive as $10^6 M_\odot$ or even higher mass.

WIMP annihilation produces energy at a rate per unit volume

$$\hat{Q}_{DM} = n_\chi^2 \langle \sigma v \rangle m_\chi = \langle \sigma v \rangle \rho_\chi^2 / m_\chi, \tag{4.1}$$

where n_χ is the WIMP number density, m_χ is the WIMP mass, and ρ_χ is the WIMP energy density. The annihilation products typically are electrons, photons, and neutrinos. The neutrinos escape the star, while the other annihilation products are trapped in the dark star, thermalize with the star, and heat it up. The luminosity from the DM heating is

$$L_{DM} \sim f_Q \int \hat{Q}_{DM} dV \tag{4.2}$$

where f_Q is the fraction of the annihilation energy deposited in the star (not lost to neutrinos) and dV is the volume element. We take $f_Q = 2/3$ as is typical for WIMPs.

The exciting new development presented here is that we follow the growth of dark stars to become Supermassive Dark Star (SMDS) of mass $M_* > 10^5 M_\odot$. Specifically we study the formation of $10^5 M_\odot$ SMDS in $10^6 M_\odot$ DM haloes and $10^7 M_\odot$ SMDS in $10^8 M_\odot$ haloes; perhaps the SMDSs become even larger. Hoyle & Fowler (1963) first postulated the existence of such large stars but were not aware of a mechanism for making them. Now the confluence of particle physics with astrophysics may be providing the answer. The key ingredient that allows dark stars to grow so much larger than ordinary fusion powered Population III stars is the fact that dark stars are so much cooler. Ordinary Pop III stars have much larger surface temperatures in excess of 50,000K. They produce ionizing photons that provide a variety of feedback mechanisms that cut off further accretion. McKee & Tan (2008) have estimated that the resultant Pop III stellar masses are $\sim 140 M_\odot$. Dark stars are very different from fusion-powered stars, and their cooler surface temperatures allow continued accretion of baryons all the way up to enormous stellar masses, $M_* > 10^5 M_\odot$, as we will see in the next chapter.

Typically $(100 - 10^4) M_\odot$ of dark matter (up to $\sim 1\%$ of the halo mass) must be consumed by the star in order for large SMDS masses $M_* \sim 10^5 M_\odot$ to be reached. We will consider two different scenarios for supplying this amount of dark matter: 1) Extended Adiabatic Contraction, labeled "without capture" below. In this case, dark matter is supplied by the gravitational attraction of the baryons in the star. The amount of DM available for DM annihilation due to adiabatic contraction may be larger than our previous estimates which were based on the assumption that DM halos are spherical. In a non-spherical DM halo, the supply of DM available to the star can be considerably enhanced, as we discuss in more detail in §4.2.2. In any case, this mechanism relies solely on the particle physics of WIMP annihilation and does not include capture of DM by baryons (discussed below).

2) Extended Capture, labeled “with capture” below. Here, the star is initially powered by the DM from adiabatic contraction (AC), but the AC phase is taken to be short $\sim 300,000$ years; once this DM runs out the star shrinks, its density increases, and subsequently the DM is replenished inside the star by capture of DM from the surroundings (Freese et al. 2008b; Iocco 2008) as it scatters elastically off of nuclei in the star. In this case, the additional particle physics ingredient of WIMP scattering is required. This elastic scattering is the same mechanism that direct detection experiments (e.g. CDMS, XENON, LUX, DAMA) are using in their hunt for WIMPs. In previous work (Freese et al. 2008a; Spolyar et al. 2009), we assumed minimal capture, where DM heating and fusion contributed equally to the luminosity once the star reached the main sequence. Here, we consider the more sensible case where DM heating dominates completely due to larger ambient DM density, and the star can grow to become supermassive.

Supermassive dark stars can result from either of these mechanisms for DM refueling inside the star. The SMDS can live for a very long time, tens to hundreds of million years, or possibly longer (even to today). We find that $\sim 10^5 M_\odot$ SDMSs are very bright $\sim 3\times 10^9 L_\odot$ which makes them potentially observable by James Webb Space Telescope (JWST). We also note that SMDS may become even more massive a) if they form in larger haloes or b) the DM haloes in which they initially form merge with other haloes so that there is even more matter to accrete (n.b. alternatively these mergers may remove the DS from their high DM homes and stop the DM heating). For example, if dark stars form in $10^8 M_\odot$ haloes, then they could in principle grow to contain all the baryons in the halo, i.e. $M_* > 10^7 M_\odot$. Since the luminosity scales as $L_* \propto M_*$ these SMDS would be even brighter, $L_* > 10^{11} L_\odot$ and are hence even better candidates for discovery in JWST.

Once the SMDS run out of DM fuel, they contract and heat up. The core reaches 10^8K and fusion begins. As fusion-powered stars they don’t last very long before collapsing to Black Hole (BH). Again, this prediction is different from standard Pop III stars, many of which explode as pair-instability supernovae (Heger & Woosley 2002) with predicted even/odd element abundance ratios that are not (yet) observed in nature. The massive BH remnants of the SMDSs are good candidates for explaining the existence of $10^9\ M_\odot$ BHs which are the central engines of the most distant ($z > 5.6$) quasars in the SDSSSloan Digital Sky Survey (Fan et al. 2001, 2004, 2006) [1].

The idea of supermassive DS and the resultant $> 10^5 M_\odot$ BH was originally proposed by Spolyar et al. (2009). Subsequently Umeda et al. (2009) took their existing stellar codes and added DM annihilation to allow the mass to grow. They started from Population III stars in which fusion was already present, assuming they then encounter a reservoir of DM. Here we start from the very beginning with collapsing protostellar clouds that transition into dark stars, which can be DM powered for millions to billions of years before fusion ever begins. The SMDSs in this study are primordial supermassive stars. More generally, the capture mechanism in particular lends itself to growth of dark stars, whether or not fusion has already set in, so that SMDS can result at various epochs in the Universe.

Begelman (2009) presents another alternative for the formation of supermassive stars: rapid accretion onto stars which already have hydrogen burning in them. His “quasistars”, another possible route to large BH, are quite different from the SDMS discussed in this chapter.

Various other authors that have explored the repercussions of DM heating in the first stars (Taoso et al. 2008; Yoon et al. 2008; Ripamonti et al. 2009; Iocco et al. 2008). Recently Ripamonti et al. (2010) study the effects of DM heating on the evolution of primordial gas clouds using a 1-D code. They argue against the idea that DM heating will stop the collapse of the proto-stellar gas cloud. However, to clarify this issue further investigations are needed. For example, the energy loss of high energy particles via electromagnetic cascade does *not* lead to substantial ionization or excitation, contrary to the assumptions in the Ripamonti et al. paper. As their results depend on these issues, it is our intention to study them in a separate future publication.

[1] We thank N. Yoshida for pointing this out to us

The possibility that DM annihilation might have effects on *today's* stars was initially considered in the $'80$s and early $'90$s (Krauss et al. 1985; Bouquet & Salati 1989; Salati & Silk 1989; Graff & Freese 1996) and has recently been studied in interesting papers by Moskalenko & Wai (2007), Scott et al. (2007), Bertone & Fairbairn (2007) and Scott et al. (2009). Other constraints on DS will arise from cosmological considerations. A first study of their effects (and those of the resultant MS stars) on reionization has been done by Schleicher et al.(2008, 2009) and further work in this direction is warranted.

In this chapter we examine the SMDS that result from the two mechanisms discussed above for DM refueling inside the star. In Section II we discuss the procedure for calculation of models; in Section III we present results; and in Section IV we end with a discussion.

4.2 Structure and Evolution of the Dark Star

DM heating is very different from fusion. In order to overcome the Coulomb barriers between nuclei, fusion requires very high temperatures and densities in the star. Fusion is not very efficient in that only $< 1\%$ of the nuclear mass is converted to heat. WIMP annihilation, on the other hand, takes place at high dark matter densities regardless of the temperature. It is almost 100% efficient since O(1) of the WIMP mass is converted to useful energy. Thus, in the evolution of the first protostars, DM heating becomes important early. Here we start the calculation when the DS is massive enough (3 $M_\odot$) so that it is in hydrostatic equilibrium and most of the hydrogen and helium is ionized. The contribution to DM luminosity is roughly constant as a function of radius throughout the DS, unlike fusion which takes place only at the (high temperature) core of the star.

4.2.1 Basic Equations

The description of the model solved by our code was already described in Section 3.2.2. To facilitate the reading, we will reproduce here that discussion. One key assumption we make is that of the stars being described by polytropes

$$P = K\rho^{1+1/n} \tag{4.3}$$

in hydrostatic equilibrium. Here P is the pressure, ρ is the density, and K is a constant. We solve the equations of stellar structure with polytropic index n initially 1.5, as appropriate for convective stars, and made a gradual transition to $n = 3$ as the star becomes radiative in the later phases. We require that at each time-step during the accretion process the star is in hydrostatic equilibrium,

$$\frac{dP}{dr} = -\rho(r)\frac{GM_r}{r^2} \tag{4.4}$$

where $\frac{dM_r}{dr} = 4\pi r^2\rho(r)$, and M_r is the mass enclosed in a spherical shell of radius r. The equation of state includes radiation pressure,

$$P(r) = \frac{k_B\rho(r)T(r)}{m_u\mu} + \frac{1}{3}aT(r)^4 \equiv P_g + P_{rad} \tag{4.5}$$

where k_B is the Boltzmann constant, m_u is the atomic mass unit and $\mu = 0.588$ is the mean atomic weight. The opacity is obtained from a zero metallicity table from OPAL (Iglesias & Rogers 1996) supplemented at low temperatures by opacities from Lenzuni et al. (1991) for $T < 6000$K. The further assumption is made that the radiated luminosity of the star L_* is balanced by the rate of energy output by all internal sources, $L_{\rm tot}$, as described below in §4.2.3.

$$L_* = 4\pi R_*^2\sigma_B T_{eff}^4 = L_{\rm tot}. \tag{4.6}$$

where T_{eff} is the surface temperature, and R_* is the total radius.

Starting with a mass M and an estimate for the outer radius R_*, the code integrates the structure equations outward from the center. The total rate of energy production $L_{\rm tot}$ is compared to the stellar radiated luminosity, as in equation (4.6) and the radius is adjusted until the condition of thermal equilibrium is met (a convergence of 1 in 10^4 is reached).

4.2.2 Dark Matter Densities

We now describe the two different mechanisms for supplying the DM density.

Extended Adiabatic Contraction: As the baryons start to collapse into a protostellar cloud at the center of the DM halo, the DM responds to the changing gravitational potential well and falls in as well. As described in our previous work (Spolyar et al. 2008), we will use adiabatic contraction (AC) to describe this increase in DM density. For the case of spherical haloes, we previously found, by performing exact calculations for comparison (Freese et al. 2009), that the simple Blumenthal method (Blumenthal et al. 1985; Barnes & White 1984; Ryden & Gunn 1987) gives reliable results for the final DM densities up to an unimportant factor of two; others confirmed this conclusion (Natarajan et al. 2009; Iocco et al. 2008; Sivertsson & Gondolo 2010). Using this simple approach during the AC phase, we found that $\rho_\chi \sim 5\mathrm{GeV/cm^3}(n_h/\mathrm{cm^3})^{0.81}$ where n_h is the gas density. These are the values we will use during AC.

In our previous work, we probably underestimated the lifetime of the DM inside the star due to AC. In our previous work we treated the DM halo as spherical and ran up the DS mass to the point where the DM initially inside the star was entirely consumed by annihilation. The DS mass at this point is $O(10^3)M_\odot$ after a lifetime of $\sim 300,000$ years, and the amount of DM consumed has only amounted to $\sim 1M_\odot$. In a spherical DM halo, the orbits of DM particles are planar rosettes (Binney & Tremaine 2008) conserving energy as well as all three components of angular momentum; consequently the central hole (or "empty loss cone") that results from DM annihilation cannot be repopulated once it is depleted. (Note that although DM annihilation creates a central hole in the DM density, the entire region is filled with baryons and hence the potential is stable.) However, it is well known that DM halos formed in hierarchical structure formation simulations are not spherical but are prolate-triaxial (Bardeen et al. 1986; Barnes & Efsthatiou 1987; Frenk et al. 1988; Dubinski & Carlberg 1991; Jing & Suto 2002; Bailin & Steinmetz 2005; Allgood et al. 2006) with typical axis ratios of (short-axis)/(long-axis) $\sim 0.6-0.8$. In triaxial potentials, the orbits do not conserve angular momentum. In particular there are two families of "centrophilic orbits" (box orbits and chaotic orbits) which oscillate back and forth through the potential and can travel arbitrarily close to the center (Schwarzschild 1979, Goodman & Schwarzschild 1981; Gerhard & Binney 1985; de Zeeuw 1985; Schwarzschild 1993; Merritt & Fridman 1986; Merritt & Valluri 1996). Unlike an orbit in a spherical potential which has a constant pericenter radius (the distance of closest approach to the center of the potential), the pericenter radius of a centrophilic orbit varies over time extending from $r_{\rm peri} = [0, r_{\rm max}]$ where $r_{\rm max}$ is sometimes referred to as the "throat" of the orbit (Gerhard & Binney 1985). As any one particle traverses the center of the dark star, it may indeed be removed from the pool by annihilation. However, it was unlikely to pass through the star (of radius r_*) on its next orbit anyhow since in general $r_{max} >> r_*$. Instead, a particle on a different "centrophilic orbit" enters the star for the first time maintaining the steady state central DM density cusp. Unlike in the case of a spherical DM halo, where annihilation steadily depletes the central density cusp, in a triaxial halo there is a high probability for a particle on a centrophilic orbit to pass through the center for the first time on any given orbital crossing. This is particularly true in potentials with central point masses which are dominated by chaotic orbits and are therefore ergodic (Merritt & Valluri 1996). Hence, the central DM density can remain much higher than we previously expected.

The dynamics of the refilling of the central "loss cone" in the case of spherical and non-spherical collisionless systems has been studied previously in the context of capture of stars by a central black hole (Gerhard & Binney 1985; Magorrian & Tremaine 1999; Merritt & Poon 2004). The details of filling rate for the specific case of the DS will be presented in a separate study; however these previous papers showed that in non spherical systems the loss cone could remain full for a factor of 2 to 10^4 times longer than in the spherical case depending on whether the potential was axisymmetric (Magorrian & Tremaine 1999) or triaxial (Merritt & Poon 2004), respectively. Since DM halos are known to be triaxial this suggests that the duration for which the central hole remains full (i.e. has orbits with the low angular momentum necessary for annihilation) can increase from 300,000 years to as much as 3×10^9 yrs possibly allowing the DS to be detectable by JWST.

These more optimistic estimates require that a significant fraction of the orbits in these early DM halos are chaotic and boxlike. One important potential concern with assuming conditions in a triaxial halo is that several studies have shown that the growth of central baryonic components tend to make DM halos more axisymmetric than in purely dissipationless simulations (Dubinski 1994, Evrard et al. 1994, Merritt & Quinlan 1998, Kazantzidis et al. 2004, Debattista et al. 2008, Tissera et al. 2009), and axisymmetric models are generally not expected to contain centrophilic orbit families. However, Valluri et al. (2010) recently showed that when a compact central baryonic component is grown adiabatically inside a triaxial DM halo, the final halo that results from the adiabatic growth of such a baryonic component looks nearly oblate, yet its orbit population can contain a significant fraction of centrophilic orbits, since box orbits preferentially deform their shapes rather than converting to centrophobic tube families. Furthermore they showed that a significant fraction of the orbits (both box orbits and tube orbits which were traditionally thought to avoid the center) experience strong chaotic scattering, a mechanism that could drive them close to the center. They found that for a fixed ratio of the mass of the baryonic component to mass of the DM halo ($M_*/M_{\mathbf{DM}} = 10^{-3}$), the smaller the radius of the baryonic component (r_*), relative to the virial radius of the DM halo ($r_{\rm vir}$) the greater was the fraction of chaotic orbits. The most compact baryonic component studied by them had $r_*/r_{\rm vir} = 4.6 \times 10^{-4}$, which is significantly larger than that for our fiducial SMDS for which $r_*/r_{\rm vir} = 2 \times 10^{-7}$. The compactness of the baryonic component in the DS relative to its halo is important since Valluri et al. (2010) showed that when the central component became very compact, orbits that were previously thought to be immune to becoming chaotic (the "long-axis tubes" which are important in prolate DM halos) also become chaotic. Valluri & Freese (2010) are currently computing the rate at which the "loss cone" at the center of the SDMS will be refilled for a range of possible halo and DS masses.

It is interesting to speculate that the Initial Mass Function of the first stars may be determined by the cutoff of the DM supply, which will take place at different SMDS masses in different haloes, depending on the details of the cosmological merger history. As the SMDS mass becomes a significant fraction of the halo mass ($\sim 5-10$%), it can significantly affect the shape of the halo, causing it to become more axisymmetric (Merritt & Quinlan 1998) and thereby potentially cutting off the DM supply; on the other hand, in the meantime the halo is growing larger due to mergers, which will replenish the population of radial orbits. Numerical simulations with better resolution than currently possible will be necessary to address these questions.

In the meantime, in our case without capture, we assume that the required DM is present and allow the stellar mass to grow to the point where most of the baryonic content of the initial halo is inside a single SMDS.

The amount of dark matter required inside the star to sustain long enough DM heating to reach a $10^5 M_\odot$ SMDS is still small, $\sim 100 M_\odot$ for accretion rate $\dot{M} = 10^{-2} M_\odot$/yr and $\sim 10^4 M_\odot$ for accretion rate $\dot{M} = 10^{-3} M_\odot$/yr, out of a total $10^6 M_\odot$ halo. In the code we accomplish this by not removing annihilated DM from the pool. More precise studies must be performed later in which we follow individual particle orbits in triaxial potentials to better determine the precise DM density at any one time.

Extended Capture: In our model labeled "with capture", we assume (as in our previous papers) that the DM due to adiabatic contraction runs out in $\sim 300,000$ yrs. For a while DM heating becomes unimportant and the DS has to contract to maintain pressure support. Then DS is refueled in the later stages due to capture of further DM from the ambient medium. This refueling requires an additional piece of particle physics: scattering of DM off the nuclei inside the star.

Some of the WIMPs from the ambient medium that have orbits passing through the star will eventually be captured and sink to the center, where they can annihilate efficiently. The capture process is irrelevant during the early evolutionary stage of the DS, since the baryon density is not high enough at that point, leading to very small scattering probabilities. However, once the DS approaches the main sequence, the baryon densities become high enough for substantial capture to be possible. This mechanism was first noticed by Freese et al. (2008b) and Iocco (2008).

In our previous work (Spolyar et al. 2009) we investigated a 'minimal capture' case which did not cause the DS to grow much more massive than the original case without capture $\sim 1000 M_\odot$; but we stated our intention to work out the case of a more substantial background DM density in which case the DS would end up supermassive. This is what we investigate here. The capture rate is sensitive to the product of two uncertain quantities: the scattering cross section of WIMP interactions with the nuclei σ_c and the ambient DM density $\bar{\rho}_\chi$. Since the capture mechanism depends only on the product of these two quantities, one can interchangeably vary either of these. For illustration purposes we will fix $\sigma_c = 10^{-39}\ \mathrm{cm}^2$ and vary $\bar{\rho}_\chi = (10^{10} - 10^{14})\mathrm{GeV/cm}^3$. The latter quantity is the largest reasonable amount based on our results for AC at the DS surface; and the former is the "minimal capture" value considered in all previous papers by Freese et al. Our fiducial cross section is just below the experimental bound for spin-dependent (SD) scattering; the bound on spin-independent (SI) scattering is much tighter: $\sigma_{c,SI} < 3.8 \times 10^{-44}$ cm^2 for $m_\chi = 100$GeV (Ahmed et al. 2009). We will show that capture can produce sufficient DM in the star to keep DM heating alive for a long time. The details of our procedure for including capture have previously been presented in Spolyar et al. (2009) and will not be repeated here.

4.2.3 Energy Sources:

There are four possible contributions to the DS luminosity:

$$L_{tot} = L_{DM} + L_{grav} + L_{nuc} + L_{cap} \tag{4.7}$$

from DM annihilation, gravitational contraction, nuclear fusion, and captured DM respectively. The heating due to DM annihilation in Eqns. (4.1) and (4.2) dominates from the time of DS formation until the adiabatically contracted DM runs out. As described previously, in our "without capture" models this stage never ends due to extended adiabatic contraction. In the models "with capture", on the other hand, we take this phase to end after $\sim$ 300,000 years, so that the DS has to contract in order to maintain pressure support. The contribution L_{grav} due to gravitational energy release is calculated as in Spolyar et al. (2009). As the DS contracts, the density and temperature increase to the point where nuclear fusion begins. We include deuterium burning starting at $T \sim 10^6 K$, hydrogen burning via the equilibrium proton-proton cycle (Bahcall 1989), and helium burning via the triple-alpha reaction (Kippenhahn & Weigert 1990). During the later stages of the pre main sequence evolution in the cases "with capture", the DS becomes dense enough to capture DM from the ambient medium via elastic scattering. Already before fusion can begin, and possibly again after the onset of fusion, captured DM can provide an important energy source with accompanying luminosity

$$L_{cap} = 2m_\chi \Gamma_{cap} = 2m_\chi f_Q \int dV \rho_{cap}^2 \langle \sigma v \rangle / m_\chi^2 \tag{4.8}$$

and again $f_Q = 2/3$.

4.3 Results of Stellar Structure Analysis

Using our polytropic model for dark stars, we have started with $3M_\odot$ stars and allowed baryonic matter to accrete onto them until they become supermassive with $M_* > 10^5 M_\odot$. We display results for the case without capture (but with extended adiabatic contraction) as well as the case with capture for a variety of WIMP masses m_χ = 10 GeV, 100 GeV, and 1 TeV. We have run models for a variety of accretion rates of baryons onto the star including constant accretion rates of $\dot{M} = 10^{-1}, 10^{-2}, 10^{-3} M_\odot$/yr. We will present results for $\dot{M} = 10^{-3} M_\odot$/yr, which is approximately the average rate calculated by Tan & McKee (2004) and by O'Shea & Norman (2007).

Our stellar evolution results can be seen in the Hertzsprung-Russell diagram of Figure 4.1 for the case of a $10^6 M_\odot$ halo. The dark star travels up to increasingly higher luminosities as it becomes more massive due to accretion. We have labeled a sequence of ever larger masses until all the baryons (150,000$M_\odot$) in the original halo are consumed by the SMDS. As the mass increases, so do the luminosity and the surface temperature. In the cases "without capture," the radius increases continuously until all the baryons have been eaten. In the cases "with capture", we have taken the (overly conservative) assumption that the DM from adiabatic contraction is depleted after $\sim 300,000$ yrs as in earlier papers; then the luminosity plateaus for a while while the DS contracts until eventually it is dense enough to capture further DM.

We note that, for the case "without capture", the H-R diagram is unchanged by varying the accretion rate: only the time it takes to get from one mass stage to the next changes, but the curves we have plotted apply equally to all accretion rates. Similarly, given m_χ, the following quantities are the same regardless of accretion rate: R_*, T_{eff}, ρ_c, and T_c.

In a beautiful paper, Hoyle & Fowler (1963) studied supermassive stars in excess of $10^3 M_\odot$ and found results germane to our work. They treated these as $n = 3$ polytropes (just as we do) dominated by radiation pressure, and found the following results: $R_* \sim 10^{11}(M_*/M_\odot)^{1/2}(T_c/10^8\mathrm{K})^{-1}\mathrm{cm}$, $L_*/L_\odot \sim 10^4 M_*/M_\odot$, and $T_{eff} \sim 10^5(T_c/10^8\mathrm{K})^{1/2}\mathrm{K}$. While some of the details of their calculations differ from ours, taking the central temperature appropriate to DS in the above relations roughly reproduces our results (to O(1)). For example, by using the temperature appropriate to dark stars with extended AC ($T_c \sim 10^6$K) rather than the much higher central temperature ($T_c > 10^8$K) appropriate to nuclear power generation, the above relations show that DS have much larger radii and smaller surface temperatures than fusion powered stars. We wish to draw particular attention to the fact that luminosity scales linearly with stellar mass, and is independent of power source.

Figure 4.2 plots the H-R diagram "with capture" for a single WIMP mass of 100 GeV, for $\dot{M} = 10^{-3} M_\odot$/yr, and for $\sigma_c = 10^{-39}$cm^2, but for a variety of ambient densities ranging from $\bar{\rho}_\chi = (10^{10} - 10^{14})$GeV cm^{-3}. The latter is the density one finds due to adiabatic contraction at the photosphere of the DS, and seems the largest sensible starting point for the value of the ambient density. A previous paper (Spolyar et al. 2009) considered the case of minimal capture with 10^{10}GeV/cm^3, which was artificially chosen so that the growth of the DS ceases at 680$M_\odot$, the radius shrinks, and then fusion and DM heating play equal roles. For ambient densities below 5×10^{10}GeV/cm^3, the DS mass growth shuts off well before the star becomes supermassive for the following reason. The cases with capture all take place at higher stellar densities than the cases without; the density must be high enough to be able to capture WIMPs. Consequently the surface temperature is larger and accretion is shut off more easily by radiation coming from the star. The case of ambient density 10^{10}GeV/cm^3 (from our previous paper) is a very carefully chosen (delicate) situation. On the low side of this density, DM heating is completely irrelevant and fusion tells the whole story; on the other hand, for any density $\bar{\rho}_\chi \geq \mathrm{few} \times 10^{10}$ GeV/cm^3, DM heating is so dominant over fusion that the DS can just continue growing in mass. At these higher densities the surface temperature never becomes hot enough ($\approx 100,000$ K) for feedback effects from the star to cut off accretion. Between 50,000 K and 100,000 K feedback effects are included, and they act to reduce the accretion rate, but they never shut it off entirely for densities above 5×10^{10}GeV/cm^3. In reality a star that is moving around can sometimes hit pockets of high $\bar{\rho}_\chi$ (where it is DM powered and grows in mass) and sometimes hit pockets of low $\bar{\rho}_\chi$ (where fusion takes over). As long as the ambient density remains at least this large, the star can reach arbitrarily large masses and eat the entire baryonic content of the halo.

As described previously, the capture mechanism depends on the product of scattering cross section times ambient density, $\sigma_c \bar{\rho}_\chi$, rather than on either of these quantities separately. Hence our current discussion could trade off ambient density vs. cross section. For example, the product is the same for $\bar{\rho}_\chi = 5 \times 10^{10}$ GeV/cm^3 and $\sigma_c = 10^{-39}$ cm^2 as it is for $\bar{\rho}_\chi = 10^{14}$GeV/cm^3 and $\sigma_c = 5 \times 10^{-43}$ cm^2. Thus, for the highest reasonable ambient density, the scattering cross section can be several orders of magnitude lower than the experimental upper bound for spin-dependent (SD) scattering and still provide substantial capture in DS. While the required σ_c is ruled out (Ahmed et al. 2009) for SI scattering at $m_\chi = 100$GeV, it is below the bounds at low masses $m_\chi \sim 10$ GeV and in this case can lead to significant DM capture in the stars.

Above $\sim 100 M_\odot$, one can see that the stellar luminosity scales as $L_* \propto M_*$ and is the same for all models for a given stellar mass; this statement is essentially true for all stars no matter the power source. The reason is that at these masses, the star is essentially radiation pressure supported throughout[2]. This same scaling in supermassive stars was already noticed by Hoyle and Fowler (1963). The luminosity essentially tracks (just below) the Eddington luminosity which scales as $L \propto M_*$.

The curves with higher values of WIMP mass m_χ lie to the left of the curves with lower m_χ. This can be understood as follows. The DM heating rate in Eqn.(1) scales as $Q \propto \rho_\chi^2/m_\chi$. Hence to reach the same amount of heating and achieve the same luminosity, at higher m_χ the DS must be at higher WIMP density, i.e., the stellar radius must be smaller, the DS is hotter, and the corresponding surface temperature T_{eff} is higher. Also, for higher m_χ the amount of DM in the star is smaller since the star is more compact for the same number of baryons but $\rho_\chi \propto n^{0.8}$ where n is the hydrogen density.

Tables 4.1 and 4.2 show various stellar properties for a DS that forms in a $10^6 M_\odot$ DM halo, as the star evolves to higher mass for the case of $m_\chi = 100$ GeV, for the two cases “without” and “with” capture respectively. While the DM density is a gently decreasing function of radius for the case without capture, it is extremely sharply peaked at the center of the DS for the case “with capture”.

One can see that, in the case “without capture”, $\sim 10^4 M_\odot$ of dark matter must be

[2] There is a slight deviation for the $10^3 M_\odot$ case without capture, where the star is still only 78% radiation pressure supported with the remaining pressure due to gas.

M_* ($M_\odot$)	L_* ($10^6 L_\odot$)	R_* (AU)	T_{eff} (10^3K)	ρ_c (g/cm^3)	T_c (10^5K)	M_χ ($M_\odot$)	$\rho_{\chi,c}$ (g/cm^3)	$M_{\rm Ann}$ ($M_\odot$)
10.1	0.13	3.1	4.3	2.8×10^{-7}	1.08	0.02	9.2×10^{-10}	7×10^{-5}
100	1.2	5.2	5.7	7.4×10^{-7}	3.4	0.1	1.5×10^{-9}	5.6×10^{-3}
500	9.7	9.3	7.2	4.3×10^{-6}	8.3	0.5	5.8×10^{-9}	0.26
10^3	17	12	7.5	4.6×10^{-6}	9.8	0.84	3.3×10^{-10}	0.9
10^4	182	18	10.8	1.3×10^{-5}	21	5.3	8.4×10^{-9}	86
10^5	2100	26	16.5	4.1×10^{-5}	46	31.2	1.6×10^{-8}	10750

Table 4.1: Properties and evolution of dark stars for $m_\chi = 100$ GeV, $\dot{M} = 10^{-3} M_\odot/\mathrm{yr}$ for the case without capture but with extended adiabatic contraction. The DM halo was taken to be at a redshift of 20 with a concentration parameter of 3.5 and with a mass of $10^6 M_\odot$. Shown are the stellar mass M_*, the DS luminosity L_*, the stellar radius R_*, the surface temperature T_{eff}, the central baryon density ρ_c, the central temperature T_c, the amount of DM in the DS M_χ (due to both adiabatic contraction and capture), the central WIMP density $\rho_{\chi,c}$, and the amount of DM consumed by the DS M_{Ann}.

M_* ($M_\odot$)	L_* ($10^6 L_\odot$)	R_* (AU)	T_{eff} (10^3K)	ρ_c (g/cm^3)	T_c (10^5K)	M_χ ($M_\odot$)	$\rho_{\chi,c}$ (g/cm^3)	$M_{\rm Ann}$ ($M_\odot$)
10.0	0.13	3.1	4.3	2.8×10^{-7}	1.08	0.02	9.2×10^{-10}	4.0×10^{-5}
100	1.2	5.1	5.7	7.4×10^{-7}	3.5	0.1	1.3×10^{-9}	2.7×10^{-3}
500	5.5	6.0	7.8	1.6×10^{-5}	13	0.3	1.6×10^{-9}	0.09
10^3	8.8	0.3	39	2.9×10^{-1}	390	3.1×10^{-6}	5.4×10^{-7}	0.27
10^4	161	0.9	47	1.1×10^{-1}	440	2.9×10^{-5}	1.1×10^{-6}	77
10^5	1950	2.7	50	3.8×10^{-2}	450	1.3×10^{-4}	3.0×10^{-6}	9900

Table 4.2: Properties and evolution of dark stars for case "with capture", for $m_\chi = 100$ GeV, $\dot{M} = 10^{-3} M_\odot/\mathrm{yr}$, and product of scattering cross section times ambient DM density $\sigma_c \bar{\rho}_\chi = 10^{-39}\mathrm{cm}^2 \times 10^{13}$ GeV/cm^3. The Halo has the same parameters as in Table 4.1. The quantities tabulated are the same as in Table 4.1. The double horizontal line delineates the transition from adiabatically contracted DM to captured DM once the DS reaches $\sim 1000 M_\odot$ (after this point, the DM from AC has been annihilated away).

annihilated away in order for the DS to reach $10^5 M_\odot$ for accretion rate $\dot{M} = 10^{-3} M_\odot$. The time to reach this mass is $\sim$ 100Myr. For an alternative faster accretion rate $\dot{M} = 10^{-2} M_\odot$, a smaller amount of DM must be annihilated away, $\sim 100 M_\odot$; then it takes the DS $\sim$ 10 Myr to reach $\sim 10^5 M_\odot$. The caveat is that the DM orbits must continue to penetrate into the middle of the DS for this length of time in order for the DM abundance and consequent heating to continue; it is the DM heat source that keeps the DS cool enough to allow it to continue to accrete baryons. Additionally, the assumption that baryons continue to accrete onto the DS must continue to hold. Yet, in the time frame required, the original $10^6 M_\odot$ halo will merge with its neighbors, so that both the baryon and DM densities are disturbed. These mergers could effect the DS in one of two ways: either they provide more baryons and DM to feed the SMDS so that it ends up being even larger, or they disrupt the pleasant high DM environment of the SMDS so that it loses its fuel and converts to an entirely fusion powered star. Continued growth of the DS is quite plausible since simulations with massive BHs in mergers show that they prefer to sit close to the center of the density distribution or find the center in a short time after the merger.

Someday detailed cosmological simulations will be required to answer this question. Individual DS in different haloes may end up with a variety of different masses depending on the details of the evolution of the haloes they live in. The case studied here is clearly a simplistic version of the more complicated reality, but illustrates the basic idea that supermassive stars may be created by accretion onto DS, either with or without capture.

Tables 4.1 & 4.2 present models for DSs which form in $10^6 M_\odot$ DM halos, but SMDS could also form in a variety of halo masses with different final stellar masses. For example, a hydrogen/helium molecular cloud may start to contract in a $10^8 M_\odot$ halo and produce a DS. Here the situation is more complicated. The virial temperature of the halo exceeds 10^4K, the surface temperature we have found for a DS in equilibrium. Hence it is not clear how accretion onto the DS will proceed. This is the subject of future work. The accretion is expected to be faster due to the increased ambient temperature. We extended our models

M_* ($M_\odot$)	L_* ($10^6 L_\odot$)	R_* (AU)	T_{eff} (10^3K)	ρ_c (g/cm^3)	T_c (10^5K)	M_χ (M$_\odot$)	$\rho_{\chi,c}$ (g/cm^3)	$M_{\rm Ann}$ (M$_\odot$)
12	0.19	3.6	4.3	1.6×10^{-7}	0.90	0.03	8.4×10^{-10}	1.1×10^{-6}
100	1.9	6.5	5.7	3.8×10^{-7}	2.7	0.2	1.3×10^{-9}	7.6×10^{-5}
10^3	23	15	7.1	2.3×10^{-6}	7.8	1.4	4.0×10^{-9}	1.2×10^{-2}
10^4	172	28	8.6	3.5×10^{-6}	14	9.7	4.3×10^{-9}	0.9
10^5	2100	39	14	1.3×10^{-5}	31	56	9.1×10^{-9}	109
10^6	2.2×10^4	61	19	3.3×10^{-5}	64	355	1.5×10^{-8}	1.1×10^4
10^7	2.2×10^5	97	27	8.3×10^{-5}	127	2200	2.3×10^{-8}	1.2×10^6

Table 4.3: Properties and Evolution of dark stars for $m_\chi = 100$ GeV, $\dot{M} = 10^{-1} M_\odot/{\rm yr}$ for the case without capture but with extended adiabatic contraction. The DM halo was taken to be at a redshift of 15 with a concentration parameter of 3.5 and with a mass of 10^8M$_\odot$. The quantities tabulated are the same as in Table 4.1.

to $10^8 M_\odot$ halos in which a more extended period of accretion can lead to SMDS with even larger masses. Tables 4.3 & 4.4 show examples of "without" and "with" capture cases respectively for $10^8 M_\odot$ halos. The baryonic mass in the halo is $1.5 \times 10^7 M_\odot$. Potentially all of this mass could go into the SMDS. Then once the DM runs out it becomes an enormous Pop III fusion powered star, which soon burns out and becomes a black hole with mass $> 10^7 M_\odot$. Such a large BH at early times would clearly help to explain the many large BH found in the Universe at early times and today. In addition, since $L_* \propto M_*$, we can predict that the luminosity of the $M_* \sim 10^7 M_\odot$ SMDSs would be $L_* \sim 10^{11} L_\odot$, even easier to detect than a 10^5 SMDS.

It can be seen in Tables 2 and 4 that in the case "with capture" the amount of DM inside the star M_χ is very low at any given moment after the star transitions from adiabatically contracted DM to captured DM. The reason is simple: after a very brief time an equilibrium regime is reached where the annihilation rate is equal to the capture rate. In other words, as soon as a WIMP gets into the DS, it quickly thermalizes and annihilates. This leads to very small amounts of DM inside the star at any one time. Notice, however, that the total amount of DM annihilated (integrated over time) is still very large, as can be seen from the

M_* ($M_\odot$)	L_* ($10^6 L_\odot$)	R_* (AU)	T_{eff} (10^3K)	ρ_c (g/cm^3)	T_c (10^5K)	M_χ ($M_\odot$)	$\rho_{\chi,c}$ (g/cm^3)	$M_{\rm Ann}$ ($M_\odot$)
11	0.18	3.64	4.3	1.6×10^{-7}	0.9	0.03	8.4×10^{-10}	5.6×10^{-7}
100	1.8	6.5	5.7	3.8×10^{-7}	2.7	0.2	1.3×10^{-9}	3.8×10^{-5}
10^3	22	14	7.2	2.3×10^{-6}	7.8	1.4	3.6×10^{-9}	6.1×20^{-3}
10^4	173	23	9.4	5.8×10^{-6}	16	8.3	2.9×10^{-9}	0.44
4.1×10^4	740	1.8	49	5.7×10^{-2}	444	0.18	7.2×10^{-9}	6.0
10^5	1.9×10^3	2.7	51	3.8×10^{-2}	452	1.3×10^{-4}	2.9×10^{-6}	91
10^6	2.1×10^4	8.5	51	1.2×10^{-2}	456	2.7×10^{-5}	1.5×10^{-4}	1.1×10^4
10^7	2.1×10^5	27	51	3.9×10^{-3}	457	4.0×10^{-10}	1.0×10^2	1.1×10^6

Table 4.4: Properties and evolution of dark stars for case "with capture", for $m_\chi = 100$ GeV, $\dot{M} = 10^{-1} M_\odot$/yr, and product of scattering cross section times ambient DM density $\sigma_c \bar{\rho}_\chi = 10^{-39}\text{cm}^2 \times 10^{13}$ GeV/cm^3. The DM halo has the same parameters as in Table 4.3. The quantities tabulated are the same as in Table 4.1. The double horizontal line delineates the transition from adiabatically contracted DM to captured DM once the DS reaches $\sim 4 \times 10^4 M_\odot$ (after this point, the DM from AC has been annihilated away).

last three entries in the column labeled M_{Ann} of Tables 2-4.

General Relativistic Instability: The pulsational stability of supermassive stars is an interesting issue. They are radiation-pressure dominated with adiabatic index close to $\gamma = 1 + 1/n = 4/3$, the value that yields neutral stability to radial pulsations for Newtonian bodies with no rotation. Indeed general relativistic corrections (which scale as GM_*/R_*) act in the direction of destabilizing stars and are particularly important for high mass stars. Fowler (1966) examined the stability of supermassive stars using polytropes with $n = 3$ (see Wagoner 1969 for a review). Fowler found that, for the case of no rotation, radial oscillations become dynamically unstable and prevent standard stars more massive than $10^5 M_\odot$ from reaching a phase of hydrogen burning before collapse. Yet he also found that a small amount of rotation can stabilize the stars, so that rotating stars as heavy as $10^8 M_\odot$ could be stable en route to reaching hydrogen burning.

In the case of DS, stability to radial pulsations is much easier to achieve. DS have much larger radii and lower temperatures than fusion powered stars, so that the GR corrections $\sim GM_*/R_*$ are much smaller. The upper limit on the allowed stellar mass will be larger. In any case, SMDSs are undoubtedly rotating, so that very large stable masses can be achieved (even in the case of rotating ordinary stars, the mass limit is $10^8 M_\odot$).

In the future we suggest a stability analysis of our models. The very interesting possibility of short term pulsational instabilities exists, which leads to SMDS as possible standard candles for learning about dark energy or other evolutionary properties of the Universe.

4.4 Detectability with JWST

We discuss the capabilities of JWST to discover dark stars, following the properties of the telescope described by Gardner et al. (2006, 2009). The telescope is designed to be diffraction limited at a wavelength $\lambda_{obs} = 2\mu$m. The Near Infrared Camera (NIRCam) will operate in the wavelength range $\lambda = (0.6-5)\mu$m and the Mid-Infrared Camera (MIRI) will operate in the wavelength range $\lambda = 5 - 27\mu$m. In an exposure of duration 10^4s, NIRCam will have a limiting sensitivity of 11.4 nJy ($1\,\mathrm{nJy} = 1 \times 10^{-32}$ ergs s^{-1} cm^{-2} Hz^{-1}) in the 2μm band, and 13.8nJy in the 3.5μm band and MIRI will have a sensitivity of 700μJy in the $\lambda = 10\mu m$ band (in all cases limiting sensitivities are for a S/N=10). With longer exposure times the limiting flux detectable will scale as $\sqrt{t}$ for the same S/N. DS will be characterized by black body spectra with surface temperatures $T_{eff} \lesssim 5\times10^4$K. In addition, DS are also predicted to have hydrogen lines.

We determine the detectability of dark stars located at various redshifts z= 5, 10, and 15 using the standard Planck spectrum of blackbody with surface temperature T_{eff} and radius R_* (for DSs similar to those from Tables 1-4) in a cosmology with $H_0 = 74, \Omega_\Lambda = 0.71, \Omega_M = 0.29$.

Figure 4.3 shows the observed black body flux distribution of two SMDSs formed at $z = 15$ for a WIMP mass $m_\chi = 100$GeV for the case of extended AC (without capture). The star in the left panel is formed in a $10^6 M_\odot$ halo and the star in the right panel is formed in a $10^8\ M_\odot$ halo and their stellar (baryonic) masses are $1.7 \times 10^5\ M_\odot$ and $1.5 \times 10^7\ M_\odot$ respectively. Curves are shown assuming the SMDS formed at $z = 15$ and survived to various redshifts, at which it is still producing blackbody radiation. The $1.7 \times 10^5\ M_\odot$ star (left panel) will be detectable by JWST (NIRCam) in an exposure of a million seconds, but only if it survives intact till $z = 10$. The $1.5 \times 10^7\ M_\odot$ star (right panel) will be detectable even in a shorter $10^4 s$ exposure even at $z = 15$ in both the 2μ and 3.5μ bands. The star on the right may be marginally detectable in a million second exposure in the 10μ band of MIRI. The relative flux levels in the three different bands will be important for distinguishing these objects from galaxies.

The curves are not corrected for Ly-α absorption by the IGM but the red vertical lines show the location of the $1216\mathring{A}$ line redshifted from the rest-frame wavelength of the star at each of the three redshifts. Flux at wavelengths to the left of the redline at each redshift is expected to be absorbed to some extent by the IGM. Since the surface temperatures of our stars are $\simeq 10^4$K, the majority of the Lyα absorption ($\lambda_{rest} = 1216\mathring{A}$) is expected to occur at wavelengths shorter than that at which the peak flux is emitted. We note that for a DS at $z = 15$ the Ly α absorption line lies at 1.94μ - roughly in the middle of the NIRCam 2μ band. In this case the flux in this band will be reduced by about a factor of two but will still be well above the detection limit (in 10^6s). A detailed calculation of the absorption by the intergalactic medium is outside the scope of the current study.

We studied numerous other cases without capture as well: a variety of WIMP masses (10Gev -2TeV) as well as various formation redshifts ($z_{\rm form} = 10-20$). We found that DSs with masses up to $M_* \sim 10^5 M_\odot$ forming in $10^6\ M_\odot$ halos at $z = 20$ and shining at that redshift will in general not be detectable for any value of m_χ (they will become detectable only if they survive to and shine at much lower redshifts).

The smaller DS with $M_* = 800 M_\odot$ discussed in our previous work (Freese et al. 2008a; Spolyar et al. 2009) will not be visible in JWST (see also Scott et al 2010); they are several orders of magnitude below the detection limit of JWST (in 10^6s).

Figure 4.4 shows the observed black body flux distribution of two dark stars formed at $z = 15$ in halos of two different masses for the case "with capture". Since DS formed via capture are smaller (in radius) and hotter (than DS formed via extended AC without capture), their peak wavelength tends to shift to lower wavelengths, in some cases out of the range detectable by JWST. $10^5 M_\odot$ stars in $10^6 M_\odot$ halos are only detectable if they survive until $z = 5$ at which time they could be detectable in a long (10^6s exposure). On the other hand $10^7 M_\odot$ stars formed in $10^8 M_\odot$ halos will be easily detectable even in an exposure of 10^4s all the way out to $z = 15$. For most other WIMP masses and formation redshifts DSs formed in $10^6 M_\odot$ halos via capture are below the detection limit of JWST.

The prospect of detecting SMDS in JWST and confirming the existence of a new phase of stellar evolution is exciting. In the most optimistic cases, detection in a number of different wavelength bands could be used to obtain a spectrum and differentiate these dark stars from galaxies or other sources.

4.5 Concluding Remarks

Using our polytropic model for dark stars, we have considered accretion of baryonic matter onto the DS as they become supermassive, $M_* > 10^5 M_\odot$. Such large masses are possible because the dark star is cool enough (as long as it is powered by DM) so that radiative feedback effects from the star do not shut off the accretion of baryons, as long as it is powered by DM. We considered two different scenarios for supplying the required amount of dark matter:

1) **The Case of Extended Adiabatic Contraction, labeled "without capture" in the figures.** In this case dark matter is supplied by the gravitational attraction of the baryons in the star. In triaxial haloes DM orbits are quite complex and the DM in the core is harder to deplete than previously estimated. This case does *not* include any captured DM, and relies solely on the particle physics of WIMP annihilation. To grow to a $10^5 M_\odot$ SMDS in a $10^6 M_\odot$ halo, or to grow to a $10^7 M_\odot$ SMDS in a $10^8 M_\odot$ halo, the amount of DM consumed can be as much as $\sim 1\%$ of the total DM in the halo (depending on the accretion rate). This amount is not unreasonable, since Valluri etal (2010) found that the fraction of box and chaotic DM orbits is as high as 85% in triaxial haloes and remains over 10%

when a significant compact baryonic component causes the halo to become axisymmetric at small radii. Future work will be required to accurately obtain WIMP orbits, densities, and timescales (work in progress). For now we took the simplistic approach of using our previous prescription for adiabatic contraction in a spherical potential but not removing the annihilated DM.

2) **The Case of Extended Capture, labeled "with capture" in the figures.** Here the original DM inside the star from adiabatic contraction is assumed to be depleted after $\sim$ 300,000 yrs, then the star begins to shrink somewhat, and capture of DM from the surroundings takes place as it scatters elastically off of nuclei in the star. In this case the additional particle physics ingredient of WIMP scattering is required.

In this chapter we studied the formation of $10^5 M_\odot$ SMDS in $10^6 M_\odot$ DM haloes and $10^7 M_\odot$ SMDS in $10^8 M_\odot$ haloes. These stars become very bright, $L_* \sim (10^9 - 10^{11}) L_\odot$. Figure 4.1 shows the H-R diagram for a variety of WIMP masses, and follows the dark star as it climbs up to ever higher masses. They live millions to billions of years, depending on the merger history with other haloes. Once the DM runs out, the SMDSs have brief lives as fusion powered Pop III stars before collapsing into $> 10^5 M_\odot$ black holes, possible seeds for many of the big BH seen in the Universe today and at early times. A proper study of the final mass of the DS and resultant BH will depend on cosmological simulations. The original halo containing the DS will merge with other haloes. No one knows what exactly will happen to the DM density in the vicinity of the DS when this happens. The DS could end up even more massive. DS may also form in larger haloes that form at later times, as long as the baryonic content is still only H and He. Localized regions with this property could exist even at redshifts $z < 7$ (Furlanetto & Loeb 2005; Choudhury & Ferrara 2007).

SMDS would make plausible precursors of the $10^9 M_\odot$ black holes observed at $z > 6$ (Fan et al. 2003) of intermediate mass black holes; of BH at the centers of galaxies; and of the BH inferred by extragalactic radio excess seen by the ARCADE experiment (Seiffert et al. 2009). In addition, the formation of BH from DS could be accompained by high-redshift gamma ray bursts thought to take place due to the gravitational collapse of supermassive stars.

In the future we suggest a stability analysis of our models. The very interesting possibility of short term pulsational instabilities exists, which leads to SMDS as possible standard candles for learning about dark energy or other evolutionary properties of the Universe.

Smdss could be detected by JWST for a variety of parameter ranges. These are extremely bright objects $L_* \sim (10^9 - 10^{11})L_\odot$ and yet are very cool $T \sim 10,000$K, so that their emitted light is in the wavebands detectable by JWST. The longer they live, the more easy they are to detect. Figures 4.3 and 4.4 give examples of what one could look for in JWST. For the most optimistic cases, one could even test for the blackbody spectrum in a number of different wavebands. In principle hydrogen or helium lines could be found to complement the blackbody emission. If, in addition, someday high energy neutrinos are found to emanate from these stars, then it will be a clincher that DM annihilation took place inside the DS.

It is interesting to speculate that the Initial Mass Function of Population III fusion powered stars may be determined by the cutoff of the DM supply, which may vary from one DS to another. Dark stars continue to accrete mass as long as the dark matter annihilation powers the star and keeps it cool enough. Once the DM fuel supply is exhausted, the star shrinks and heats up, fusion begins, and the mass growth of the star is quickly halted due to feedback from hot emitted photons. Hence the details of the cutoff of the DM supply may determine the sizes of Population III stars entering the fusion era. The cutoff will take place at different DS masses in different haloes, depending on the details of the cosmological merger history. Different final DS masses may result for different individual DS depending on the evolution of their parent haloes.

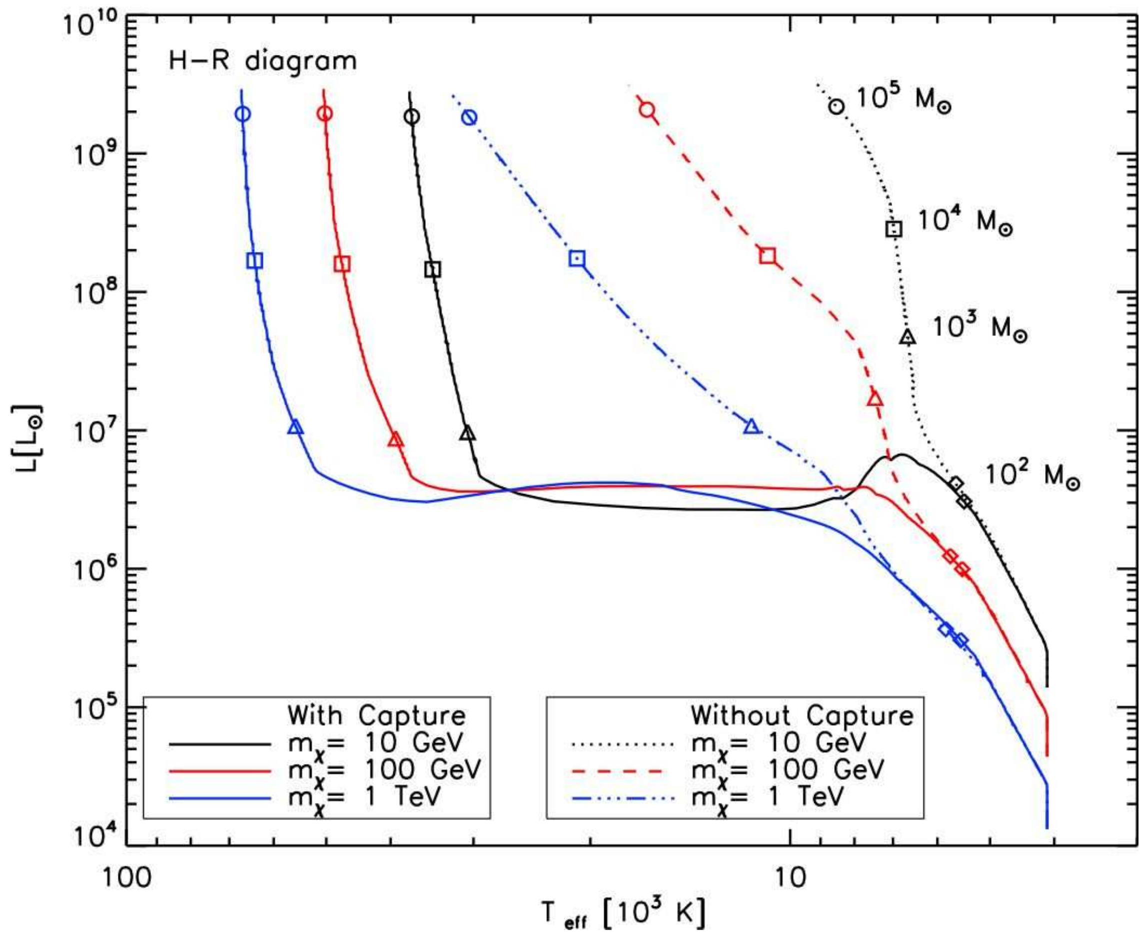

Figure 4.1: Hertzsprung-Russell diagram for dark stars for accretion rate $\dot{M} = 10^{-3} M_\odot$/yr. and a variety of WIMP masses as labeled for the two cases: (i) "without capture" but with extended adiabatic contraction (dotted lines) and (ii) "with capture" (solid lines). The case with capture is for product of scattering cross section times ambient WIMP density $\sigma_c \bar{\rho}_\chi = 10^{-39}\text{cm}^2 \times 10^{13}$GeV/cm^3. Also labeled are stellar masses reached by the DS on its way to becoming supermassive. The final DS mass was taken to be $1.5 \times 10^5 M_\odot$ (the baryonic mass inside the initial halo), but could vary from halo to halo, depending on the specifics of the halo mergers.

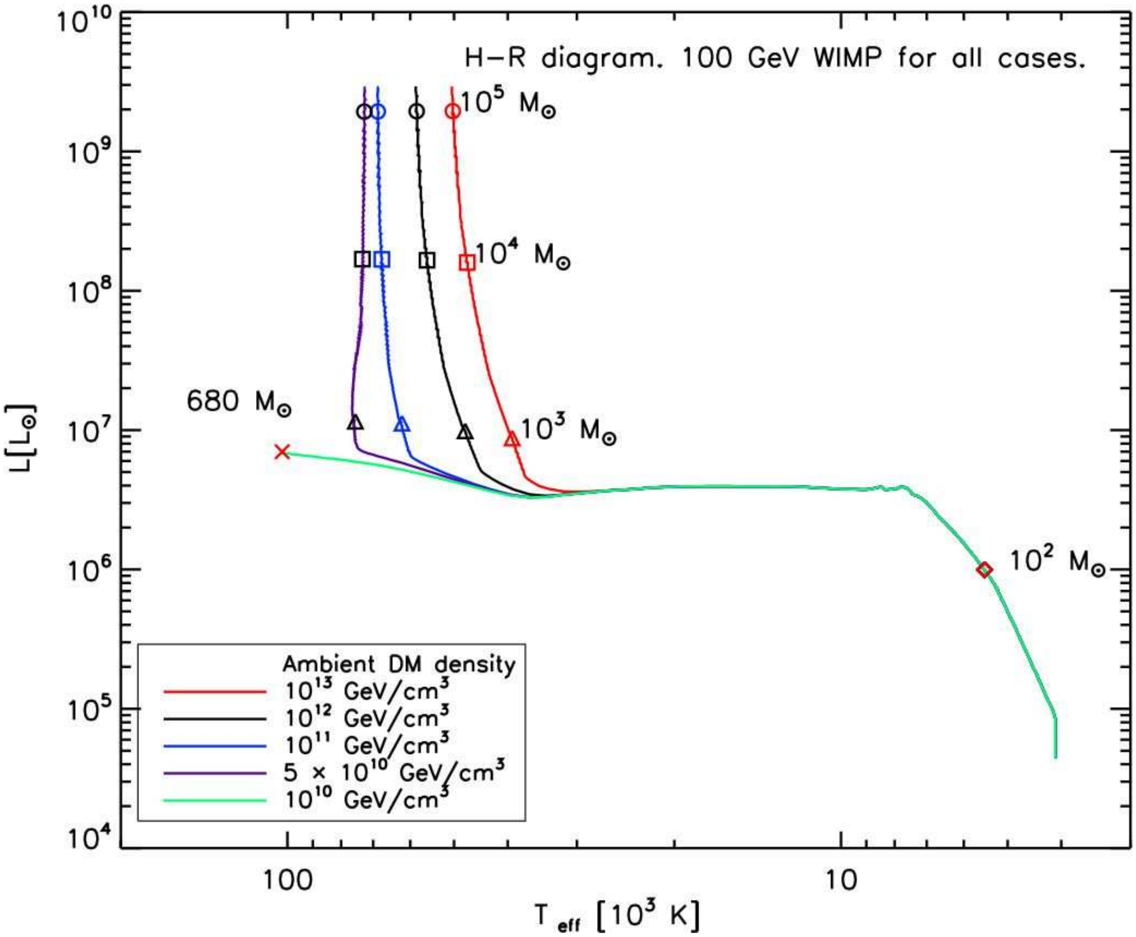

Figure 4.2: Hertzsprung-Russell diagram for DS for the case "with capture" for 100 GeV WIMP mass and accretion rate $\dot{M} = 10^{-3} M_{\odot}$/yr. The different curves are for a variety of ambient DM densities $\bar{\rho}_\chi$ as labeled for scattering cross section $\sigma_c = 10^{-39}\mathrm{cm}^2$. The results depend only on the product $\sigma_c \bar{\rho}_\chi$ so the different curves could equivalently refer to different σ_c for a given $\bar{\rho}_\chi$.

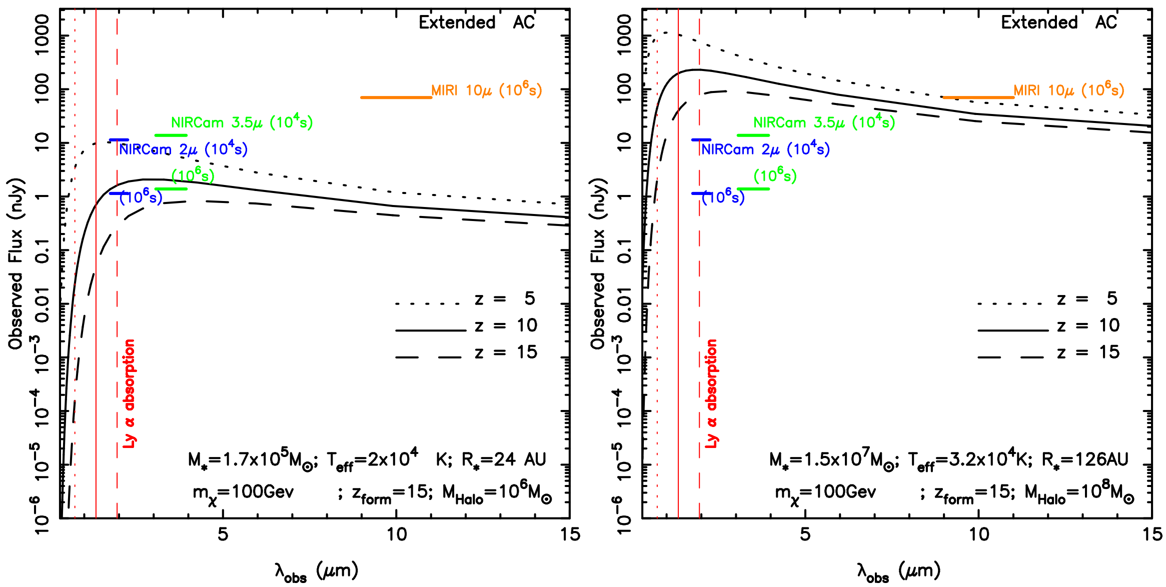

Figure 4.3: Black body spectra of two dark stars formed via extended adiabatic contraction ("without capture") for m_χ=100 GeV. Left panel: 1.7×10^5 $M_\odot$ SMDS in a 10^6 $M_\odot$ halo. Right panel: 1.5×10^7 $M_\odot$ SMDS in 10^8 $M_\odot$ halo. The black body flux is shown at $z = 15$ (formation redshift) and at $z = 10$ and 5 (see line legends) assuming that the dark star survives till the lower redshifts. Blue dashes show sensitivity limit and bandwidth of NIRCam 2μ (R=4) while the green dashes show the sensitivity limit and band width of the NIRCam 3.5μ (R=4) band. The upper and lower dashes show the sensitivity limits after exposure times of 10^4s, 10^6s respectively. The sensitivity of MIRI (10μ, R=5) is shown for exposure time of 10^6s (orange dash). All sensitivities are computed assuming a S/N=10. The red vertical lines show the location of the 1216$\mathring{A}$ line redshifted from the rest-frame wavelength of the star at each of the three redshifts. The observed flux to the left of the vertical lines will decrease relative to the black curves depending on the model assumed for IGM absorption up to the redshift of reionization. Credit: Monica Valluri.

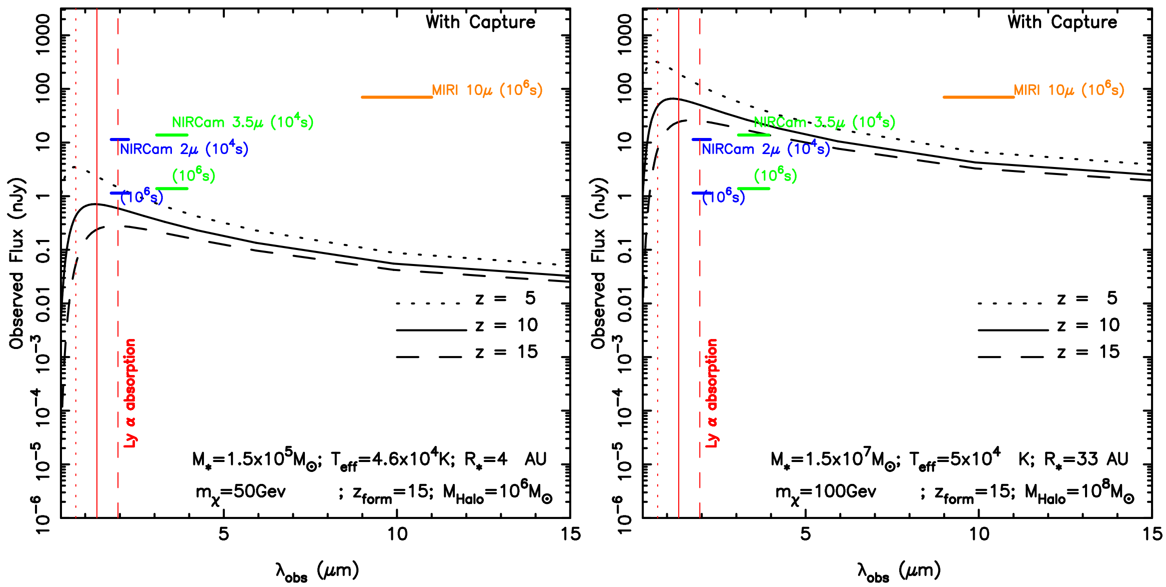

Figure 4.4: Similar to Fig. 4.3 for dark stars formed "with capture". Left panel: $1.7 \times 10^5\ M_\odot$ SMDS formed in $10^6 M_\odot$ halo ($m_\chi = 50$Gev). Right panel: $1.7 \times 10^7\ M_\odot$ SMDS formed in $10^8 M_\odot$ halo ($m_\chi = 100$Gev).Credit: Monica Valluri.

CHAPTER V

Observability of Dark Stars with JWST

5.1 Dark Star Spectra

We use the TLUSTY stellar atmosphere code to determine the spectrum from the Dark Stars, therefore extending our analysis from Section 4.4 where we only considered a pure black body spectrum. Figure 5.1a illustrates the spectrum for a $10^6 M_\odot$ dark star of 1.9×10^4K surface temperature for the case where it grew via extended AC. Since the first stars are composed only of hydrogen and helium, with no other elements present, no other lines should appear. One can see the Lyman edge at roughly 0.1 microns[1]. Similarly, Figure 5.1b illustrates the spectrum for a million solar mass dark star which grew via captured DM. As discussed previously, these stars with captured DM are much hotter (T$_{eff} = 5.1 \times 10^4$K); hence their spectra are quite different from those with extended AC. The most prominent difference is the shift of the peak in the spectrum to lower wavelengths for the case "with capture". This will lead in turn to a lower detectability in the near infrared spectrum.

[1]Compared to a blackbody of the same temperature, photons have typically been shifted to higher wavelengths (lower energy). However, the excess seen at wavelengths just below the Lyman edge is due to photons coming from deeper inside the star (the photosphere is at roughly an optical depth ~ 1, and at this wavelength there is very little absorption).

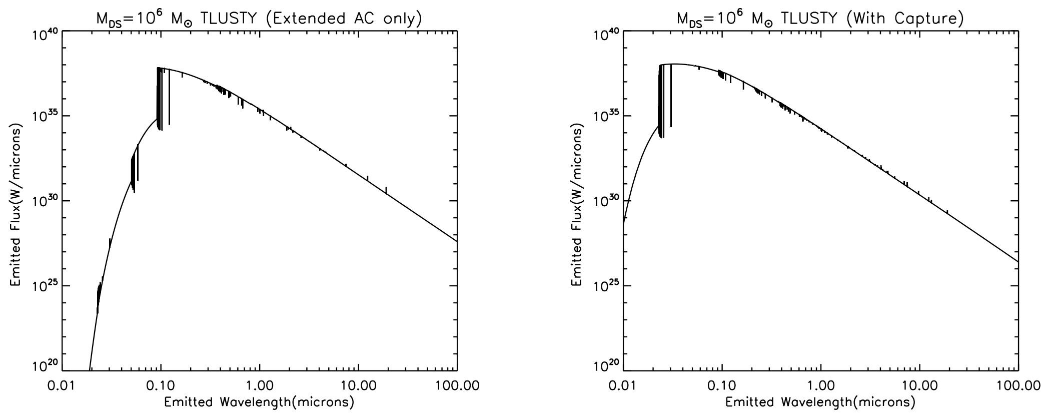

(a) (b)

Figure 5.1: Expected spectral energy distribution (SEDs) of $10^6 M_\odot$ supermassive dark stars. Left panel: DS with a surface temperature of 1.9×10^4K and formed via the extended adiabatic contraction (AC) only mechanism. Right panel: with a surface temperature of 5.1×10^4 and formed "with capture".

5.2 Dark Star Formation Rate

The first Dark Stars can form in the early Universe inside minihaloes of $\sim 10^6 M_\odot$, where protostellar clouds collapse via molecular hydrogen cooling until the DM heating sets in. Later in $10^8 M_\odot$ haloes, where clouds collapse via atomic cooling, larger DS can form. We therefore need to know the formation rate of $10^6 - 10^8 M_\odot$ dark matter haloes in order to estimate the Dark Star formation rate. We will then assume that a fraction $\mathrm{f}_{\mathrm{SMDS}}$ of these haloes contain Dark Stars, and in later sections constrain this fraction.

We use date from N-Body simulations for structure formation at high redshifts from *Iliev et al.* (2010). The CubeP^{3}M N-Body code, based on the particle-mesh PM-FAST (*Merz et al.*, 2005) was used to simulate a comoving volume of $6.3h^{-1}$ Mpc with 1728^3 particles of mass $5.19 \times 10^3 M_\odot$. From the simulated data we obtain the formation rate of minihaloes within a certain mass range. Figures 5.2 and 5.3 plot the halo formation rate dn/dt as a function of redshift per comoving Mpc^3 per year. We note that the formation rate peaks roughly at $z \sim 12$.

We will examine two different cases:

- I. We count the number of minihaloes formed in a mass range that is binned within a

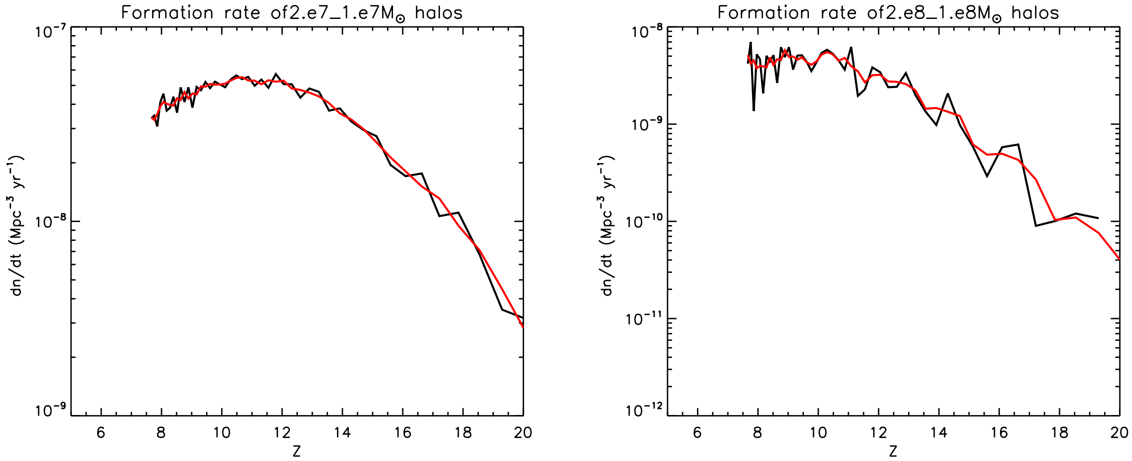

Figure 5.2: Left panel: the formation rate of $1-2\times10^7 M_\odot$ minihaloes per comoving Mpc^3 and year. This is a potential host for the $10^6 M_\odot$ SMDS. Right panel: formation rate for $1-2\times10^8 M_\odot$ minihaloes in which a $10^7 M_\odot$ SMDS can form.

factor of two. This is the case considered in Figure 5.2. The left panel indicates the formation rate as a function of redshift of haloes in the mass range $(1-2)\times10^7 M_\odot$ and the right panel indicates the formation rate of haloes in the mass range $(1-2)\times 10^8 M_\odot$. We will then assume that DS of a given mass form inside haloes that are roughly 10-20 times as massive as the DS. In other words, the $10^7 M_\odot$ SMDS formed in a $(1-2)\times10^8 M_\odot$ minihalo. The formation rates in Case I are plotted in Figure 5.2.

- II. Here we broaden the bin range for haloes forming dark stars, and count the number of haloes forming in a mass range that varies within a factor of five. This is the case considered in Figure 5.3. The left panel indicates the formation rate as a function of redshift for haloes in the mass range $(1-5)\times10^7 M_\odot$ and the right panel indicates the formation rate of haloes in the mass range $(1-5)\times10^8 M_\odot$. In this case we consider that the SMDS of a given mass could be formed in a minihalo $10-50$ times larger than the DS itself. The formation rates in Case II are plotted in Figure 5.3.

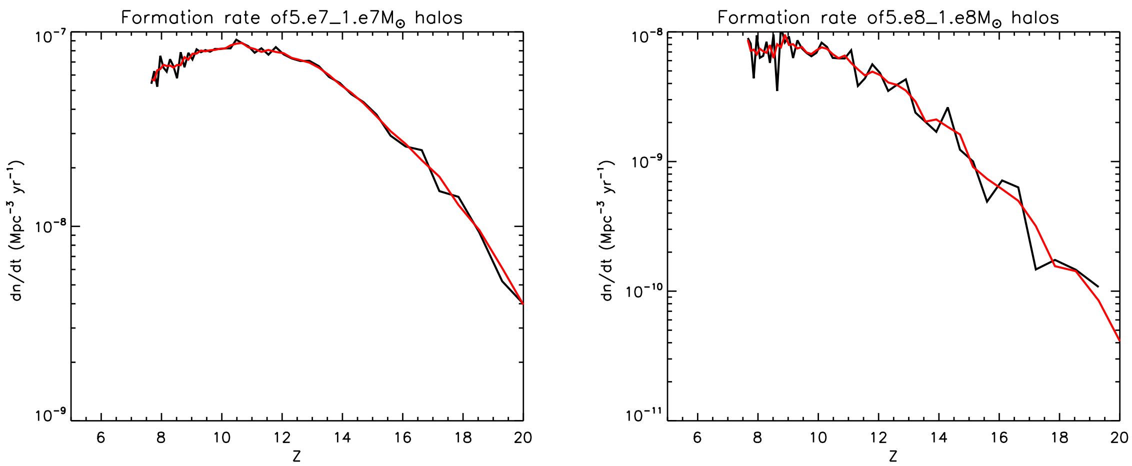

Figure 5.3: As in Figure5.2, but with a larger mass bin width now, as needed for scenario II. In the left panel we plot the formation rate of minihaloes with a mass in the $1-5\times10^7 M_\odot$ range, where a DS of $10^6 M_\odot$ could form. The panel on the right is for haloes in the $1-5\times10^8 M_\odot$ range, where a DS of $10^7 M_\odot$ could form.

The formation rate of minihaloes per unit redshift and arcmin^2 is then given by

$$\frac{dN}{dzd\theta^2} = \frac{dn}{dt}\left(V_c(z_{max}) - V_c(z_{min})\right)\frac{C}{4\pi}\Delta t(min;max) \tag{5.1}$$

Defining $\mathrm{z_{start}}$ to be the formation redshift of minihaloes capable of hosting DS, we take $\mathrm{z_{min}} = \mathrm{z_{start}} - 1/2$ and $\mathrm{z_{max}} = \mathrm{z_{start}} + 1/2$. We will be careful to make a distinction between the following two redshifts: at $\mathrm{z_{start}}$ the minihaloes capable of forming DS form; the initial $\sim 1M_\odot$ dark stars come into existence very soon after. However, it then takes a while for the DS to accrete mass at $10^{-2} - 10^{-1} M_\odot$/yr before they grow to supermassive sizes. We will use the terminology $\mathrm{z_{form}}$ to indicate the redshift of formation of the SMDS, i.e. the redshift where the DS has accreted enough baryonds to become supermassive with a given mass $\sim 10^5 - 10^7 M_\odot$. Above, V_c denotes the comoving volume at a given redshift, C is the conversion factor between arcmin^2 and steradians, and $\Delta t(min;max)$ is the cosmic time interval between z_{min} and z_{max}:

$$\Delta t(min; max) = t_H \int_{z_{min}}^{z_{max}} \frac{1}{(1+z)\left(\Omega_m(1+z)^3 + \Omega_\Lambda\right)^{\frac{1}{2}}}. \tag{5.2}$$

where we assume a standard flat ΛCDM Universe in which $\Omega_m = 0.27$ is the matter fraction of the Universe and $\Omega_\Lambda = 0.73$ is the dark energy fraction.

The redshift at which DS are observable as J-band dropouts in the HST is roughly $z = 10$. We now consider three different redshifts $\mathrm{z_{form}}$ when the DS has accreted enough baryons to become supermassive:

- Case A: $\mathrm{z_{form}}$ =10
- Case B: $\mathrm{z_{form}}$ =12
- Case C: $\mathrm{z_{form}}$ =15

Depending on the accretion rate and the final mass of the SMDS. these three cases will then correspond to three different values of $\mathrm{z_{start}}$ at which the relevant minihaloes formed. To be concrete we use an accretion rate of $10^{-1} M_\odot$ /yr to determine the values for $\mathrm{z_{start}}$. Using the minihalo formation rates in Figure 5.2 at the corresponding redshift, we can then evaluate $\frac{dN}{dz d\theta^2}$ in Eq. (5.1). Our results are summarized in Table 5.1

By comparing Figs. 5.2 and 5.3, one can see that the number of host haloes does not vary significantly between cases I and II. Henceforth, in the remainder of this study, we our analysis will therefore be applied only to case I, where the halo mass is binned within a factor of two of its value.

Scenario Name	Halo Mass Range ($M_\odot$)	$\mathrm{z_{form}}$	$\mathrm{z_{start}}$	dn/dt ($\mathrm{Mpc^{-3}yr^{-1}}$)	$\frac{dN}{dzd\theta^2}$ arcmin^{-2}
A.I	$(1-2)\times 10^8$	10	13	5×10^{-9}	235
B.I	$(1-2)\times 10^8$	12	16	7×10^{-10}	16
C.I	$(1-2)\times 10^8$	15	22	1×10^{-10}	0.77
A.I	$(1-2)\times 10^7$	10	10.7	5×10^{-8}	4435
B.I	$(1-2)\times 10^7$	12	12.8	6×10^{-8}	2965
C.I	$(1-2)\times 10^7$	15	16	2×10^{-8}	466

Table 5.1: DM halo formation rates: dn/dt expressed in $\mathrm{Mpc^{-3}yr^{-1}}$, and $\frac{dN}{dzd\theta^2}$ as number formed per unit redshift and arcmin^2 for cases considered in the text. Values for the first three rows AI-CI are for a $10^7 M_\odot$ SMDS forming in a (1-2) $\times 10^8 M_\odot$ DM halo; values for the last three rows, separated by the first three with a horizontal line, are for the $10^6 M_\odot$ SMDS forming in a (1-2) $\times 10^7 M_\odot$ DM halo. We have assumed that the DS started accreting baryons with a constant rate of $10^{-1} M_\odot$/yr at $\mathrm{z_{start}}$ and reached its SMDS mass by $\mathrm{z_{form}}$.

5.3 Dark Stars in Hubble Space Telescope

5.3.1 Comparison of DS stellar output with HST Sensitivity

In this section we examine the observability of dark stars in Hubble Space Telescope (HST) surveys. It is interesting to speculate that HST could already have seen the brightest of these objects, if they survive to redshift z=10. Recent results by *Bouwens et al.* (2011) find a candidate $z \sim 10$ object in the HUDF as a J-band dropout using the two full years HUDF09 WFC3/IR data. Currently it is thought to be a galaxy, the most distant one observed to date. This object could instead be a SMDS, but the resolution is not good enough to tell the difference; nor are spectra available. Even though it may be hard to identify a DS uniquely in HST, the fact that at most one candidate has been found can be used to place bounds on the numbers of dark stars at redshifts up to z=10. In this section we examine the observability of DS of various masses in HST data, and in a later section examine the resulting bounds.

Figures 5.4-5.6 illustrate the stellar output of Dark Stars and compare it to the sensitivity of various HST surveys. The horizontal lines indicate HST sensitivity in the two HST filters NICMOS F110 (J-band) and F160 (H-band) for 10^4 seconds of data for various deep field surveys compiled in *Bouwens et al.* (2008): HUDF-NICPAR, HUDF Thompson, HUDF Stiavelli, HDF-N Thompson, HDF-N Dickinson and GOODS Parallels. We also plot J_{110} (blue) and H_{160} (red) apparent magnitudes M_{AB} for Dark Stars of various masses as a function of redshift. These lines are generated using simulated atmospheres spectra from TLUSTY. We define a J-band dropout to be any observation to the right of the green vertical line; the criterion used here is that a difference in apparent magnitudes of 1.3 or larger between the values in the two filters leads to a dropout. Such an observation would allow a rough determination of the DS redshift.

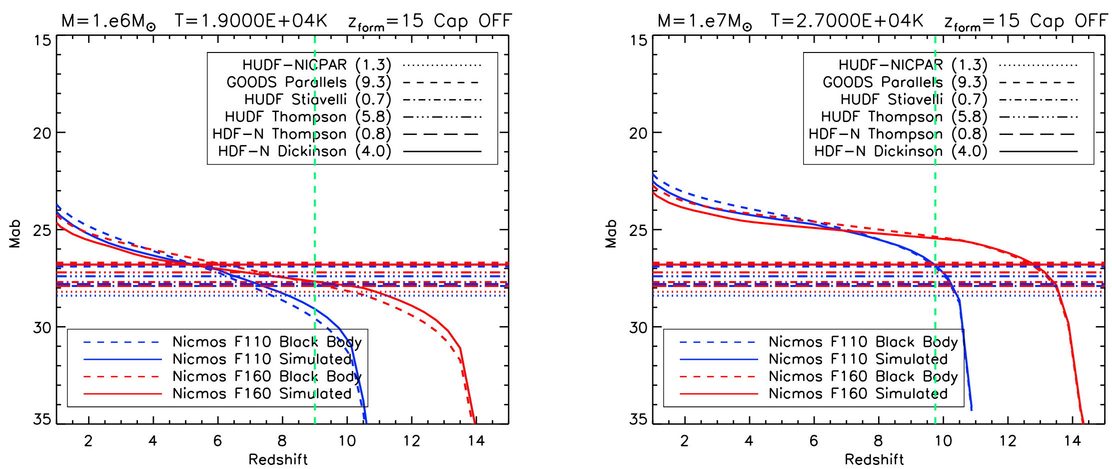

Figure 5.4: Left (right) panels: Apparent magnitudes for the $10^6 M_\odot$ ($10^7 M_\odot$) dark star formed via extended adiabatic contraction in a $10^7 M_\odot$ ($10^8 M_\odot$) minihalo at redshift of 15. We have also plotted all the sensitivity limits of the various deep field surveys compiled in *Bouwens et al.* (2008), and indicate in parentheses the areas of the surveys in arcmin^2. The vertical dashed line is placed at a redshift where the J band dropout criterion is satisfied.

In Figures 5.4 and 5.5, the Dark Stars are considered to be formed via the extended adiabatic contraction mechanism, without any captured DM. In Figure 5.4 we plot the apparent magnitudes in the two bands for $10^6 M_\odot$ (left panel) and $10^7 M_\odot$ (right panel) dark stars formed at z=15 and surviving to various redshifts as shown. The surface temperatures are 1.9×10^4K and 2.7×10^4K for the $10^6 M_\odot$ and $10^7 M_\odot$ DS respectively. The vertical dashed line is placed at a redshift where the J band dropout criterion is satisfied. Also shown are the sensitivity limits for various deep field surveys complied in *Bouwens et al.* (2008). The most sensitive of the surveys, HUDF-NICPAR, is further shown in Figure 5.5: we plot J_{110} (blue) and H_{160} (red) apparent magnitudes M_{AB} for Dark Stars of mass ranging between $\sim 10^4 M_\odot - 10^7 M_\odot$ as a function of redshift. The dark stars can be seen in the F110 (F160) passbands out to redshifts of 9 (11.5). One can see that an observation of a Dark Star as a J-band dropout in this survey would correspond to a redshift roughly $9.5 < z < 10.5$. Of course with HST data alone it remains impossible to distinguish a Dark Star from a galaxy.

Similarly, Figures 5.7 and 5.6 illustrate the observability of million solar mass dark stars which grew via captured DM (rather than via extended AC). Comparing Figure 5.7 and Figure 5.5 one can see that, for a given stellar mass, the dark stars fueled by captured DM are less detectable, an effect also observed in *Freese et al.* (2010a). The main reason is due to the fact that the DSs formed via extended capture are hotter than their extended AC counterparts for a given mass. Therefore the peak in the spectrum moves to lower wavelengths, out of the passbands we consider here. Here only the $10^7 M_\odot$ star satisfies the J band dropout criterion in the $9.5 - 10.5$ redshift range. The lower mass $10^6 M_\odot$ case is visible only in the J_{110} up to redshifts of 6 and would already have been detected as an i_{775} dropout in HUDF which has a 29.9 m_{ab} detection limit for 10σ detection in the i_{775} passband (*Bouwens et al.*, 2006). As none of the i dropouts found in HUDF has been yet identified as a plausible candidate at $z \sim 6$ for a supermassive dark star, one could infer that the probability of those objects surviving to such low redshifts is very low.

For each of the surveys in Figs. 5.4 and 5.6, we have also indicated (in parentheses in the plots) the area (in arcmin^2) observed by the survey. For DS of a given mass, we can add up the areas of all those surveys which are capable of observing DS as J-band dropouts to obtain a total effective area of observability for that DS mass. In other words, we add the area of all surveys in which the fluxes in the H_{160} are still above the sensitivity limits while the fluxes in the J_{110} are a least 1.3 lower in apparent magnitude. From Figure 5.4 we estimate $\theta^2 = 1.3$ arcmin^2 as the effective area of the surveys in which a $10^6 M_\odot$ SMDS formed via extended AC could have been observed as a Jband dropout with HST. For the $10^7 M_\odot$ stars formed via extended AC, this area is increased to 21.9 arcmin^2 .

For the hotter DS fueled by captured DM, we can see from Figure 5.6 that the total area of the surveys in which $10^7 M_\odot$ DS could have been detected is 8.6 arcmin^2 (smaller than for the extended AC DS of the same mass). Now at redshifts higher than ~ 10 where the Jband dropout criterion starts to be satisfied the apparent magnitude for the H_{160} passband drops below or is right around the value of the sensitivity limits for the HDF-N Dickinson and GOODS Parallels surveys. The $10^6 M_\odot$ DS fueled by captured DM are too dim to be observed.

5.3.2 Using HST data to constrain the Numbers of Dark Stars

We will use HST data to constrain the fraction $\mathrm{f_{SMDS}}(\mathrm{z_{start}})$ of early haloes at $\mathrm{z_{start}} \sim 13$ for $(1-2)\times 10^8 M_\odot$ DM Haloes and $\mathrm{z_{start}} \sim 11$ for the $(1-2)\times 10^7 M_\odot$ DM haloes hosting dark stars; as can be seen from Table 5.1 this corresponds to a $\mathrm{z_{form}} \sim 10$ in both cases, i.e. at a redshift of 10 the dark stars become supermassive. This is the redshift of DS observability in HST as J-band dropouts. *Bouwens et al.* (2008) analyzed near-IR data over both the HUDF and the two GOODS fields to search for star-forming galaxies at $\gtrsim 7$ and reported null results. More recently, as mentioned previously, *Bouwens et al.* (2011) found a candidate $z \sim 10$ object in the HUDF as a J-band dropout using the two full years HUDF09 WFC3/IR data. Thus, following *Zackrisson et al.* (2010a, 2011), we can use the fact that at most one observable DS at this redshift can exist to obtain bounds on $\mathrm{f_{SMDS}}(\mathrm{z_{start}})$:

$$N = \frac{dN}{dzd\theta^2} f_{SMDS}(z = z_{start})\theta^2 f_{surv} f_{\Delta t} \leq 1 \tag{5.3}$$

Eq. (5.3) states that the number of observations in the patch of sky surveyed should be less or equal to unity. Here $\frac{dN}{dzd\theta^2}$ is the number of halos forming per unit redshift and arcmin^2 in which a given mass DS is hosted. We have multiplied by unit redshift interval $\Delta z = 1$, θ^2 is the total area surveyed in which the SMDS could have been detected, $\mathrm{f_{surv}}$ is the fraction of DS that survives from the redshift where the DS starts forming, $\mathrm{z_{start}}$, until it could be observed as a dropout (at $z \sim 10$ in HST) and $\mathrm{f_{\Delta t}}$ is the fraction of the observational window of time Δt during which the DS is still alive. Here, Δt is the cosmic time elapsed between the minimum and maximum redshift where the DS could be observed as a dropout. For the case of HST, $\Delta t = 6.5 \times 10^7$yr (the time between the minimum redshift of 9.5 and maximum redshift of 10.5 where the DS could be observed as a J-band dropout).

We comment here on the three redshifts of formation we have previously defined. For a conversion between $\mathrm{z_{form}}$ (redshift where the DS reaches its final mass) and $\mathrm{z_{start}}$ (the redshift where the DS starts accreting baryons) see Table 5.1. The reason we cho0se to label the three different cases with the redshift where the DS becomes supermassive ($\mathrm{z_{form}}$) rather than the redshift of minihalo formation ($\mathrm{z_{start}}$) where the DS starts forming is that the DS are observable only once they become very massive.

- Case A: $\mathrm{z_{form}} = 10$. Here it is the DS becoming supermassive $z = 10$ that are observable (we are assuming in this case that those forming at higher redshift don't live long enough to be seen at $z \sim 10$). We can only constrain the product $f_{SMDS} \times f_{surv} \times f_{\Delta t}$. The fraction of the observational window during which the DS is alive and can be observed, is $f_{\Delta t} = \min(\tau - \tau_{min}, \Delta t)/\Delta t$, where τ_{min} is the minimum DS lifetime that allows the DS to survive to $z = 10.5$ where it can be observed as a J-band dropout in HST. In the case of a $10^7 M_\odot$ SMDS $\tau_{min} \sim 1.15 \times 10^8$yrs (time elapsed between $z = 13$ and $z = 10.5$) whereas for the $10^6 M_\odot$ SMDS $\tau_{min} \sim 3.6 \times 10^7$yrs (cosmic time elapsed between $z = 10.7$ and $z = 10.5$). We note that the limits we place on $\mathrm{f_{SMDS}(z_{start})}$ are only valid at $\mathrm{z_{start}} \sim 13$ (for the $10^7 M_\odot$ SMDS) and $\mathrm{z_{start}} \sim 11$ (for the $10^6 M_\odot$ SMDS) as can be seen from Table 5.1.

- Case B: $\mathrm{z_{form}} = 12$. Here we consider the DS to become supermassive at $\mathrm{z_{form}} \sim 12$ and not at later redshifts. We will assume that the DS could survive until $z \sim$

10 ($f_{surv} = 1$) in order to constrain $f_{SMDS}(z_{start})$ using null detection from HST J_{110} dropouts. From Table 5.1 we see that the $\mathrm{z_{start}}$ value for the $10^7 M_\odot$ SMDS in this case is ~ 16 and for the $10^6 M_\odot$ SMDS it is ~ 13. In the case of a $10^7 M_\odot$ SMDS $\tau_{min} \sim 2.0 \times 10^8$yrs whereas for the $10^6 M_\odot$ SMDS $\tau_{min} \sim 1.1 \times 10^8$yrs.

- Case C: $\mathrm{z_{form}} = 15$. Here we assume the dark stars become supermassive by $\mathrm{z_{form}} \sim 15$. The values for $\mathrm{z_{start}}$ can be read off from Table 5.1 again. For the $10^7 M_\odot$ SMDS $\mathrm{z_{start}} \sim 22$ and for the $10^6 M_\odot$ SMDS $\mathrm{z_{start}} \sim 16$. This case is treated in a similar fashion as case B. For the $10^7 M_\odot$ SMDS, $\tau_{min} = 2.9 \times 10^8$yrs (the time elapsed between redshifts 22 and 10.5) whereas for the $10^6 M_\odot$ SMDS $\tau_{min} = 2.0 \times 10^8$yrs (the time elapsed between redshifts 16 and 10.5).

In all three cases, regardless of when the SMDS form, they are potentially observable as J-band dropouts in HST at z=10. From Eqn. (5.3), we obtain the following bounds:

For $10^7 M_\odot$ DS in $1 - 2 \times 10^8$ haloes,

$$\mathrm{Case\,A}, M_{DS} = 10^7 M_\odot: \quad \log\left(f_{smds}(z_{start} = 13) \times f_{surv} \times f_{\Delta t}\right) \leq \begin{cases} -3.7 & \text{(extended AC only)} \\ -3.3 & \text{(with capture)} \end{cases} \tag{5.4}$$

As previously defined, $\mathrm{f_{\Delta t}} = \min(\Delta\tau, \Delta t)/\Delta t$, where $\Delta\tau$ is how much of the its lifetime the DS has spent while being in the redshift window that allows observability as a dropout ($z = [9.5, 10.5]$ for J band dropouts) and Δt is the cosmic time elapsed during this redshift window, i.e. 6.5×10^7yrs. As a reminder, DS with extended AC only are cooler than those with captured DM, so that the former are easier to observe and the bounds are tighter. In the above inequalities, for Case A.1, following the table, we have taken the number of DS per unit redshift interval per arcmin^2 to be $dN/dzd\theta^2 = 235$.

To convert the above inequality into bounds on $\mathrm{f_{SMDS}}$ at $\mathrm{z_{start}} \sim 13$ one needs to make some assumptions regarding the fraction of DS surviving (f_{surv}) from the redshift where they start forming (13 in this case) until the maximum redshift where they could be observed as dropouts (10.5 in the case of Jband dropouts). The time elapsed between these two redshifts is 1.14×10^8yrs. If we consider both f_{surv} and $f_{\Delta t}$ to be equal to unity, the maximum value they can attain, we obtain the strongest bounds; however, more realistically these numbers are likely to be smaller than unity corresponding to weaker bounds on $\mathrm{f_{SMDS}}$.

In case B we get:

$$\mathrm{Case\,B}, M_{DS} = 10^7 M_\odot : \quad \log\left(f_{smds}(z_{start} = 16) \times f_{surv} \times f_{\Delta t}\right) \leq \begin{cases} -2.55 & \text{(extended AC only)} \\ -2.15 & \text{(with capture)} \end{cases} \tag{5.5}$$

In the above inequalities, for Case B.1, following Table 5.1, we have taken the number of DS per unit redshift interval per arcmin^2 to be $dN/dzd\theta^2 = 16$.

For scenario C, using a formation rate of 0.77 minihaloes forming per unit redshift and arcmin^2 at $\mathrm{z_{start}} = 22$ one gets:

$$\mathrm{Case\,C}, M_{DS} = 10^7 M_\odot : \quad \log\left(f_{smds}(z_{start} = 22) \times f_{surv} \times f_{\Delta t}\right) \leq \begin{cases} -1.2 & \text{(extended AC only)} \\ -0.8 & \text{(with capture)} \end{cases} \tag{5.6}$$

The tightest bounds on $\mathrm{f_{SMDS}}$ result if all the stars survive at least 3.5×10^8 years, from the start of their formation at $\mathrm{z_{start}} \sim 22$ all the way down to $z = 9.5$ (throughout the window of observability), so that $f_{surv} = f_{\Delta t} = 1$.

For the case of the $10^6 M_\odot$ SMDS forming in a $1 - 2 \times 10^7$ minihalo, only the DS formed via extended AC can be seen in HST; those forming via capture DM are too dim. For extended AC we get the following limits:

$$\log f_{smds}(M_{halo} = 1{-}2{\times}10^7 M_\odot) \leq \begin{cases} -3.7 - \log(f_{surv} \times f_{\Delta t}) & \text{for case A.1 } (z_{form} = 10) \\ -3.6 - \log(f_{surv} \times f_{\Delta t}) & \text{for case B.1 } (z_{form} = 12) \\ -2.8 - \log(f_{surv} \times f_{\Delta t}) & \text{for case C.1 } (z_{form} = 15) \end{cases} \tag{5.7}$$

For the corresponding values of $\mathrm{z_{start}}$ see the last three rows of Table 5.1. If the DS lives throughout the window of observability, then the tightest bounds result as this implies $\mathrm{f_{surv}}$ $=\mathrm{f_{\Delta t}}$ =1, the maximum value they could attain. A summary of our bounds can be found in Figure5.8 where we plot the exclusion limits for $\mathrm{f_{SMDS}}$. The bounds in Case A are ~ 10 (~ 300) times stronger than the bounds in Case C for the $10^6 M_\odot$ ($10^7 M_\odot$) SMDS. The reason for the very large discrepancy in the bounds in cases A and C for the $10^7 M_\odot$ DS is due to the fast decrease of the formation rate of $1-2{\times}10^8 M_\odot$ DM haloes at redshifts higher than $z \sim 15$ as can be seen from Figure 5.2.

All the bounds in this section were obtained for our Case I, where the host halo mass lies within a factor of two in value. If we were to consider case II, where the uncertainty in the mass of the host halo is taken into account (it lies within a factor of five in value), the limits on f_{SMDS} would only be slightly more stringent. One can see that the numbers of host haloes does not change by much between Cases I and II by comparing the values of the formation rates of the minihaloes in Figure 5.2 and Figure 5.3. Hence the numbers of DS and the bounds on them are roughly the same.

5.4 Dark Stars in JWST

Supermassive Dark Stars can be detected by the upcoming James Webb Space Telescope (JWST). In Figure 5.9 we show the spectra of 10^6 and $10^7 M_\odot$ DS (obtained from TLUSTY as discussed in Section 1) emitted at $z = 15, 10$ and 5 and redshifted to today, and compare to the various bands detectable by JWST. The number before the letter W in the name of each filter corresponds to the wavelength in the center of the passband in $100\ \mu\mathrm{m}$ units. Since the DS are detectable in multiple bands in JWST, the observed spectra can be used to differentiate them from other objects at similar redshifts.

Figures 5.9 and 5.10 illustrate the stellar output of SMDSs of various masses and formation redshifts, and compare to the sensitivity of JWST. As can be seen from those two figures for the filters with wavelengths shorter than $2\ \mu\mathrm{m}$, for which the Ly-α absorption becomes a factor at redshifts lower than 15, its very difficult to say if the DS could be detectable or not just by comparing the fluxes to the sensitivity limits. The Ly-α line is in some of those cases in the middle of the passband. To make a better prediction regarding the observability of the dark stars we will again use the apparent magnitude method, as this is a measure of the integrated flux over the entire width of the filter.

Apparent magnitudes for various SMDS through the NIR camera wide passband filters are shown for comparison. In Figure 5.11 the DS are formed via the extended adiabatic contraction (AC) mechanism; while in Figure 5.12 the SMDS are fueled by captured DM. We show the sensitivity of a variety of wide passband filters on the NIR camera on JWST: The two horizontal lines correspond to sensitivity limits for each filter for 10^4s exposure time (the dotted line) and $10^6 s$ exposure time (the dash-dotted line).

Ly$-\alpha$ absorption at the Gunn-Peterson trough cuts off the photons with wavelengths lower than 1216Å(in the rest frame) as can be seen in the first two panels of Figs. 5.11 and 5.12; we treat the absorption as being complete and not allowing any photons at all to come through. Thus the SMDSs drops below the JWST sensitivity limit at $z \sim 6$ for the F070W filter and at $z \sim 10$ for the F115W case.

The most massive dark stars are the brightest. From Figures 5.11 and 5.12 one can see that $10^7 M_\odot$ dark stars, both with and without capture, are individually observable in 10^4 seconds of data even at redshifts as high as 15 in filters with a passband centered at $2\ \mu\mathrm{m}$ and higher (F200W-F444W filters). For the case of a $10^6 M_\odot$ SMDS, a longer exposure time of 10^6s allows the dark star, both with and without capture, to be individually observable in all filters from F200W to F444W even at $z \sim 15$. For $10^5 M_\odot$ SMDS, those formed via extended AC are visible in these filters out to $z \sim 15$ with 10^6 sec exposure time while those formed with capture are too dim. Lighter ones can be seen only if they still exist at lower redhshifts, e.g. z=5, but those would already have been found in HST and other telescopes; hence any such SMDS apparently did not survive to such low redshifts.

We plot in Figure5.12 the apparent magnitudes for the same mass dark stars but now formed using the extended DM capture mechanism. As noted before, the DS in this case have lower fluxes if compared with the same mass DS formed via the extended AC mechanism. Still the $10^7 M_\odot$ star (with capture) is bright enough to be detectable to redshifts as high as 15 in the F200W-F444W filters with 10^4s exposure. The $10^6 M_\odot$ star (with capture) has a magnitude above the sensitivity limit in the higher than $2\ \mu\mathrm{m}$ passbands if the exposure time is 10^6s (the dotted horizontal line in Figure5.12).

5.4.1 Detection at $z \sim 10$ as a J_{115} band dropout

As expected, the dark stars that could have been detected as J-band dropouts in HST are also detectable using the same technique in JWST. Figure 5.13 shows the sensitivity of JWST in 10^4 seconds of data in the 115μ (J-band) and 150μ (H-band) filters for NIRCam. The apparent magnitudes for 10^6 and $10^7 M_\odot$ SMDS with and without capture are also shown for comparison. Here, the SMDS form at z=15 and are assumed to survive to various redshifts as shown. Comparing Figures 3 and 6, one can see that JWST is half a magnitude more sensitive than HST to finding SMDS as J-band dropouts. The $10^6 M_\odot$ Dark Star formed via captured DM (lower left plot) in Figure 5.13 will be individually observable in both bands if it survives to redshifts as low as 8, but does not appear as a dropout. However increasing the exposure time to 10^6s (which would correspond to the same exposure time as the 2004 HUDF survey) would reveal even the $10^6 M_\odot$ SMDS formed "with capture" as a J_{115} dropout. Increasing 100 times the exposure time corresponds to increased sensitivity limits in m_{ab} by 2.5 magnitudes. All the other three cases ($10^7 M_\odot$ with or without capture;

$10^6 M_\odot$ without capture) could be detectable in a JWST survey as Jband dropouts in the redshift range $9.5 - 11.5$ even with the lower 10^4 s exposure times.

In order to predict how many would be visible in a JWST deep field survey we have to assume something about the total field of view (FOV) of all future JWST surveys in which the stars would be observable. The instantaneous FOV for the instrument is $2.2' \times 4.4' = 9.68$ arcmin^2 . To be conservative we will take a fiducial value of the area of a typical JWST survey to be 5.8 arcmin^2 , the same area as that of the HUDF Thompson survey. This value is likely to be an underestimate. For comparison, for HST for the $10^7 M_\odot$ cases without and with capture, we used 21.9 arcmin^2 and 8.6 arcmin^2 respectively, and for the $10^6 M_\odot$ case without capture we used 1.3 arcmin^2 . Thus we are taking the JWST survey area to exceed that of HST only in the latter case of $10^6 M_\odot$ case without capture. We find that the number of expected SMDS in JWST as J-band dropouts is $N \lesssim 1$ and therefore conclude that SMDS are hard to detect in JWST as J-band dropouts. This is expected since HST was already sensitive enough to observe them as J-band dropouts, assuming enough would have survived from their formation redshift until $z \sim 10$. The only improvement in this case could be made by a larger FOV compared to the one in HST. Actually with our assumption regarding the value for the FOV we predict even less chances of detection for the $10^7 M_\odot$ DS at $z \sim 10$. However, the situation is reversed for the $10^6 M_\odot$ dark stars, as the total FOV of the HST surveys sensitive enough to detect them was smaller than even our conservative estimate for the FOV of a typical JWST deep field survey.

5.4.2 Detection at $z \sim 12$ as a H_{150} band dropout

Whereas JWST is not particularly better than HST at finding J-band dropouts, it will be significantly better at finding SMDS as H-band and K-band dropouts.

From Figure 5.2 the formation rate of the host minihaloes has a maximum at redshifts around 12. We will investigate the detectability of SMDS existing at $z \sim 12$. Therefore we will use an additional band, the K_{200} , and compare the magnitudes through this filter, which are essentially unaffected by the Lyman Alpha absorption until $z \sim 15$, to those for the H_{150} , for which the IGM absorption will cut off most of the flux at $z \gtrsim 11.5$. (see Figure5.14)

First we will consider the case of SMDS forming at $\mathrm{z_{form}}$ =12, the same as the time of observation (the equivalent of Scenario A above in HST). Figure 5.14 shows that the three cases of $10^7 M_\odot$ SDMSs with and without capture as well as $10^6 M_\odot$ SMDSs without capture are all detectable in a JWST survey as H_{150} dropouts in the redshift range $11.5 - 12.5$. The $10^6 M_\odot$ Dark Star formed via captured DM (lower left plot) will be individually observable only in the F150W band if it survives to redshifts as low as 7, but does not appear as a dropout. For the $10^7 M_\odot$ DS, assuming a formation redshift of $\mathrm{z_{form}} \sim 12$ and using a formation rate of 7×10^{-10} Mpc^{-3}yr^{-1} we found $dN/dzd\theta^2 \sim 16$ (the number of minihalos formed per unit redshift and arcmin^2) at $\mathrm{z_{start}} \sim 16$ (see table 5.1). The number of H_{150} dropout events (see Eq. (5.3); n.b. $\Delta z = 1$) are $N_{obs} = f_{smds}(dN/dzd\theta^2)\theta^2 f_{\Delta t}$.

Now the question is whether or not we should apply the bounds from HST on the numbers of SMDS at z=10 to those at z=12. If we assume that all the SMDS at z=12 have the same properties as those at z=10, then the HST bounds are so stringent that JWST will not be able to see many of them. In particular, one finds $N_{obs} = 0.2$ for $10^7 M_\odot$ DS formed via extended AC and 0.6 for the $10^7 M_\odot$ DS with DM capture. Therefore the null results from HST Jband dropouts seem to be enough to predict relatively low chances of detectability within JWST at $z \sim 12$.

However, it is very likely that there are more SDMS at z=12 than at z=10, and their lifetime is likely to be longer. First, the host halo formation peaks at z=12. Second, after the first SDMS die (before z=10), they turn into fusion powered stars that produce ionizing photons; such photons, which disrupt the formation and evolution of later DS, become more and more abundant as redshift decreases. Moreover at lower redshifts ($z \sim 10$) the DM halos that could host those SMDSs are much more likely to merge to form even larger halos. This process could in turn shorten the lifetime of the DS at $z \sim 10$ considerably compared to the lifetime at z=12.

We will recalculate the number of events under the following assumptions: i) the DS formed at $z_{\rm form} \sim 12$ survives from $z = 12.5$ to $z = 11.5$, i.e. $f_{\Delta t}$ =1 in this case. ii) At $z_{\rm form} \sim 10$ we will assume it survives 10^6yrs out of the 3.5×10^7yrs between $z = 10.5-9.5$, i.e. an $f_{\Delta t}$ of 1.5×10^{-2} in this case. Under those conditions one gets ~ 17 F150W dropouts in the JWST field of view for the $10^7 M_\odot$ DS in the extended AC case and ~ 44 events for the $10^7 M_\odot$ DS powered by captured DM. Those values are computed with a conservative area of the FOV of 5.8arcmin^2 . Corresponding to $z_{\rm form} \sim 12$ there are roughly 2965 $1-2\times10^7 M_\odot$ minihalos forming at $z_{\rm start}$ =12.8 per unit redshift and arcmin^2 that could host a $10^6 M_\odot$ DS. Even assuming the same lifetime for the DS at $z \sim 10$ and $z \sim 12$ we predict about 4 H_{150} dropout events in the JWST FOV for this star. If instead we use the assumptions i) and ii) above this number increases to ~ 290! Therefore JWST has a very good chance of detecting the lower mass $10^6 M_\odot$ dark stars and a reasonable chance of detecting the $10^7 M_\odot$ SMDS as H_{150} band dropouts at $z \sim 12$. If one assumes that the DS survives longer at $z \sim 10$ the numbers we get for the predicted H_{150} dropout events woulds scale linearly, and in any case will range between the values quoted here.

If, on the other hand, these SMDS do not survive to z=10 where HST could have observed them, and HST places no bounds whatsoever, then JWST should see 93 H_{150} dropout events due to the $10^7 M_\odot$ SMDS formed at $z_{\rm form}$ =12 and 17197 events due to the $10^6 M_\odot$ dark stars formed at the same redshift. Of course, those are just naive upper bounds obtained under the assumption that $f_{\rm SMDS}$ =1, which is likely to be an overestimate.

5.4.3 Detection at $z \sim 15$ as a K_{200} dropout

DS at $z \sim 15$ can be detected as K_{200} band dropouts using the F200 and F277 NirCam filters in JWST, as shown in Figure 5.15 for 10^6 and $10^7 M_\odot$ SMDS formed via extended AC (no capture) at $z_{form} = 20$. For the K_{200} band the IGM absorption starts to cut off the fluxes at $z \sim 14$, whereas the SMDS stellar output is still well above the sensitivity for the

F277 filter.

The $10^6 M_\odot$ DS could be observed in the redshift range $z \sim 14.5-15.5$ as a K_{200} dropout. If we now assume that these DS survive to z=10 and use the bounds from HST on $\mathrm{f_{SMDS}}$ derived in case C (valid for $\mathrm{z_{form}} \sim 15$ and $z_{obs} = 10$), and further assuming the DS exists throughout the window from $z = 15.5 - 14.5$ (i.e $\mathrm{f_{\Delta t}} = 1$), we expect about ~ 4 F200W dropout events for the $10^6 M_\odot$ DS in JWST. Again this is derived under the unrealistic assumption that $\mathrm{f_{\Delta t}}$ =1 both at z=10, where HST could observe them and at z=15. If on the other hand we assume $\mathrm{f_{\Delta t}}$ 10^-1 at the lower redshift and $\mathrm{f_{\Delta t}}$ =1 at $\mathrm{z_{form}}$ then we get a number of events 10 times higher, i.e. 40 K_{200} dropouts in a typical JWST deep field survey due to $10^6 M_\odot$ SMDS.

If, on the other hand, these SMDS do not survive to z=10 where HST could have observed them, and HST places no bounds whatsoever, then JWST should see at most 2700 of them in a survey with a FOV of 5.8arcmin^2 . Again, this is an overestimate based on the assumption that both $\mathrm{f_{\Delta t}}$ and $\mathrm{f_{SMDS}}$ are equal to unity.

In the case of the $10^7 M_\odot$ star, it would appear as a K_{200} dropout in the $15.5 - 16.5$ redshift range. However due to the sharp drop in the formation rate of DM halos in the $1 - 2{\times}10^8 M_\odot$ at such high redshift the number of dropout events we predict in this case is less than one (of order unity). Therefore the probability of detecting $10^7 M_\odot$ SMDS in JWST at $z \sim 15$ is relatively low.

5.5 SMDS vs PopIII galaxies in JWST

The first galaxies are believed to form at z$\lesssim$ 15 within DM halos of $10^{7-8} M_\odot$ and contain population III stars (*Scannapieco et al.*, 2003; *Tornatore et al.*, 2007; *Johnson et al.*, 2008; *Stiavelli and Trenti*, 2010). The high surface temperatures of massive PopIII stars leads to their contribution to the photoionization of the interstellar medium, and could play an important role in the cosmic reionization at z $\gtrsim 6$. Galaxies containing mostly PopIII stars will have very strong spectral signatures. For instance they could be identified based on the strength of the Lyα line or the HeII $\lambda 1640$ and $\lambda 4686$ lines. (see *Schaerer*, 2002, 2003; *Stiavelli and Trenti*, 2010, and references therein). *Zackrisson et al.* (2011) presents a comprehensive study of the integrated spectra signatures of PopIII stars in the wide filters of JWST. Their main findings are that PopIII galaxies cold be detectable to redshifts as high as 20, if the stellar population mass is $\sim 10^7 M_\odot$, or in the case of $10^5 M_\odot$ stellar population mass up to redshifts of 10. Moreover, the authors propose a selection criterion using two of the MIRI filters of JWST that would clearly differentiate between PopIII galaxies and PopII or PopI galaxies at z$\sim 7-8$.

Using the Yggdrasil model grids (*Zackrisson et al.*, 2011) found at http://ttt.astro.su.se/ ez/ we will study the signatures in the NIRCam passbands of PopIII galaxies at z$\sim 10-15$ and compare them to those of SMDS. All the nomenclature we will be using for PopIII galaxies is identical to the one in *Zackrisson et al.* (2011). As such, we will consider three different Initial Mass Function (IMF) for PopIII galaxies:

- PopIII.1: A zero-metallicity population with an extremely top heavy IMF and a Single Stellar Population (SSP) from *Schaerer* (2002). The population has stellar masses in the range $50-500 M_\odot$ with a Salpeter slope.

- PopIII.2: A zero-metallicity population with a moderately top-heavy IMF. The characteristic mass is 10 $M_\odot$ and the wings of the mass function extend from 1 to $500 M_\odot$. A SSP from *Raiter et al.* (2010) is used.

- PopIII, Kroupa IMF: In view of recent simulations (e.g. *Greif et al.*, 2010) the mass of PopIII stars might be lower than previously predicted. Therefore in this case a normal Kroupa IMF with stellar masses ranging in the $0.1-100 M_\odot$ is used and the SSP is a rescaled version of the one used in *Schaerer* (2002)

As shown in *Zackrisson et al.* (2011) the nebular emission dominates the spectrum of PopIII galaxies even at z$\sim 10-15$ if they are not extremely old. For instance at z=10 for PopIII galaxies there is equal contribution of nebular to stellar light only if the age of the galaxy is $\gtrsim 10^7$ yrs. For PopIII galaxies younger than this nebular emission dominates. We will consider two cases for the gas covering factor, keeping the same nomenclature as in *Zackrisson et al.* (2011):

- Type A galaxies: $f_{cov} = 1$, implying maximal nebular contribution to the SED and no escape of Lyman continuum photons.

- Type C galaxies: $f_{cov} = 0$, where there is no nebular contribution to the SEDs. We will not consider here the intermediate case of Type B galaxies.

In Fig. 5.16 we plot the apparent magnitudes of SMDS and PopIII galaxies at z=12 as a function of the center wavelength of the NIRCam and MIRI filters of JWST. The horizontal segments along the solid black line represent the individual filters of JWST. For NIRCam we did not plot the F090W filter, since the throughput profile was not available at the time when this research was conducted. Therefore in the NIRCam region we have, in order, the following filters:F070W, F115W, F150W, F200W, F277W, F356W and F444W. As can be seen from the left panel, given the mass of the DS is equal to the stellar population mass in a PopIII galaxy, a SMDS formed via extended AC will be more detectable than even the brightest PopIII galaxies. From the right panel we note that only the $10^7 M_\odot$ SMDS formed via extended AC mechanism will be detectable in the lowest two center wavelength of the MIRI filters (F560W and F770W). The PopIII.1 galaxies with stellar population mass of $10^6 M_\odot$ could be detected as a H_{150} dropout in a deep field survey with an exposure of 100 hours. In the case of PopIII.2 they are still above the sensitivity limits in the required filters for a H_{150} dropout study, but only barely. However the PopIII galaxies with a Kroupa IMF are not detectable as a H_{150} dropout, assuming the stellar population mass is $10^6 M_\odot$.

We will consider that the spectrum of a SMDS is essentially unaltered by nebular emission. They are much cooler than PopIII stars, therefore the nebula surrounding the DS is not ionized. Also, since most of the baryons are already accreted into the central SMDS, the density of the nebular gas is very small. This, in turn leads again to very small nebular emission. It can be seen from Fig. 5.16 that at z=12 for the $10^6 M_\odot$ SMDS formed by extended AC will be detectable only in the F150W, F200W, F277W, F356W and F444W filters for 100 h exposures. This is equivalent to JWST being sensitive to a restframe wavelength band ranging from: $0.107\ \mu\mathrm{m}$ to $0.365\ \mu\mathrm{m}$. For higher redshifts this range is even smaller. In that interval there are two major signatures in the spectra for galaxies with significant nebular emission: I) the HeII line at $0.1640\ \mu\mathrm{m}$ and II) the continuum limit Balmer series, which corresponds to a rest frame wavelength of $0.3646\ \mu\mathrm{m}$.

For $10^7 M_\odot$ SMDS one could use the MIRI F560W filter in conjunction to the NIRCam F444W filter and exploit the distinct signature of the full Balmer emission lines.

As the most favorable redshift to look for SMDS is ~ 12 we will focus on the different signatures in the broadband filters of JWST of DS and PopIII galaxies at z~ 12 in what fallows. In Fig. 5.17 we plot the differences in magnitudes for SMDS and PopIII instantaneous burst galaxies in successive NIRCam filters at z=12. At that redshift due to the Gun-Peterson trough the flux in F150W and lower center wavelength filters is significantly reduced. Actually from Fig. 5.16 we can see that all PopIII instantaneous burst galaxies with stellar population mass of $10^6 M_\odot$ are too dim to be detected in F150W if the exposure time is 100 h. Therefore we cannot use that filter (F150W) to exploit the HeII line at $0.1640\ \mu\mathrm{m}$ that could render the the PopIII type A galaxies bluer in the $m_{150} - m_{200}$. However this could be used at z~ 11 since at that redshift the flux in the F150W filter is much less affected by the Gun-Peterson trough and the HeII1640 line will still be within the F200W filter.

In Fig. 5.17 we will focus on differences in colors that are much less sensitive to minor changes in redshifts. The star symbols correspond to magnitudes for SMDS. We note that, due to the similar temperatures, SMDS formed "with capture" of either $10^6 M_\odot$ or $10^7 M_\odot$ occupy the same spot on the diagrams. PopIIIA galaxies with lifetimes less than 10 Myr will exhibit redder colors in the $m_{356} - m_{444}$ as can be seen from the lower left panel. This is due to the increased fluxes in the F444W filter due to the Balmer emission lines.

The SMDS spectra within those wavelengths is essentially an UV continuum. The higher temperature case of SMDS formed "with capture"(T$_{eff} \sim 5 \times 10^4 K$ which is still much cooler than PopIII stars) has a steeper slope of this continuum compared to the SMDS formed via extended AC and therefore their colors are bluer, i.e. they lie deeper in the first quadrant of the plots. However when comparing SMDS to type C PopIII galaxies (with no nebular emission) we note that the PopIII galaxies have now the steepest UV continuum slope, and therefore have the bluest colors. This leads to an easy way to identify SMDS formed via extended AC from PopIII galaxies, as ca be seen from the left panel plots in Fig. 5.17. However the SMDS formed "with capture" have similar spectra with type C PopIII galaxies and are almost indistinguishable from them using only broadband JWST filters.

5.6 Summary and Conclusions

Figure 5.9, lower left panel, illustrates the capability of JWST to detect million solar mass Dark Stars formed via extended AC at z=15 and surviving to various redshifts as shown. Figure 5.4 shows the sensitivity of HST in 10^4 seconds of data in the 110μ (J-band) and 160μ (H-band) filters. Comparing Figures 5.4 and 5.13, one can see that JWST is half a magnitude more sensitive than HST to finding SMDS as J-band dropouts. The real advantage of JWST is shown in Figures 5.14 and 5.15, with passbands at 150, 200, and 277 μ. Figures 5.14 and 5.15 illustrate the JWST capability for detecting SMDS as H-band and K-band dropouts respectively. 10^6 SMDS can be seen as H-band dropouts at z=13-14.

Figures 5.12 - 5.15 study the observability in JWST of million solar mass dark stars which grew instead via captured DM, in the same bands as described above. These hotter stars, while harder to see, are still observable by JWST.

A key ingredient in identifying an object as a Dark Star is that is has only Hydrogen and Helium, and no other lines. JWST has the capability of observing various lines and will be able therefore to make the differentiation between Dark Stars and other objects.

At $z \sim 10$ the detection of $10^7 M_\odot$ SMDS is relatively slim, however the $10^6 M_\odot$

SMDS could be observable there, even if we don't predict much more than one dropout at $z \sim 10$ for it in a typical JWST deep field survey.This apparent paradox, that the brighter DS is less detectable is due to the following: at the same redshift the formation rate of DM halos hosting the lower mass DS is higher by about one order of magnitude, therefore those objects are much more abundant. However if one uses the F200W and F150W filters of NIRCam even the 10^7 have a significant chance of being observed as a dropout at $z \sim 12$, whereas the $10^6 M_\odot$ SMDS could show up in extremely large numbers (~ 200) in a typical deep field survey as an F150W dropout. At $z \sim 15$ the $10^6 M_\odot$ SMDS could still be easily detected as F200 band dropout in a JWST survey but for the more massive $10^7 M_\odot$ DS this occurrence is relatively unlikely. We therefore conclude that the most promising technique to use in searching for SMDS would be the F150W dropouts as $z \sim 12$ is a sweetspot for the formation of SMDS.

For the case of z=12 detection we have proposed several methods of distinguishing the broadband spectral signatures of SMDS and PopIII galaxies within JWST. Those results are presented in Fig. 5.17. In the case of type A PopIII galaxies the Balmer emission lines render the colors in the $m_{356} - m_{444}$ red. For type C PopIII galaxies we can use the differences in the slope of the UV continuum to differentiate between them and SMDS.

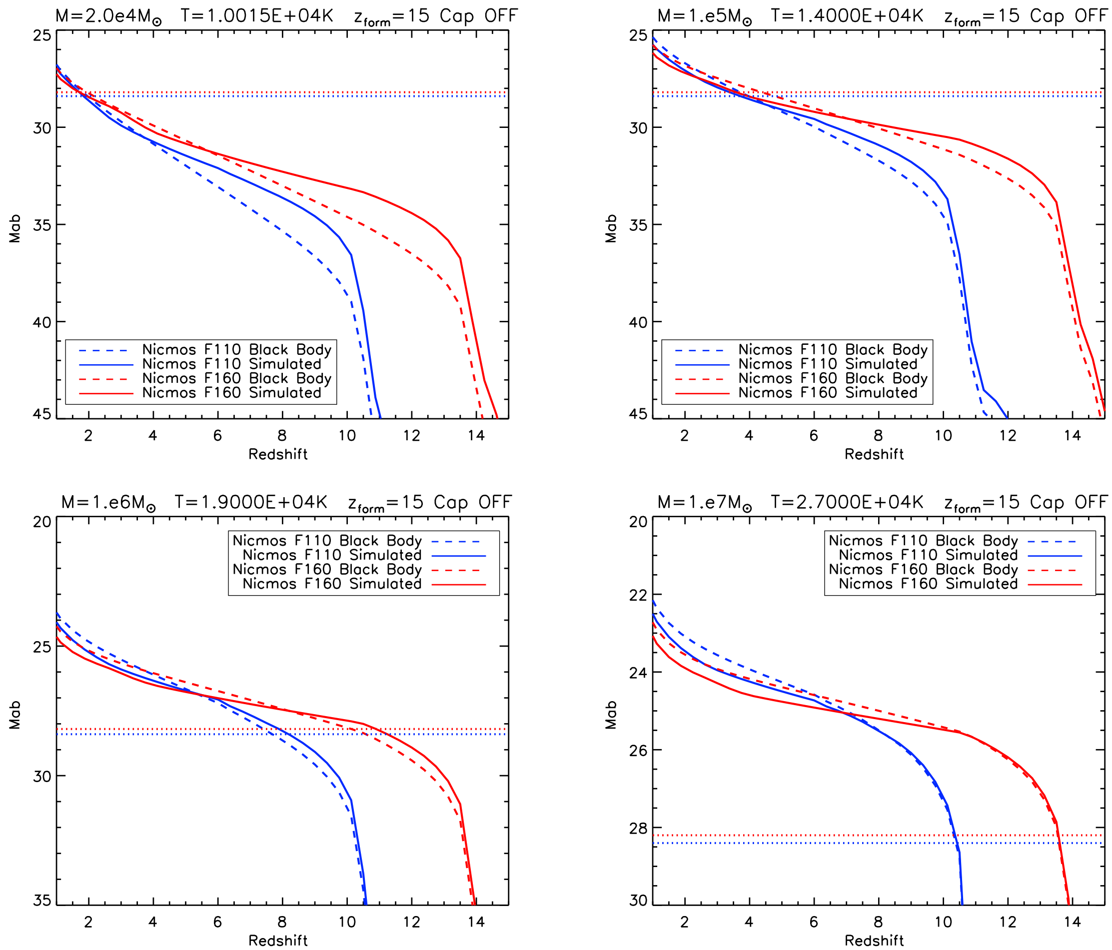

Figure 5.5: J_{110} (blue) and H_{160} (red) apparent magnitudes M_{AB} for Dark Stars of mass ranging between $\sim 10^4 M_\odot - 10^7 M_\odot$ as a function of redshift. Here the Dark Stars are considered to be formed via the extended adiabatic contraction mechanism, without any captured DM. The dashed horizontal lines represent the sensitivity limits for the two passbands considered in HUDF-NICPAR. The solid lines are generated using simulated atmospheres spectra using TLUSTY whereas the dashed lines for apparent magnitudes are generated using a black body spectrum with the bolometric luminosity as the one from the simulated spectra and the same temperature.

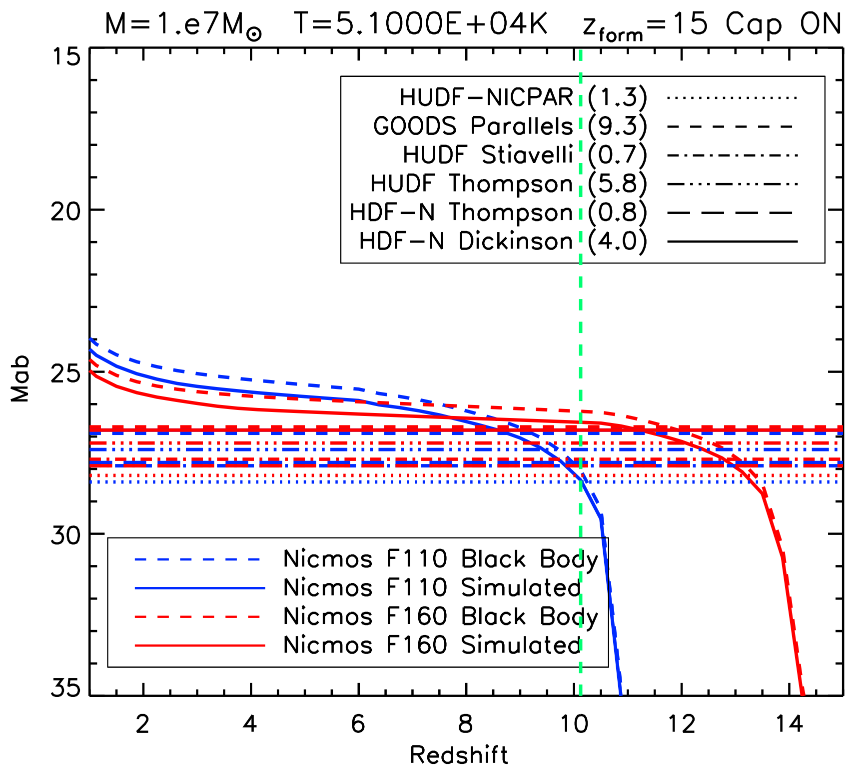

Figure 5.6: Same as Figure 5.4 for the $10^7 M_\odot$ Dark Star fueled by captured DM.

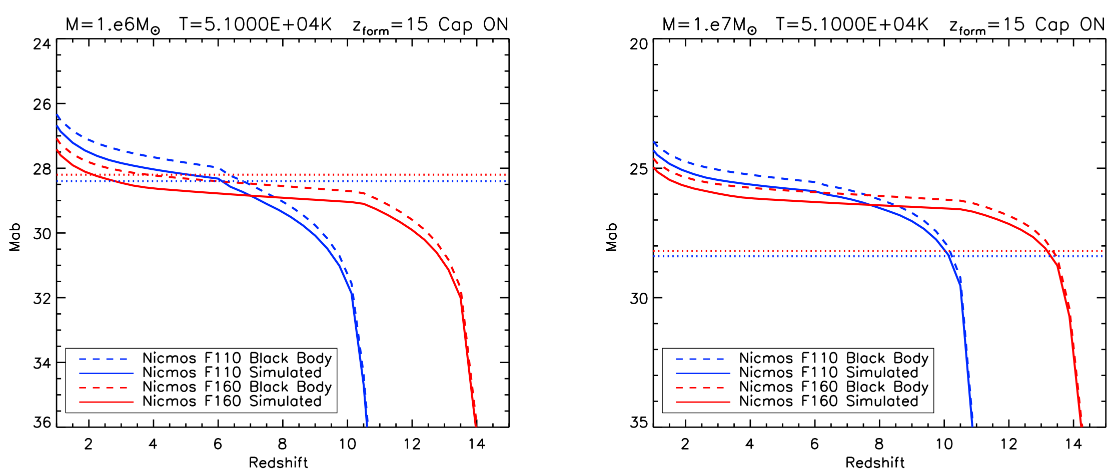

Figure 5.7: J_{110} (blue) and H_{160} (red) apparent magnitudes M_{AB} for Dark Stars of various increasing mass as a function of redshift. The Dark Stars described here are considered to have capture as their main source of DM.The dashed horizontal lines represent the sensitivity limits for the two passbands considered within HUDF-NICPAR. Left panel: $10^6 M_\odot$ Dark Star. Right Panel: $10^7 M_\odot$ Dark Star.

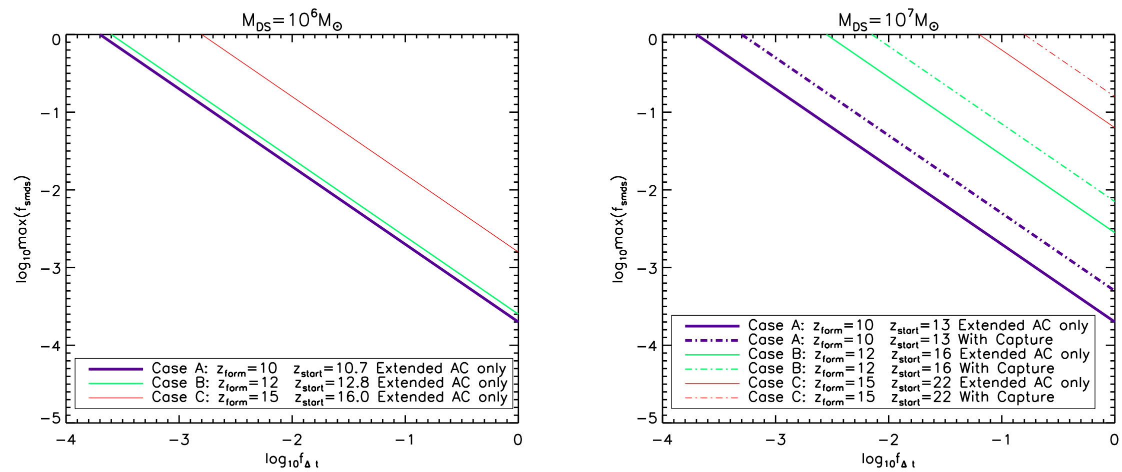

Figure 5.8: Upper bounds on $\mathrm{f_{SMDS}}$. The various cases are labeled by values of the redshift where the DS attains its mass labeled above the plot ($\mathrm{z_{form}} = 10, 12,$ and 15). Values for $\log(\mathrm{f_{SMDS}}$) above the lines are excluded. The horizontal axis in both plots is $\log_{10} f_{\Delta t}$, for which a value of 0 corresponds to the DS lifetime being sufficiently large that it survives throughout redshift range where it could be observed as a J_{110} band dropout in HST. Left panel: for a $10^6 M_\odot$ DS ($T_{eff} = 1.9 \times 10^4 K$) which started to form via the extended AC mechanism in a $10^7 M_\odot$ DM halo at three different redshifts, labeled by $\mathrm{z_{start}}$. Right panel: for a $10^7 M_\odot$ DS formed either via the extended AC mechanism (solid lines, $T_{eff} = 2.7 \times 10^4 K$) or formed with captured DM (dashed lines, $T_{eff} = 5.1 \times 10^4 K$).

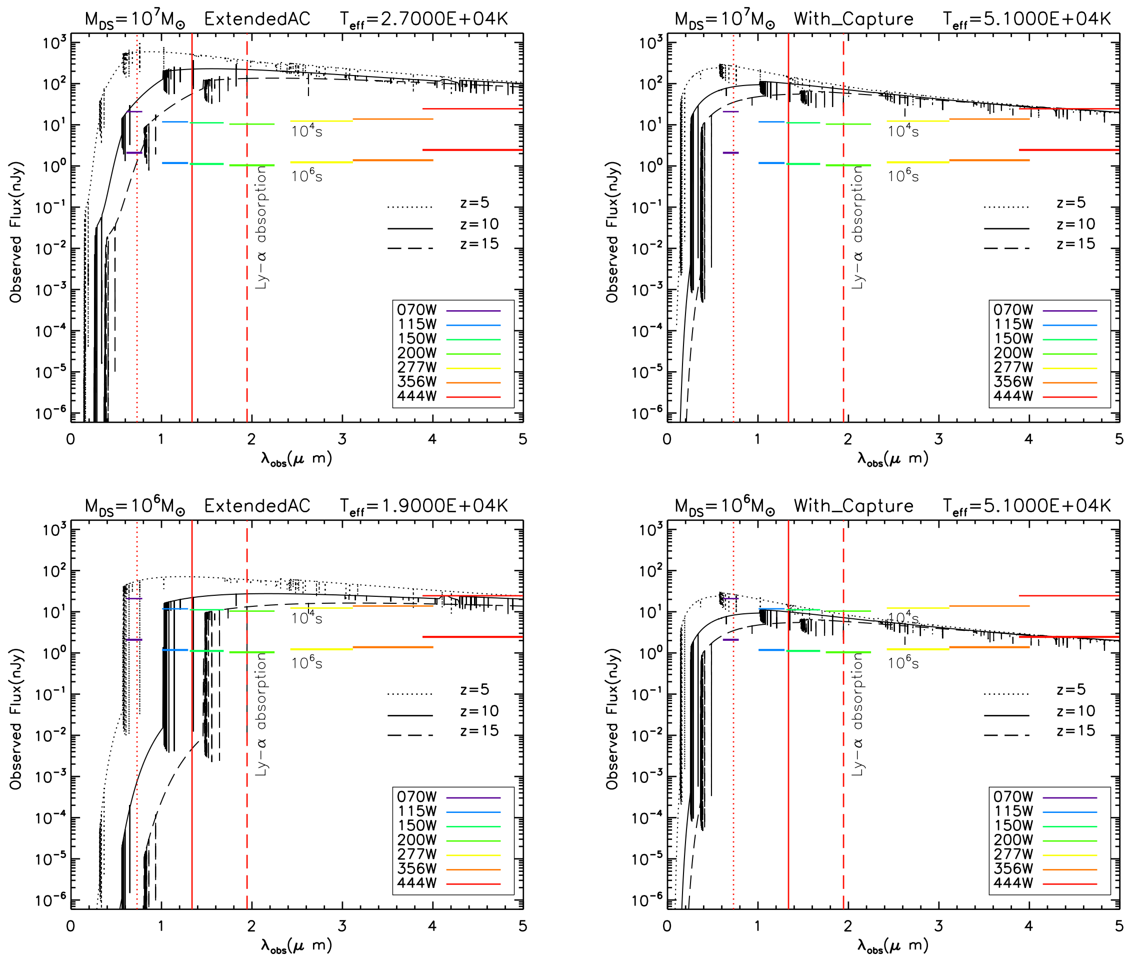

Figure 5.9: TLUSTY spectra for supermassive dark stars formed at $\mathrm{z_{form}} = 15$ via extended adiabatic contraction (AC) or "with capture" . Listed above each panel are the mass of the DS in solar masses, the formation mechanism and the effective temperature, T_{eff} in K. The fluxes are shown at $z = 15$ (dashed line), 10 (solid line) and 5 (dotted line) and compared to the detection limits of NirCam wide passband filters. The horizontal lines of colors ranging from violet to red represent the sensitivity limits for the filters labeled in the legend. The upper set corresponds to an exposure time of 10^4s whereas the lower set to 10^6s. The vertical red lines mark the location of the observed wavelength for the Ly-α line (1216Å) redshifted from the rest-frame of the star, taken to be at $z = 15, 10$ or 5. IGM absorption will decrease the fluxes for wavelengths shortward of the vertical lines.

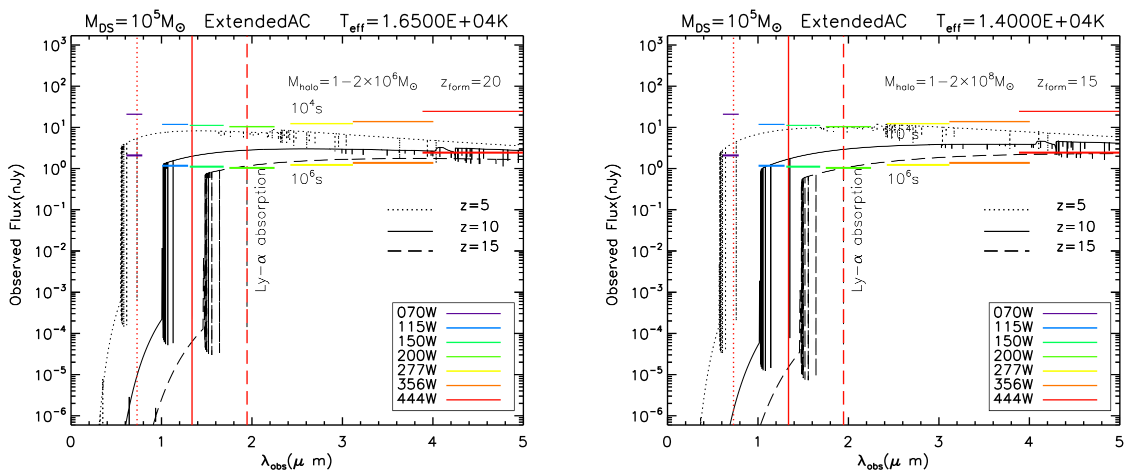

Figure 5.10: Similar to Figure 5.9, now for a $10^5 M_\odot$ DS formed either at $z_{\rm form}$ =20 in a $10^6 M_\odot$ DM halo (left panel) or at $z_{\rm form}$ =15 in a $10^8 M_\odot$ DM halo (right panel).

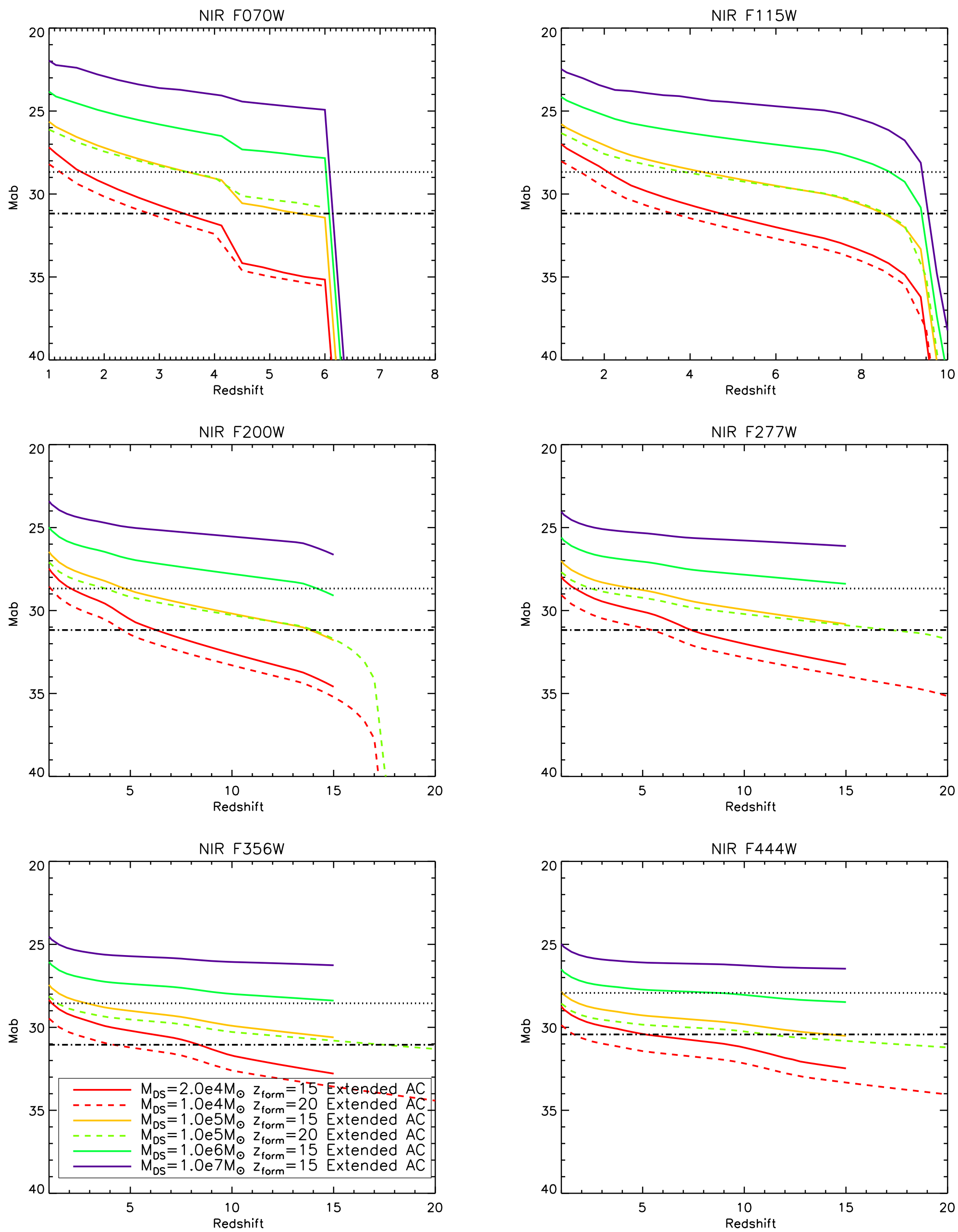

Figure 5.11: Apparent magnitudes for various SMDS through the NIR camera wide passband filters on JWST. The number after the letter F and before the letter W in the name of each filter corresponds to the wavelength in the center of the passband in $100\ \mu\mathrm{m}$ units. In all cases considered the DS are formed via the extended adiabatic contraction (AC) mechanism. The two horizontal lines correspond to sensitivity limits for each filter for 10^4s exposure time (the dotted line) and $10^6 s$ exposure time (the dash-dotted line).

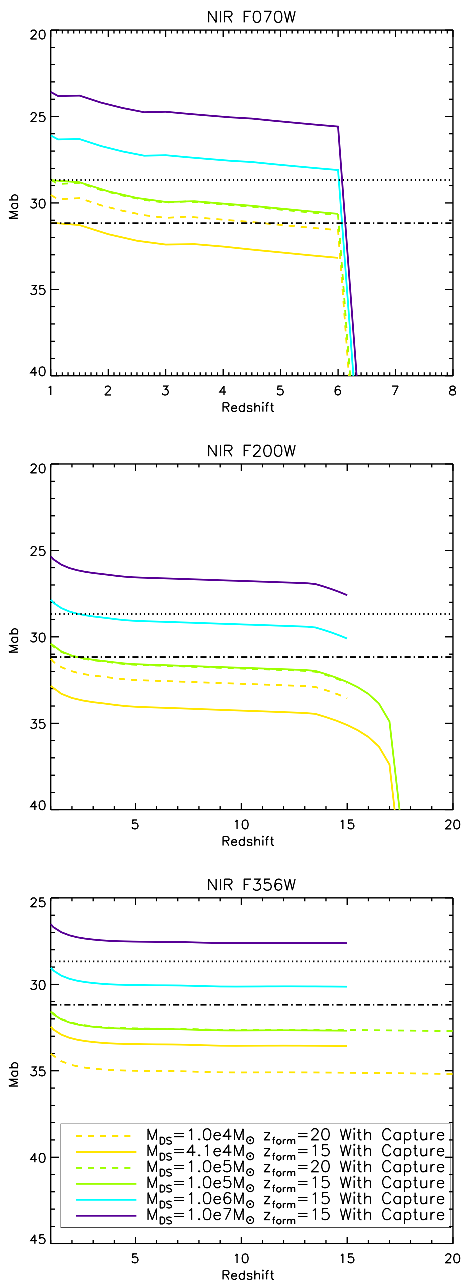

Figure 5.12: Apparent magnitudes for various SMDS formed "with capture" in various JWST bands as labeled. The two horizontal lines correspond to sensitivity limits for each filter for 10^4s exposure time (the dotted line) and $10^6 s$ exposure time (the dash-dotted line).

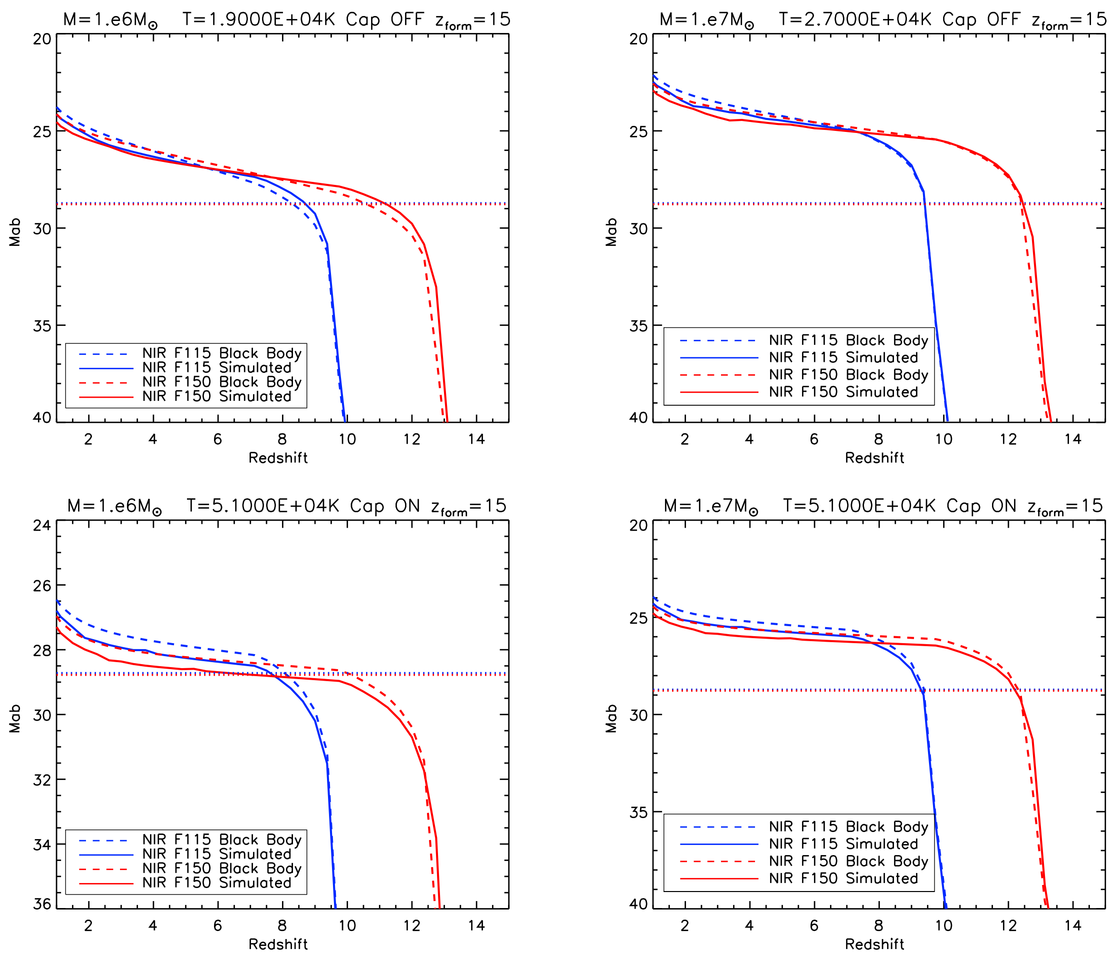

Figure 5.13: SMDS in JWST as J_{115} band dropouts: Apparent magnitudes for various SMDS through the F115W and F150W filters for NirCam. Top panel: $10^6 M_\odot$ and $10^7 M_\odot$ Dark Stars formed without DM capture. Lower panel: $10^6 M_\odot$ and $10^7 M_\odot$ Dark Stars formed "with capture". Detection limits are calculated assuming a 10^4 s exposure.

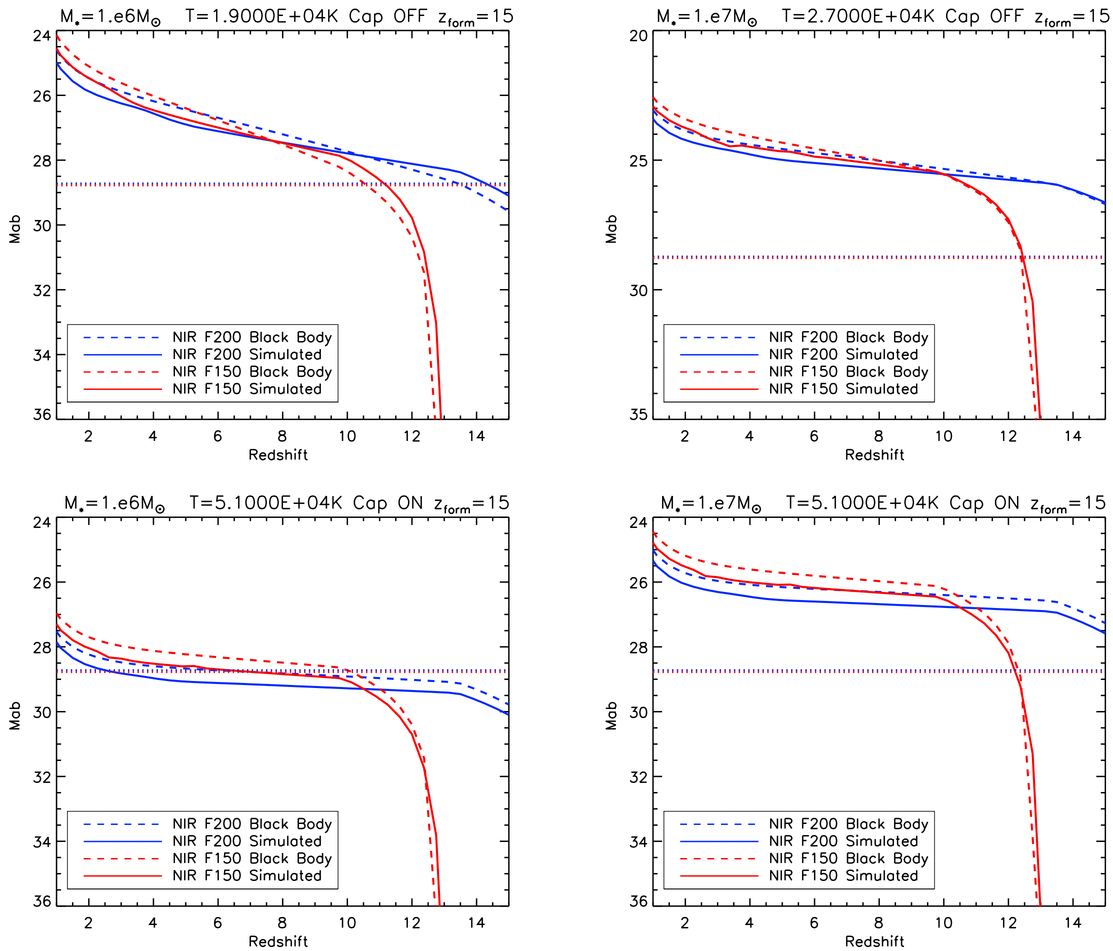

Figure 5.14: SMDS in JWST as H_{150} band dropouts: Apparent magnitudes for SMDS through the F150W and F200W NirCam filters. Those could be used to establish dropout detection criteria in the $12 - 14$ redshift range. Top panel: cases of interest ($10^6 M_{\odot}$ and $10^7 M_{\odot}$) Dark Stars formed without considering DM capture. Lower panel: $10^6 M_{\odot}$ and $10^7 M_{\odot}$ Dark Stars formed including DM capture. In both cases sensitivity limits correspond to 10^4 s exposures.

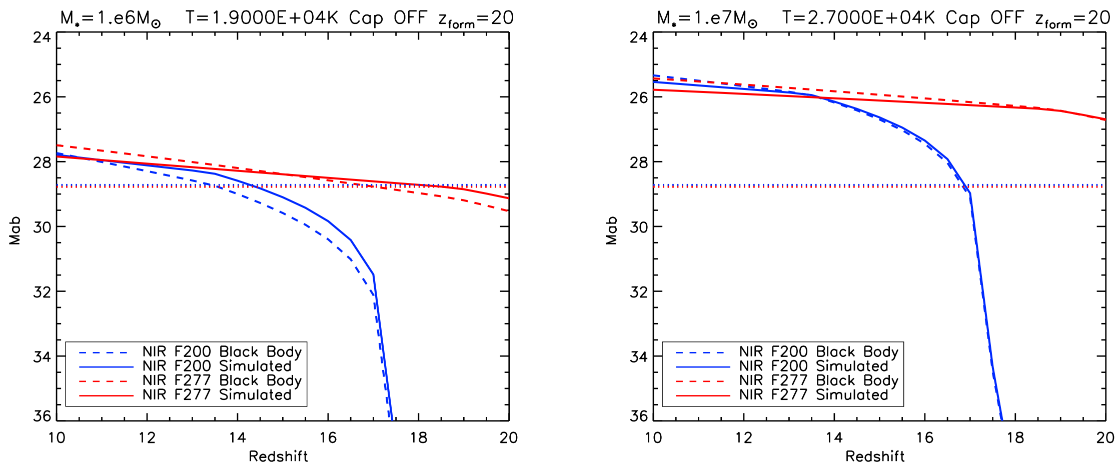

Figure 5.15: SMDS in JWST as K_{200} band dropouts: Apparent magnitudes for SMDS formed without DM capture through the F200W and F277W NirCam filters. Left panel: for the $10^6 M_\odot$ dark star. Right panel: for the $10^7 M_\odot$ dark star.

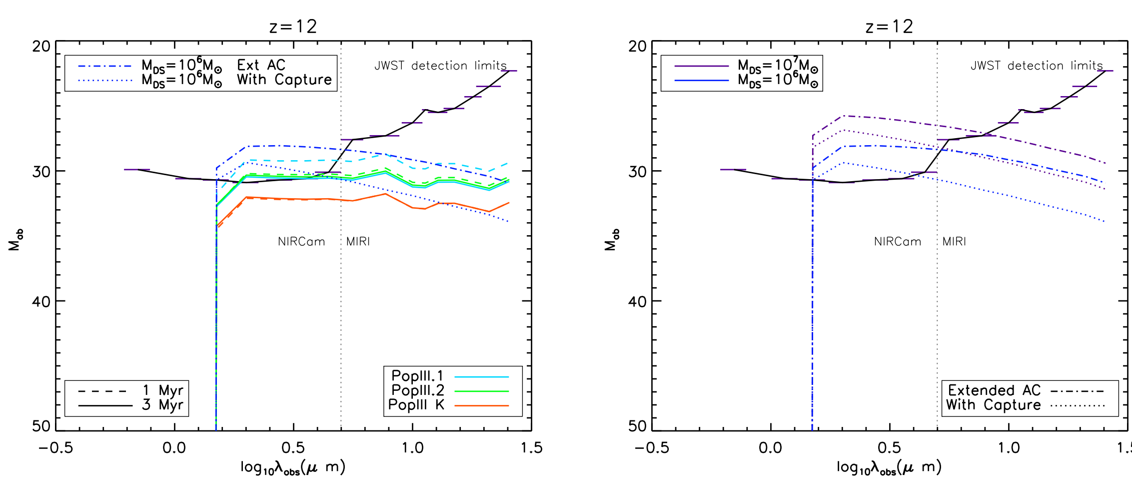

Figure 5.16: JWST detection limits and apparent magnitudes of SMDS and PopIII galaxies.The solid black line, with filters superimposed, represents the sensitivity limits for JWST NIRCam and MIRI wide filters for 100 hours of exposure time. Left panel: Apparent magnitudes of SMDS of $10^6 M_\odot$ and PopIII instantaneous burst galaxies with the same stellar population mass as the SMDS. Right panel: Apparent magnitudes for SMDS in the $10^6 M_\odot$ -$10^7 M_\odot$ mass range.

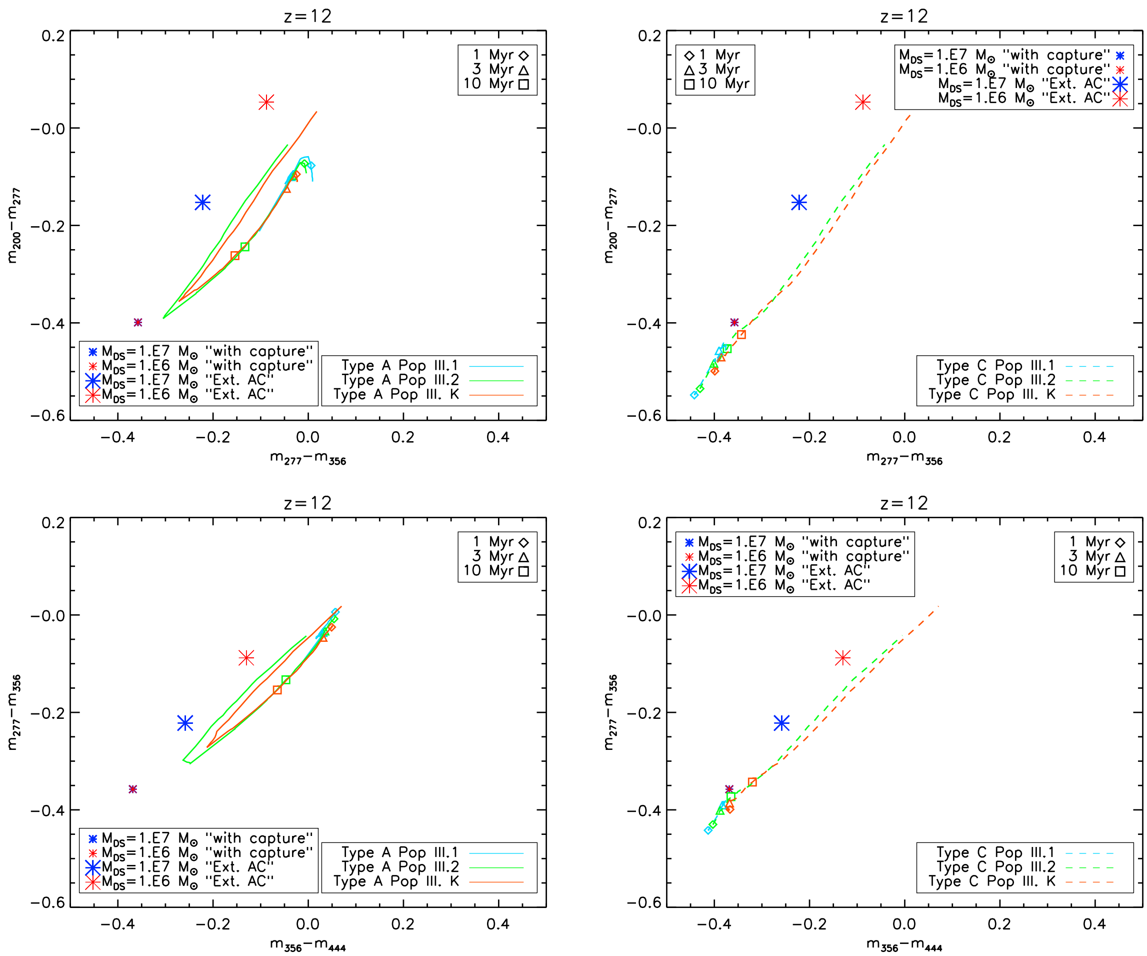

Figure 5.17: Signatures of SMDS and instantaneous burst PopIII galaxies in $m_{277} - m_{356}$ vs $m_{200} - m_{277}$ (top row) and $m_{356} - m_{444}$ vs $m_{277} - m_{356}$ (bottom row) color diagrams. The left column corresponds to Type A PopIII galaxies (maximal nebular emission) and the right column to Type C PopIII galaxies (no nebular emission). The points along the solid lines represent three different ages of the galaxies.

CHAPTER VI

Conclusions and Future Work

6.1 Conclusions

In Chapter II we have studied a cyclical model of the universe where the energy density cycles between a minimum value, typically of the order of meV^4 and a maximum value roughly set by the GUT scale. This effectively provides a connection between the current accelerated expansion we observe today and the inflationary era in the past. The scale factor continues to grow from one cycle to the next (there is no ”turnaround”). In order to achieve this model we postulated the existence of some ‘hidden’ sector matter coupled to a ghost like scalar field. This mechanism is responsible for a super-accelerated phantom expansion. Allowing for hidden sector particles to be converted to light degrees of freedom of the standard model ameliorates the phantom behavior, effectively transitioning to a deSitter like expansion, therefore avoiding the Big-Rip singularity. Although dominated by radiation, in this phase all the energy densities remain constant. Therefore, if most of the cosmological perturbations are generated during this exponential inflationary era the spectrum is expected to be scale invariant. Even if not favored by the data, this is still a possibility. Another possibility would be to have some of the fluctuations generated during the phantom phase which will show up as a blue tilt in the spectrum. In that case we will see a running of the tilt which could be a unique possible signature of the model.

In order to achieve the cyclic behavior we have postulated that the coupling between the ghost scalar field and the hidden sector is constant piecewise. This procedure might seem ad-hoc, but it is just the simplest possibility. We found that no fine tuning seems to be involved when requiring to have a long enough radiation/matter dominated phase. It is also worth mentioning that the “smallnesss” problem associated with dark energy is circumvented. The only parameter we need in order to describe the current acceleration is the coupling between the hidden sector and the ghost field, and it has a value not much greater than one.

In Chapter III we have investigateed the dependance of properties of DS with the boost factor for the annihilation cross section of DM particles and the concentration parameter of the DM halos where they are formed. Our basic results are that the final stellar properties, once the star enters the main sequence, are always roughly the same, regardless of the value of boosted annihilation or concentration parameter in the range between c=2 and c=5: stellar mass $\sim 1000 M_\odot$, luminosity $\sim 10^7 L_\odot$, lifetime $\sim 10^6$ yrs (for the minimal DM models considered here; additional DM would lead to more massive dark stars). However, the lifetime, final mass, and final luminosity of the DS show some dependence on boost factor and concentration parameter.

In Chapters IV-V we study supermassive dark stars (SMDS) and their observability. First, by considering triaxial DM haloes we show that the amount of DM to fuel the star could be much larger than previously thought: chaotic orbits could refill the loss cone generated by DM annihilations. We demonstrate that DS could grow as big as $10^7 M_\odot$ and shine as bright as $10^{10} L_\odot$. In the future we suggest a stability analysis of our models. The very interesting possibility of short term pulsational instabilities exists, which leads to SMDS as possible standard candles for learning about dark energy or other evolutionary properties of the Universe. Using a simple Black Body as a model for the SED of those stars we show SMDS could be detected by JWST for a variety of parameters. In Chapter V we extend this study by now including the stellar atmosphere and its effects on the SED and using the null results from J Band dropouts in HST to predict a maximum number of dark stars that could be observed in a deep field survey with JWST. We conclude that the most promising technique to use in searching for SMDS would be as K_{200} dropouts at z~ 12 although the instrument is sensitive enough to observe them individually to redshifts up to 15 or more. For the case of detection at redshift 12 we present two methods of distinguishing SMDS from PopIII galaxies broadband spectra, in the case of maximal or no nebular emission for the galaxies.

6.2 Future Work

Several extension of the work presented in Chapter II could be made. First, as previously stated, phantom fields suffer from vacuum instabilities. This issue needs to be addressed in any type of scenario that gives an effective equation of state parameter $w_{eff} < 1$. One such approach would be to use a modified version of the ghost condensate model of *Hamed et al.* (2004), in a similar fashion as *Creminelli et al.* (2006). A rigorous calculation of the spectrum of primordial perturbations would then become possible, therefore offering a way to test our model.

Regarding dark stars there are several important questions that one could ask. From an observational standpoint one would need to be able to distinguish between them and any other object luminous enough to be detected at redshifts higher than ~ 12. A comparison of the SEDs of Dark Stars to that of their nearest competitors in JWST at those high redshifts, namely $10^9 M_\odot$ -$10^{10} M_\odot$ galaxies would settle this issue. One way of breaking this degeneracy is by looking for recombination lines, especially those of He. Dark Stars are too cool to emit such re-ionizing photons. Yet another interesting question is that of pulsation modes for Dark Stars. Regarding their formation an interesting feedback effect that deserves further attention is given by possible soft UV photons from the collapsing gas cloud that would form the DS, if DM annihilations are included. This could lead to a dissociation of hydrogen molecules, which was the main coolant available. Another very interesting question is how will Dark Stars influence the re-ionization history of the universe. It is certain that they would delay the onset of this event, but placing a quantitative estimate on this would require knowledge of the fraction of DM halos that can host them and of their initial mass function, two parameters not constrained well enough yet.

APPENDICES

APPENDIX A

Stability of scaling solutions in phantom coupled models

We will look at ghost fields coupled to radiation or matter via the term $\rho_\gamma = \tilde{\rho_\gamma}\epsilon^{2\mu\phi}$ and study the stability of the critical points, generalising the analysis done in *Copeland et al.* (1998). In this way we will find the stable attractors and conditions necessary to obtain them. Here the subscript γ refers to the adiabatic index of the fluid the phantom field couples to, defined as $\gamma = 1 + \omega_h$. Throughout the main body of the paper we have used ρ_h, but for notational convenience here we will replace it by ρ_γ. It will be assumed that the phantom field has a self-interaction potential of the following forms: $V(\phi) = V_0\epsilon^{-2\alpha\phi}$ and $V(\phi) = -V_0\epsilon^{2\alpha\phi}$. We have not used a potential in deriving our main results in the paper, but we keep it here for generality and further reference.

For

$$V(\phi) = V_0 e^{-2\alpha\phi} \tag{A.1}$$

we have the following equations:

$$\begin{aligned}
\ddot{\phi} + 3H\dot{\phi} &= V_{eff}(\phi)' \\
\dot{H} &= -\frac{1}{2}(-\dot{\phi}^2 + \gamma\tilde{\rho_\gamma}\epsilon^{2\mu\phi}) \\
H^2 &= \frac{1}{3}\left[-\frac{\dot{\phi}^2}{2} + V(\phi) + \tilde{\rho_\gamma}\epsilon^{2\mu\phi}\right]
\end{aligned} \tag{A.2}$$

where $V_{eff} = V(\phi) + \tilde{\rho_\gamma}\epsilon^{2\mu\phi}$. Although we are treating here only two fluids, this case is relevant during the phantom phase, when the energy density of any (third) component not coupled to the phantom field, such as regular matter, will quickly become sub-dominant. Introducing the variables

$$x = \frac{\dot{\phi}}{\sqrt{6}H} \tag{A.3}$$

and

$$y = \frac{\sqrt{V(\phi)}}{\sqrt{3}H} \tag{A.4}$$

and using $\eta \equiv \log a(t)$ as the independent variable, instead of the cosmological time t, we can rewrite the equations in the form of an autonomous system supplemented with the Hubble constraint.

$$\begin{aligned}
x' &= -3x + \sqrt{6}\left[\mu(1 + x^2 - y^2) - \alpha y^2\right] + \\
&\quad + \frac{3}{2}x\left[\gamma\left(1 + x^2 - y^2\right) - 2x^2\right] \\
y' &= -\sqrt{6}\alpha xy + \frac{3}{2}y\left[\gamma(1 + x^2 - y^2) - 2x^2\right] \\
1 &= \left[y^2 - x^2 + \tilde{\Omega}_\gamma\right]
\end{aligned} \tag{A.5}$$

In order to find the critical points one has to set the $r.h.s$ of the first two equations to zero and solve for x and y. We find five distinct solutions,

$$(x,y)=\begin{cases}(i & , \quad 0) \qquad\qquad\qquad I. \\ (-i & , \quad 0) \qquad\qquad\qquad II. \\ (-\frac{2}{3}\frac{\sqrt{6}\mu}{-2+\gamma} & , \quad 0) \qquad\qquad\qquad III. \\ (\frac{1}{4}\frac{\sqrt{6}\gamma}{\alpha+\mu} & , \quad \frac{1}{4}\frac{\sqrt{2}\sqrt{8\mu\alpha+8\mu^2-6\gamma+3\gamma^2}}{\alpha+\mu}) \quad IV. \\ (-\frac{1}{3}\sqrt{6}\alpha & , \quad -\frac{1}{3}\sqrt{3}\sqrt{3+2\alpha^2}) \qquad V.\end{cases}$$

Note that the first two are nonphysical so we will no longer consider them. Next we compute the fractional densities for the 'phantom' field and its adiabatic constant near the five critical points. The Hubble constraint will then enforce additional existence conditions.

$$\Omega_\phi = y^2 - x^2 = \begin{cases} -\frac{8}{3}\frac{\mu^2}{(-2+\gamma)^2} & III. \\ -\frac{1}{4}\frac{-4\mu\alpha-4\mu^2+3\gamma}{(\alpha+\mu)^2} & IV. \\ 1 & V. \end{cases} \tag{A.6}$$

One solution is completely dominated by the scalar field ϕ and the other two exhibit a scaling behaviour. For the first of those the Hubble constraint will not give any additional inequalities in the parameter space since $\Omega_{\phi(III)}$ is clearly negative, hence less than 1. Here the roman numeral subscript refers to all the solutions, including the non-physical ones, i.e (I) corresponds to the solutions with $(x,y)=(i,0)$ and so on. Also $\Omega_{\phi(IV)}<1$ is trivially satisfied for positive parameters. So the only nontrivial existence constraint comes from imposing reality of the y_{IV} solution:

$$\mu(\mu+\alpha)\geq\frac{3}{8}\gamma(2-\gamma) \tag{A.7}$$

Let us now look at the 'effective' values of the adiabatic constant $\gamma=1+w$ for the ghost field near the critical points. For completeness we will keep even the nonphysical solutions.

$$\gamma_\phi = 1 + \frac{p_\phi}{\rho_\phi} = \frac{\dot{\phi}^2}{\frac{1}{2}\dot{\phi}^2 - V(\phi)} = \frac{2x^2}{x^2 + y^2} \tag{A.8}$$

With this definition we get,

$$\gamma_\phi = \frac{2x^2}{-y^2 + x^2} = \begin{cases} 2 & I. \\ 2 & II. \\ 2 & III. \\ -\frac{3\gamma^2}{-4\mu\alpha - 4\mu^2 + 3\gamma} & IV. \\ -\frac{4}{3}\alpha^2 & V. \end{cases} \tag{A.9}$$

The total, or 'effective' DE equation of state parameter that drives the expansion can be defined since we have scaling solutions.

$$\omega_{tot} = \frac{p_\phi + p_\gamma}{\rho_\phi + \rho_\gamma} \tag{A.10}$$

Some algebra leads to

$$\omega_{tot} = \Omega_\phi(\gamma_\phi - 1) + (1 - \Omega_\phi)(\gamma - 1) \tag{A.11}$$

For the three physical solutions it leads to the following values:

$$\omega_{tot} = \begin{cases} \frac{1}{3}\frac{3\omega_h(\omega_h - 1) + 8\mu^2}{\omega_h - 1} & III. \\ \frac{1}{2}\frac{3(1+\omega_h)^2 + 2(\mu+\alpha)(\omega_h\alpha - \mu)}{(\alpha+\mu)^2} & IV. \\ -1 - \frac{4}{3}\alpha^2 & V. \end{cases} \tag{A.12}$$

Next we will study the stability of the relevant critical points, ignoring the non-physical first two solutions. The technique is the following. One expands around the critical solution setting $x = x_c + u$ and $y = y_c + v$ into (A.5) and then keep only linear terms. In order to have a stable solution the eigenvalues of the matrix describing the linearized system must have negative real parts. For solution III. one finds the following equations

$$
\begin{aligned}
u' &= -\frac{1}{2}\frac{-8\mu^2 - 3\gamma^2 + 12\gamma - 12}{-2+\gamma}u \\
v' &= -\frac{1}{2}\frac{(-3\gamma^2 - 8\mu\alpha - 8\mu^2 + 6\gamma)}{-2+\gamma}v
\end{aligned}
\tag{A.13}
$$

For both radiation ($\gamma = \frac{4}{3}$) and dust ($\gamma = 1$) the coefficient u is negative independent of the value of μ. From the second equation one gets that the node is stable when:

$$
3\gamma(2-\gamma) < 8\mu(\alpha + \mu) \tag{A.14}
$$

Otherwise we have a saddle point. It is interesting to notice that this is exactly the same condition we got in (A.7) for the existence of the fourth solution.

Let us move on to the stability of solution IV, for which the linearized system becomes:

$$
\begin{aligned}
u' &= -\frac{1}{8}\frac{24\alpha^2 - 24\gamma\mu^2 + 24\mu^2 + 48\mu\alpha + 18\gamma^2 - 36\gamma\alpha\mu - 9\gamma^3 - 12\gamma\alpha^2}{(\mu+\alpha)^2}u \\
&\quad -\frac{1}{8}\frac{\sqrt{3}\sqrt{8\mu\alpha + 8\mu^2 - 6\gamma + 3\gamma^2}(16\mu\alpha + 3\gamma^2 + 8\mu^2 + 8\alpha^2)}{(\alpha+\mu)^2}v \\
v' &= \frac{1}{8}\frac{\sqrt{3}\sqrt{8\mu\alpha + 8\mu^2 - 6\gamma + 3\gamma^2}(-4\alpha^2 + 3\gamma^2 - 4\mu\alpha - 6\gamma)}{(\alpha+\mu)^2}u - \frac{3}{8}\frac{\gamma(8\mu\alpha + 8\mu^2 - 6\gamma + 3\gamma^2)}{(\alpha+\mu)^2}v
\end{aligned}
\tag{A.15}
$$

The eigenvalues are:

$$
\begin{aligned}
e_{1(4)} &= \frac{1}{4}\frac{1}{\alpha+\mu}\left(3\alpha\gamma - 6\alpha - 6\mu + B^{\frac{1}{2}}\right) \\
e_{2(4)} &= \frac{1}{4}\frac{1}{\alpha+\mu}\left(3\alpha\gamma - 6\alpha - 6\mu - B^{\frac{1}{2}}\right)
\end{aligned}
\tag{A.16}
$$

where B is the following combination of the parameters:

$$
\begin{aligned}
B &= 72\mu\alpha\left(\gamma^2+1+\tfrac{8}{3}(\mu+\alpha)^2\right)+54\gamma^2(\gamma-2)+ \\
&\quad +\alpha^2(36+81\gamma^2-180\gamma)+36\gamma(\gamma-\alpha\mu+4\mu^2)
\end{aligned}
$$

The study of stability of the solutions is quite complicated here but there is a range of parameters for which the real part of the two eigenvalues is negative. Independent of the value of B one necessary condition for stability here is

$$
2(1+\frac{\mu}{\alpha})<\gamma \tag{A.17}
$$

For positive parameters, and if γ is either 1 or $\frac{4}{3}$ this inequality cannot be satisfied; thus the fourth attractor is unstable if the hidden sector is comprised of some component that behaves like matter or radiation.

Let us look now at the stability conditions for the critical point labeled by V. The linearized autonomous system becomes in this case:

$$
\begin{aligned}
u' &= (-3+2\alpha^2(\gamma-3)-4\mu\alpha)u+ \\
&\quad +\sqrt{2}\sqrt{3+2\alpha^2}(2\mu-\alpha\gamma+2\alpha)v \\
v' &= \sqrt{2}\sqrt{3+2\alpha^2}(\alpha\gamma-\alpha)u-\gamma(3-2\alpha^2)v
\end{aligned} \tag{A.18}
$$

The eigenvalues read $-(3+2\alpha^2)$ and $-(4\alpha^2+4\mu\alpha+3\gamma)$ which are clearly both negative and real so one has a stable node as a late time attractor. Also remember that this solution does not have a scaling behavior, since in this case the energy density is dominated by the phantom. In conclusion we found two stable late time attractors, one of which exhibits a scaling behaviour. Notice also that this scaling solution corresponds to a critical point where $y=0$, so in effect it is equivalent to the case where the potential is actually zero.

Next let us look at the tracking ratio in the two cases of interest, namely the third and fourth critical points. The tracking ratio is defined to be the ratio of relic densities of the two components.

$$r = \frac{\Omega_\phi}{1-\Omega_\phi} \tag{A.19}$$

With this definition we find, using (A.6):

$$r = \begin{cases} -\frac{8}{3}\frac{\mu^2}{(-2+\gamma)^2\left(1+\frac{8}{3}\frac{\mu^2}{(-2+\gamma)^2}\right)} & III. \\ -\frac{1}{4}\frac{-4\mu\alpha-4\mu^2+3\gamma}{(\mu+\alpha)^2\left(1+\frac{1}{4}\frac{-4\mu\alpha-4\mu^2+3\gamma}{(\mu+\alpha)^2}\right)} & IV. \end{cases}$$

Since we have established that we will be using the late time attractor described by critical point III. as our model for the phantom phase, let us actually see under what conditions we cross the 'phantom divide' and if this phase will be stable. Comparing ω_{tot} given by (A.12) the following restriction on μ:

$$\mu^2 \geq \begin{cases} \frac{3}{8} & \text{for matter hidden sector} \\ \frac{1}{3} & \text{for radiation hidden sector} \end{cases} \tag{A.20}$$

Looking back at (A.14) and taking $\alpha = 0$ as appropriate for the case of no potential one can check that the stability conditions are actually identical with the conditions for achieving a phantom phase, listed above. Hence, we have verified that the late time attractor solution for $V(\phi) = 0$ is stable once we have μ such that we get a phantom phase.

Now for generality we will repeat the same analysis for a negative potential,

$$V(\phi) = -V_0 \exp 2\alpha\phi. \tag{A.21}$$

Here we will define $y = \frac{\sqrt{-V(\phi)}}{\sqrt{3}H}$.In this case the autonomous system will take the following form

$$\begin{aligned} x' &= -3x + \sqrt{6}\left[\mu(1+x^2+y^2) - \alpha y^2\right] + \\ &\quad + \tfrac{3}{2}x\left[\gamma\left(1+x^2+y^2\right) - 2x^2\right] \\ y' &= \sqrt{6}\alpha xy + \tfrac{3}{2}y\left[\gamma(1+x^2+y^2) - 2x^2\right] \\ 1 &= \left[-y^2 - x^2 + \tilde{\Omega_\gamma}\right] \end{aligned} \tag{A.22}$$

There will be only two physical critical points in this case:

$$(x,y) = \begin{cases} (-\frac{2}{3}\frac{\sqrt{6}\mu}{-2+\gamma} \quad , \quad 0) & I.B \\ (\frac{1}{4}\frac{\sqrt{6}\gamma}{-\alpha+\mu} \quad , \quad \frac{1}{4}\frac{\sqrt{2}\sqrt{8\mu\alpha-8\mu^2+6\gamma-3\gamma^2}}{-\alpha+\mu}) & II.B \end{cases}$$

Just to clear any possible confusion please note that the labels $I.B$ and $II.B$ here are not related to the labeling of the different regions in Fig. 1. Notice that the first critical point in this case is identical to the third critical point for the case of positive potential. (see equation below (A.5)) The existence condition for the second critical point reads $\mu(\mu-\alpha) < \frac{3}{8}\gamma(2-\gamma)$. Fractional density values are

$$\Omega_\phi = -y^2 - x^2 = \begin{cases} -\frac{8}{3}\frac{\mu^2}{(-2+\gamma)^2} & I.B \\ \frac{1}{4}\frac{-4\mu\alpha+4\mu^2-3\gamma}{(-\alpha+\mu)^2} & II.B \end{cases} \tag{A.23}$$

From here we get an additional existence constraint on the second critical point, namely:

$$\alpha(\mu-\alpha) \leq \frac{3}{4}\gamma \tag{A.24}$$

The adiabatic constant for ϕ is

$$\gamma_\phi = \frac{2x^2}{y^2+x^2} = \begin{cases} 2 & I.B \\ -\frac{3\gamma^2}{-4\mu\alpha+4\mu^2-3\gamma} & II.B \end{cases} \tag{A.25}$$

Notice the difference between the last value in (A.25) and the fourth in (A.9). Here we can set $\mu \to 0$ and recover γ as the adiabatic index. Before the naive limit was $-\gamma$ but one was not actually allowed to take that limit due to (A.7). Now the inequality has been reversed so the second critical point in the case of the negative potential could be used for a scaling solution in a phase where the hidden sector decouples from the ghost field.

As before let us look at the effective equation of state parameter:

$$\omega_{tot} = \begin{cases} \frac{1}{3}\frac{3\omega_h(\omega_h-1)+8\mu^2}{\omega_h-1} & I.B \\ \frac{\omega_h\alpha+\mu}{\alpha-\mu} & II.B \end{cases} \tag{A.26}$$

Expanding around the critical points for the first solution we get the following conditions for stability:

$$\begin{aligned} 0 &> -\frac{1}{2}\frac{-8\mu^2-3\gamma^2+12\gamma-12}{-2+\gamma} \\ 0 &> -\frac{1}{2}\frac{(-3\gamma^2+8\mu\alpha-8\mu^2+6\gamma)}{-2+\gamma} \end{aligned} \tag{A.27}$$

The first inequality is trivially satisfied and the second implies:

$$\gamma(2-\gamma) < \frac{8}{3}\mu(\mu-\alpha) \tag{A.28}$$

This could be used as a constraint on the steepness of the potential in order to preserve the tracking behavior in the phantom phase. For the second critical point we have the following eigenvalues:

$$\begin{aligned} e_{1(2)} &= \frac{1}{4}\frac{1}{\alpha-\mu}\left(3\alpha\gamma-6\alpha+6\mu+B_2^{\frac{1}{2}}\right) \\ e_{2(2)} &= \frac{1}{4}\frac{1}{\alpha-\mu}\left(3\alpha\gamma-6\alpha+6\mu-B_2^{\frac{1}{2}}\right) \end{aligned} \tag{A.29}$$

Here B_2 is a combination of the parameters, the exact form of which we will not be using.

A necessary condition for the stability of this critical point is:

$$\alpha(1-\omega_h) < 2\mu \tag{A.30}$$

The tracking ratios can be easily computed:

$$r = \begin{cases} -\frac{8}{3}\frac{\mu^2}{(-2+\gamma)^2\left(1+\frac{8}{3}\frac{\mu^2}{(-2+\gamma)^2}\right)} & I.B \\ -\frac{-4\mu\alpha+4\mu^2-3\gamma}{-4\alpha^2+4\alpha\mu-3\gamma} & II.B \end{cases}$$

In this appendix we have found the conditions for scaling behavior in the phantom phase, for the cases of positive, zero, and negative exponential potentials. An exponential coupling between a ghost like field and some hidden sector fluid is used to generate a phantom phase, where the effective equation of state is less than negative one. We found the stable attractors and conditions necessary to obtain them. As a side result we notice that for negative potentials one could have a scaling stable late time attractor even if the ghost field is decoupled from the hidden sector. In that case the ghost will just track the hidden sector component.

APPENDIX B

Estimating the minimum value of $\mathscr{R}$

Here we will estimate the minimum value of the ratio between the hidden sector energy density and the radiation energy density

$$\mathscr{R} \equiv \frac{\rho_h}{\rho_\gamma}. \tag{B.1}$$

during the reheating phase (see Fig.1 regions $\mathrm{I.A}$ and $\mathrm{I.B}$). Once we enter the transition phase (region $\mathrm{I.A}$), if μ is large enough, most of the energy density will be stored in radiation, followed by the phantom field, and the least amount is contained by the hidden matter sector. To a good approximation we will use 'radiation domination' in what follows, since we are only interested in order of magnitude estimates.

First we will look at the case when the hidden matter is non-relativistic when this transition occurs, i.e. $\omega = 0$. Setting μ_r to zero, as appropriate for the transition to radiation, we will have the following equations for the evolution of the system:

$$\begin{aligned} \dot{\rho}_h + 3H\rho_h &= -\rho_h \Gamma & \text{(B.2)} \\ \ddot{\phi} + 3H\dot{\phi} &= 0 & \text{(B.3)} \\ \dot{\rho}_\gamma + 4H\rho_\gamma &= 0 & \text{(B.4)} \end{aligned}$$

along with the Hubble equation

$$H^2 = \frac{1}{3M_p^2}(\rho_\gamma) \tag{B.5}$$

We have neglected the annihilation term in equation (B.4) because $\rho_h \Gamma \ll 4H\rho_\gamma$ will be satisfied very quickly after the transition from the deSitter phase is started. The solutions for the energy densities are simple:

$$\rho_h(t) = \frac{1}{t^{\frac{3}{2}}C_1 - 2tm^{-3}} \tag{B.6}$$

$$\rho_\gamma(t) = \frac{3M_p^2}{4t^2} \tag{B.7}$$

where C_1 is an integration constant we still have to fix. We have used the fact that during radiation domination $H \sim \frac{1}{2t}$ in order to get the coefficient for the radiation energy density. Since it takes a longer time for the annihilation term to be sub-dominant with respect to the Hubble dampening term in the hidden matter continuity equation, we will have a short period where the energy density in hidden matter is decreasing faster than a^{-3}. This yields a minimum value for the parameter $\mathscr{R}$. Simply setting $\dot{\mathscr{R}}(t) = 0$ leads to $\Gamma(t_c) \sim H(t_c)$. In order to fix the integration constant C_1, we need to know at what time we start the transition from deSitter to radiation dominated phase. Using the initial condition[1] in (2.35) along with equation (B.7), the transition time is found to be:

$$t_{1A} = \left(\frac{3M_p^4 \xi}{m^6 \eta^3}\right)^{\frac{1}{2}}. \tag{B.8}$$

Furthermore, C_1 is obtained by requiring that the hidden matter density ρ_h value in the deSitter phase matches the value estimated at the transition time t_{1A}, obtained from (B.6). The initial conditions (2.33) together with (2.32) allows us to evaluate the initial value of

[1] Here we consider the transition from dS phase to the radiation dominated phase due to the sudden drop in the coupling between the hidden sector fields and the ghost field. The asymptotic value (valid for the dS phase) for the energy density in equation (2.35) (the right hand side of the equation) here becomes an initial condition for the transition phase, Region IA.

hidden matter density at the beginning of the transition phase. In the limit of $\mu_p \gg 1$ we get the following simplified form for the integration constant:

$$C_1 = \frac{\sqrt{3}(3M_p^2 + 32\sqrt{3}\mu_p^3 m^3 t_{1A})}{48 m^6 \mu_p^3 t_{1A}^{\frac{3}{2}}} \tag{B.9}$$

In order to get the minimum value for $\mathscr{R}$ we go back to the condition $\Gamma = \frac{\rho_h(t_c)}{m^3} \sim H(t_c)$, where t_c represents the time at which this minimum is attained. This can be rewritten as:

$$\frac{\rho_h}{m^3} \sim \frac{\rho_\gamma^{\frac{1}{2}}}{\sqrt{3}M_p} \tag{B.10}$$

leading to

$$\mathscr{R}_{\mathtt{min}} \sim \frac{2m^3 t_c}{3M_p^2} \tag{B.11}$$

Also, from (B.10) we can solve for t_c using (B.6) and (B.7): $t_c = \frac{16}{C_1^2 m^6}$. Plugging into (B.11) we get the simplified form:

$$\mathscr{R}_{\mathtt{min}} = \frac{32}{3M_p^2 m^3 C_1^2} \tag{B.12}$$

Using (B.8) and (B.9) in the above equation we obtain the final result, expressed only in terms of μ_p:

$$\mathscr{R}_{\mathtt{min}} = \frac{16}{\sqrt{3}\mu_p^{\frac{3}{2}}(1 + 4\sqrt{\mu_p})^2} \tag{B.13}$$

Let us now turn our attention to the case where the hidden matter becomes relativistic at the energy scales where the transition between the deSitter and the radiation phases occurs. At the beginning there will still be a regime where the annihilation is effective, thus lowering the value of the ratio between the hidden matter energy density and the radiation energy density. If $\mu_r = 0$, instead of a minimum we will now have a constant asymptotic value towards which this ratio will tend. This is due to the fact that once the conversion is no longer efficient, both hidden matter and radiation energy densities will scale as a^{-4}. For completeness and generality we will study the case where $\mu_r \neq 0$. As we shall shortly see here a minimum develops, just as we have seen in the case of non-relativistic hidden matter. The approximative equations we need to solve are:

$$\begin{aligned} \dot{\rho}_h + 4H\rho_h &= -\rho_h\Gamma + 2\rho_h\dot{\phi}\frac{\mu_r}{M_p} && \text{(B.14)} \\ \ddot{\phi} + 3H\dot{\phi} &= 0 && \text{(B.15)} \\ \dot{\rho}_\gamma + 4H\rho_\gamma &= 0 && \text{(B.16)} \end{aligned}$$

along with the Hubble equation

$$H^2 = \frac{1}{3M_p^2}\rho_\gamma \tag{B.17}$$

Notice that we have neglected the ρ_h terms in the second and third equations since we are interested in the phase of rapid conversion of hidden sector particles to radiation. Therefore, in this regime the energy density stored in the hidden sector will decay much faster than a^{-4}. Essentially the reason for this being that μ has transitioned from large to small values, i.e $\mu_p \gg \mu_r$. The system admits the following solutions:

$$\begin{aligned} H(t) &= \frac{1}{2t} && \text{(B.18)} \\ \rho_\gamma(t) &= \frac{3M_p^2}{4t^2} && \text{(B.19)} \\ \dot{\phi}(t) &= \frac{A_\phi}{t^{\frac{3}{2}}} && \text{(B.20)} \\ \rho_h\,(t) &= \frac{8\,m^3{A_\phi}^2{\mu_r}^2}{D(t)} && \text{(B.21)} \end{aligned}$$

Where D(t) is:

$$D(t) = 4\,t^{3/2}M_pA_\phi\mu_r + t^2{M_p}^2 + 8\,t^2 \mathrm{e}^{4\,\frac{A_\phi\mu_r}{M_p\sqrt{t}}}C_hm^3{A_\phi}^2{\mu_r}^2$$

In order to obtain the integration constants C_h and A_ϕ we match the energy densities above, evaluated at the transition time t_{1A} with the corresponding values from the deSitter phase, given in (2.32) to (2.35). As before, t_{1A} is given by (B.8). For A_ϕ this leads to:

$$A_\phi = \frac{2}{3}\,\frac{\mu_p {M_p}^2 3^{3/4} \xi^{3/4}}{\eta^{5/4} m^{3/2}} \tag{B.22}$$

The expression for C_h for general μ_p turns out to be messy, but it can be simplified in the limit $\mu_p \gg 1$ to:

$$C_h = -\frac{1}{3}\,\frac{\sqrt{3}\mu_p \left(-4\,{\mu_r}^2 + 4\,\mu_p\mu_r + \mu_p\right) \mathrm{e}^{-4\,\mu_r}}{{M_p}^2 {\mu_r}^2} \tag{B.23}$$

Above we have used $\xi \sim \frac{3\sqrt{3}}{\mu_p}$ and $\eta \sim 4\sqrt{3}\mu_p$, expressions valid in the $\mu_p \gg 1$ limit.

Since we have $\mu_r \neq 0$ it we expect a minimum of the ratio $\mathscr{R}$ to develop. Re-expressing $\dot{\mathscr{R}} = 0$ by use of the definition of $\mathscr{R}$, the ratio between the hidden sector and the radiation energy densities, and of the equations (B.14) and (B.16) we get,

$$\Gamma\left(\rho_h + \rho_r\right) = 2\rho_r\dot{\phi}\frac{\mu_r}{M_p} \tag{B.24}$$

Defining t_c the time at which the above equation holds, we find that

$$\mathscr{R}_{\mathtt{min}} \sim \frac{2m^3\dot{\phi}(t_c)\mu_r}{M_p\rho_\gamma(t_c)} = \frac{8}{3}\frac{m^3\mu_r A_\phi\sqrt{t_c}}{{M_p}^3} \tag{B.25}$$

From (B.24) we can also obtain t_c by using the solutions we have for the energy densities in (B.19) and (B.21) . In order to get a closed form we will need to do some approximation of the exponent in the denominator of (B.21). Since $t > t_{1A}$ we can show using t_{1A} from (B.8) and A_ϕ from (B.22) that $\frac{4A_\phi\mu_r}{M_p\sqrt{t}} \leq 4\mu_r$. Since $\mu_r \ll 1$ we will truncate the expansion of the exponential at terms of $\mathcal{O}(\mu_r^2)$, leading to:

$$t_c = 1024\,\frac{{C_h}^2 m^6 {A_\phi}^6 {\mu_r}^6}{{M_p}^2\left({M_p}^2 + 8\,C_h m^3 {A_\phi}^2 {\mu_r}^2\right)^2} \tag{B.26}$$

Going back to (B.25) we get, after some algebra, the following form for $\mathscr{R}_{\mathtt{min}}$:

$$\mathscr{R}_{\mathtt{min}} = \frac{4}{\sqrt{3}} \frac{{\mu_r}^2}{{\mu_p}^2} \mathrm{e}^{-4\,\mu_r} \left| \frac{1}{\mathrm{e}^{-4\mu_r} - \mu_p \left(\mu_p + 4\mu_r(\mu_p - \mu_r)\right)^{-1}} \right|$$

We can double expand this expression in μ_r and μ_p^{-1} and keep only the leading terms:

$$\mathscr{R}_{\mathtt{min}} \sim \frac{1}{18} \frac{\sqrt{3}(3 + 8\mu_r)}{\mu_p^2} + \mathcal{O}(\mu_r^2, \mu_p^{-3}) \tag{B.27}$$

In the limit $\mu_r \to 0$ we get the result in eq.(2.41).

BIBLIOGRAPHY

BIBLIOGRAPHY

Abazajian, K. N., P. Agrawal, Z. Chacko, and C. Kilic (2010), Conservative Constraints on Dark Matter from the Fermi-LAT Isotropic Diffuse Gamma-Ray Background Spectrum, *arXiv:1002.3820*.

Abdo, A. A., et al. (2009a), Fermi Large Area Telescope Measurements of the Diffuse Gamma-Ray Emission at Intermediate Galactic Latitudes, *Phys. Rev. Lett.*, *103*, 251,101, doi:10.1103/PhysRevLett.103.251101.

Abdo, A. A., et al. (2009b), Measurement of the Cosmic Ray e+ plus e- spectrum from 20 GeV to 1 TeV with the Fermi Large Area Telescope, *Phys. Rev. Lett.*, *102*, 181,101.

Abdo, A. A., et al. (2010), Constraints on Cosmological Dark Matter Annihilation from the Fermi-LAT Isotropic Diffuse Gamma-Ray Measurement, *JCAP*, *1004*, 014, doi: 10.1088/1475-7516/2010/04/014.

Adriani, O., et al. (2009a), An anomalous positron abundance in cosmic rays with energies 1.5.100 GeV, *Nature*, *458*, 607–609.

Adriani, O., et al. (2009b), A new measurement of the antiproton-to-proton flux ratio up to 100 GeV in the cosmic radiation, *Phys. Rev. Lett.*, *102*, 051,101.

Adriani, O., et al. (2010), A statistical procedure for the identification of positrons in the PAMELA experiment, *arXiv:1001.3522*.

Ahlers, M., P. Mertsch, and S. Sarkar (2009), On cosmic ray acceleration in supernova remnants and the FERMI/PAMELA data, *Phys. Rev.*, *D80*, 123,017, doi: 10.1103/PhysRevD.80.123017.

Alam, U., V. Sahni, T. Deep Saini, and A. A. Starobinsky (2004), Is there supernova evidence for dark energy metamorphosis?, MNRAS, *354*, 275–291, doi:10.1111/j.1365-2966.2004.08189.x.

Alexander, S., T. Biswas, A. Notari, and D. Vaid (2009), Local void vs dark energy: confrontation with WMAP and type Ia supernovae, J. Cosmology Astropart. Phys., *9*, 25–+, doi:10.1088/1475-7516/2009/09/025.

Alpher, R. A., and R. C. Herman (1948), On the Relative Abundance of the Elements, *Physical Review*, *74*, 1737–1742, doi:10.1103/PhysRev.74.1737.

Amendola, L. (2000), Coupled quintessence, Phys. Rev. D, *62*(4), 043,511–+, doi: 10.1103/PhysRevD.62.043511.

Amendola, L., and C. Quercellini (2003), Tracking and coupled dark energy as seen by the Wilkinson Microwave Anisotropy Probe, Phys. Rev. D, *68*(2), 023,514–+, doi: 10.1103/PhysRevD.68.023514.

Amendola, L., and D. Tocchini-Valentini (2001), Stationary dark energy: The present universe as a global attractor, Phys. Rev. D, *64*(4), 043,509–+, doi: 10.1103/PhysRevD.64.043509.

Amendola, L., M. Gasperini, and F. Piazza (2004), Fitting type Ia supernovae with coupled dark energy, J. Cosmology Astropart. Phys., *9*, 14–+, doi:10.1088/1475-7516/2004/09/014.

Aref'eva, I. Y. (2007), Stringy Model of Cosmological Dark Energy, in *Particles, Strings, and Cosmology-PASCOS 2007*, *American Institute of Physics Conference Series*, vol. 957, edited by A. Rajantie, C. Contaldi, P. Dauncey, & H. Stoica, pp. 297–300, doi: 10.1063/1.2823785.

Aref'eva, I. Y., A. S. Koshelev, and S. Y. Vernov (2005), Crossing the w=-1 barrier in the D3-brane dark energy model, Phys. Rev. D, *72*(6), 064,017–+, doi: 10.1103/PhysRevD.72.064017.

Aref'eva, I. Y., L. V. Joukovskaya, and S. Y. Vernov (2007), Bouncing and accelerating solutions in nonlocal stringy models, *Journal of High Energy Physics*, *7*, 87–+, doi: 10.1088/1126-6708/2007/07/087.

Arkani-Hamed, N., D. P. Finkbeiner, T. R. Slatyer, and N. Weiner (2009), A Theory of Dark Matter, *Phys. Rev.*, *D79*, 015,014.

Bahcall, J. N. (1989), *Neutrino astrophysics*, Cambridge and New York, Cambridge University Press, 1989, 584 p.

Bai, Y., M. Carena, and J. Lykken (2009), The PAMELA excess from neutralino annihilation in the NMSSM, *Phys. Rev.*, *D80*, 055,004, doi:10.1103/PhysRevD.80.055004.

Bajc, B., T. Enkhbat, D. K. Ghosh, G. Senjanovic, and Y. Zhang (2010), MSSM in view of PAMELA and Fermi-LAT, *JHEP*, *05*, 048, doi:10.1007/JHEP05(2010)048.

Baltz, E. A., J. Edsjo, K. Freese, and P. Gondolo (2002), The cosmic ray positron excess and neutralino dark matter, *Phys. Rev.*, *D65*, 063,511, doi:10.1103/PhysRevD.65.063511.

Barenboim, G., and J. Lykken (2006), Slinky inflation, *Physics Letters B*, *633*, 453–457, doi:10.1016/j.physletb.2005.12.041.

Barger, V., Y. Gao, W. Y. Keung, D. Marfatia, and G. Shaughnessy (2009a), Dark matter and pulsar signals for Fermi LAT, PAMELA, ATIC, HESS and WMAP data, *Phys. Lett.*, *B678*, 283–292, doi:10.1016/j.physletb.2009.06.030.

Barger, V., W. Y. Keung, D. Marfatia, and G. Shaughnessy (2009b), PAMELA and dark matter, *Phys. Lett.*, *B672*, 141–146.

Barkana, R., and A. Loeb (2001), In the Beginning: The First Sources of Light and the Reionization of the Universe, *Phys. Rept.*, *349*, 125–238.

Barnaby, N., T. Biswas, and J. M. Cline (2007), p-adic inflation, *Journal of High Energy Physics*, *4*, 56–+, doi:10.1088/1126-6708/2007/04/056.

Barnes, J., and S. D. M. White (1984), The response of a spheroid to a disc field or were bulges ever ellipticals?, MNRAS, *211*, 753–765.

Barrow, J. D., and C. G. Tsagas (2009), On the stability of static ghost cosmologies, *Classical and Quantum Gravity*, *26*(19), 195,003–+, doi:10.1088/0264-9381/26/19/195003.

Barwick, S. W., et al. (1997), Measurements of the cosmic-ray positron fraction from 1-GeV to 50-GeV, *Astrophys. J.*, *482*, L191–L194.

Bean, R., É. É. Flanagan, I. Laszlo, and M. Trodden (2008a), Constraining interactions in cosmology's dark sector, Phys. Rev. D, *78*(12), 123,514–+, doi: 10.1103/PhysRevD.78.123514.

Bean, R., É. É. Flanagan, and M. Trodden (2008b), Adiabatic instability in coupled dark energy/dark matter models, Phys. Rev. D, *78*(2), 023,009–+, doi: 10.1103/PhysRevD.78.023009.

Bergstrom, L., J. Edsjo, and G. Zaharijas (2009), Dark matter interpretation of recent electron and positron data, *Phys. Rev. Lett.*, *103*, 031,103.

Bertone, G., and M. Fairbairn (2008), Compact Stars as Dark Matter Probes, *Phys. Rev.*, *D77*, 043,515.

Bi, X.-J., et al. (2009), Non-Thermal Production of WIMPs, Cosmic $e^{\pm}$ Excesses and γ-rays from the Galactic Center, *Phys. Rev.*, *D80*, 103,502, doi: 10.1103/PhysRevD.80.103502.

Biswas, T. (2008), Emergence of a Cyclic Universe from the Hagedorn Soup, *ArXiv e-prints*.

Biswas, T., and S. Alexander (2009), Cyclic inflation, Phys. Rev. D, *80*(4), 043,511–+, doi:10.1103/PhysRevD.80.043511.

Biswas, T., and A. Mazumdar (2005), Can we have a Stringy Origin Behind $\Omega_\Lambda(t) \propto \Omega_M(t)$?, in *PASCOS 2004 Part I: Particles, Strings and Cosmology*, edited by G. Alverson, E. Barberis, P. Nath, & M. T. Vaughn, pp. 32–37.

Biswas, T., and A. Mazumdar (2006), A stringy origin of the recent acceleration, *Phys.Lett.*, *B634*, 437–441, doi:10.1016/j.physletb.2006.02.015.

Biswas, T., and A. Mazumdar (2009), Inflation with a negative cosmological constant, Phys. Rev. D, *80*(2), 023,519–+, doi:10.1103/PhysRevD.80.023519.

Biswas, T., R. Brandenberger, A. Mazumdar, and T. Multamäki (2006), Current acceleration from the dilaton and stringy cold dark matter, Phys. Rev. D, *74*(6), 063,501–+, doi:10.1103/PhysRevD.74.063501.

Biswas, T., R. Mansouri, and A. Notari (2007), Non-linear structure formation and 'apparent' acceleration: an investigation, J. Cosmology Astropart. Phys., *12*, 17–+, doi:10.1088/1475-7516/2007/12/017.

Blasi, P. (2009), The origin of the positron excess in cosmic rays, *Phys. Rev. Lett.*, *103*, 051,104.

Blumenthal, G. R., S. M. Faber, R. Flores, and J. R. Primack (1986), Contraction of Dark Matter Galactic Halos Due to Baryonic Infall, *Astrophys. J.*, *301*, 27.

Boulares, A. (1989), The nature of the cosmic-ray electron spectrum, and supernova remnant contributions, *Astrophys. J.*, *342*, 807–813.

Bouquet, A., and P. Salati (1989), Dark matter and the suppression of stellar core convection, ApJ, *346*, 284–288.

Bouwens, R. J., G. D. Illingworth, J. P. Blakeslee, and M. Franx (2006), Galaxies at z ˜ 6: The UV Luminosity Function and Luminosity Density from 506 HUDF, HUDF Parallel ACS Field, and GOODS i-Dropouts, ApJ, *653*, 53–85, doi:10.1086/498733.

Bouwens, R. J., G. D. Illingworth, M. Franx, and H. Ford (2008), z ˜ 7-10 Galaxies in the HUDF and GOODS Fields: UV Luminosity Functions, ApJ, *686*, 230–250, doi:10.1086/590103.

Bouwens, R. J., et al. (2011), A candidate redshift z˜10 galaxy and rapid changes in that population at an age of 500Myr, Nature, *469*, 504–507, doi:10.1038/nature09717.

Bromm, V., and R. B. Larson (2004), The First Stars, *Ann. Rev. Astron. Astrophys.*, *42*, 79–118.

Brown, M. G., K. Freese, and W. H. Kinney (2008), The phantom bounce: a new oscillating cosmology, J. Cosmology Astropart. Phys., *3*, 2–+, doi:10.1088/1475-7516/2008/03/002.

Cai, Y., T. Qiu, X. Zhang, Y. Piao, and M. Li (2007), Bouncing universe with Quintom matter, *Journal of High Energy Physics*, *10*, 71–+, doi:10.1088/1126-6708/2007/10/071.

Caldwell, R. R. (2002), A phantom menace? Cosmological consequences of a dark energy component with super-negative equation of state, *Physics Letters B*, *545*, 23–29, doi:10.1016/S0370-2693(02)02589-3.

Caldwell, R. R., and M. Kamionkowski (2009), The Physics of Cosmic Acceleration, *Annual Review of Nuclear and Particle Science*, *59*, 397–429, doi:10.1146/annurev-nucl-010709-151330.

Caldwell, R. R., M. Kamionkowski, and N. N. Weinberg (2003), Phantom Energy: Dark Energy with w ¡-1 Causes a Cosmic Doomsday, *Physical Review Letters*, *91*(7), 071,301–+, doi:10.1103/PhysRevLett.91.071301.

Carroll, S. M., M. Hoffman, and M. Trodden (2003), Can the dark energy equation-of-state parameter w be less than -1?, Phys. Rev. D, *68*(2), 023,509–+, doi: 10.1103/PhysRevD.68.023509.

Catena, R., N. Fornengo, M. Pato, L. Pieri, and A. Masiero (2009), Thermal Relics in Modified Cosmologies: Bounds on Evolution Histories of the Early Universe and Cosmological Boosts for PAMELA, *arXiv:0912.4421*.

Célérier, M. (2007), The Accelerated Expansion of the Universe Challenged by an Effect of the Inhomogeneities. A Review, *ArXiv Astrophysics e-prints*.

Chandrasekhar, S. (1939), *An introduction to the study of stellar structure*, Chicago, Ill., The University of Chicago press [1939].

Chang, J., et al. (2008), An excess of cosmic ray electrons at energies of 300.800 GeV, *Nature*, *456*, 362–365.

Chen, C.-R., and F. Takahashi (2009), Cosmic rays from Leptonic Dark Matter, *JCAP*, *0902*, 004.

Chen, C.-R., M. M. Nojiri, F. Takahashi, and T. T. Yanagida (2009a), Decaying Hidden Gauge Boson and the PAMELA and ATIC/PPB- BETS Anomalies, *Prog. Theor. Phys.*, *122*, 553–559.

Chen, C.-R., F. Takahashi, and T. T. Yanagida (2009b), Gamma rays and positrons from a decaying hidden gauge boson, *Phys. Lett.*, *B671*, 71–76.

Chen, C.-R., S. K. Mandal, and F. Takahashi (2010), Gamma-ray Constraints on Hadronic and Leptonic Activities of Decaying Dark Matter, *JCAP*, *1001*, 023.

Cholis, I., G. Dobler, D. P. Finkbeiner, L. Goodenough, and N. Weiner (2009a), The Case for a 700+ GeV WIMP: Cosmic Ray Spectra from ATIC and PAMELA, *Phys. Rev.*, *D80*, 123,518.

Cholis, I., D. P. Finkbeiner, L. Goodenough, and N. Weiner (2009b), The PAMELA Positron Excess from Annihilations into a Light Boson, *JCAP*, *0912*, 007.

Cholis, I., L. Goodenough, D. Hooper, M. Simet, and N. Weiner (2009c), High Energy Positrons From Annihilating Dark Matter, *Phys. Rev.*, *D80*, 123,511.

Cirelli, M., and A. Strumia (2008), Minimal Dark Matter predictions and the PAMELA positron excess, *arXiv:0808.3867*.

Cirelli, M., R. Franceschini, and A. Strumia (2008), Minimal Dark Matter predictions for galactic positrons, anti-protons, photons, *Nucl. Phys.*, *B800*, 204–220, doi:10.1016/j.nuclphysb.2008.03.013.

Cirelli, M., M. Kadastik, M. Raidal, and A. Strumia (2009), Model-independent implications of the e+, e-, anti-proton cosmic ray spectra on properties of Dark Matter, *Nucl. Phys.*, *B813*, 1–21.

Clayton, D. D. (1968), *Principles of stellar evolution and nucleosynthesis*, New York: McGraw-Hill, 1968.

Cline, J. M., S. Jeon, and G. D. Moore (2004), The phantom menaced: Constraints on low-energy effective ghosts, Phys. Rev. D, *70*(4), 043,543–+, doi:10.1103/PhysRevD.70.043543.

Cognola, G., E. Elizalde, S. Nojiri, S. D. Odintsov, L. Sebastiani, and S. Zerbini (2008), Class of viable modified f(R) gravities describing inflation and the onset of accelerated expansion, Phys. Rev. D, *77*(4), 046,009–+, doi:10.1103/PhysRevD.77.046009.

Cognola, G., E. Elizalde, S. D. Odintsov, P. Tretyakov, and S. Zerbini (2009), Initial and final de Sitter universes from modified f(R) gravity, Phys. Rev. D, *79*(4), 044,001–+, doi:10.1103/PhysRevD.79.044001.

Copeland, E. J., A. R. Liddle, and D. Wands (1998), Exponential potentials and cosmological scaling solutions, Phys. Rev. D, *57*, 4686–4690, doi:10.1103/PhysRevD.57.4686.

Creminelli, P., M. A. Luty, A. Nicolis, and L. Senatore (2006), Starting the Universe: stable violation of the null energy condition and non-standard cosmologies, *Journal of High Energy Physics*, *12*, 80–+, doi:10.1088/1126-6708/2006/12/080.

Creminelli, P., G. D'Amico, J. Noreña, and F. Vernizzi (2009), The effective theory of quintessence: the $w < -1$ side unveiled, J. Cosmology Astropart. Phys., *2*, 18–+, doi:10.1088/1475-7516/2009/02/018.

Dabrowski, M. P., T. Stachowiak, and M. Szydłowski (2003), Phantom cosmologies, Phys. Rev. D, *68*(10), 103,519–+, doi:10.1103/PhysRevD.68.103519.

de Boer, W., C. Sander, M. Horn, and D. Kazakov (2002), Positron fraction from dark matter annihilation in the CMSSM, *Nucl. Phys. Proc. Suppl.*, *113*, 221–228, doi:10.1016/S0920-5632(02)01845-5.

Delahaye, T., et al. (2009), Anti-Matter in Cosmic Rays : Backgrounds and Signals, *arXiv:0905.2144*.

Di Bernardo, G., D. Gaggero, D. Grasso, and f. t. F.-L. collaboration (2009), The High Energy Cosmic Ray Electron Spectrum measured by Fermi Gamma-Ray Space Telescope: some possible interpretations, *arXiv:0912.3887*.

Diemand, J., M. Kuhlen, and P. Madau (2007), Formation and evolution of galaxy dark matter halos and their substructure, *Astrophys. J.*, *667*, 859, doi:10.1086/520573.

Diemand, J., et al. (2008), Clumps and streams in the local dark matter distribution, *Nature*, *454*, 735–738, doi:10.1038/nature07153.

Drukier, A. K., K. Freese, and D. N. Spergel (1986), Detecting cold dark-matter candidates, *Phys. Rev. D*, *33*(12), 3495–3508, doi:10.1103/PhysRevD.33.3495.

Dubovsky, S., T. Grégoire, A. Nicolis, and R. Rattazzi (2006), Null energy condition and superluminal propagation, *Journal of High Energy Physics*, *3*, 25–+, doi:10.1088/1126-6708/2006/03/025.

Feldman, D., Z. Liu, and P. Nath (2009), PAMELA Positron Excess as a Signal from the Hidden Sector, *Phys. Rev.*, *D79*, 063,509.

Feng, B., X. Wang, and X. Zhang (2005), Dark energy constraints from the cosmic age and supernova, *Physics Letters B*, *607*, 35–41, doi:10.1016/j.physletb.2004.12.071.

Fox, P. J., and E. Poppitz (2009), Leptophilic Dark Matter, *Phys. Rev.*, *D79*, 083,528.

Freese, K. (1986), Can scalar neutrinos or massive Dirac neutrinos be the missing mass?, *Physics Letters B*, *167*, 295–300, doi:10.1016/0370-2693(86)90349-7.

Freese, K., and D. Spolyar (2005), Chain inflation: 'Bubble bubble toil and trouble', *JCAP*, *0507*, 007, doi:10.1088/1475-7516/2005/07/007.

Freese, K., P. Bodenheimer, D. Spolyar, and P. Gondolo (2008a), Stellar Structure of Dark Stars: a first phase of Stellar Evolution due to Dark Matter Annihilation, *Astrophys. J.*, *685*, L101–L112.

Freese, K., D. Spolyar, and A. Aguirre (2008b), Dark Matter Capture in the first star: a Power source and a limit on Stellar Mass, *JCAP*, *0811*, 014.

Freese, K., P. Gondolo, J. A. Sellwood, and D. Spolyar (2009), Dark Matter Densities during the Formation of the First Stars and in Dark Stars, *Astrophys. J.*, *693*, 1563–1569.

Freese, K., C. Ilie, D. Spolyar, M. Valluri, and P. Bodenheimer (2010a), Supermassive Dark Stars: Detectable in JWST, *Astrophys.J.*, *716*, 1397–1407, doi:10.1088/0004-637X/716/2/1397.

Freese, K., C. Ilie, D. Spolyar, M. Valluri, and P. Bodenheimer (2010b), Supermassive Dark Stars: Detectable in JWST, *arXiv:1002.2233*.

Fujita, Y., et al. (2009), Is the PAMELA anomaly caused by the supernova explosions near the Earth?, *Phys. Rev.*, *D80*, 063,003, doi:10.1103/PhysRevD.80.063003.

Gamow, G. (1946), Expanding universe and the origin of elements, *Phys.Rev.*, *70*, 572–573, doi:10.1103/PhysRev7.0.572.

Gamow, G. (1948), The Origin of Elements and the Separation of Galaxies, *Physical Review*, *74*, 505–506, doi:10.1103/PhysRev.74.505.2.

Gao, L., et al. (2007), The first generation of stars in LCDM cosmology, *Mon. Not. Roy. Astron. Soc.*, *378*, 449.

Gelmini, G. B., and P. Gondolo (2008), Ultra-cold WIMPs: relics of non-standard pre-BBN cosmologies, *JCAP*, *0810*, 002, doi:10.1088/1475-7516/2008/10/002.

Gibbons, G. W. (2003), Phantom Matter and the Cosmological Constant, *ArXiv High Energy Physics - Theory e-prints*.

Gondolo, P., and J. Silk (2000), Dark matter at the galactic center, *Nucl.Phys.Proc.Suppl.*, *87*, 87–89, doi:10.1016/S0920-5632(00)00640-X.

Gondolo, P., J.-H. Huh, H. D. Kim, and S. Scopel (2010), Dark Matter that can form Dark Stars, *arXiv:1004.1258*.

Grajek, P., G. Kane, D. Phalen, A. Pierce, and S. Watson (2009), Is the PAMELA Positron Excess Winos?, *Phys. Rev.*, *D79*, 043,506, doi:10.1103/PhysRevD.79.043506.

Grasso, D., et al. (2009), On possible interpretations of the high energy electron- positron spectrum measured by the Fermi Large Area Telescope, *Astropart. Phys.*, *32*, 140–151, doi:10.1016/j.astropartphys.2009.07.003.

Greif, T. H., S. C. O. Glover, V. Bromm, and R. S. Klessen (2010), The First Galaxies: Chemical Enrichment, Mixing, and Star Formation, ApJ, *716*, 510–520, doi: 10.1088/0004-637X/716/1/510.

Grinstein, B., D. O'Connell, and M. B. Wise (2008), The Lee-Wick standard model, Phys. Rev. D, *77*(2), 025,012–+, doi:10.1103/PhysRevD.77.025012.

Guo, W.-L., and Y.-L. Wu (2009), Enhancement of Dark Matter Annihilation via Breit-Wigner Resonance, *Phys. Rev.*, *D79*, 055,012.

Guo, Z., Y. Piao, X. Zhang, and Y. Zhang (2005), Cosmological evolution of a quintom model of dark energy, *Physics Letters B*, *608*, 177–182, doi: 10.1016/j.physletb.2005.01.017.

Guth, A. H. (1981), Inflationary universe: A possible solution to the horizon and flatness problems, *Phys. Rev. D*, *23*(2), 347–356, doi:10.1103/PhysRevD.23.347.

Hamed, N. A., H. S. Cheng, M. A. Luty, and S. Mukohyama (2004), Ghost Condensation and a Consistent IR Modification of Gravity, *Journal of High Energy Physics*, *5*, 74–+, doi:10.1088/1126-6708/2004/05/074.

Hao, J., and X. Li (2003), Attractor solution of phantom field, Phys. Rev. D, *67*(10), 107,303–+, doi:10.1103/PhysRevD.67.107303.

Hao, J., and X. Li (2004), Phantom cosmic dynamics: Tracking attractor and cosmic doomsday, Phys. Rev. D, *70*(4), 043,529–+, doi:10.1103/PhysRevD.70.043529.

He, X.-G. (2009), Dark Matter Annihilation Explanation for e+- Excesses in Cosmic Ray, *Mod. Phys. Lett.*, *A52*, 2139–2160.

Hisano, J., S. Matsumoto, and M. M. Nojiri (2004), Explosive dark matter annihilation, *Phys. Rev. Lett.*, *92*, 031,303.

Hooper, D., and J. Silk (2005), Searching for dark matter with future cosmic positron experiments, *Phys. Rev.*, *D71*, 083,503, doi:10.1103/PhysRevD.71.083503.

Hooper, D., and K. M. Zurek (2009), The PAMELA and ATIC Signals From Kaluza-Klein Dark Matter, *Phys. Rev.*, *D79*, 103,529.

Hooper, D., J. E. Taylor, and J. Silk (2004), Can supersymmetry naturally explain the positron excess?, *Phys. Rev.*, *D69*, 103,509, doi:10.1103/PhysRevD.69.103509.

Hooper, D., P. Blasi, and P. D. Serpico (2009a), Pulsars as the Sources of High Energy Cosmic Ray Positrons, *JCAP*, *0901*, 025.

Hooper, D., A. Stebbins, and K. M. Zurek (2009b), Excesses in cosmic ray positron and electron spectra from a nearby clump of neutralino dark matter, *Phys. Rev.*, *D79*, 103,513, doi:10.1103/PhysRevD.79.103513.

Hooper, D., D. Spolyar, A. Vallinotto, and N. Y. Gnedin (2010), Inelastic Dark Matter As An Efficient Fuel For Compact Stars, *arXiv:1002.0005*.

Ibarra, A., and D. Tran (2009), Decaying Dark Matter and the PAMELA Anomaly, *JCAP*, *0902*, 021, doi:10.1088/1475-7516/2009/02/021.

Ibarra, A., A. Ringwald, D. Tran, and C. Weniger (2009), Cosmic Rays from Leptophilic Dark Matter Decay via Kinetic Mixing, *JCAP*, *0908*, 017.

Ibe, M., H. Murayama, S. Shirai, and T. T. Yanagida (2009a), Cosmic Ray Spectra in Nambu-Goldstone Dark Matter Models, *JHEP*, *11*, 120.

Ibe, M., H. Murayama, and T. T. Yanagida (2009b), Breit-Wigner Enhancement of Dark Matter Annihilation, *Phys. Rev.*, *D79*, 095,009.

Ichiki, K., M. Yahiro, T. Kajino, M. Orito, and G. J. Mathews (2002), Observational constraints on dark radiation in brane cosmology, Phys. Rev. D, *66*(4), 043,521–+, doi: 10.1103/PhysRevD.66.043521.

Iglesias, C. A., and F. J. Rogers (1996), Updated Opal Opacities, *Astrophys. J.*, *464*, 943.

Iliev, I. T., K. Ahn, J. Koda, P. R. Shapiro, and U. Pen (2010), Cosmic Structure Formation at High Redshift, *arXiv: 1005.2502*.

Iocco, F. (2008), Dark Matter capture and annihilation over the First Stars: preliminary estimates, *Astrophys. J.*, *677*, L1.

Iocco, F., et al. (2008), Dark matter annihilation effects on the first stars, *Mon. Not. Roy. Astron. Soc.*, *390*, 1655–1669.

Ishiwata, K., S. Matsumoto, and T. Moroi (2009), Cosmic-Ray Positron from Superparticle Dark Matter and the PAMELA Anomaly, *Phys. Lett.*, *B675*, 446–449.

Johnson, J. L., T. H. Greif, and V. Bromm (2008), Occurrence of metal-free galaxies in the early Universe, MNRAS, *388*, 26–38, doi:10.1111/j.1365-2966.2008.13381.x.

Johri, V. B. (2004), Phantom cosmologies, Phys. Rev. D, *70*(4), 041,303–+, doi:10.1103/PhysRevD.70.041303.

Kadota, K., K. Freese, and P. Gondolo (2010), Positrons in Cosmic Rays from Dark Matter Annihilations for Uplifted Higgs Regions in MSSM, *arXiv:1003.4442*.

Kamionkowski, M., S. M. Koushiappas, and M. Kuhlen (2010), Galactic Substructure and Dark Matter Annihilation in the Milky Way Halo, *Phys. Rev.*, *D81*, 043,532, doi:10.1103/PhysRevD.81.043532.

Kane, G. L., L.-T. Wang, and J. D. Wells (2002), Supersymmetry and the positron excess in cosmic rays, *Phys. Rev.*, *D65*, 057,701, doi:10.1103/PhysRevD.65.057701.

Khoury, J., B. A. Ovrut, P. J. Steinhardt, and N. Turok (2001), A Brief Comment on ”The Pyrotechnic Universe”, *ArXiv High Energy Physics - Theory e-prints*.

Khoury, J., B. A. Ovrut, P. J. Steinhardt, and N. Turok (2002), Density perturbations in the ekpyrotic scenario, Phys. Rev. D, *66*(4), 046,005–+, doi:10.1103/PhysRevD.66.046005.

Kippenhahn, R., and A. Weigert (1990), *Stellar Structure and Evolution*, Springer-Verlag.

Klypin, A., S. Trujillo-Gomez, and J. Primack (2010), Halos and galaxies in the standard cosmological model: results from the Bolshoi simulation, *arXiv:1002.3660*.

Komatsu, E., et al. (2009), Five-Year Wilkinson Microwave Anisotropy Probe Observations: Cosmological Interpretation, ApJS, *180*, 330–376, doi:10.1088/0067-0049/180/2/330.

Krauss, L. M., K. Freese, W. Press, and D. Spergel (1985), Cold dark matter candidates and the solar neutrino problem, *Astrophys. J.*, *299*, 1001.

Krauss, L. M., M. Srednicki, and F. Wilczek (1986), Solar System Constraints and Signatures for Dark Matter Candidates, *Phys.Rev.*, *D33*, 2079–2083, doi:10.1103/PhysRevD.33.2079, revised version of NSF-ITP-85-58.

Lattanzi, M., and J. I. Silk (2009), Can the WIMP annihilation boost factor be boosted by the Sommerfeld enhancement?, *Phys. Rev.*, *D79*, 083,523.

Lee, S. (2008), Lee Wick Dark Energy, *ArXiv e-prints*.

Lee, T. D., and G. C. Wick (1969), Negative Metric and the Unitarity of the S Matrix, *Nucl. Phys.*, *B9*, 209–243, doi:10.1016/0550-3213(69)90098-4.

Lee, T. D., and G. C. Wick (1970), Finite Theory of Quantum Electrodynamics, Phys. Rev. D, *2*, 1033–1048, doi:10.1103/PhysRevD.2.1033.

Lenzuni, P., D. F. Chernoff, and E. E. Salpeter (1991), Rosseland and Planck mean opacities of a zero-metallicity gas, ApJS, *76*, 759–801.

Libanov, M., V. Rubakov, E. Papantonopoulos, M. Sami, and S. Tsujikawa (2007), Ultraviolet stable, Lorentz-violating dark energy with transient phantom era, J. Cosmology Astropart. Phys., *8*, 10–+, doi:10.1088/1475-7516/2007/08/010.

Lidsey, J. E., D. J. Mulryne, N. J. Nunes, and R. Tavakol (2004), Oscillatory universes in loop quantum cosmology and initial conditions for inflation, Phys. Rev. D, *70*(6), 063,521–+, doi:10.1103/PhysRevD.70.063521.

Lyth, D. H., and A. Riotto (1999), Particle physics models of inflation and the cosmological density perturbation, *Phys.Rept.*, *314*, 1–146, doi:10.1016/S0370-1573(98)00128-8.

Malyshev, D., I. Cholis, and J. Gelfand (2009), Pulsars versus Dark Matter Interpretation of ATIC/PAMELA, *Phys. Rev.*, *D80*, 063,005, doi:10.1103/PhysRevD.80.063005.

March-Russell, J., S. M. West, D. Cumberbatch, and D. Hooper (2008), Heavy Dark Matter Through the Higgs Portal, *JHEP*, *07*, 058.

McKee, C. F., and J. C. Tan (2008), The Formation of the First Stars. II. Radiative Feedback Processes and Implications for the Initial Mass Function, ApJ, *681*, 771–797.

Meade, P., M. Papucci, and T. Volansky (2009), Dark Matter Sees The Light, *JHEP*, *12*, 052, doi:10.1088/1126-6708/2009/12/052.

Meade, P., M. Papucci, A. Strumia, and T. Volansky (2010), Dark Matter Interpretations of the Electron/Positron Excesses after FERMI, *Nucl. Phys.*, *B831*, 178–203, doi:10.1016/j.nuclphysb.2010.01.012.

Mertsch, P., and S. Sarkar (2009), Testing astrophysical models for the PAMELA positron excess with cosmic ray nuclei, *Phys. Rev. Lett.*, *103*, 081,104, doi:10.1103/PhysRevLett.103.081104.

Merz, H., U.-L. Pen, and H. Trac (2005), Towards optimal parallel PM N-body codes: PMFAST, *New Astron.*, *10*, 393–407, doi:10.1016/j.newast.2005.02.001.

Moeller, N., and B. Zwiebach (2002), Dynamics with Infinitely Many Time Derivatives and Rolling Tachyons, *Journal of High Energy Physics*, *10*, 34–+, doi:10.1088/1126-6708/2002/10/034.

Moskalenko, I. V., and L. L. Wai (2007), Dark matter burners, *Astrophys. J.*, *659*, L29–L32.

Mulryne, D. J., N. J. Nunes, R. Tavakol, and J. E. Lidsey (2005a), Inflationary Cosmology and Oscillating Universes in Loop Quantum Cosmology, *International Journal of Modern Physics A*, *20*, 2347–2357, doi:10.1142/S0217751X05024614.

Mulryne, D. J., R. Tavakol, J. E. Lidsey, and G. F. Ellis (2005b), An emergent universe from a loop, Phys. Rev. D, *71*(12), 123,512–+, doi:10.1103/PhysRevD.71.123512.

Navarro, J. F., C. S. Frenk, and S. D. M. White (1996), The Structure of Cold Dark Matter Halos, *Astrophys. J.*, *462*, 563–575.

Nelson, A. E., and C. Spitzer (2008), Slightly Non-Minimal Dark Matter in PAMELA and ATIC, *arXiv:0810.5167*.

Nojiri, S., and S. D. Odintsov (2003), Quantum de Sitter cosmology and phantom matter, *Physics Letters B*, *562*, 147–152, doi:10.1016/S0370-2693(03)00594-X.

Nojiri, S., and S. D. Odintsov (2008), Dark energy, inflation and dark matter from modified F(R) gravity, *ArXiv e-prints*.

Nomura, Y., and J. Thaler (2009), Dark Matter through the Axion Portal, *Phys. Rev.*, *D79*, 075,008.

Olive, K. A., G. Steigman, and T. P. Walker (2000), Primordial nucleosynthesis: theory and observations, Phys. Rep., *333*, 389–407, doi:10.1016/S0370-1573(00)00031-4.

Omukai, K., and R. Nishi (1998), Formation of Primordial Protostars, *Astrophys. J.*, *508*, 141.

Pallis, C. (2010), Cold Dark Matter in non-Standard Cosmologies, PAMELA, ATIC and Fermi LAT, *Nucl. Phys.*, *B831*, 217–247, doi:10.1016/j.nuclphysb.2010.01.015.

Peebles, P. J., and B. Ratra (2003), The cosmological constant and dark energy, *Reviews of Modern Physics*, *75*, 559–606, doi:10.1103/RevModPhys.75.559.

Profumo, S. (2005), TeV gamma-rays and the largest masses and annihilation cross sections of neutralino dark matter, *Phys. Rev.*, *D72*, 103,521.

Profumo, S. (2008), Dissecting Pamela (and ATIC) with Occam's Razor: existing, well-known Pulsars naturally account for the 'anomalous' Cosmic-Ray Electron and Positron Data, *arXiv:0812.4457*.

Raiter, A., D. Schaerer, and R. A. E. Fosbury (2010), Predicted UV properties of very metal-poor starburst galaxies, A&A, *523*, A64+, doi:10.1051/0004-6361/201015236.

Ripamonti, E., and T. Abel (2005), The Formation of Primordial Luminous Objects, *arXiv:astro-ph/0507130*.

Ripamonti, E., et al. (2009), WIMP annihilation effects on primordial star formation, *PoS*, *IDM2008*, 075.

Ripamonti, E., et al. (2010), First star formation with dark matter annihilation, *arXiv:1003.0676*.

Rubakov, V. A. (2006), Phantom without pathologies in the ultraviolet domain, *Theoretical and Mathematical Physics*, *149*, 1651–1664, doi:10.1007/s11232-006-0149-7.

Rubin, V. C., and W. K. Ford, Jr. (1970), Rotation of the Andromeda Nebula from a Spectroscopic Survey of Emission Regions, ApJ, *159*, 379–+, doi:10.1086/150317.

Ryden, B. S., and J. E. Gunn (1987), Galaxy formation by gravitational collapse, ApJ, *318*, 15–31.

Sadeghi, J., M. R. Setare, and A. Banijamali (2009), String inspired quintom model with non-minimally coupled modified gravity, *Physics Letters B*, *678*, 164–167, doi:10.1016/j.physletb.2009.06.008.

Salati, P., and J. Silk (1989), A stellar probe of dark matter annihilation in galactic nuclei, ApJ, *338*, 24–31.

Sami, M., and A. Toporensky (2004), Phantom Field and the Fate of the Universe, *Modern Physics Letters A*, *19*, 1509–1517, doi:10.1142/S0217732304013921.

Scannapieco, E., R. Schneider, and A. Ferrara (2003), The Detectability of the First Stars and Their Cluster Enrichment Signatures, ApJ, *589*, 35–52, doi:10.1086/374412.

Schaerer, D. (2002), On the properties of massive Population III stars and metal-free stellar populations, A&A, *382*, 28–42, doi:10.1051/0004-6361:20011619.

Schaerer, D. (2003), The transition from Population III to normal galaxies: Lyalpha and He II emission and the ionising properties of high redshift starburst galaxies, A&A, *397*, 527–538, doi:10.1051/0004-6361:20021525.

Schulz, A. E., and M. White (2001), Tensor to scalar ratio of phantom dark energy models, Phys. Rev. D, *64*(4), 043,514–+, doi:10.1103/PhysRevD.64.043514.

Scott, P., J. Edsjö, and M. Fairbairn (2007), Low mass stellar evolution with WIMP capture and annihilation, *arXiv:0711.0991*.

Scott, P., M. Fairbairn, and J. Edsjo (2008), Dark stars at the Galactic centre - the main sequence, *Mon. Not. Roy. Astron. Soc.*, *394*, 82.

Shalaby, A. M. (2009), Possible treatment of the ghost states in the Lee-Wick standard model, Phys. Rev. D, *80*(2), 025,006–+, doi:10.1103/PhysRevD.80.025006.

Shaviv, N. J., E. Nakar, and T. Piran (2009), Natural explanation for the anomalous positron to electron ratio with supernova remnants as the sole cosmic ray source, *Phys. Rev. Lett.*, *103*, 111,302, doi:10.1103/PhysRevLett.103.111302.

Shirai, S., F. Takahashi, and T. T. Yanagida (2009), Decaying hidden gaugino as a source of PAMELA/ATIC anomalies, *Physics Letters B*, *675*, 73–76.

Silk, J., K. A. Olive, and M. Srednicki (1985), The Photino, the Sun and High-Energy Neutrinos, *Phys.Rev.Lett.*, *55*, 257–259, doi:10.1103/PhysRevLett.55.257.

Silvestri, A., and M. Trodden (2009), Approaches to understanding cosmic acceleration, *Reports on Progress in Physics*, *72*(9), 096,901–+, doi:10.1088/0034-4885/72/9/096901.

Singh, P., M. Sami, and N. Dadhich (2003), Cosmological dynamics of a phantom field, Phys. Rev. D, *68*(2), 023,522–+, doi:10.1103/PhysRevD.68.023522.

Sivertsson, S., and P. Gondolo (2010), The WIMP capture process for dark stars in the early universe, *arXiv:1006.0025*.

Sommerfeld, A. (1931), Über die Beugung und Bremsung der Elektronen, *Annalen der Physik*, *403*, 257–330.

Spolyar, D., K. Freese, and P. Gondolo (2008), Dark matter and the first stars: a new phase of stellar evolution, *Phys. Rev. Lett.*, *100*, 051,101.

Spolyar, D., P. Bodenheimer, K. Freese, and P. Gondolo (2009), Dark Stars: a new look at the First Stars in the Universe, *Astrophys. J.*, *705*, 1031–1042.

Springel, V., et al. (2008), The Aquarius Project: the subhalos of galactic halos, *Mon. Not. Roy. Astron. Soc.*, *391*, 1685–1711, doi:10.1111/j.1365-2966.2008.14066.x.

Starobinskiĭ, A. A. (1979), Spectrum of relict gravitational radiation and the early state of the universe, *Soviet Journal of Experimental and Theoretical Physics Letters*, *30*, 682–+.

Steinhardt, P., and N. Turok (2002), A cyclic model of the universe, *Science*, *296*, 1436–1439, doi:10.1126/science.1070462.

Steinhardt, P. J., and N. Turok (2002), Cosmic evolution in a cyclic universe, Phys. Rev. D, *65*(12), 126,003–+, doi:10.1103/PhysRevD.65.126003.

Steinhardt, P. J., and N. Turok (2005), The cyclic model simplified, New A Rev., *49*, 43–57, doi:10.1016/j.newar.2005.01.003.

Stiavelli, M., and M. Trenti (2010), The Clustering Properties of the First Galaxies, ApJ, *716*, L190–L194, doi:10.1088/2041-8205/716/2/L190.

Tan, J. C., and C. F. McKee (2004), The Formation of the First Stars I. Mass Infall Rates, Accretion Disk Structure and Protostellar Evolution, *Astrophys. J.*, *603*, 383–400, doi:10.1086/381490.

Taoso, M., G. Bertone, G. Meynet, and S. Ekstrom (2008), Dark Matter annihilations in Pop III stars, *Phys. Rev.*, *D78*, 123,510.

Tinker, J. L., et al. (2010), The Large Scale Bias of Dark Matter Halos: Numerical Calibration and Model Tests, *arXiv:1001.3162*.

Tolman, R. (1934), *Relativity, Thermodynamics, and Cosmology.*, Oxford, Claredon.

Tornatore, L., A. Ferrara, and R. Schneider (2007), Population III stars: hidden or disappeared?, MNRAS, *382*, 945–950, doi:10.1111/j.1365-2966.2007.12215.x.

van Tonder, A. (2008), Unitarity, Lorentz invariance and causality in Lee-Wick theories: An asymptotically safe completion of QED, *ArXiv e-prints*.

Yin, P.-f., et al. (2009), PAMELA data and leptonically decaying dark matter, *Phys. Rev.*, *D79*, 023,512.

Yoon, S.-C., F. Iocco, and S. Akiyama (2008), Evolution of the First Stars with Dark Matter Burning, *Astrophys. J.*, *688*, L1–L5.

Yoshida, N., T. Abel, L. Hernquist, and N. Sugiyama (2003), Simulations of Early Structure Formation: Primordial Gas Clouds, *Astrophys. J.*, *592*, 645–663.

Yoshida, N., K. Omukai, L. Hernquist, and T. Abel (2006), Formation of Primordial Stars in a LCDM Universe, *Astrophys. J.*, *652*, 6–25.

Young, P. (1980), Numerical models of star clusters with a central black hole. I - Adiabatic models, ApJ, *242*, 1232–1237.

Zackrisson, E., P. Scott, C. Rydberg, F. Iocco, S. Sivertsson, G. Östlin, G. Mellema, I. T. Iliev, and P. R. Shapiro (2010a), Observational constraints on supermassive dark stars, MNRAS, *407*, L74–L78, doi:10.1111/j.1745-3933.2010.00908.x.

Zackrisson, E., C. E. Rydberg, D. Schaerer, G. Ostlin, and M. Tuli (2011), The spectral evolution of the first galaxies. I. JWST detection limits and colour criteria for population III galaxies.

Zackrisson, E., P. Scott, C. E. Rydberg, F. Iocco, S. Sivertsson, G. Östlin, G. Mellema, I. T. Iliev, and P. R. Shapiro (2011), Erratum: Observational constraints on supermassive dark stars, MNRAS, *410*, L57–L58, doi:10.1111/j.1745-3933.2010.00981.x.

Zackrisson, E., et al. (2010b), Finding High-redshift Dark Stars with the James Webb Space Telescope, ApJ, *717*, 257–267, doi:10.1088/0004-637X/717/1/257.

Zhao, D.-H., Y. P. Jing, H. J. Mo, and G. Borner (2003), Mass and Redshift Dependence of Dark Halo Structure, *Astrophys. J.*, *597*, L9–L12.

Zhao, D. H., Y. P. Jing, H. J. Mo, and G. Boerner (2009), Accurate universal models for the mass accretion histories and concentrations of dark matter halos, *Astrophys. J.*, *707*, 354–369, doi:10.1088/0004-637X/707/1/354.

Zurek, K. M. (2009), Multi-Component Dark Matter, *Phys. Rev.*, *D79*, 115,002.

Zwicky, F. (1933), Die Rotverschiebung von extragalaktischen Nebeln, *Helvetica Physica Acta*, *6*, 110–127.

Zwicky, F. (1937), On the Masses of Nebulae and of Clusters of Nebulae, ApJ, *86*, 217–+, doi:10.1086/143864.